The Evolution and Propagation of Solar Transients through the Heliosphere

Ailsa Joanne Prise

Thesis submitted for the degree of

Doctor of Philosophy (PhD)

of

University College London

Mullard Space Science Laboratory

Department of Space and Climate Physics

University College London

April 2015

I, Ailsa Prise, confirm that the work presented in this thesis is my own. Where information has been derived from other sources, I confirm that this has been indicated in the thesis.

_____

_____

Much of the work undertaken during study for this Ph.D. can be found in the following articles:

- Prise, A., Harra, L., Matthews, S., Long, D. and Aylward, A. (2014), An Investigation of the CME of 3 November 2011 and Its Associated Widespread Solar Energetic Particle Event, *Solar Physics* **289**(5), 1731-1744.

- Prise, A. J., Harra, L. K. Matthews, S. A., Arridge, C. S. and Achilleos, N. (2015), Analysis of a coronal mass ejection and corotating interaction region as they travel from the Sun passing Venus, Earth, Mars and Saturn, *Journal of Geophysical Research: Space Physics* **120**(3), 1566-1588. 2014JA020256.

Abstract

There are several different transient structures that propagate in the solar wind, including Coronal Mass Ejections (CMEs), Solar Energetic Particles (SEPs) and Co-rotating Interaction Regions (CIRs). A CME is an explosion of plasma and magnetic field from the Sun's corona. SEPs are high energy particles, produced directly by solar flares, or accelerated ahead of a shock associated with CMEs. CIRs are large scale structures in the solar wind, which arise from the interaction between fast solar wind as it catches up with slow solar wind. All these phenomena are capable of driving significant space weather effects on the Earth. This thesis studies the evolution and propagation of these different structures through the heliosphere, by making use of remote sensing, in-situ, and planetary data, as well as solar wind modelling. Widespread energetic particles associated with a CME were studied, and the longitudinal range of the particles connected with the lateral expansion of the CME. As the CME expands, it connects with more field lines on the Parker spiral, allowing the SEPs to propagate out across a wider range of longitudes. As CMEs are one of the most significant drivers of space weather, it is important to study how they evolve as they propagate. Multipoint observations and solar wind modelling of a CME and preceding CIR are used to study how both transients propagate and interact. The structures merge beyond the inner solar system and the impacts of the resulting structure are observed at Saturn. The ENLIL solar wind model is then analysed in more detail, by comparing the model outputs with multipoint in-situ data at 1 AU. Different initial conditions for the model were set up, including different magnetograms and coronal models. The variation of the model output with the addition of several CMEs were also studied.

Acknowledgements

First and foremost, I would like to thank my supervisors, Louise Harra and Sarah Matthews for their support and encouragement throughout my PhD. However busy your schedules, you never failed to find the time to sit down and discuss things with me when it felt like I was drowning in data! You were both practical and reassuring when I had set backs and your confidence in me has helped me to grow more confident in myself.

I'd also like to thank all of the solar group; you are truly such a friendly and welcoming group of people that I've never doubted that we are the best group at the lab! There's always someone able to answer a question, and plenty of people available for a pub lunch for any occasion. You've all made the experience an enjoyable one. In particular, I'd like to thank my office mates in G01 over the last few years, who have kept the kettle boiled and the conversation interesting and encouraging. A special mention goes to David Shelton for all the impassioned discussions about Formula One and Star Trek, and Deb Baker, for several well-timed pep talks that veered me away from major stress outs.

In addition to the solar group, several people deserve my thanks for helping a poor solar student understand data from planetary satellites! Nick Achilleos, Andrew Coates and Geraint Jones all took the time to sit down with me, discuss my work and answer all my questions and in particular, Chris Arridge has been invaluable with his help using Cassini data and has provided input and useful suggestions on much more besides that.

I've also had a little extra encouragement from Hawkeye, B.J. and the rest, who gave me an essential break from work and a great way to put life in perspective.

My long-suffering house-mates Jason Hunt and Kirthika Mohan deserve a huge amount of thanks for putting up with me for the entire PhD! You have been there at all levels of ludicrous stress and anxiety, for every baking disaster and all the dodgy driving. Despite that, I think we've had fun! There's been lots of movies and lots of good food, as well as the necessary commiserating over PhDs and all the problems they entail. More importantly, we've looked out for each other over the past three and a half years and I will miss you both. I look forward to catching up in the future with Dr. Hunt and Dr. Mohan, whatever you might be doing.

Finally, I have to thank my family, in particular my parents and my sister. Mum, you have honestly fed my way with season-appropriate care packages, plenty of jars of marmalade and as much baking as can be reasonably fit into a suitcase. Dad, my third PhD supervisor, you never failed to ask how it's going, even when I didn't want to answer, but you managed to sound encouraging however I replied. Katrina, thank you for listening to me when I was feeling optimistic, and repeating it back to me when I was feeling pessimistic, and being there with a hug and a bottle of wine for any panic at all, particularly the non-PhD related ones.

List of Abbreviations

Abbreviation	Details
2D/3D	Two-/Three-Dimensional
3DP	3-Dimensional Plasma Experiment
ACE	Advanced Composition Explorer
AIA	Atmospheric Imaging Assembly
ASPERA	Analyser of Space Plasmas and Energetic Atoms
AU	Astronomical Unit (1.5 x 10^{11} m)
CAPS	Cassini Plasma Spectrometer
CCD	Charge-Coupled Device
CCMC	Community Coordinated Modeling Center
CEM	Channel Electron Multiplier
CIR	Co-rotating Interaction Region
CME	Coronal Mass Ejection
CR2102/CR2013	Carrington Rotation 2102/2103
CSHKP	Carmichael, Sturrock, Hirayama, Kopp and Pneuman
DPU	Digital Processing Unit
EIT	Extreme-ultraviolet Imaging Telescope
ELS	Electron Spectrometer
EPACT	Energetic Particles: Acceleration, Composition Transport
ESA	European Space Agency
EUV	Extreme Ultraviolet
EUVI	Extreme Ultraviolet Imager
FGM	Fluxgate Magnetometer
FWHM	Full Width at Half Maximum
GLE	Ground Level Event
GOES	Geostationary Operational Environmental Satellite
GONG	Global Oscillation Network Group
GSM	Geocentric Solar Magnetospheric
HET	High Energy Telescope
HI	Heliospheric Imager
HXR	Hard X-ray
ICME	Interplanetary Coronal Mass Ejection
IMF	Interplanetary Magnetic Field
IMPACT	In-situ Measurements of Particles and CME Transients
IR	Infrared
KRTP	Kronocentric Radial, Theta, Phi

Abbreviation	Details
$L_\odot$	Solar luminosity (3.85 x 10^{23} kW)
LASCO	Large Angle Spectrometric Coronagraph
LET	Low Energy Telescope
$M_\odot$	Solar mass (1.99 x 10^{30} kg)
MAG	Magnetometer
MAS	Magnetohydrodynamics Algorithm outside a Sphere
MCP	Micro-Channel Plate
MEx	Mars Express
MHD	Magnetohydrodynamic(s)
MIR	Merged Interaction Region
NASA	National Aeronautics and Space Administration
NOAA	National Oceanic and Atmospheric Administration
PFSS	Potential Field Source Surface
PLASTIC	Plasma and Suprathermal Ion Composition
$R_\odot$	Solar radius (6.96 x 10^8 m)
R_E	Earth Radius (6.38 x 10^6 m)
R_s	Saturn Radius (6.03 x 10^7 m)
S/WAVES	STEREO/WAVES
SDO	Solar Dynamics Observatory
SECCHI	Sun Earth Connection and Heliospheric Investigation
SEP	Solar Energetic Particles
SEPT	Solar Electron and Proton Telescope
SIR	Stream Interaction Region
SOHO	Solar and Heliospheric Observatory
SPE	Solar Particle Release
STEREO	Solar Terrestrial Relations Observatory
SWEPAM	Solar Wind Electron, Proton and Alpha Monitor
SXR	Soft X-Ray
UT	Universal Time
UV	Ultraviolet
VEx	Venus Express
VSO	Venus Solar Orbital
WSA	Wang-Sheeley-Arge

Contents

List of Figures

List of Tables

Chapter 1

Introduction

1.1 The Sun

The Sun is a main sequence star, consisting chiefly of hydrogen and helium, about halfway through its lifetime. The Sun has a mass of $M_\odot = 1.99 \times 10^{30}$ kg, which is over 99% of the mass in the solar system. It has a luminosity of $L_\odot = 3.85 \times 10^{23}$ kW and a radius of $R_\odot = 6.96 \times 10^8$ m. Like other stars, it was formed by the gravitational collapse of an interstellar gas cloud. The collapse of the cloud continues until it reaches a central temperature high enough to begin the process of hydrogen fusion, which for the Sun, occurred around 4.6×10^9 years ago. The hydrogen fusion produces enough energy to balance the gravitational collapse and the star becomes stable reaching a state of hydrostatic equilibrium ($\nabla P = -\rho g$, where P is the pressure, ρ is the mass density and g is the gravity). After the Sun runs out of hydrogen for fusion, it will leave the main sequence and become a red giant, expanding to roughly 100 times its current size. Ultimately, it will shed its outer envelope after depleting all nuclear fuel and leave behind a white dwarf.

1.1.1 Solar Interior

The interior of the Sun consists of three main regions, described by the energy generation and transport mechanisms that dominate. In the standard solar model, the Sun is treated as spherically symmetric and quasi-static, powered by nuclear reactions in the hot, dense core. These reactions fuse hydrogen into helium, providing the energy source of the Sun. Above the core, between around 0.25 $R_\odot$ and 0.71 $R_\odot$, lies the radiative zone, where energy is

transported primarily via radiation. Further away from the Sun's core, the temperature and pressure decreases radially. A decreasing temperature increases the opacity, which inhibits radiation as a method of energy transport. Beyond $\sim$0.71 $R_\odot$ convection begins to dominate the energy transport, so this region is known as the convective zone of the Sun. The established convection cycle is observed on the surface of the Sun as patterns of granulation and supergranulation. These are cellular features covering the entire surface of the Sun on scales of $\approx$1000 km and $\approx$30 000 km respectively. Both the core and radiative zones of the solar interior rotate rigidly, however the convective zone is more fluid and rotates differentially. Between these two regions lies a thin layer known as the tachocline, which consists of highly sheared flow. These flows are believed to be the mechanism by which the solar dynamo is powered, as electric fields are induced in the fluid, generating the magnetic field. The magnetic field of the Sun is approximately a dipole, symmetric to the first order about the axis of rotation. Initially this field is poloidal (connecting the poles), however, differential rotation draws these field lines out in longitude, predominantly in the activity belts (latitude $\sim$30°).

As the field is twisted up, the magnetic field density increases and this increases the magnetic pressure, which can cause bundles of field lines (flux ropes) to become unstable and rise up. When these flux ropes rise through the surface as magnetic loops, they are visible as sunspot pairs, which have several characteristic behaviours. The tilt angle of a bipolar pair is such that the leading polarity sunspot lies closer to the equator, with a mean angle of 5.6° (Joy's Law). Sunspot pairs in the same hemisphere have the same leading polarities, with the opposite polarity in the other hemisphere, and this alternates per solar cycle (Hale's Law). At the beginning of a solar cycle, the first sunspots of the new orientation will appear at high latitudes and successive sunspots will migrate towards the equator over roughly 11 years (Spörer's Law). This results in flux cancellation at the equator, which leads to the reversal of the dipole field. Thus, a complete magnetic cycle of the Sun lasts 22 years, as the dipole flips from north to south to north. The activity of the Sun and the sunspot number increases and decreases with this cycle,

along with other solar parameters such as sunspot area, 10.7 cm microwave radio flux emission and solar irradiance.

As they are regions of enhanced magnetic density, sunspots are observed in optical wavelengths as dark regions on the solar surface. More generally, these regions can be known as active regions, visible as bright emission from coronal loops in extreme ultraviolet (EUV) and X-ray wavelengths and are often the source of plasma heating, solar flares and coronal mass ejections (CMEs).

1.1.2 The Solar Atmosphere

The lowest layer of the solar atmosphere is the surface of the Sun, called the photosphere. It is defined as the layer below which the Sun becomes opaque to visible light. Above this lies the chromosphere, the transition region and the solar corona. These regions are defined by their temperature and density. In general, the density decreases with increasing distance from the solar surface, as shown in Figure 1.1. The temperature decreases with height, reaching a minimum in the chromosphere, but then begins rising again slowly. The temperature increases sharply during the transition region, into the corona, giving rise to the coronal heating problem. These high temperatures in the solar atmosphere allow it to be observed in ultraviolet (UV), EUV and soft x-ray (SXR) wavelengths.

1.1.2.1 Chromosphere and Transition Region

The chromosphere is the region directly above the photosphere, approximately 2000 km thick. Its spectrum is dominated by emission lines, the strongest of which is H-α line of the Balmer series, which lies near the peak of the visible spectrum at 656.3 nm. The temperature of the photosphere reaches a minimum of 4500 K, which is the start of the chromosphere. The temperature then rises to about 25 000 K at the top of the chromosphere. This temperature increase is not yet completely understood, but is likely to be magnetic in origin.

Several notable features are observed in the chromosphere, such as filaments or prominences, and spicules. Prominences are large bright structures, often loop shaped, viewed off the solar limb. These structures are cooler than their surroundings, and therefore, when seen on the disk of the Sun they appear

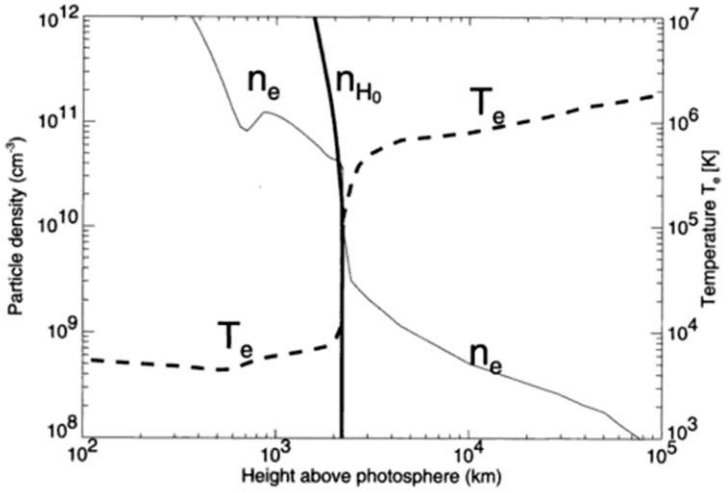

Fig. 1.1: Shown are the electron density, n_e, and temperature, T_e, variations with height from the chromosphere to the lower corona. The transition region is the narrow region with a sharp jump in temperature and a fall in electron density as the plasma becomes full ionised. The density of neutral hydrogen is also shown, n_{H_0} (Aschwanden 2005)

.

as dark features and are known as filaments. Spicules are dynamic narrow, jet-like features that occur frequently in the chromosphere, lasting only a matter of minutes. They have temperatures between 5000 and 15 000 K and move upwards with an average velocity of 25 km s^{-1}.

Above the chromosphere lies the thin transition region, where many characteristics of the solar atmosphere change. Above this region, the plasma becomes fully ionized, so it no longer radiates energy as easily. The temperature of the solar plasma increases sharply during this region, reaching coronal temperatures of 1 x 10^6 K.

1.1.2.2 The Solar Corona

The highest layer of the solar atmosphere is the hot and tenuous corona. It is highly influenced by the magnetic field of the Sun and is visible mainly in the EUV and X-ray wavelengths. However, it can be seen in white light during a solar eclipse due to Thomson scattering of the photospheric light by free electrons in the corona. The density of the corona ranges from roughly 10^{11} cm^{-3} at its base, to less than 10^9 cm^{-3} at heights greater than 1 $R_\odot$. The two main components of the solar corona are known as the K-corona and F-corona. The

K-corona dominates out to $\sim$2 $R_\odot$ and consists of photospheric light that has been Thomson-scattered by electrons. The high temperature of these coronal electrons means that they have very high thermal velocities. This washes out the Fraunhofer lines due to thermal broadening, leaving a featureless white-light continuum. The F-corona dominates beyond $\sim$2.5 $R_\odot$ and consists of photospheric light that has been Rayleigh-scattered by dust particles. This results in a continuous spectrum with Fraunhofer lines superimposed.

The main coronal features are visible from coronagraph images where the photosphere and lower corona is blocked out by an occulter, leaving only the outer corona visible. These features can be closed loops or open streamers and coronal holes. Coronal streamers tend to extend out from the equatorial region and appears to be the source of the slow solar wind. Coronal holes are open magnetic field lines, believed to be the source of the fast solar wind, which travels at speeds of around 700 $\mathrm{km\,s^{-1}}$. Chromospheric upflows at their footpoints push heated plasma from the corona into the solar wind (Aschwanden 2005). As a result, coronal holes are depleted of plasma, leading to densities of $\sim 10^7$ - 10^8 $\mathrm{cm^{-3}}$. They are therefore visible as dark regions on the solar disk in X-ray wavelengths. There are always coronal holes at the poles, and often some at lower latitudes, predominantly during solar minimum, the period of the Sun's cycle where activity is at its lowest. These low latitude holes start off as small features, eventually growing and often merging with the polar hole of the same polarity before disappearing. Coronal holes have temperatures of 1 - 1.5 MK and sizes of 0.7 - 0.9 x 10^6 km for polar holes and 0.3 - 0.6 x 10^6 km for low latitude holes (Phillips 1992).

1.2 The Physics of the Sun

1.2.1 Magnetohydrodynamics

The Sun consists of highly magnetised plasma, which allows its physics to be approximately described by magnetohydrodynamics (MHD). MHD describes the hydrodynamics of a conducting fluid in a magnetic field. As the plasma flows through a magnetic field this will induce currents that create forces on the fluid and change the magnetic field. MHD is described by a set of equa-

tions that combine the equations of fluid dynamics and Maxwell's equations of electromagnetism. Maxwell's equations describe the interplay between magnetic (**B**) and electric (**E**) fields, and can be written in the derivative form as follows:

Ampère's law:

$$\nabla \times \mathbf{B} = \mu_0 \mathbf{j} + \frac{1}{c^2} \frac{\partial \mathbf{E}}{\partial t} \tag{1.1}$$

Where μ_0 is the magnetic permeability of a vacuum, c is the speed of light, t is time and **j** is the current density. This equation means that magnetic fields may be produced by currents or time-varying electric fields.

Gauss' law for B:

$$\nabla \cdot \mathbf{B} = 0 \tag{1.2}$$

which means that there are no magnetic sources or monopoles.

Faraday's law:

$$\nabla \times \mathbf{E} = -\frac{\partial \mathbf{B}}{\partial t} \tag{1.3}$$

which means that electric fields can be produced by time-varying magnetic fields.

Poisson's equation, or Gauss' law for E:

$$\nabla \cdot \mathbf{E} = \frac{\rho_e}{\epsilon_0} \tag{1.4}$$

where ρ_e is the charge density and ϵ_0 is the permittivity of free space. This equation implies that charge is conserved.

In addition to Maxwell's equations, Ohm's law is also used in ideal MHD:

$$\mathbf{j} = \sigma(\mathbf{E} + \mathbf{v} \times \mathbf{B}) \tag{1.5}$$

where σ is the electrical conductivity and **v** is the velocity of the plasma. This equation expresses that a plasma moving in a magnetic field is subject to an electric field described by $\mathbf{v} \times \mathbf{B}$.

A number of assumptions are used to describe the plasma for MHD: The plasma is quasi-neutral, so $\rho_{electrons} = \rho_{ions}$ and local charge densities can be neglected. As a result of this assumption, equation 1.4 becomes $\nabla \cdot E = 0$. It is assumed that an inertial frame of reference is used, rather than rotating

or accelerating. The plasma is treated as a fluid, with a length scale greater than internal plasma lengths such as the ion gyroradius and mean free path length. It is assumed that the plasma is in thermodynamic equilibrium with distribution functions near to Maxwellian, so the characteristic timescale is greater than internal plasma timescales such as the ion gyrofrequency and mean free path time. All relevant speeds in solar physics, such as the bulk plasma flow speed, sound speed ($\sqrt{P/\rho}$) and Alfvén speed (the speed of an MHD wave = $B/\sqrt{\mu_0\rho}$) are much less than the speed of light, c, so relativistic effects are ignored. This also means that Ampère's law can be simplified, neglecting the final term (equation 1.1). μ and ϵ are assumed to be constant, and have their vacuum values. In addition, the MHD approximation can be further simplified by assuming the plasma is incompressible (density does not change with time), inviscid (viscous forces are neglected) and adiabatic. Resistivity can also be taken to be negligible in the ideal MHD approximation, as the gas is assumed to be highly conductive.

This leads to the fundamental MHD equations:

$$\frac{\partial \rho}{\partial t} + \nabla \cdot (\rho \mathbf{v}) = 0 \tag{1.6}$$

$$\frac{\partial \rho}{\partial t} + \mathbf{v} \cdot \nabla P = -\gamma P \nabla \cdot \mathbf{v} \tag{1.7}$$

$$\rho(\frac{\partial}{\partial t} + \mathbf{v} \cdot \Delta)\mathbf{v} = \mathbf{j} \times \mathbf{B} - \Delta P + \rho g \tag{1.8}$$

In this equation, the jxB term is the Lorentz force:

$$\mathbf{j} \times \mathbf{B} = \frac{(B \cdot \Delta)B}{\mu_0} - \Delta(\frac{B^2}{2\mu_0}) \tag{1.9}$$

Of this equation, the first term, (B·Δ)B/μ_0, is the magnetic tension force, which acts to straighten bent magnetic field lines. The second term, -Δ(B^2/2μ_0), is the gradient of the magnetic pressure. This force acts to oppose a compression of a magnetic fluid.

Rewriting Ohm's law using Ampère's law (1.1) yields:

$$\mathbf{E} = -\mathbf{v} \times \mathbf{B} + \frac{1}{\mu_0 \sigma} \nabla \times \mathbf{B} \tag{1.10}$$

which can then be used with Faraday's law (1.3) to become:

$$\frac{\partial \mathbf{B}}{\partial t} = \nabla \times (\mathbf{v} \times \mathbf{B}) - \eta \nabla \times (\nabla \times \mathbf{B}) \tag{1.11}$$

where $\eta = 1/\mu_0 \sigma$ is the magnetic diffusivity, which is assumed to be constant. Using a vector identity and Gauss' law (1.2), this can then be rewritten:

$$\frac{\partial \mathbf{B}}{\partial t} = \nabla \times \mathbf{v} \times \mathbf{B} + \eta \nabla^2 \mathbf{B} \tag{1.12}$$

which is the MHD induction equation. This equation describes how changes in the magnetic field can be due to plasma motion and/or diffusion. The first term on the right hand side describes how the magnetic field convects with the plasma moving at a velocity, v, and the second term describes how it can diffuse through the plasma. The magnetic Reynolds number, R_M, is the ratio of these two terms. If the characteristic plasma speed is V and the plasma length scale is L, $\nabla \sim 1/L$, which makes $R_M \sim \mu_0 \sigma V L$. When $R_M \ll 1$ then the diffusion term dominates over the convection term and the magnetic field can diffuse through the plasma. In a typical space plasma, conductivities are very high and length scales are large, so usually $R_M \gg 1$ and the convection term dominates over the diffusion term. In this case, the magnetic flux is 'frozen-in' to the plasma. This means that the flux through a fully conducting surface remains constant even as the surface changes location and shape and that oppositely-directed magnetic fields remain separate plasma domains. In such a scenario, a thin current sheet lies between the two regions, across which magnetic field changes in direction or magnitude.

Another important parameter frequently used to describe a magnetised plasma is the plasma beta, which is the ratio of plasma pressure to magnetic pressure:

$$\beta = \frac{\text{plasma pressure}}{\text{magnetic pressure}} = \frac{p}{B^2/2\mu_0} = \frac{2\mu_0 p}{B^2} \tag{1.13}$$

If β is greater than one, plasma pressure dominates over the magnetic pressure, meaning that plasma forces dominate over the magnetic forces. This is the case in the solar wind and also below the photosphere, where the magnetic field is then moved around by the plasma convection motion. If β is less than one, as is the case in the solar corona, then the magnetic pressure

dominates over the plasma pressure and magnetic forces will dominate over plasma forces.

1.2.2 Magnetic Reconnection

Magnetic reconnection is a rearrangement of the magnetic topology (changing the connectivity of field lines), where magnetic energy is converted into thermal and kinetic energy. Magnetic reconnection can occur when the conditions for frozen-in flux breaks down, so the diffusion term of the induction equation (equation 1.12) dominates over the convection term. It requires the dissipation of field across the current sheet, meaning there is a diffusion region between the two different magnetic domains where $R_M \ll 1$. When two oppositely directed field lines move together, they diffuse across this region and reconnect, creating two new field lines. These new field lines are strongly kinked, so the tension force is strong and quickly acts to straighten them. Outflow jets of accelerated plasma are created, running along the current sheet, away from the diffusion region. This process of magnetic reconnection allows magnetically isolated plasma populations to mix.

The simplest description of magnetic reconnection was put forward by Sweet (1958) and Parker (1957) and is shown in Figure 1.2 (top). The Sweet-Parker reconnection model has a diffusion region that is a long, thin sheet ($\Delta \gg \delta$). The reconnection outflow speed is around the Alfvén speed, v_A, the inflow speed, v_{in} is fairly slow (about 0.01 $\mathrm{km\,s^{-1}}$) and can be related to the Alfvén speed in the outflow region, the magnetic diffusivity, η, and length of the current sheet, L:

$$v_{in}^2 = \eta \frac{v_A}{L} \tag{1.14}$$

The resulting reconnection rate equals v_{in}/v_A, which in typical coronal conditions gives values of 10^{-4} - 10^{-6}. This reconnection rate is too slow to explain the energy release of a solar flare. Petschek (1964) suggested a faster model of magnetic reconnection, shown in Figure 1.2 (bottom). This model involves a smaller diffusion region ($\delta \approx \Delta$), which shortens the time for field lines to propagate through this region, speeding up the reconnection process. A smaller reconnection region also reduces the amount of plasma able

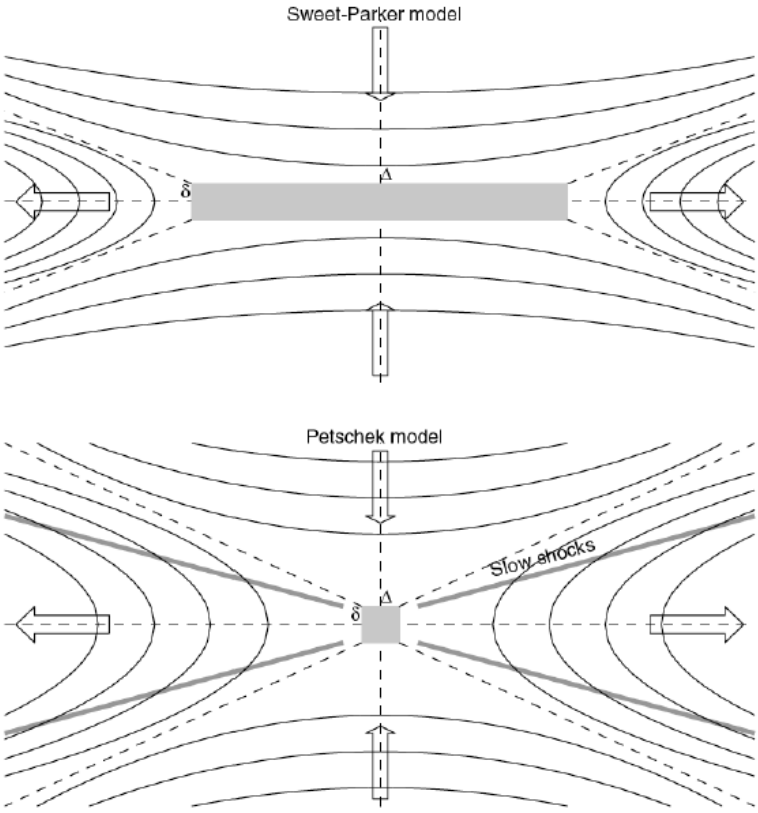

Fig. 1.2: The geometry of the Sweet-Parker (top) and Petschek (bottom) reconnection models. The diffusion region (grey box) has a width of δ and length Δ. (Aschwanden 2005)

to flow in, meaning that much of the inflowing plasma turns around outside the diffusion region, abruptly changing from v_{in} to v_{out}. The result of this is two slow-mode shocks, which are the main site where inflowing magnetic energy is then converted to thermal and kinetic energy. The Petschek model of reconnection yields much higher reconnection rates of around 0.01 - 0.02, about three orders of magnitude faster than the Sweet-Parker model.

1.2.3 Single particle dynamics

Individual particles within a plasma are subjected to both an electric and magnetic field. A particle with a charge q and velocity $\mathbf{v}$ will experience the Lorentz force: $\mathbf{F}_L = q(\mathbf{E} + \mathbf{v} \times \mathbf{B})$. In a uniform magnetic field, without an electric field, the particle will experience a force perpendicular to its direction of motion and the direction of the magnetic field. This results in gyromotion of the particle, where it will move in a circle around the magnetic field line. The radius and frequency of this motion around the field line are known as the gyroradius, r_L, and gyrofrequency, Ω_L, respectively:

$$r_L = \frac{mv_\perp}{qB} \tag{1.15}$$

$$\Omega_L = \frac{qB}{m} \tag{1.16}$$

where $v_\perp$ is the component of the particle's velocity which is perpendicular to the magnetic field line and m is the mass of the particle. As both the gyroradius and gyrofrequency depend on the particle mass and charge, electrons and ions will behave differently: a negative particle will gyrate in the opposite direction to a positive particle, and a heavier particle will have a larger radius about the field line and a lower frequency than a lighter particle. An important parameter to describe the motion of a particle in a magnetic field is the pitch angle, $\alpha = tan^{-1}(v_\perp / v_\parallel)$, which describes how much the particle travels along the field or perpendicular to it.

If the magnetic field is not uniform, or an electric field is also present, then this basic motion of a charged particle is modified. If a force acts parallel to the magnetic field, this will accelerate the particle along this direction. However, if a force acts perpendicular to the magnetic field it will accelerate and decelerate

the particle at different points in its gyro-orbit, causing the particle to drift in a direction perpendicular to the magnetic field and the force. In general, this drift velocity is described by the relation: $\mathbf{v}_F = (\mathbf{F}\times\mathbf{B})/qB^2$, where $\mathbf{F}$ is the force causing the drift. If this force is a result of the presence of an electric field, $\mathbf{F}$=q$\mathbf{E}$, both positive and negative particles will drift in the same direction, with a velocity $\mathbf{v}_{E\times B} = (\mathbf{E}\times\mathbf{B})/B^2$. This is known as an ExB drift. Two other types of particle drifts are particularly important for space plasmas: the magnetic gradient and magnetic curvature drifts (Figure 1.3). The magnetic gradient drift acts when a particle is travelling through a non-uniform magnetic field, with a significant gradient ($\nabla|B|$), perpendicular to the field direction. Magnetic curvature drift acts if the particles are travelling along field lines with a local curvature, and therefore experience a centrifugal force, F_C, acting along the local radius of the curvature vector, R_C. The resulting drift velocity for both of these drifts acts perpendicular to the magnetic field direction and the direction of the force (the direction in which the field strength changes and the direction of the centrifugal force). They are also both dependent on the charge q, so positive and negative particles will drift in opposite directions, resulting in net currents associated with these drifts.

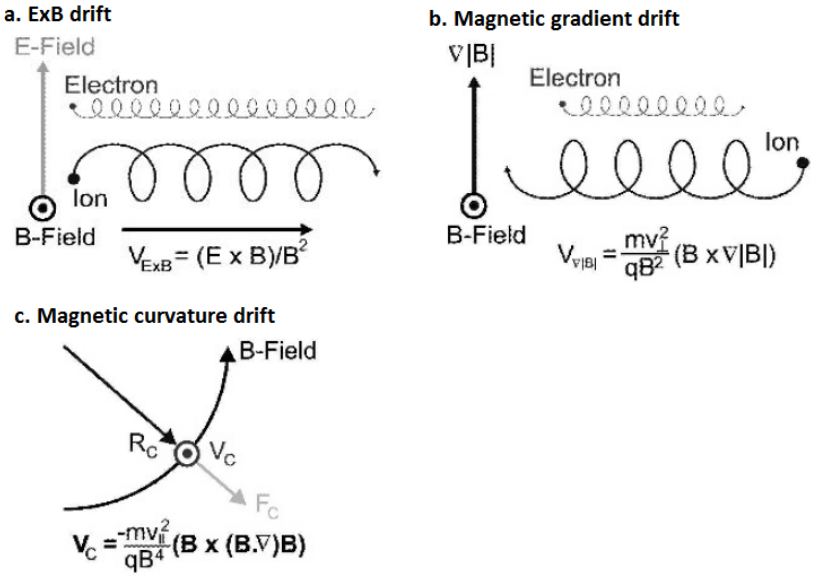

Fig. 1.3: Drifts of electrons and ions due to the presence of an electric field perpendicular to the magnetic field direction (a), a magnetic field gradient perpendicular to the magnetic field direction (b) and a curved magnetic field geometry (c) (Harra and Mason 2004).

1.2.4 Plasma Instabilities

Plasma instabilities can facilitate activity on the Sun. One such instability is the kink instability, which can arise on a thin column of plasma, such as a flux rope. If a kink-like displacement arises on a flux rope with an azimuthal magnetic field, the field lines on the inward side of the kink will move closer together, and the field lines on the outer side will move further apart. This will increase the magnetic pressure on the inward side of the kink and decrease it on the outer side. The resulting pressure difference will act as a force in the same direction as the original kink displacement, enhancing the perturbation.

The Rayleigh-Taylor and Kelvin-Helmholtz instabilities are both fluid instabilities, arising at the interface between between two fluid layers. If a fluid with a higher density lies above a fluid with a lower density in a vertical gravitational field, then a small ripple at the interface will allow the higher density fluid element to fall and lose potential energy and the lower density fluid element to rise and gain potential energy. This eventually leads to mixing of the two fluids and is known as the Rayleigh-Taylor instability. The Kelvin-Helmholtz instability arises when two fluids of different velocities travel parallel to an interface. If there is only a small difference between these velocities, stable flow can occur, but larger differences will cause the interface to become turbulent. In the case of plasmas, the presence of a magnetic field can act to stabilise the interface.

1.3 The Dynamic Sun

Space weather refers to the influence that conditions on the Sun and in the solar wind can have on the near-Earth environment. Disturbances from normal conditions can affect the magnetosphere and upper atmosphere of Earth, which can in turn affect a wide range of systems on the Earth and in orbit. Such disturbances in the solar wind are usually caused by events on the Sun such as solar flares and CMEs, which are closely related.

The standard model of solar flares is based on several phenomenological models that explain the observations of solar flares and coronal eruptions. It incorporates work byCarmichael (1964), Sturrock (1966), Hirayama (1974) and

Kopp and Pneuman (1976) and is therefore sometimes known as the CSHKP model. The main features of the model are shown in Figure 1.4.

In the model, a strongly sheared or twisted magnetic field, e.g. a flux rope, can erupt as a CME. The flux rope rises, for example due to a loss of equilibrium, an instability, or magnetic rearrangement. A flux rope below the solar surface may rise due to magnetic buoyancy. As a flux rope has a much higher magnetic density than its surroundings, and total pressure balance between the flux tube and its surroundings is maintained, this implies that the plasma density of the flux rope is less than its surroundings, allowing it to rise (Kivelson and Russell 1995). As the flux rope rises, it creates a Y-shaped magnetic configuration, with a current sheet drawn out below the flux rope and above closed loops. Magnetic reconnection in the current sheet can lead to a flare and allows the flux rope to be released and erupt. The upward reconnection outflow pushes the flux rope up and the downward reconnection jet impacts upon the closed underlying loops, potentially leading to a hard X-ray source at the top of the loops. Energy as accelerated electrons and protons then travels down the loops to the footpoints, leading to flare loops and ribbons.

1.3.1 Solar Flares

Solar flares are releases of magnetic energy that is converted to electromagnetic radiation over a wide wavelength range. They are thought to be produced by magnetic reconnection in the solar corona and can heat material to temperatures above 10^7 K. They pose significant problems in terms of space weather, as the radiation can arrive at the Earth within minutes and it is not always easy to predict when they will occur. Solar flares can release energy of up to 10^{25} J, which is predominantly radiation, but some also goes in to accelerating and heating particles, resulting in associated relativistic electrons, protons and ions, as well as radio bursts.

Solar flares are usually classified by their peak soft X-ray flux in the 1 - 8 Å range. This is labelled between the lowest class B, to the highest class X as shown in Table 1.1. Soft X-rays from flares are a result of coronal heating, thermal bremsstrahlung radiation and some very sudden heating which leads

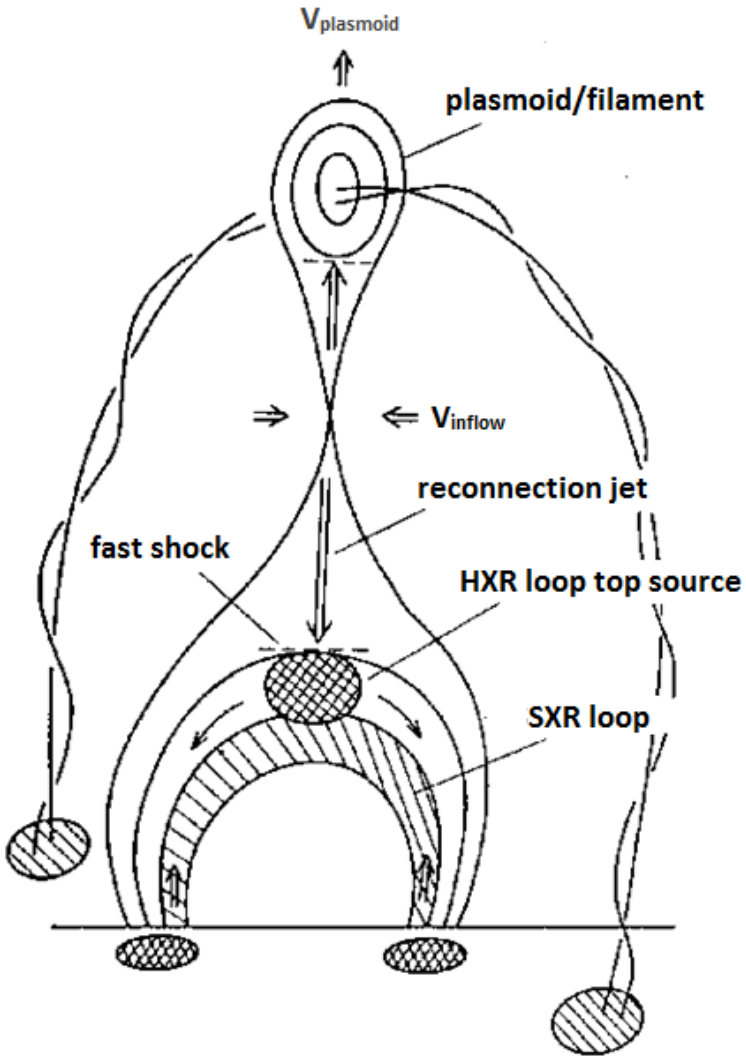

Fig. 1.4: The main features of the standard model of solar flares, including reconnection, an erupting flux rope, soft X-ray loops and hard X-ray (HXR) footpoint sources (Shibata et al. 1995).

Table 1.1: The X-ray classification of solar flares

Class	Intensity (W m^{-2})
B	10^{-7}
C	10^{-6}
M	10^{-5}
X	10^{-4}

to chromospheric evaporation. The hard X-ray signal is non-thermal radiation, due to accelerated electrons impacting the dense layers of the chromosphere and causing bremsstrahlung radiation.

EUV emission from flares tends to originate from lower levels of the solar atmosphere, in the chromosphere. The strongest signal is often the H-α line at 656.3 nm. For this reason, in the past, this peak was used to classify solar flares. Higher up in the chromosphere, the Lyman-α hydrogen line at 121.6 nm gives the strongest signal.

Solar flares are often associated with radio bursts, in particular Type III bursts. Type III radio bursts are short-lived bursts with frequencies from MHz to a few kHz, decreasing rapidly with time. They are caused by accelerated electrons with energies in the keV range that excite plasma oscillations (also known as Langmuir waves). The frequency, f_p, of these waves depend on the electron density, n_e, by the relationship:

$$f_p = 9\sqrt{n_e} \tag{1.17}$$

where f_p is in kHz and n_e is in cm^{-3}. The frequency of the waves decrease as they travel through a radial density gradient, which is observed as the decrease in frequency of the radio emission.

Solar flares are often, but not always associated with CMEs (Feynman and Hundhausen 1994). Stronger flares have a higher rate of association with CMEs than weaker flares, with 100% of X3 or above, but only 20% of C3-C9 flares having associated CMEs (Yashiro et al. 2005). Longer duration (eruptive) flares are also more likely to have associated CMEs than shorter duration impulsive flares (Sheeley et al. 1983; Kahler et al. 1989).

The space weather effect of solar flares alone is predominantly limited to heating and expansion of the Earth's atmosphere, mainly from the flare's increased EUV radiation. An expansion of the atmosphere leads to an increase in drag on low-earth orbit satellites which can cause their orbits to drop (Pulkkinen 2007). This can lead to early re-entry in severe cases. Solar flares can also result in an increase in the ionisation density in the ionosphere, which can disrupt telecommunications. Flares are also often associated with CMEs, which have more significant space weather effects such as geomagnetic storms.

1.3.2 Coronal Mass Ejections (CMEs)

CMEs are explosive releases of plasma clouds and magnetic field from the Sun that are observed as white light features in the field of view of a coronagraph. They can be classified by their angular width, speed and central position angle. If CMEs originate near the centre of the solar disk, they often appear as a 'halo' around the disk, while 'partial halos' have angular widths between 120° and 360° projected in the plane of the sky, as observed in a coronagraph. A large number of CMEs display an obvious 3-part structure of a bright kernel, surrounded by a dark cavity, bounded by a bright outer loop as shown in Figure 1.5. This CME has an angular width of ≈70°.

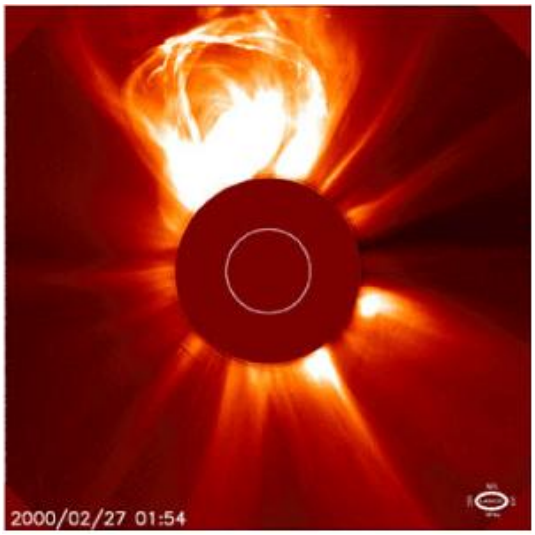

Fig. 1.5: Shown is a *SOHO*/LASCO image of a typical CME demonstrating the three-part structure, on 27 February 2000, (Chen 2011).

CME speeds can be as high as 2500 $\mathrm{km\,s^{-1}}$ and are measured from the white light signature on a coronagraph. There are several limitations with coronagraph images however, that may misrepresent the apparent properties of the observed CMEs. For example, projection effects mean that the shape of a CME depends on the angle of view, the brightness observed is the integral of photons scattered along the line of sight and the position and speed of a CME seen in coronagraphs are the 2D projection of the true speed and position on the plane of the sky. The occulting disk of a coronagraph blocks the photons directly from the photosphere, but will also affect the observations of CMEs. A CME originating from disk centre will reach the field of view of the coronagraph at a different time and heliocentric distance than it would do if it originated from the solar limb and it will appear fainter and diffuser. The angle between the observer and the CME also affects the brightness of the observed CME due to Thomson scattering. The maximum scattering (and therefore maximum emission) occurs on a sphere centred halfway between the Sun and the observer, with a diameter equal to the Sun-observer distance (Vourlidas and Howard 2006).

The speed of a CME can be determined more accurately when images from multiple viewpoints are compared, as has been possible with the *Solar TErrestrial RElations Observatory* (STEREO; Kaiser et al. 2008) spacecrafts, which orbit ahead and behind the Earth. This is significant for space weather prediction as it allows the CME geometry and direction to be reconstructed and its propagation modelled to better determine when and if it will reach Earth (Liu et al. 2010a,b; Byrne et al. 2010; Liewer et al. 2011). The initiation of a CME can be observed on the solar disk by the presence of various features such as solar flares, filament eruptions (Munro et al. 1979), coronal dimmings and coronal waves (Thompson et al. 1998). However, an on-disk signature is not always present and the only certain indication of a CME is in a coronagraph (Robbrecht et al. 2009). CMEs without any signatures on-disk are known as stealth CMEs.

1.3.3 Large scale propagating waves

Waves propagating across the disk of the Sun can be observed in association with solar flares and CMEs. In the chromosphere, Moreton waves were first discovered in 1960 (Moreton and Ramsey 1960). They appear in H-α as disturbances propagating away from the flare site and have radial speeds of 500 - 1000 $\mathrm{km\,s^{-1}}$, away from the source location of the wave. These waves have been interpreted as chromospheric signatures of coronal waves.

Coronal EUV waves or 'EIT waves' (Thompson et al. 1998; Moses et al. 1997) are also observed in the solar corona. They were first observed using the Extreme-ultraviolet Imaging Telescope (EIT; Delaboudinière et al. 1995) aboard the *Solar and Heliospheric Observatory* (SOHO; Domingo et al. 1995), (Thompson et al. 1998; Moses et al. 1997) and were initially assumed to be the coronal counterpart to Moreton waves. An example of an EUV wave is shown in Figure 1.6. They are visible as diffuse bright fronts propagating through the corona with average speeds of 100 - 400 $\mathrm{km\,s^{-1}}$. The nature of these large-scale waves is still under debate, but they have been suggested as MHD waves (Wang 2000) or shock waves (Warmuth et al. 2001), magnetosonic waves (Thompson et al. 1998), solitons (Wills-Davey et al. 2007) or pseudo-waves, a result of restructuring of the magnetic field during a CME (Chen et al. 2002; Attrill et al. 2007). The association with Moreton waves has been questioned as coronal waves propagate more slowly than Moreton waves and occur more frequently. Coronal waves propagate freely in the quiet corona, but are known to reflect and refract at the boundaries of coronal holes and active regions (Gopalswamy et al. 2009).

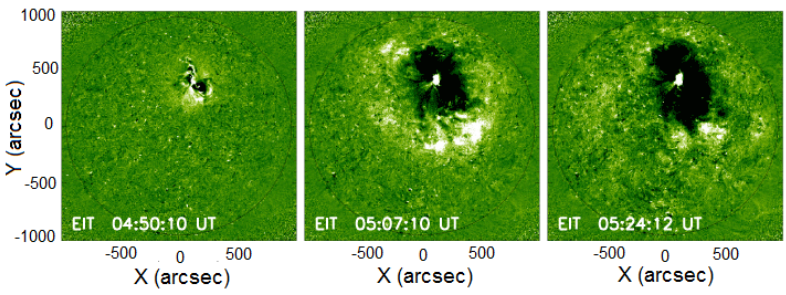

Fig. 1.6: The evolution of a typical coronal wave, seen as a propagating bright front, observed by EIT on 12 May 1997 in 195Å difference images (Chen 2011).

1.4 The Heliosphere

1.4.1 The Solar Wind

The hot tenuous gas of the corona cannot maintain complete hydrostatic equilibrium with its surroundings, and as a result, it was shown by Parker (1958) that it must be expanding out into interplanetary space. This is known as the solar wind. It consists mostly of protons and electrons, with a small He^{2+} component of typically about 5% and a heavy ion content of 0.5%. The number density of positive ions at 1 AU is typically around 5 cm^{-3}, varying between 3 and 10 cm^{-3}, with a similar number of electrons to maintain charge neutrality overall.

A standard model of the solar wind can be obtained by considering the conservation of mass, momentum and energy flux. By applying reasonable boundary conditions to the equation of motion that results, a unique solution is found which predicts a high velocity outflow of material into the solar system that becomes supersonic beyond some critical radius.

By assuming a spherically symmetric flow radially away from the Sun and considering the conservation of particles:

$$\frac{1}{r^2}\frac{d}{dr}(r^2\rho u) = 0 \tag{1.18}$$

where ρ is the mass density, r is the radius of the sphere and u is the fluid bulk flow velocity. The equation for conservation of momentum in the fluid is given by:

$$\rho u\frac{du}{dr} = -\frac{dP}{dr} - \rho\frac{GM}{r^2} \tag{1.19}$$

and the energy equation is:

$$\frac{1}{\rho}\frac{dP}{dr} = -\frac{k_B T}{m}\left(\frac{1}{u}\frac{du}{dr} + \frac{2}{r}\right) + \frac{k_B}{m}\frac{dT}{dr} \tag{1.20}$$

For an ideal gas, assuming $n_e = n_i = n$ and $T_e = T_i$, the equation of state of the solar wind is taken to be:

$$P = nk_B(T_e + T_i) = 2nk_B T \tag{1.21}$$

By assuming that T is constant (the solar wind is isothermal), solving these equations for $u = u(r)$ can give the equation of motion of the fluid:

$$\frac{1}{u}\frac{du}{dr}\left(u^2 - \frac{2k_B T}{m}\right) = \frac{4k_B T}{mr} - \frac{GM}{r^2} \tag{1.22}$$

As r increases, the right-hand side of this equation will decrease, with the second term decreasing at a faster rate than the first. When the second term becomes smaller than the first term, the right-hand side of this equation will change sign. This will occur at a critical radius:

$$r_c = \frac{GMm}{4k_B T} \tag{1.23}$$

At this critical radius, the left-hand side of the equation of motion must go to zero, which would be the case if:

$$u^2 - \frac{2k_B T}{m} = 0 \tag{1.24}$$

or if:

$$\frac{1}{u}\frac{du}{dr} = 0 \tag{1.25}$$

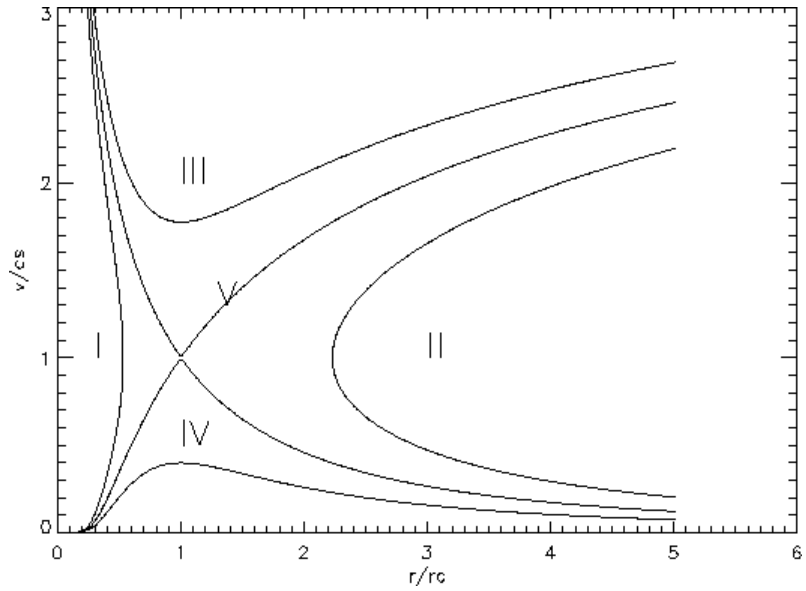

Fig. 1.7: Solar wind velocity, v, as a function of the radial distance, r. This shows the five different classes of solutions to the solar wind equation. `http://www-solar.mcs.st-andrews.ac.uk/~alan/sun_course/Chapter6/node3.html`

There are five classes of solutions to this equation of motion which would satisfy these conditions, shown in Figure 1.7. Two have an expansion velocity which starts very high near the solar surface (class I and class III), which would be unphysical, so these are discounted. Class II is also clearly unphysical as it doesn't even start from the solar surface. The remaining two classes (class IV and V) start with lower velocities near the solar surface, with one then

increasing monotonically outward (class V), while the other increases until $r \approx r_c$ and then decreases (class IV). This results in a finite pressure and density as $r \to \infty$ which is also unphysical. The unique solution is therefore class V the one for which $u(r) > u_c$ for $r > r_c$, so the expansion speed of the solar wind continues to increase outwards. The pressure and particle density will approach zero at large values of r. Using the equation of state above (equation 1.21), finding u_c, the speed when $r = r_c$:

$$u_c = u(r_c) = \sqrt{\frac{2k_B T}{m}} = \sqrt{\frac{P}{\rho}} \tag{1.26}$$

where $\sqrt{P/\rho}$ is equal to the sound speed, c_s. This model therefore predicts that the solar wind begins with a low speed near the solar surface and increases as it approaches r_c, at which point it becomes supersonic. The solar wind has a sonic Mach number typically between 2 and 10 at 1 AU.

The solar wind properties can have large fluctuations of up to a factor of 10, occurring over a period of minutes or hours. The speed of the solar wind at 1 AU varies between 200 and 800 $\mathrm{km\,s^{-1}}$, and over one solar rotation can vary several times between these values. The density also varies over a solar rotation, roughly in anti-correlation with the solar wind velocity. The solar wind can be described as two separate components, dependent on the speed. The slow solar wind tends to have velocities between 300 and 400 $\mathrm{km\,s^{-1}}$ and a composition close to that of the corona. It is believed to originate from the streamer belt of the corona and has a density higher than that of the fast solar wind. The fast solar wind has velocities up to 800 $\mathrm{km\,s^{-1}}$ and a composition similar to that of the photosphere of the Sun. It has a lower density than the slow solar wind and appears to originate from coronal holes on the Sun, which are more prevalent at low latitudes during solar minimum.

The solar wind also carries a magnetic field of a few nanoteslas, which is 'frozen in' to the highly conductive gas and is therefore carried with the solar wind plasma as it flows away from the Sun. As the Sun rotates, this creates a spiral of magnetic field, called the Parker spiral, which has a spiral angle dependent on the solar wind velocity.

In a spherical coordinate system (r,θ,ϕ), if the Sun is rotating with angular

velocity ω and the radial component of velocity is $u = u(r)$, then the direction of the magnetic field at any radius r is found from:

$$\tan\phi = r\frac{d\phi}{dr} = \frac{-r\omega\sin\theta}{u} \tag{1.27}$$

At a large distance from the Sun it is assumed that the solar wind has a constant outflow velocity, so u can be approximated by a constant U beyond a distance r_0. With the condition $\nabla \cdot \mathbf{B} = 0$ (equation 1.2), this yields the result:

$$B_r = B_0\left(\frac{r_0}{r}\right)^2 \tag{1.28}$$

and

$$B_\phi = -B_0\frac{\omega r_0}{U}\frac{r_0}{r}\sin\theta \tag{1.29}$$

and $B_\theta = 0$ for all latitudes. B_0 is the magnetic field at the radius r_0. This results in a spiral with angle ϕ described by:

$$\tan\phi = \frac{B_\phi}{B_0} = \frac{\omega r}{U} \tag{1.30}$$

The angle ϕ approaches $\pi/2$ at large distances from the Sun, so the magnetic field appears wound up. It is roughly equal to 45° at the Earth. There is a large scale, heliospheric current sheet which lies between the 'inward' and 'outward' magnetic fields, which can be tilted with respect to the equatorial plane, as shown in Figure 1.8.

1.4.2 Interplanetary Coronal Mass Ejections (ICMEs)

When a CME travels out into interplanetary space, it interacts with the ambient solar wind and is then known as an interplanetary coronal mass ejection (ICME). ICMEs can consist of a number of different regions observed in the solar wind that may include a shock, plasma sheath, solar wind pile-up, ejecta, compression regions and driver gas (e.g. Rouillard et al. (2011)). An ICME demonstrating some of these regions is shown in Figure 1.9. These different structures can be observed in-situ by a variety of indicators as compared to the ambient solar wind (see review by Zurbuchen and Richardson (2006)). Examples include decreases in proton temperature, an enhanced α/proton ratio and bidirectional suprathermal (>100 eV) electrons and ∼MeV ions.

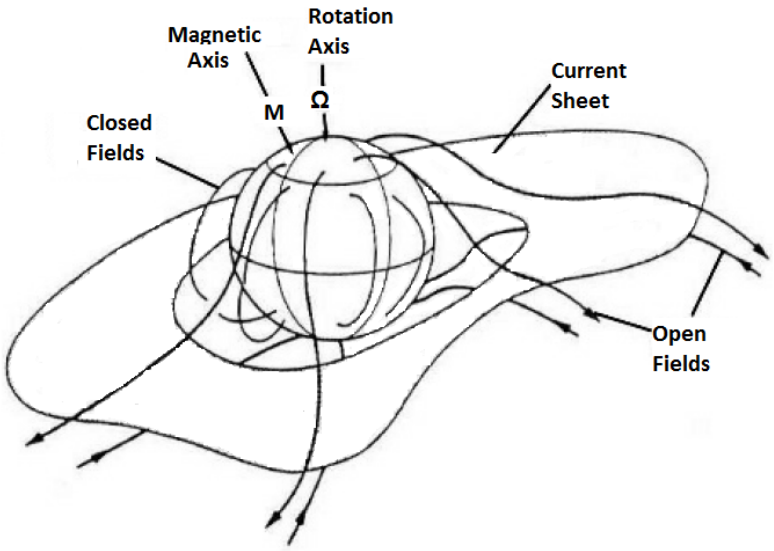

Fig. 1.8: A diagram of the heliospheric current sheet. Along the plane of the Sun's magnetic equator, oppositely directed open field lines run parallel to each other, separated by a thin current sheet. The magnetic axis of the Sun is tilted with respect to the rotation axis, resulting in a wavy spiral shape, often known as the 'ballerina skirt'. (Harra and Mason 2004)

One particular structure of an ICME is a magnetic cloud, a subclass of ejecta. These are identified by a smooth rotation of the interplanetary magnetic field (IMF), an overall enhancement of the magnetic field magnitude and often a low plasma beta or proton temperature (Klein and Burlaga 1982). An example of an ICME with a magnetic cloud observed in-situ is shown in Figure 1.10. The low proton temperature is thought to arise due to magnetically isolated ejected material expanding faster than the ambient solar wind. Richardson and Cane (1995) report that the proton temperature within an ICME is less than half of the expected proton temperature. A magnetic cloud often follows a shock and a sheath, as seen in Figure 1.9. A sheath is a turbulent region with high total solar wind pressure. A shock is characterised in-situ by a discontinuity in solar wind conditions such as velocity and density, but they can also be observed by several signatures in white-light images of the corona. Such signatures include deflected streamers (Cliver et al. 1999; Sheeley et al. 2000) and the layer of electrons observed on the surface of the CME (Vourlidas et al. 2003). Interplanetary shocks can spread over very large

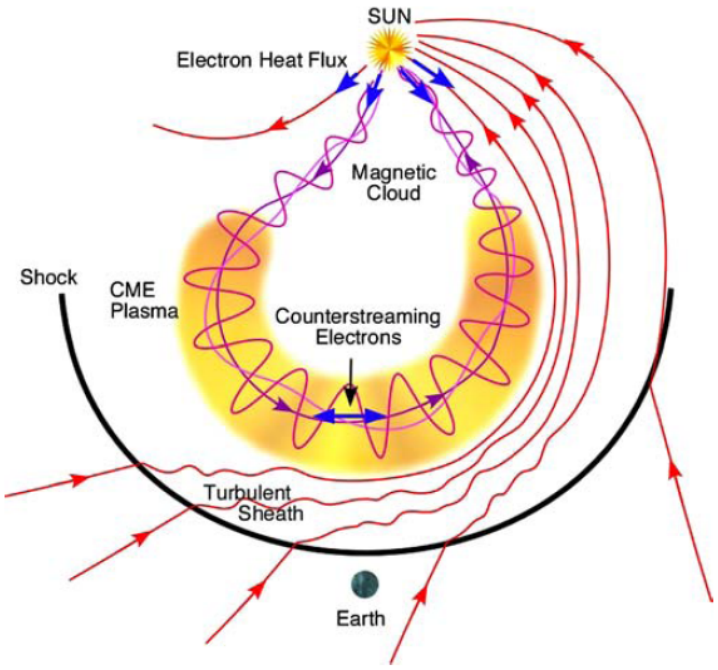

Fig. 1.9: Schematic of the 3D structure of an ICME including a plasma sheath, ejecta (magnetic cloud) and an upstream shock. (Zurbuchen and Richardson 2006)

longitudes, up to 180 degrees (Torsti et al. 1999; Cliver and Cane 1996).

If a CME is fast and wide, it is often associated with Type II radio bursts and large energetic particle events (Liu et al. 2009), although deviations from this picture can occur (Gopalswamy et al. 2008; Gopalswamy 2008). Type II radio bursts are characterized by enhanced emission drifting slowly from high to low frequencies and are caused by accelerated electrons at a propagating shock front (Golub and Pasachoff 1997). These radio bursts are usually observed with a fundamental and harmonic frequency and as for Type III bursts (see Section 1.3.1), the radial distance from the source and therefore the speed of the shock can be determined from the rate of frequency drift (Schwenn 2006).

ICMEs can have quite severe space weather effects, accelerating energetic particles and radio bursts ahead of shocks and causing geomagnetic storms. This is a particular risk if the ICMEs magnetic field is southward-pointing, which is able to reconnect with the Earth's magnetic field (Gosling et al. 1991). These magnetic storms can lead to strong auroral currents and enhanced particle fluxes, which can disrupt radio communications and satellites.

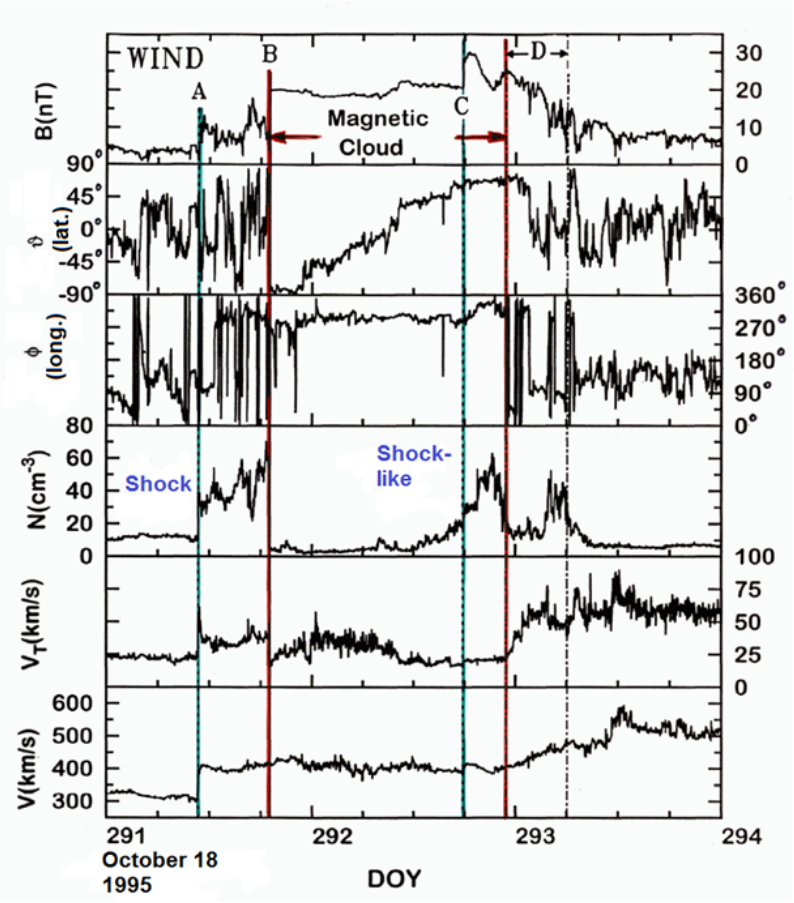

Fig. 1.10: The in-situ signatures of an ICME with a magnetic cloud and preceding shock, shown with data from the *Wind* spacecraft. The panels show from top to bottom: the magnetic field strength (B) and direction (θ, ϕ), the solar wind density, the proton thermal velocity and the solar wind flow speed. (Lepping et al. 1997)

1.4.3 Co-rotating Interaction Regions (CIRs)

Co-rotating Interaction Regions are formed when a region of fast solar wind catches up with a region of slow solar wind, creating a density enhancement at the interface between them, known as a Stream Interaction Region or SIR. The average duration of this interaction region at 1 AU is 36.7±0.9 hours, with a radial size of 0.41±0.01 AU (Jian et al. 2006). A schematic of this structure is shown in Figure 1.11. There will be a compression region ahead of this interface and a rarefaction region behind. Pairs of shocks may also form at the edges of the interaction region, particularly at higher heliocentric distances, beyond ∼3 AU, as the compression wave steepens (Gosling and Pizzo 1999; Gosling et al. 1976; Hundhausen and Gosling 1976; Smith and Wolfe 1976).

The fast solar wind originates from coronal holes that become more frequent at lower solar latitudes during the declining phase of the solar cycle. These high speed streams of solar wind, and therefore the associated interaction region, rotate with the Sun, sweeping out large areas of longitude. If they persist for multiple solar rotations, they become known as CIRs (Gosling and Pizzo 1999). A CIR has an average duration at 1 AU of 36.8±1.2 hours and a radial size of 0.44±0.02 AU (Jian et al. 2006). They can be observed in-situ as an increase and then decrease in density, an increase in solar wind velocity, entropy and proton temperature, velocity deflections, a pile-up of total pressure and a compression of the magnetic field (Jian et al. 2006, 2008). The presence of at least five of these signatures are required for a CIR to be identified (Jian et al. 2006). The stream interface is the actual boundary between the fast and slow solar wind streams, and is identified by the peak in total pressure, often accompanied by the increase in solar wind velocity and proton temperature, as well as the fall in density following the compression region. Figure 1.12 shows the in-situ signatures of a CIR with forward and reverse shocks. CIRs can be very long-lived structures in the heliosphere, and have the potential to influence vast areas of it. During solar minimum when low-latitude coronal holes are common, CIRs can be the source of 27-day recurrent geomagnetic activity at the Earth.

1.4.4 Shocks

In the solar system there are many shocks, including those that lie in front of all the planets, and ones propagating ahead of solar transients in the corona and solar wind. Shocks are essentially non-linear waves, where the conditions in the plasma such as density, temperature, magnetic field strength and velocity, change abruptly. They are therefore seen in in-situ solar system data as a sharp discontinuity in these parameters. Examples of this are seen in Figures 1.10 and 1.12, ahead of the ICME and CIR respectively. A shock wave in a normal gas will tend to arise from a sound wave, where momentum and energy are transferred among molecules via collisions. However, the solar wind is a collisionless plasma, with a collisional mean free path of roughly 1 AU, implying that collisions are not important for interplanetary shocks. In

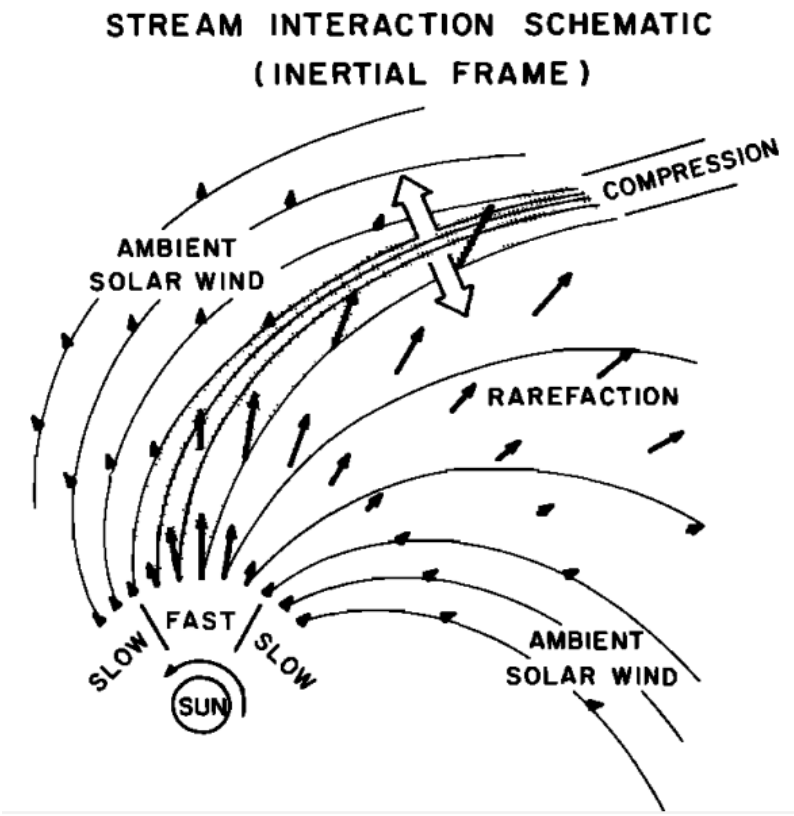

Fig. 1.11: Schematic of a stream interaction region in the inertial frame. The view is looking down on the ecliptic plain from solar north. (Pizzo 1978)

collisionless plasmas, waves arise from the behaviour of particles in magnetic and electric fields.

An interplanetary shock can arise as the ejecta material of a CME expands supersonically. This can drive a shock upstream and downstream of the CME. CIRs can also drive shocks as the fast solar wind stream rapidly decelerates as it reaches a slower stream. Interplanetary shocks are generally associated with fast magnetosonic waves, so are known as fast mode shocks. Slow mode shocks can also occur in space plasmas, associated with Alfvén waves. The plasma conditions upstream and downstream of a shock can be found using the conservation of mass, energy and momentum. The relations that describe this are known generally as the shock jump relations, or Rankine-Hugoniot relations, but differ from normal in the case of MHD waves.

Another important consideration with such shocks is the angle between the shock surface and the direction of the magnetic field, which can vary

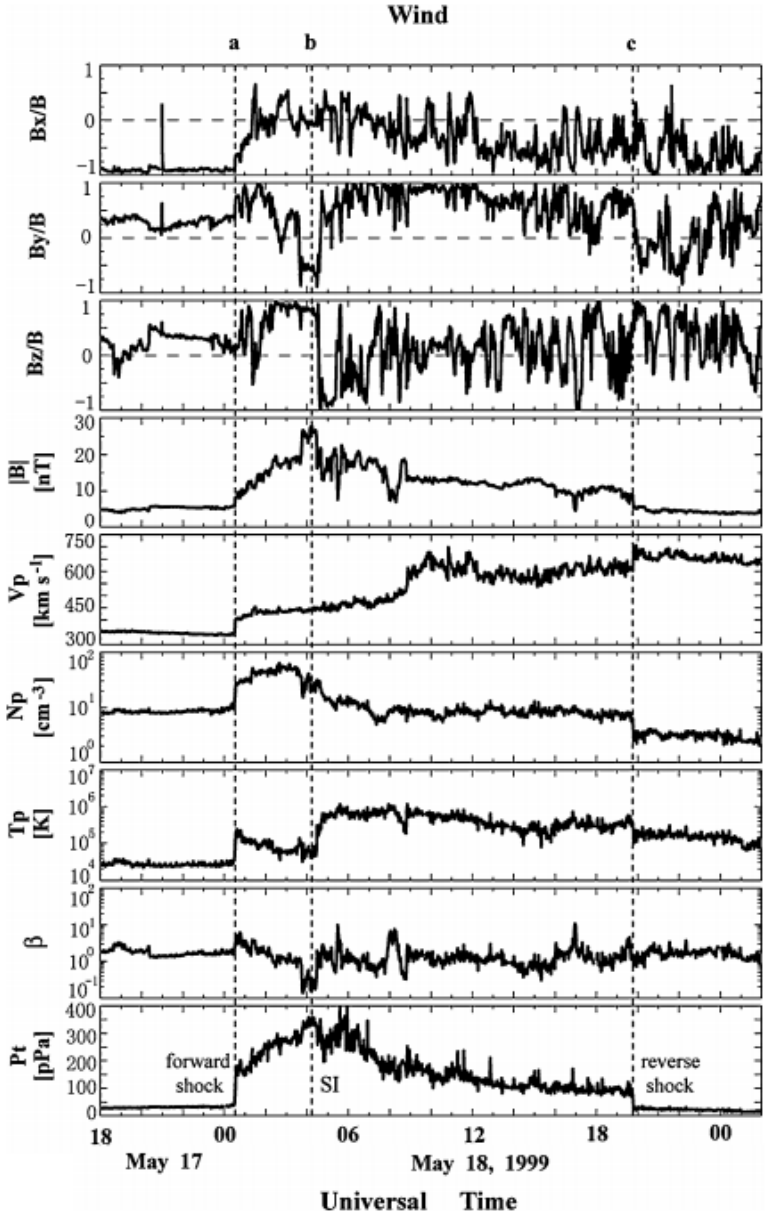

Fig. 1.12: The in-situ signatures of a CIR with forward and reverse shocks, shown with data from the *Wind* spacecraft. The panels show from top to bottom: the magnetic field directions in GSM coordinates (B_x, B_y and B_z), the magnitude of the magnetic field, the solar wind speed, the proton density, the proton temperature, plasma beta and total perpendicular pressure. The CIR lies between boundaries a and c, with boundary b indicating the location of the stream interface. (Jian et al. 2006)

at different points on the shock front. In a quasi-perpendicular shock, the magnetic field lines are close to lying perpendicular to the shock normal. In this situation, the flow across the shock will decrease in speed by the same

factor that density and magnetic field strength will increase, and this factor has a maximum value of four. A quasi-parallel shock is one in which the upstream magnetic field lines are close to parallel to the shock normal. In this shock the plasma is compressed as it slows, but the magnetic field strength doesn't change significantly.

Interplanetary shocks can be an important source of acceleration for particles to high energies. The mechanism for particle acceleration can vary depending on if the shock is quasi-parallel or quasi-perpendicular. For a quasi-perpendicular shock, a portion of the particles through the shock will be reflected back to the shock front. If that happens multiple times, the particle will drift along the shock surface, in the direction of the convection magnetic field if the particle is positively-charged, or opposite to this for negatively-charged particles. The convection electric field, E_{conv} arises from the frozen-in magnetic field moving with the solar wind and equals $-v_{sw} \times B$, where v_{sw} is the bulk velocity of the solar wind and B is the magnetic field strength. In this scenario, shown in Figure 1.13a, the particles gain energy as they move along the shock surface. For quasi-parallel shocks, the mechanism of particle acceleration tends to be a form of Fermi acceleration. Particles which are reflected from these shocks can move back upstream, where turbulent field structures or wave-particle interactions can reflect it again towards the shock, shown in Figure 1.13b. If the reflecting structure was moving towards the shock front, the particle will gain energy. Multiple interactions with the shock will cause the particle to gain even more energy.

1.4.5 Solar Energetic Particles (SEPs)

Solar energetic particles are charged particles accelerated to very high energies during a solar event such as a flare or a CME-driven shock. The energies of these particles range from suprathermal particles at a few keV, to GeV particles which can arrive only minutes after the light flash of a flare.

Energetic particles caused by flares and shocks tend to have distinct profiles that easily distinguish between the two. Impulsive SEP events have been identified from the acceleration of particles in a small region on the Sun, such as a solar flare, and produce short-duration events (several hours) over a nar-

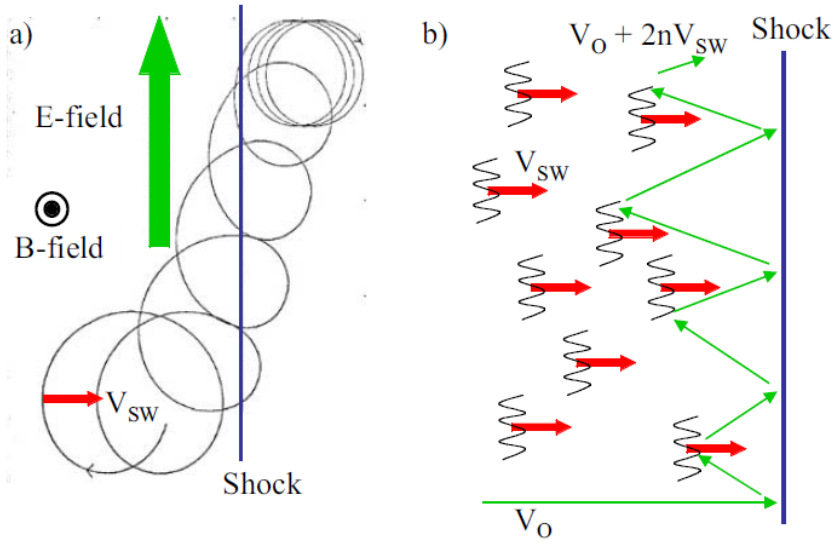

Fig. 1.13: Acceleration mechanisms at shocks. (a) At a quasi-perpendicular shock, particles interacting with the shock can drift along the shock surface and gain energy. (b) At a quasi-parallel shock, particles are reflected upstream by the shock surface, where they can be scattered by solar wind irregularities and gain energy via Fermi acceleration. (Harra and Mason 2004)

row longitudinal range. They tend to be electron-rich and often associated with Type III radio bursts. Gradual events are identified with a wider source region of acceleration such as CME-driven shocks. They can have a duration of several days, are proton-rich and are often associated with Type II radio bursts (Cliver 2009).

It was shown by Kahler (1994) and Tylka et al. (2003) that SEPs from a gradual event are initially released close to the Sun, when the shock reaches around ∼3 - 10 $R_\odot$. These accelerated particles will then propagate out along the magnetic field lines. The resulting longitudinal spread of the particles will depend on how broad the shock is. It was generally assumed that the azimuthal angular spread of SEPs was at least 100° (Cane and Erickson 2003; Kallenrode et al. 1993), but Cliver et al. (1995) used single spacecraft observations to study a flare on the far side of the Sun, with an observed coronal shock and an associated SEP event which had a spread of at least 150°. This implies a coronal shock that could extend to up to 300°. The STEREO mission has provided a better chance to study SEP events from different viewpoints,

comparing with observations at the Earth (Rouillard 2011; Liu et al. 2011; Chollet et al. 2010). As the two spacecraft travel further apart, it has become evident that SEP events can be detected over much wider angles than previously assumed.

Several characteristics of SEP events such as anisotropies, onset times and particle intensities can yield information about the source position of the particles and their magnetic field line connections (Bieber et al. 2005; Torsti et al. 2004). Reames et al. (1996) show that the shape of the time-intensity profile of a gradual SEP event depends on the strength of the shock and therefore the strength of the connection with the source region. Particles accelerated by a strong shock have a fairly constant time-intensity profile, which indicates that they are well-connected to the source region. A weaker shock will be poorly-connected to the source region of the particles and will display a time-intensity profile that decreases with time (see Figure 1.14).

SEPs of particularly high energies can present dangerous levels of radiation for astronauts such as those in the International Space Station. Damage to spacecrafts can also occur, by single event upsets that damage onboard electronics and charging of the spacecraft surface. SEPs can also lead to the ionization of the atmosphere over the poles, producing nitrates and sometimes leading to ozone depletions (Schwenn 2006; Pulkkinen 2007). Some GeV proton events are capable of causing radiation in the Earth's atmosphere that penetrates to the surface where they are detected by neutron monitors. These are known as ground level events (GLEs).

1.5 Solar Wind Interactions with Planets

The interaction of the solar wind with planets in the solar system varies greatly, mainly depending on the presence of a planet's intrinsic magnetic field. The interaction of the solar wind with planets that have a strong magnetic field, such as the Earth, Jupiter and Saturn, creates a protective cavity around the planet, known as a magnetosphere. For planets without a magnetic field, such as Venus and Mars, the solar wind interacts directly with the atmosphere or ionosphere. This can create an induced magnetosphere, which has some similar

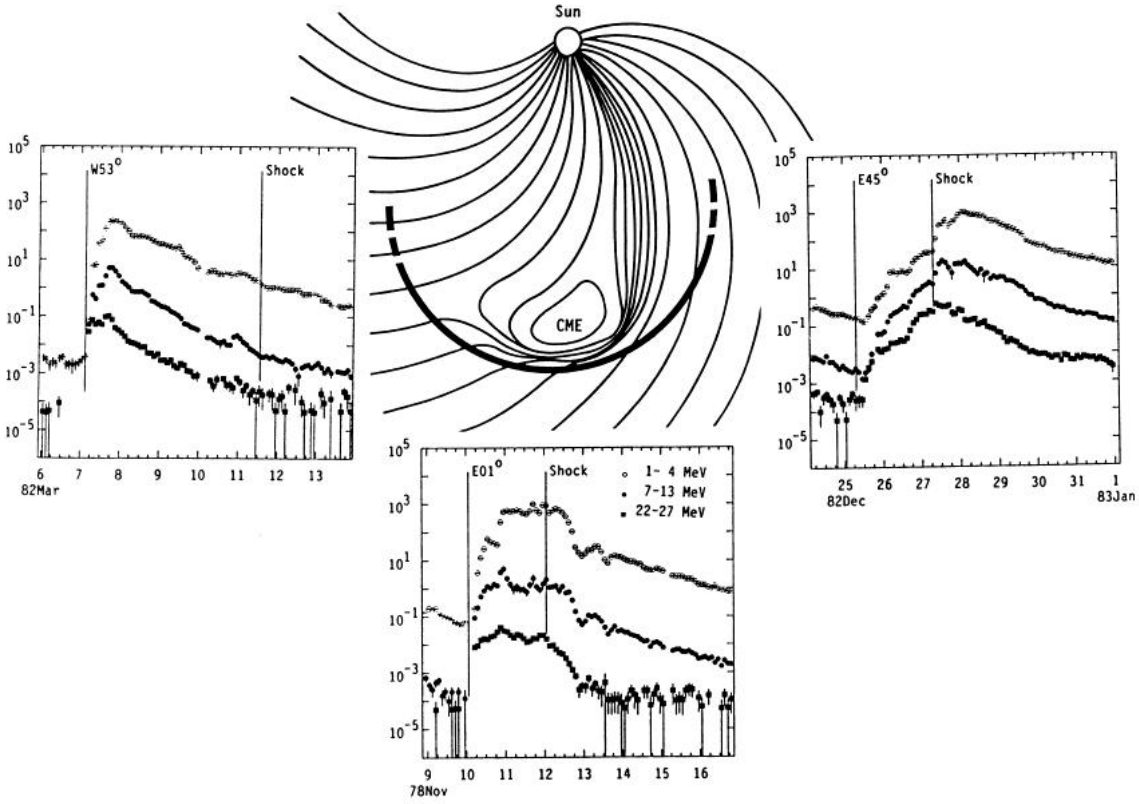

Fig. 1.14: Intensity-time profiles of 3 different proton energies are shown for observations at 3 different longitudes viewing a large CME-driven shock. For an observer that sees the event as a Western source (originating from the right hand side of the Sun), as shown on the left hand side of the figure, there is a fast rise and decline as it is well connected to the nose of the shock from the start. An observer that views the event from central meridian, as shown in the middle of the figure, sees a flat profile as it remains well connected until the shock passes. For an observer that views the event as an Eastern event (originating from the left hand side of the Sun), as shown on the right hand side of the figure, is poorly connected to the observer until after the shock passes, so shows a slower rise (Reames et al. 1996).

characteristics to a true magnetosphere formed by an intrinsic magnetic field.

1.5.1 Planetary Magnetospheres

A typical magnetosphere consists of several different regions arising from the interaction of the planetary magnetic field with the solar wind. A schematic of the terrestrial magnetosphere is shown in Figure 1.15.

The outermost layer of the magnetosphere is the bow shock, when the

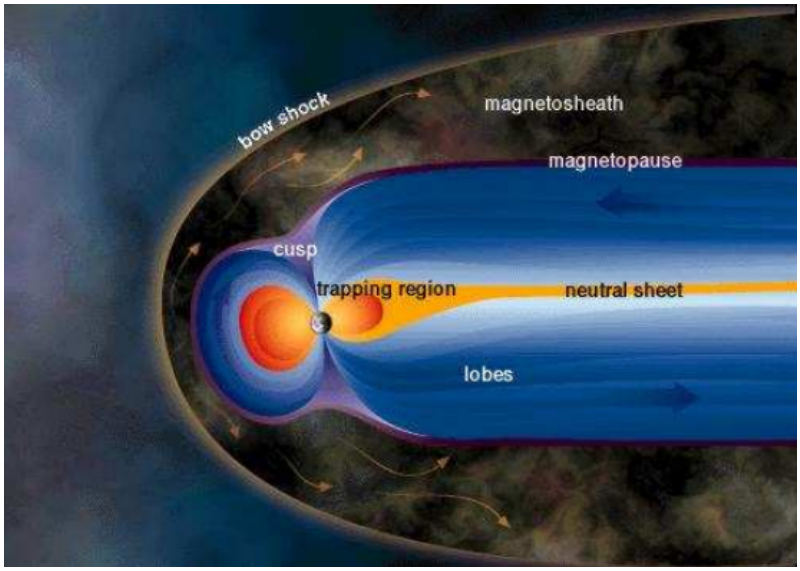

Fig. 1.15: Schematic of the terrestrial magnetosphere, where the direction of the Sun is to the left. (Pulkkinen 2007).

supersonic solar wind is decelerated to subsonic speeds as it approaches the magnetic obstacle of the planet. It is observed in-situ as a sharp discontinuity in plasma properties of the solar wind, corresponding to a shock. At the Earth the bow shock lies around 90 Mm upstream of the Earth and is roughly 17 km thick (Schwartz et al. 2011). Behind the bow shock lies the magnetosheath of heated and turbulent solar wind. It is characterised by lower density plasma, with magnetic field lines draped around the magnetosphere. The magnetopause is the boundary between the magnetosheath and magnetosphere of a planet. It is defined as the region where the solar wind pressure is balanced with the magnetic pressure of the planet's field. A simple estimate of the magnetopause stand-off distance, r, can be obtained from this assumption, and the assumption that the magnetic field strength of the planet $B(r) = B_0/r^3$ for a dipole field:

$$r \approx \sqrt[6]{\frac{B_0^2}{2\mu_0 \rho v^2}} \tag{1.31}$$

where ρ is the solar wind density and v is the solar wind velocity. At the Earth, dependent on the solar wind pressure, the magnetopause stand off distance can vary from 6 - 15 R_E (where R_E = Earth radius = 6.38 x 10^6 m).

The shape of the magnetospheric cavity is that of a dipole being com-

pressed on the dayside by the oncoming solar wind. On the nightside the magnetosphere is extended into a wake in the solar wind flow, called the magnetotail.

At the Earth, the interaction between the magnetosphere and the solar wind varies significantly dependent on the conditions in the solar wind. Periods of high pressure solar wind, for example as a result of an ICME, can compress the magnetosphere, sometimes pushing the magnetopause beyond the level of geosynchronous satellite orbits (6.6 R_E). If there is a period of southwards IMF, magnetic reconnection can occur with the northwards directed magnetic field of the Earth. This opens the magnetosphere and allows access to the solar wind plasma. The open field lines are then drawn over the poles by the solar wind flow, building up magnetic energy in the tail. Reconnection in the tail can subsequently accelerate plasma up towards the Earth, along magnetic field lines, where it impacts upon the upper atmosphere, creating aurora on the nightside of the planet. The resulting closed field lines then travel back to the dayside, allowing this process, known as the Dungey cycle, to repeat (Dungey 1961). The majority of the aurora at the Earth are observed in 2 bright bands centred over the northern and southern magnetic poles, known as the auroral ovals. The location of these bands tends to lie on the poleward boundary between closed terrestrial field lines and field lines open to the solar wind. During disturbed conditions in the solar wind, if strong magnetic reconnection has occurred at the magnetopause, then this region of open field lines is larger and aurora are observed at lower latitudes (Siscoe and Huang 1985).

The interaction between a magnetosphere and the solar wind can vary a lot for different planets, with different dipole field strengths and orientations, planetary rotation rates and sources of particles, as well as different solar wind conditions.

1.5.1.1 Saturn

Saturn has a magnetic moment of 4.6 x 10^{18} T m^3, which is over 580 times larger than the Earth's. This higher magnetic field strength, as well as a lower solar wind pressure, results in a larger magnetosphere than the Earth's, with a magnetopause stand-off distance $\sim$17 times larger than the Earth's.

Processes in the magnetosphere of Saturn are driven by both the solar wind and internal processes. Saturn is a rapidly rotating planet, with a rotation rate of 10 hours and 39 minutes. This has a significant effect on the dynamics of the magnetosphere, increasing the proportion of plasma in the magnetosphere and ionosphere that co-rotates with the planet.

Saturn, like the Earth, also has aurorae, with the main emission lying in an oval at the poles in the boundary between magnetic field lines open to the solar wind and internal closed field lines (Bunce et al. 2008). Secondary auroral features are also observed at Saturn that are driven by processes within the magnetosphere. These can include diffuse aurora, bifurcations of the auroral oval and mid-latitude auroral ovals (Grodent et al. 2010; GéRard et al. 2005; Stallard et al. 2008)

Saturn's aurorae respond strongly to solar wind conditions, but unlike the Earth the orientation of the interplanetary magnetic field is less significant, as the magnetic field strength of the magnetosheath is a smaller fraction of the magnetospheric field, making magnetic reconnection much less efficient here. This means that at Saturn, the solar wind dynamic pressure and electric field play more of a role (Crary et al. 2005). In particular, compression regions with high dynamic pressure in the solar wind have a strong influence on Saturn's aurorae, triggering morphological changes such as brightenings, particularly on the dawn sector, and shifting the auroral oval over to higher latitudes. Compression regions in the solar wind can also lead to more transport of magnetic flux in outer closed field regions of magnetospheres. This means that such flows become more significant in comparison to rotational transport, which more often dominates due to Saturn's fast rotation rate (Badman and Cowley 2007).

1.5.2 Non-magnetised Planets

Planets without a strong intrinsic magnetic field cannot generate a magnetosphere and will interact with the solar wind differently to magnetised planets. This interaction depends on the thickness of the planetary atmosphere and ionosphere. The gases of an atmosphere can experience impact ionisation, due to sunlight, which creates an ionosphere. In this case, the ionosphere acts

as a conductor and generates currents that act against the magnetic field in the solar wind, preventing it from penetrating through the atmosphere. This magnetic barrier can act somewhat like a magnetosphere, though it presents a much smaller obstacle to the solar wind flow. Like a conventional magnetosphere, there is a bow shock, as solar wind slows down to pass the obstacle, with 'magnetosheath' plasma between the shock and the obstacle consisting of magnetic field lines draped over the ionosphere. The magnetic field lines pile up by the planet in what is known as the magnetic barrier or magnetic pile-up region which interacts with the ionosphere at the ionopause current layer. The ionopause, the boundary between the ionospheric and solar wind plasma, is defined as the region inaccessible for external plasma. This boundary layer exists when the thermal pressure of the ionosphere balances the dynamic pressure from the solar wind.

1.5.2.1 Venus

Venus has a very thick atmosphere and is close to the Sun, leading to high levels of photo-ionisation, and consequently, a dense ionosphere. As a result of this, at Venus during solar minimum, the solar wind dynamic pressure only occasionally exceeds the thermal pressure of the ionosphere. At solar maximum, and during periods of high pressure solar wind, the magnetic field in the magnetosheath can penetrate the ionosphere, which increases the obstacle presented to the solar wind. The interaction of the solar wind and Venus is summarised in Figure 1.16.

Aurorae have been observed on Venus, though unlike that of the Earth and giant planets, they are continuous and highly variable. These auroral emissions are seen at 130.4 nm on the nightside of Venus and are believed to be caused by the precipitation of suprathermal electrons (Phillips et al. 1986).

The Venusian ionosphere is created on the dayside by solar EUV and X-ray photon flux, like the Earth's ionosphere. It is predominantly made up of oxygen ions (O^+ in the upper ionosphere and O_2^+ below 200 km). The nightside ionosphere at Venus is maintained by dayside ionospheric plasma crossing the terminator due to plasma pressure gradients. This occurs around 150 - 300 km above the surface and at these altitudes, the lifetime of O^+ and

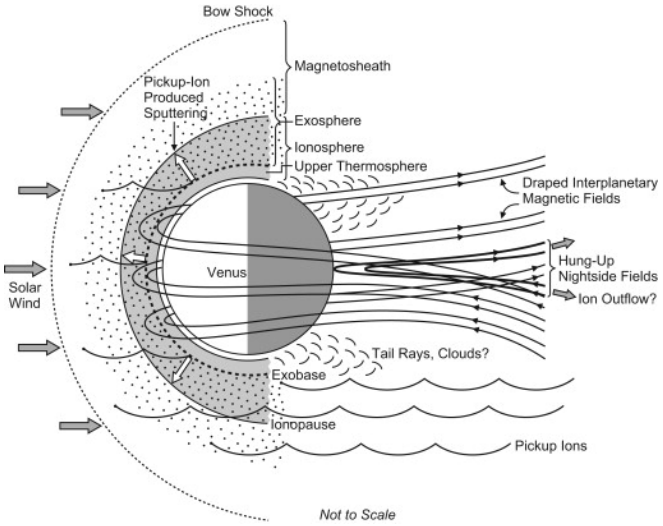

Fig. 1.16: The interaction of the solar wind with Venus and related atmospheric escape processes.(Russell et al. 2007)

O_2^+ ions is more than 10 days, so they can maintain the nightside ionosphere before recombining to neutral particles.

The atmosphere of Venus is very dense, but very dry. Though it has less water vapour than expected, estimated rates of oxygen ion escape do not explain this deficit. Therefore, the mechanisms of atmospheric escape due to impacts of the solar wind are of particular interest. One process that may enhance the rate of ion escape is scavenging, which is the process of 'picking-up' ions by the solar wind. It occurs when neutral particles in the exosphere of the planet may reach higher than the ionopause before they are photo-ionised. These newly created ions are then 'picked-up' by the solar wind and transported away downstream (Barabash et al. 2007a). This process is asymmetric, as shown by Figure 1.16, as the ions created on one side of the planet are spiralled towards it, rather than away. This is driven by the convection electric field. This process loads extra mass onto the IMF lines flowing past Venus, further slowing the solar wind here. The result is the draping of these field lines around the ionosphere obstacle, which creates a structure similar to a magnetotail. The convection electric field is greatest when the velocity and magnetic field are high and perpendicular to each other. As both of these parameters are increased during the passage CIRs and ICMEs,

atmospheric loss through this process should be greater during these times.

The ionosphere of Venus is also directly impacted by disturbed interplanetary conditions, as periods of high solar wind pressure and IMF can lead to compressions and/or magnetisations of the ionosphere. Elphic et al. (1980) reported that the altitude of the dayside ionopause decreases with increasing solar wind pressure. Such conditions can also cause the IMF to diffuse into the ionosphere of Venus, as the ionospheric thermal pressure is unable to balance the solar wind magnetic pressure.

1.5.2.2 Mars

Mars is similar to Venus in many ways, as it also lacks a dipole magnetic field. This leads to a similar induced magnetosphere with a bow shock, magnetic pile-up boundary and ionopause, as shown in Figure 1.17. The main difference between Mars and Venus arises from the remnant crustal magnetic fields on Mars. These are small scale magnetic fields found predominantly in the southern hemisphere of Mars which can perturb the global scale features of the induced magnetosphere of Mars. They can create mini-magnetospheres which cause plasma convection across the ionosphere. This drift of charged particles across strong crustal magnetic fields is similar to behaviour observed with terrestrial magnetic fields (Breus et al. 2005). These remnant crustal fields are thought to be the cause of aurora observed on Mars in highly concentrated and localised regions. These aurorae were observed by Bertaux et al. (2005) in the UV band near the equator and suggest that particles could precipitate along remnant magnetic field lines connecting the surface to the solar wind.

Another key difference is that the Martian ionosphere is weaker than that of Venus, and the dynamic pressure of the solar wind often exceeds the thermal pressure of the ionosphere, even at solar minimum. This leads to the magnetisation of the ionosphere to balance the pressure of the solar wind. The dayside ionosphere of Mars is also shown to have vertical density 'bulges' in it over regions of strong vertical crustal magnetic field, where these field lines will be connected to the solar wind (Gurnett et al. 2008). These regions on the nightside of Mars are also shown to have higher total electron concentration (Safaeinili et al. 2007).

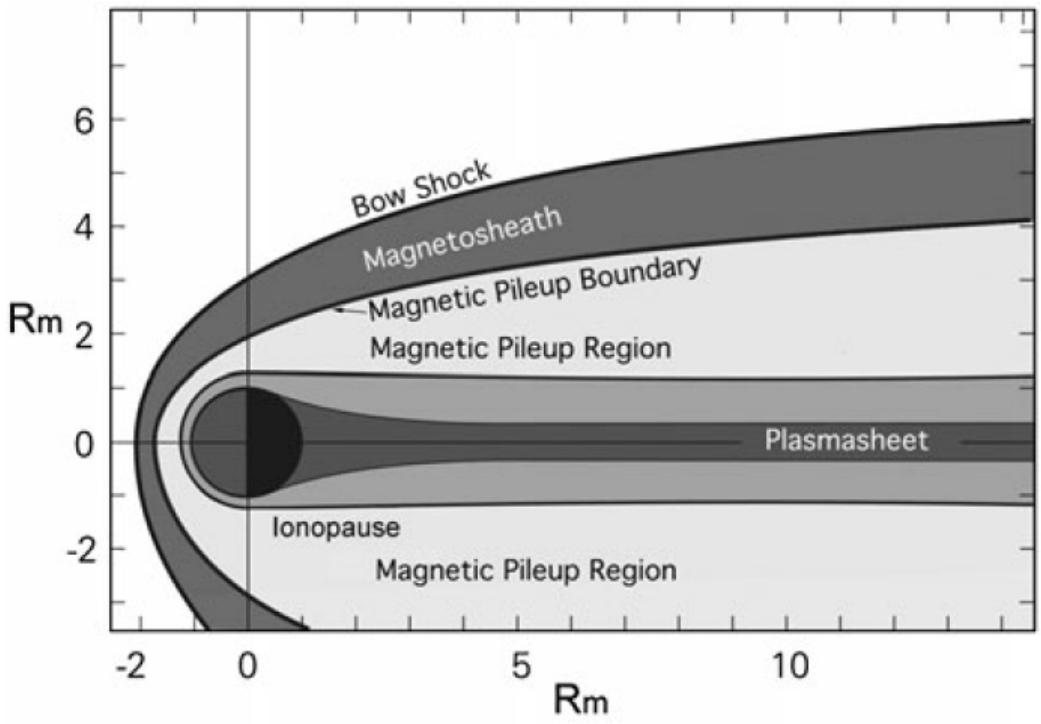

Fig. 1.17: The major plasma regions around Mars.(Nagy et al. 2004)

The interaction between Mars and the solar wind has many similarities with the interaction between Venus and the solar wind. This includes atmospheric loss during disturbed solar wind conditions. High solar wind pressure during solar storms compresses the plasma environment of Mars and results in asymmetries in the plasma boundaries and exosphere (Edberg et al. 2009). This gives the solar wind access to lower altitudes of the atmosphere which leads to more atmospheric mass loss as shown by Crider et al. (2005) for the 2003 Halloween solar superstorm.

Such storms can also impact the Martian ionosphere as solar wind protons and magnetosheath hydrogen atoms precipitate down in to the lower atmosphere and deposit energy (Haider 2012). Solar storms also lead to an enhancement of the total electron count of the ionosphere (Mahajan et al. 2009; Haider et al. 2009).

1.6 Thesis Aim and Outline

Dynamic events that originate from the Sun can create a variety of impacts at the Earth, which can be highly disruptive and damaging to infrastructure

and technological systems. In order to be able to mitigate the effects of such events, the likelihood of their arrival at the Earth and predictions of when this will occur are needed. This requires an understanding of how solar transients propagate and evolve throughout the solar system and the limitations of simulations used for space weather forecasting. This thesis studies a number of propagating solar events, including solar energetic particle events (SEPs), which can reach the Earth in less than an hour, Interplanetary Coronal Mass Ejections (ICMEs) which tend to have the most severe space weather impacts, and Stream Interaction Regions (SIRs), which can be very long lived structures in the heliosphere and influence the propagation of other transient events. It makes use of a wide range of multi-spacecraft observations throughout the solar system, as well as simulations, in order to obtain a large scale view of how these events travel and evolve.

Chapter 2 of this thesis describes the various space instrumentation that provided in-situ and remote sensing data for this thesis, including solar telescopes and several planetary spacecraft. It also describes models that were used in support of these observations, and as a comparison tool. Chapter 3 aims to discover the cause of a widespread SEP event which occurred in 2011. The event's behaviour is linked to the expansion of an associated CME and EUV wave. Chapter 4 presents work tracking an ICME and SIR through the solar system, with the aim of understanding how these structures propagate and interact. The events are observed throughout the inner heliosphere and simulated beyond that, to Saturn, using the Enlil solar wind model. Chapter 5 aims to further investigate the properties of the Enlil model, by finding out how the results change with different input parameters. This was achieved by comparing observations at 1 AU with simulation results of the ambient solar wind and changing several different initial model options, including different model resolutions, coupled coronal models and input synoptic magnetograms. Finally, Chapter 6 discusses the main conclusions of this thesis and its collective contribution to the study of propagating solar transients, as well as considering possibilities for future work.

Chapter 2

Instrumentation and Modelling

The data used in this thesis comes from a variety of spacecraft, including solar telescopes and planetary spacecraft at Venus, Mars, Earth and Saturn. These spacecraft have provided in-situ measurements, for example from magnetometers and plasma analysers, and remote observations including EUV images and coronagraph images. The science objectives of this thesis included to study the cause of a widespread SEP event, to study the propagation and interaction of ICMEs and CIRs and to investigate the properties of the Enlil solar wind model, used for space weather predictions. These aims could be achieved by this range of instrumentation, enabling solar transients to be observed at multiple locations throughout the heliosphere, from their source on the Sun, out to 1 AU and beyond. This allows for the evolution and propagation of these events to be studied, over wide longitudes and large radial distances from the Sun. In addition to this wide range of data types and sources, simulations were also used, complementing the observations and being compared to them as a validation tool. In particular, Enlil was used extensively in Chapters 4 and 5.

2.1 Solar and Heliospheric Observatory (SOHO)

SOHO (Domingo et al. 1995) is a collaborative mission between ESA and NASA, launched from the Kennedy Space Center on 2 December 1995. The primary science objectives of the mission were to use helioseismology techniques to study the solar interior, to gain an understanding of the physical processes that lead to coronal heating and to understand how the solar wind

is formed and accelerated. To achieve these goals, SOHO carries a payload of twelve instruments, that can be divided into three categories: helioseismology, solar corona remote sensing and solar wind in-situ instruments. In this thesis, only data from the remote sensing instrument LASCO are used. The SOHO spacecraft is situated in a halo orbit around the L1 Lagrangian point (approximately 1.5 x 10^6 km upstream of the Earth), allowing for continuous uninterrupted observation of the Sun and in-situ measurements of the solar wind.

2.1.1 Large Angle Spectrometric Coronagraph (LASCO)

LASCO (Brueckner et al. 1995) comprises of three coronagraphs with nested, concentric annular fields of view that image the solar corona from 1.1 to 30 $R_\odot$. Using three coronagraphs with overlapping fields of view allows LASCO to overcome two limitations of externally occulted coronagraphs. The first of these limitations is that the spatial resolution in the inner corona is poor due to very small effective apertures. This arises because for a given distance from the occulting disk to the first imaging element, the instrument can only provide images of the corona for distances >1.5 $R_\odot$, because at the inner edge of the field of view, most of the imaging element is shadowed by the occulter. The second limitation restricts the aperture to no more than a few centimetres due to size limitations. The C1 coronagraph (with a field of view of 1.1 - 3.0 $R_\odot$) is a mirror coronagraph using a Fabry-Perot interferometer, but has not been operational since 1998. This thesis uses data from the C2 and C3 coronagraphs only, which are externally occulted white-light Lyot coronagraphs with field of views of 1.5 - 6.0 and 3.7 - 30 $R_\odot$ respectively. Figure 2.1 shows a conceptual diagram for C2 and C3.

The external occulter D1 completely shadow the entrance aperture A1 from direct sunlight. The objective lens O1 images the corona onto the field stop and also images D1 onto a stop D2. This is the internal occulter which intercepts residual diffracted light from the edges of the external occulter D1. Beyond D2 lies the field lens O2, which collimates the image of the corona and images the entrance aperture A1 onto the Lyot stop A3. The Lyot stop intercepts diffracted light originating from the edges of A1 and prevents it from

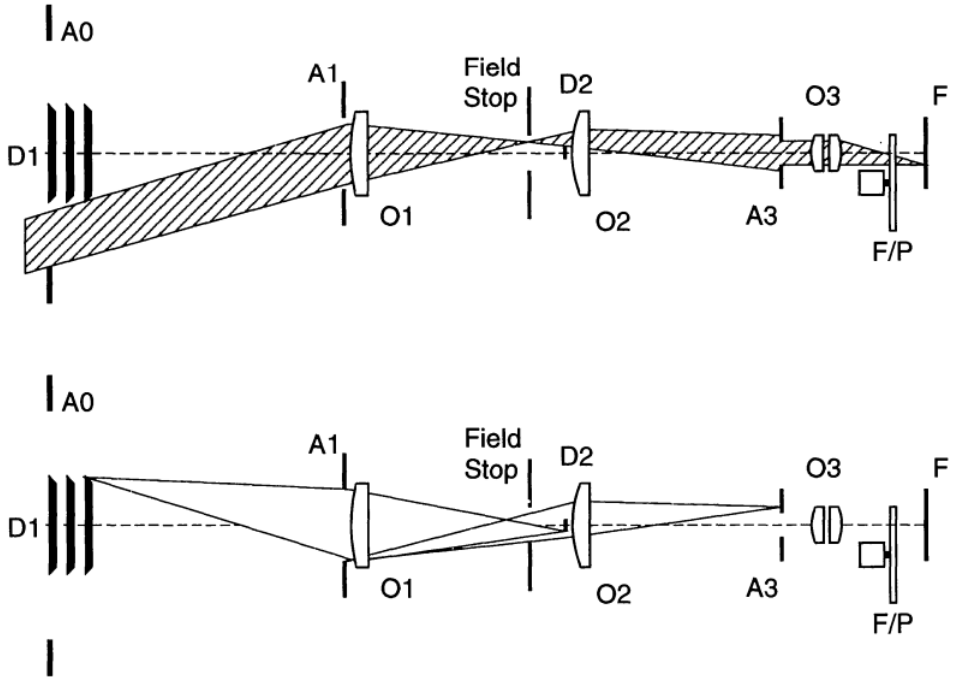

Fig. 2.1: An externally occulted Lyot coronagraph e.g. LASCO C2 or C3. A0 is the front aperture, D1 the external occulter, A1 the entrance aperture, O1 the objective lens, D2 the internal occulter, O2 the field lens, A3 is the Lyot stop, O3 is the relay lens with Lyot stop, F/P is the filter/polariser wheels and F is the focal plane. The top diagram traces a ray for the coronal image, while the bottom diagram shows how stray light is suppressed.

reaching the CCD at the focal plane, F. Finally behind A3, the relay lens O3 re-images and magnifies the primary coronal image onto the 1024x1024 pixel front-side illuminated CCD camera at F.

2.2 Solar Terrestrial Relations Observatory (STEREO)

STEREO (Kaiser et al. 2008) is a NASA mission launched from Cape Canaveral Air Force Station on 26 October 2006. The mission consists of two near-identical spacecraft that have been placed in orbit around the Sun at approximately 1 AU, drifting away from the Earth at a rate of $\sim 22^{\circ}$ per year. One spacecraft (STEREO-A) travels ahead of the Earth, with an orbit slightly closer to the Sun, while the other (STEREO-B) lags behind the Earth, slightly further from the Sun. The STEREO mission is designed to study the causes and mechanisms of CME initiation and to follow their propagation through the inner heliosphere to the Earth. It also aims to study the mechanisms and sites of solar energetic particle acceleration in the low corona and interplanetary medium, as well as developing a 3D time-dependent model of the ambient solar wind, including its magnetic topology, temperature, density and velocity structure. To achieve these science objectives, each STEREO spacecraft carries a set of optical, radio and in-situ particles and field instruments. These consist of four instrument suites: Sun-Earth Connection Coronal and Heliospheric Investigation (SECCHI, Howard et al. 2008), In-situ Measurements of Particles and CME Transients (IMPACT, Luhmann et al. 2008), Plasma and Suprathermal Ion Composition (PLASTIC, Galvin et al. 2008) and STEREO/WAVES (S/WAVES, Bougeret et al. 2008). A view of the STEREO-B spacecraft with the locations of all these instruments is shown in Figure 2.2. The Ahead and Behind spacecraft are mainly identical, although some instrument placements differ slightly. This is because they fly upside down relative to one another, but the high-gain antenna must always face towards Earth, so some of the particle instruments have slightly different placements so they can still point into the solar wind magnetic field direction.

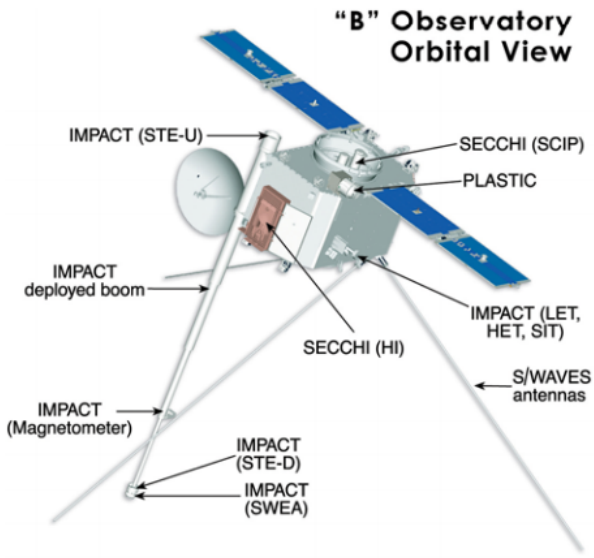

Fig. 2.2: An illustration of the STEREO-B spacecraft and the locations of its instruments. The SECCHI instruments point sunwards and the IMPACT boom and S/WAVES antennas point antisunwards (Kaiser et al. 2008).

2.2.1 Sun-Earth Connection Coronal and Heliospheric Investigation (SECCHI)

SECCHI (Howard et al. 2008) is a suite of five remote sensing instruments, including an extreme ultra-violet imager (EUVI), two white-light coronagraphs (COR-1 and COR-2) and two white-light heliospheric imagers (HI-1 and HI-2). This suite can image from the solar surface out to the vicinity of Earth, from two perspectives, allowing for the possibility of 3D reconstructions of solar features, including CMEs. All these instruments use 2048x2048 pixel CCD arrays in a backside-in mode. The primary objectives of the SECCHI instrument suite include to study the structure and timings of the physical properties involved in CME initiation, to determine the 3D structure and kinematic properties of CMEs, to study the 3D structure of active regions, coronal loops and helmet streamers, and to discover the critical forces that control the propagation of CMEs in the corona and interplanetary medium.

2.2.1.1 Extreme Ultraviolet Imager (EUVI)

SECCHI's extreme ultraviolet imager (EUVI: Wuelser et al. (2004)) observes the solar disk and atmosphere up to 1.7 $R_\odot$ in four spectral channels, spanning

a temperature range of 1 x 10^5 K to 2 x 10^7 K, that were chosen to match those of its predecessor SOHO/EIT. EUVI provides a pixel-limited resolution of 1.6 arcsecond per pixel across the entire field of view and an image cadence of up to 2.5 minutes, which is a substantial improvement over SOHO/EIT. EUVI is a normal-incidence Ritchey-Chrétien telescope with thin metal filters, multilayer coated mirrors and a back-thinned CCD detector. The layout of the telescope is shown in Figure 2.3.

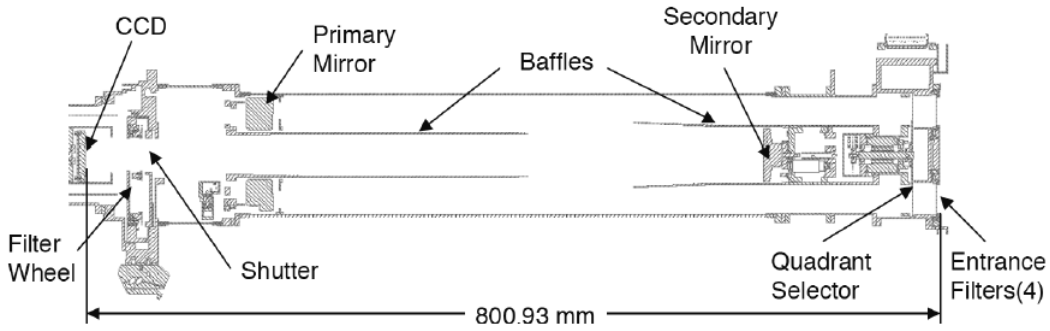

Fig. 2.3: A cross-section of the EUVI telescope (Wuelser et al. 2004).

Light enters the telescope through the entrance filter of 150 nm thick aluminium, which blocks undesired UV, visible and IR radiation, keeping the solar heat out of the telescope. Light then passes through the quadrant selector to one of the four quadrants. Each quadrant of the primary and secondary mirror is coated with a multilayer narrow-band reflective coating which is optimised for one of the four wavelength bands (He II 304Å, Fe IX 171Å, Fe XII 195Å or Fe XV 284Å). After bouncing off these mirrors, the light continues through a filter wheel to remove any remaining visible or IR radiation. A rotating blade shutter controls the exposure time and the image is formed on the CCD camera.

2.2.1.2 COR-1 and COR-2

COR-1 and COR-2 are traditional visible light Lyot coronagraphs with overlapping fields of view (COR-1: 1.5 - 4 $R_\odot$ and COR-2: 2.5 - 15 $R_\odot$). They were split into two separate telescopes due to the large radial gradient of coronal brightness in this range. They both take sequences of three polarised observations at 0° and ±60° which are then combined on the ground to obtain total

brightness and polarised brightness (pB) images.

The inner coronagraph, COR-1 (Thompson et al. 2003), was the first space-borne internally occulted refractive telescope (unlike the internally occulted *reflective* coronagraph of LASCO/C1). It images the inner corona at a wavelength of 656 nm and a resolution of 7.5" per pixel, with a time cadence of 8 minutes. COR-1 is dominated by instrumentally scattered light, which is unable to be removed by Lyot principles. However this light is predominantly unpolarised, so can be greatly reduced by making polarised observations in the three states of linear polarisation and then calculating the polarised brightness. This requires a high signal to noise ratio in spite of the scattered light, which is partly achieved by on-board binning of the pixels.

The outer coronagraph, COR-2 is an externally occulted Lyot coronagraph, similar in design to LASCO C2 and C3. This enables a lower stray light level than COR-1, as the external occulter shields the objective lens from direct sunlight. It images the corona in white light (650 - 750 nm) with a resolution of 14.7" per pixel and a time cadence of 15 minutes.

2.2.1.3 Heliospheric Imagers (HI)

The aim of the Heliospheric Imagers (Eyles et al. 2009) is to observe CMEs and other structures in visible light as they propagate from the corona into the heliosphere. The HI package has two wide-angle refractive optical telescopes, HI-1 and HI-2, mounted on the side of each spacecraft, which image the region between the Sun and the Earth, out from 15 $R_{\odot}$. HI-1 observes in the 630 - 730 nm wavelength range with a field of view of 20°, centred on an elongation of 13.28°. The image pixel size is 70" and the nominal image cadence is 40 minutes. HI-2 observes in the 400 - 1000 nm range with a field of view of 70° centred on an elongation of 53.36° from the Sun. The pixel size is 2' and the cadence is 120 minutes. This allows for an overlap of roughly 5°, as shown in Figure 2.4. The concept of the HI instrument was derived from laboratory measurements of Buffington et al. (1996) who found the scattering rejection as a function of the number of occulters and their angle below the occulting edge. The anticipated major contributions to the observed intensity is shown in the bottom of Figure 2.4, including the CME intensities and the contribution from

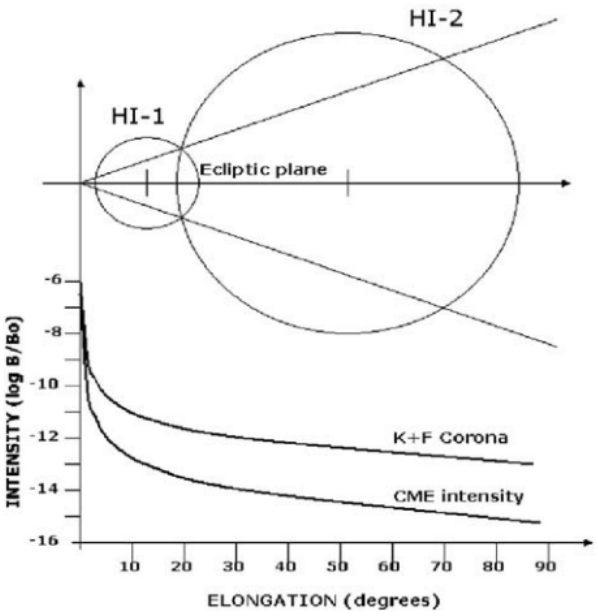

Fig. 2.4: The fields of view and geometry of the HI telescopes, and the anticipated major intensity contributions (Eyles et al. 2009).

the F-corona and K-corona. The CME signal intensity is around two orders of magnitude lower than the F+K coronal intensity, meaning that high levels of light rejection are required to detect faint CMEs. This is achieved by the baffle system, consisting of the forward, internal and perimeter baffles. The forward baffle aims to reject the solar disk intensity and reduce the stray light to the necessary levels, the perimeter baffles are designed to reject stray light from the spacecraft and the internal baffle aims to reject light from the Earth and stars.

Viewing faint CMEs also requires the HI images to have long exposure times in order to decrease the signal-to-noise ratio. To avoid cosmic ray swamping, and due to the limited dynamic range, HI takes a series of shorter exposures which are summed on board. For HI-1 this is 30 images of 40 second exposures, resulting in a total exposure time of 1200 seconds and a cadence of 40 minutes. HI-2 takes 99 images with exposure times of 50 seconds each, summed to a total exposure time of 4950 seconds, which results in an image cadence of 2 hours. HI has no mechanisms except a door to protect the instrument during launch, and therefore takes images in shutterless mode. This results in smearing of the image as each row sees the scene from the pixel

below it, which is corrected for on the ground. The HI telescopes are also designed to bleed along columns if an object is bright enough to saturate the CCD, allowing them to be easily identified and corrected.

2.2.2 In-situ Measurement of PArticles and CME Transients (IMPACT)

The IMPACT instrument suite measures in-situ thermal and suprathermal solar wind electrons, energetic electrons and ions, and the interplanetary magnetic field strength and direction. To do this it has seven separate instruments, four of which are dedicated to measuring solar energetic particles (SEPs) and are located on the main spacecraft body (the low energy telescope, LET, the high energy telescope, HET, the suprathermal ion telescope, SIT, and the solar electron and proton telescope, SEPT). The remaining three instruments (the solar wind electron analyser, SWEA, the suprathermal electron instrument, STE, and the magnetic field experiment, MAG) are mounted on a six metre boom. This boom is located on one corner of the spacecraft to minimise interference from the high gain and S/WAVES antennas, and is deployed anti-sunward so these instruments are usually in the shadow of the spacecraft. This is shown on Figure 2.2. Only data from LET, HET, SEPT and MAG are used in this thesis, so the other instruments are not described in detail.

2.2.2.1 Low Energy Telescope (LET)

The LET (Mewaldt et al. 2008) is part of IMPACT's SEP suite, consisting of LET, HET, SIT and SEPT. The electronics box for LET and HET also includes a SEP-central Digital Processing Unit (DPU), where much of the suite's data handling is performed. LET itself measures the energy spectra, angular distributions, elemental composition and arrival times of He to Ni ions in the energy range of ∼2 - 40 MeV/nucleon (depending on species) and H over a more limited range of ∼2 - 13 MeV. This energy range is low enough to include a large number of solar events, but not too low that the time structure of acceleration effects near the Sun is washed out by velocity dispersion. It lies between the range of SIT and HET. LET can carry out onboard particle identification of sixteen species (from H to Fe), within ∼12 energy intervals, using approaches that were initially developed for the *Wind* spacecraft (von

Rosenvinge et al. 1995).

LET is a dual directional fan-like solid state detector telescope that uses a $\mathrm{d}E/\mathrm{d}x$ vs. E telescope configuration. This involves comparing the energy loss of a particle as it traverses the detector with the residual energy after passing through the detector. A photo of LET and HET is shown in Figure 2.5. The sensor system of LET is made up of one double-ended detector stack, consisting of 14 ion-implanted solid state detectors of varying thickness and segmentation, with three different detector designs. There are 10 entrance apertures (five directed sunward and five antisunward) arranged in two fan-like layouts of 133° by 29°. There are four additional solid-state detectors in the central area of the instrument. The detectors are all segmented into a total of 54 multiple active areas, which provide some position sensitivity to determine particle trajectories. This also helps to reduce noise and improve the instrument performance when experiencing high particle intensities.

Fig. 2.5: A photograph of the Low Energy Telescope (top centre), High Energy Telescope (centre left) and SEP central (bottom), which is the control unit for the SEP suite of IMPACT. (von Rosenvinge et al. 2008)

The axis of the telescope is in the ecliptic plane, aligned along the average Parker spiral, ∼45° from the solar direction. A geometric factor of 4.0 cm^2 sr and anisotropy measurements over ∼260° are achieved by the telescope's multi-element double-ended front end.

2.2.2.2 High Energy Telescope (HET)

HET (von Rosenvinge et al. 2008) is designed to measure the intensity and energy spectra of higher energy H and He ions, as well as electrons that have been accelerated by SEP events. The kinetic energy range for protons and He ions that stop in the telescope is ∼13 to 40 MeV/nucleon, with penetrating protons and He ions (that do not stop in the telescope), measured up to ∼100 MeV/nucleon. HET can also provide compositional measurements of Z>2 ions with energies greater than 30 MeV/nucleon, extending the LET energy range for key species. Stopping electrons are measured in the 0.7 - 6 MeV energy range. During solar quiet times, HET also measures the composition and spectra of cosmic rays.

HET has two thick detectors on one end of a traditional cylindrical telescope, to determine the geometry of the incident particles, with subsequent elements of the detector stack made by combining thinner devices. Incident particles which stop in the telescope are identified using the standard $\mathrm{d}E/\mathrm{d}x$ total energy analysis, while penetrating particles are identified using multiple $\mathrm{d}E/\mathrm{d}x$ measurements by the stack detectors. The telescope axis is in the ecliptic, pointed upstream along the average Parker spiral angle. A photo of HET, with LET is shown in Figure 2.5. The telescope body is designed to protect the detector surfaces from external light by blocking the front end with two foils that are coated with vapour deposited aluminium.

Nine particle species from H to Fe can be identified onboard, with an average of nine energy intervals. Electrons can be identified in 3 energy intervals. The telescope has a field of view of 55° and a geometry factor of 0.61 cm^2 sr.

2.2.2.3 Solar Electron and Proton Telescope (SEPT)

SEPT (Müller-Mellin et al. 2008) has a two-part double-ended solid state detector design, which detects the energetic electrons, dominant proton and helium ions of the SEP population. It provides measurements of protons and alphas in the 60-7000 keV energy range and electrons in the 30-400 keV range. The proton range fills in some of the gap between the solar wind energies (covered by PLASTIC) and higher energy measurements of LET and HET (2-100 MeV). The electron range covers the gap (with some overlap)

between suprathermal electrons measured by STE and higher energy electrons measured by HET.

There were several instrumental challenges in developing the SEPT telescope: As the STEREO spacecrafts are not spinning, acquiring the anisotropy information must be achieved another way. Also, in this energy range of tens of keV to several MeV, singly charged particles deposit only small amounts of energy in a solid state detector, meaning the requirements for the suppression of noise must be more stringent than with heavier ions. At higher energy ranges separating protons from electrons would be achieved by using the well-proven $\mathrm{d}E/\mathrm{d}x$ - E approach, but this is not viable here, as one cannot have two measurements in different detectors. The $\mathrm{d}E/\mathrm{d}x$ detector would either stop all low energy particles before they arrived at the E detector, or it would have to be so thin that the signal from the singly-charged penetrating particle would be indistinguishable from noise. In order to address the issue of obtaining anisotropy information, the SEPT telescope actually consists of two telescopes pointing in different directions. SEPT-E is directed sunward and anti-sunward in the ecliptic plane, along the Parker spiral, while SEPT-NS looks North and South, vertical to the ecliptic plane. This partially complements the ion viewing directions of LET, which views in the ecliptic. The full angle of the viewing cone is 52° for an unobstructed field of view. Each of these four viewing directions has two adjacent sensor apertures for protons and electrons. The geometry factor for the four electron telescopes is 0.13 cm^2 sr, resulting in a total geometry factor for electrons of 0.52 cm^2 sr. For protons, the total geometry factor is 0.68 cm^2 sr, with each of the four proton telescopes having a geometry factor of 0.17 cm^2 sr.

The double-ended set up of the detector refers to the detector stack with view cones in two opposite directions. The electron side is covered by a thin foil, which leaves the electron spectrum unchanged but stops protons with energies <400 keV. The proton side is surrounded by a magnet, which sweeps away electrons and allows ions to pass in the 400 keV to 7 MeV range. This allows for the contribution of >400 keV ions in the foil detector to be computed and subtracted to find the electron fluxes here.

2.2.2.4 Magnetic Field Experiment (MAG)

The magnetometer (Acuña et al. 2008) onboard STEREO is on the IMPACT boom, measuring the in-situ vector magnetic field with a time resolution of 1/8 seconds. It measures the magnetic field in two ranges, ±65536 nT and ±500 nT, which allows it to operate in all phases of the mission, including spacecraft testing and integration while still within the geomagnetic field. The ranges can be switched by automatic or manual control. The instrument is a triaxial, wide-range, low-power fluxgate magnetometer (FGM), with updated features based on the Messenger magnetometer design.

The aim of the magnetometer is to study the IMF, its relationship to solar wind structures and how it responds to solar activity. By measuring the time-variable large scale structure of the IMF continuously at both spacecraft locations, and the gradients between them, MAG allows for the interpretation of solar wind parameters, particle distributions and the paths of energetic particles. It can also enable the analysis of local sources for shocks and discontinuities that could be acceleration mechanisms.

Its location on the boom, ∼3 m away from the main spacecraft helps to minimise the contribution of any spacecraft fields to the magnetic field measured by the instrument. In addition the spacecraft itself was kept as magnetically clean as possible, for example by screening troublesome parts such as reaction wheels and by characterising unavoidable signals in the data from the spacecraft during the integration and test phases.

The IMPACT magnetometer sensor is a ring-core fluxgate magnetometer, with three orthogonally mounted ring core fluxgate sensors to determine the vector components of the ambient field. The basic principle of a fluxgate magnetometer involves a ferromagnetic core surrounded by two coils of wire, as shown in Figure 2.6. When an alternating current flows in the primary coil, wrapped around the core, it becomes an electromagnet and is driven through a cycle of magnetic saturation, flipping the core's magnetic polarity back and forth. The secondary coil, wrapped in the opposite direction to the primary coil, will then have a current induced in it, which will be equal to the input current in the absence of an external magnetic field. If the electromagnet is

subjected to an external field, some component of which will be aligned with the core, the symmetry of the cycle of magnetic saturation is distorted. Where the external field is parallel to the field in the core, saturation will be reached more easily, and where the external field is opposite to the field in the core, saturation will be delayed because the sum of the fields will be weaker. The output current induced in the secondary coil will therefore be out of step with the input current, the extent of which is dependent on the strength of the external field aligned with the core.

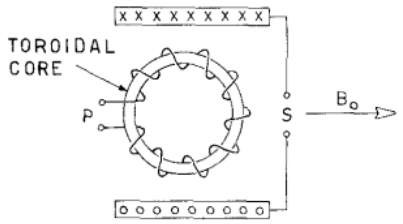

Fig. 2.6: The ring core geometry of the saturable core sensing element for a fluxgate magnetometer. (Ness 1970).

The magnetometer's nominal time resolution is 1/8 seconds, but it can take measurements at a time resolution of 1/32 seconds, during IMPACT burst mode periods. This raw data is processed by the IMPACT/PLASTIC instrument DPU (IDPU), where it is low pass filtered, digitized, averaged and then packeted to be transmitted to the ground. The data has a nominal accuracy of 0.1nT, with a digital resolution in the 500nT range of 16pT.

2.2.3 PLAsma and SupraThermal Ion Composition (PLASTIC)

The PLASTIC instrument (Galvin et al. 2008) measures the in-situ plasma characteristics of protons, heavy ions and alpha particles. It can provide diagnostic measurements of the mass and charge state composition of the heavy ions, as well as characterising CME plasma from ambient plasma. It can study ions in the mass range from H to Fe and has an energy range of $\sim$0.3 to 80 keV.

The PLASTIC instrument is a time-of-flight/energy mass spectrometer with nearly complete angular coverage in the ecliptic plane. It has three main elements, the Entrance System (Energy/charge Analyser), the Time-of-

Flight/Energy (TOF/E) Chamber and its housing and the Electronics Box (EBox), as shown in Figure 2.7. The Entrance System selects incoming particles for analysis based on their energy-per-charge (E/Q) value and their incident direction. The TOF/E Chamber contains the detectors and their electronics, the ion optics and signal processing board. The Electronics Box carries the remaining analogue electronics, all the digital electronics, the power supplies and the connections to the spacecraft power and the IDPU.

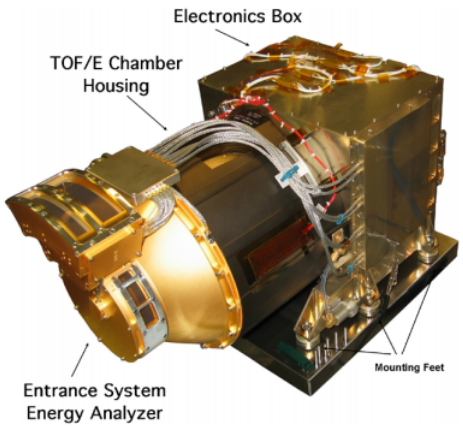

Fig. 2.7: A photo of the PLASTIC instrument, showing the Entrance System, Time-of-Flight/Energy Chamber and its housing, and the Electronics Box. (Galvin et al. 2008)

The PLASTIC sensor has three separate instrument sections, with distinct fields of view and geometric factors in order to measure plasma and suprathermal populations within a single instrument. Each of these fields of view and geometric factors are optimised for a particular ion population by combining with an ion optics section. The three sections are the Solar Wind Sector (SWS) Small Channel and SWS Main Channel, which have the same fields of view, but different geometric factors, and the Suprathermal Ions Wide-Angle Partition Sector (WAP).

SWS uses electrostatic deflectors to provide a field of view of 45° in the azimuth ($\sim$ the ecliptic plane) and 40° in elevation ($\sim$ polar direction), centred on the Sun-spacecraft line. The SWS Small Channel provides proton density, velocity, thermal speed and alpha to proton ratios by measuring the distribution functions of solar wind protons and alphas. The SWS Main Channel has a larger geometric factor, and measures the more abundant solar wind minor

ions such as C, O, Mg, Si and Fe. For these ions it provides the elemental composition, charge state distribution and bulk and thermal speeds. WAP has a larger geometrical factor, but less directional information than the SWS channels. It has a field of view of 210° (B) and 225° (A) in the remaining unobstructed off-Sun azimuth directions, and <10° in the polar direction.

These three instrument sections share a 360° toroidal top-hat electrostatic analyser with its azimuth entrance in the ecliptic plane. This measures the energy per charge, which is followed by post-acceleration voltage measurement, time-of-flight measurement and an energy measurement by solid state detectors. Combining these measurements allow for the determination of the mass-per-charge, and combined with the residual energy can determine the ion mass.

2.2.4 STEREO/WAVES

S/WAVES (Bougeret et al. 2008) is a radio and plasma wave instrument, which tracks radio disturbances from the Sun to the Earth. Observing these radio bursts can shed light on the location of CME-driven shocks and the 3D topology of open field lines that flare-accelerated particles can flow down. The main science goals of S/WAVES include to remotely observe and measure radio waves excited by energetic particles associated with CMEs and solar flares, and to measure the properties of CMEs and interplanetary shocks and their associated plasma waves in-situ at 1 AU.

The instrument uses three six metre monopole antenna elements that are mutually orthogonal in order to take comprehensive measurements of the three components of the fluctuating electric field. The antenna are deployed antisunward to avoid the fields of view of the Sun-facing instruments. Each antenna is a Beryllium-Copper 'stacer' spring, which were chosen for their excellent thermal properties, stiffness and reliability. The antenna is designed to maintain a high signal-to-noise ratio for expected Type II and Type III radio bursts and other solar and interplanetary radio emissions. It is deployed from a common baseplate that also holds the preamplifier housing. The high input impedance preamplifiers minimise the effects of the base capacity, which can limit the receiver sensitivity and prevent loading of the antennas.

S/WAVES has three different frequency receivers that take measurements of different frequency domains. The Low Frequency Receivers (LFR) is a direct conversion receiver, to carry out spectral analysis and direction finding of radio noise that is generated from ∼0.5 AU (160 kHz) to 1 AU (2.5 kHz). This frequency range is divided into three 2-octave bands which each have two channels, apart from the lowest band (2.5 -10 kHz). This is needed for processing the cross-correlation used in direction finding. The digital spectral analysis is processed with 16 log-spaced frequencies in each band using a wavelet-like transform, which gives a spectral resolution of 8.66%. The High Frequency Receivers (HFR) is a dual sweeping receiver used for spectral analysis and direction finding of radio noise that is generated from a few solar radii (16.025 MHz) to ∼0.5 AU (125 kHz). The antenna signal is down-converted using a programmable synthesizer and mixers using a super-heterodyne technique. Frequencies at odd multiples of 25 kHz are produced by the synthesizer, which is then sharply filtered, resulting in a comb filter across the HF band. This odd/even 'picket fence' filtering technique allows for sampling between lines of noise that may be produced by power supply harmonics at even multiples of 25 kHz. It allows the very sensitive radio receiver to coexist with a potentially noisy spacecraft power supply. The finished signal is digitized and analysed using the same hardware as the LFR. The Fixed Frequency Receiver (FFR) is a single channel super-heterodyne receiver near 31 MHz for connection with ground based measurements.

S/WAVES also has a Time Domain Sampler, which is a broadband waveform sampler with 3 channels, that makes wideband waveform measurements at one of several sample rates and bandwidths. It is intended to measure impulsive events of large amplitude such as Langmuir waves and the precursors to Type II and III radio bursts. It carries out rapid simultaneous sampling of the three antennas and a pseudo-dipole channel obtained by taking the difference of any two monopoles, allowing the study of waveforms and their distortions. A highly accurate frequency determination can also be obtained from ground-based Fourier analysis.

2.3 Solar Dynamics Observatory (SDO)

SDO (Pesnell et al. 2012) is the first mission in NASA's Living With a Star program and launched from the Kennedy Space Center on 11 February 2010. Its mission is to understand solar variations that influence life and technology, with an aim towards predictive capability. The specific science goals aim to determine how the magnetic field of the Sun is structured and generated and how this stored magnetic energy is released into the heliosphere as the solar wind, energetic particles and variations in solar irradiance. SDO carries three instrument suites: the Atmospheric Imaging Assembly (AIA), Extreme-ultraviolet Variability Experiment (EVE) and Helioseismic and Magnetic Imager (HMI). Only data from AIA are used in this thesis. SDO continuously transmits data from these three instruments to the ground, at a rate of roughly 1.5 terabytes per day consisting of roughly 150 000 high-resolution full-disk images and 9000 EUV spectra. This incredibly high downlink data rate requires SDO to have continuous contact with a single dedicated ground station, and as a result, the satellite was placed in an inclined geosynchronous orbit. One of the disadvantages of this orbit is that SDO experiences two Earth-shadow eclipse seasons per year, and three lunar transits. The eclipse periods last for three weeks each and will result in daily interruptions of solar observations.

2.3.1 Atmospheric Imaging Assembly (AIA)

AIA (Lemen et al. 2012) consists of four telescopes to view the solar surface and atmosphere with high-resolution full-disk images. It achieves a spatial resolution of 1.5" with a field of view of at least 40' (up to 0.5 $R_{\odot}$ above the solar limb) and a temporal resolution of 12 seconds. The telescopes use filters to cover ten wavelength bands consisting of seven extreme-ultraviolet, two ultraviolet and one visible light band, covering a temperature diagnostic range of the full thermal range of the corona (from 6000 K to 2 x 10^7 K). The seven EUV wavelength bands are centred on specific lines, summarised in table 2.1, along with the region of the atmosphere observed, and the characteristic emission temperature of all ten wavelength bands. In addition, AIA also provides high signal-to-noise ratios for two to three second exposures that can reach 100 during flaring in the higher-temperature channels and in quiescent

Table 2.1: AIA wavelength bands, primary ions and characteristic emission temperatures (Lemen et al. 2012)

Channel (Å)	Primary ion(s)	Region of Atmosphere	log(T)
4500	continuum	photosphere	3.7
1700	continuum	temperature minimum, photosphere	3.7
304	He II	chromosphere, transition region	4.7
1600	C IV + continuum	transition region, upper photosphere	5.0
171	Fe IX	quiet corona, upper transition region	5.8
193	Fe XII, XXIV	corona and hot flare plasma	6.2, 7.3
211	Fe XIV	active-region corona	6.3
335	Fe XVI	active-region corona	6.4
94	Fe XVIII	flaring corona	6.8
131	Fe VIII, XXI	transition region, flaring corona	5.6, 7.0

conditions for the low-temperature channels.

The four AIA telescopes are dual-channel, normal-incidence telescopes with 0.6” pixels and 4096x4096 back-thinned CCDs. Each telescope has a 20 cm primary mirror, along with an active secondary mirror, giving an effective focal length of 4.125 m. The mirrors have multilayer coatings, optimised for specific EUV wavelengths, with three of the telescopes (1,2 and 4) having two different EUV band passes. Visible and IR radiation is blocked at the telescope aperture by entrance filters. The exposure time is regulated by a mechanical shutter. By design the CCD corners are shaded by the filter-wheel mechanism which selects the wavelength channel of interest and lies in front of the focal plane. These corner areas therefore do not receive solar emission which allows for the monitoring of detector noise levels. The telescope is baffled to prevent charged particles from reaching the CCDs, but these shaded areas also allow to check for this.

2.4 Advanced Composition Explorer (ACE)

The ACE spacecraft (Stone et al. 1998) is a NASA mission, launched on 25 August 1997 from the Cape Canaveral Air Station. Its primary objective is to compare the composition of the solar corona, interstellar medium, and galactic matter, but its location at the L1 point also allows it to provide in-situ solar wind measurements for use in space weather forecasting. ACE carries nine instruments, including six high-resolution spectrometers for measuring the elemental, isotopic and ionic charge-state composition of nuclei from H to Ni, ranging from solar wind energies (≈1 keV nucl^{-1}) to galactic cosmic-ray energies (≈500 MeV nucl^{-1}). In this thesis, only two instruments were used to analyse the solar wind conditions upstream of the Earth: SWEPAM (the Solar Wind Electron, Proton, and Alpha Monitor; McComas et al. 1998) and MAG (the magnetometer; Smith et al. 1998). The instruments onboard ACE are shown in Figure 2.8.

2.4.1 Solar Wind Electron, Proton and Alpha Monitor (SWEPAM)

SWEPAM (McComas et al. 1998) consists of an electron and ion curved plate electrostatic analyser, designed to measure the 3D characteristics of the solar wind and suprathermal electrons. This provides the context for the isotopic and elemental composition measurements made by ACE, as well as directly studying solar wind phenomena for space weather forecasting. It consists of modernised and refurbished versions of flight spares from Ulysses. In particular, the instruments have been enhanced by increasing the sensitivity to suprathermal electrons, increasing angular resolution for ions and increasing sensitivity for suprathermal ions coming from directions adjacent to the solar wind direction.

The electron and ion electrostatic analysers are independent instruments, with SWEPAM-E measuring electrons from ≈ 1-900 eV and SWEPAM-I measuring ions in the 0.26 - 35 keV energy range. SWEPAM-E has an energy resolution of $\Delta E/E \approx 12\%$, with an angular resolution of 9 - 28° in the azimuthal direction and 21° in the polar direction. SWEPAM-I has an energy resolution of $\Delta E/E \approx 5\%$, an angular resolution in the azimuthal direction of 3 - 4.5° and in the polar direction of 5%. Both of these instruments are

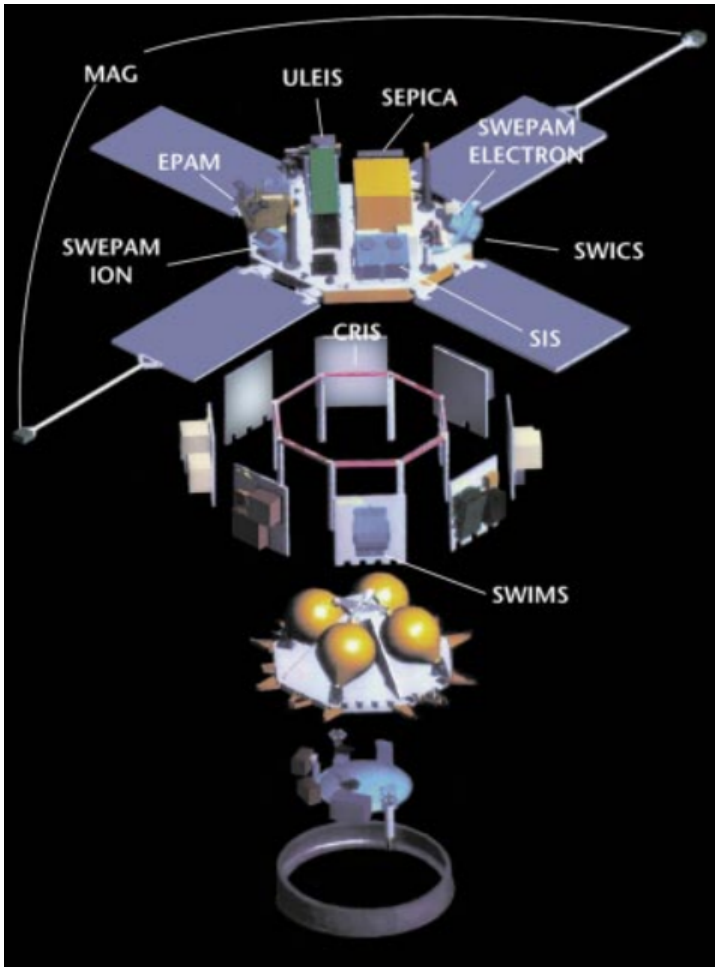

Fig. 2.8: An expanded view of the ACE spacecraft, showing the instruments onboard (Stone et al. 1998).

electrostatic energy per charge (E/q) analysers with channel electron multiplier (CEM) sensors that allow individual particles to be counted. They both make 3D plasma measurements every 64 seconds, with fan-shaped fields of view that cover all necessary directions as the spacecraft spins. A schematic of SWEPAM-I is shown in Figure 2.9.

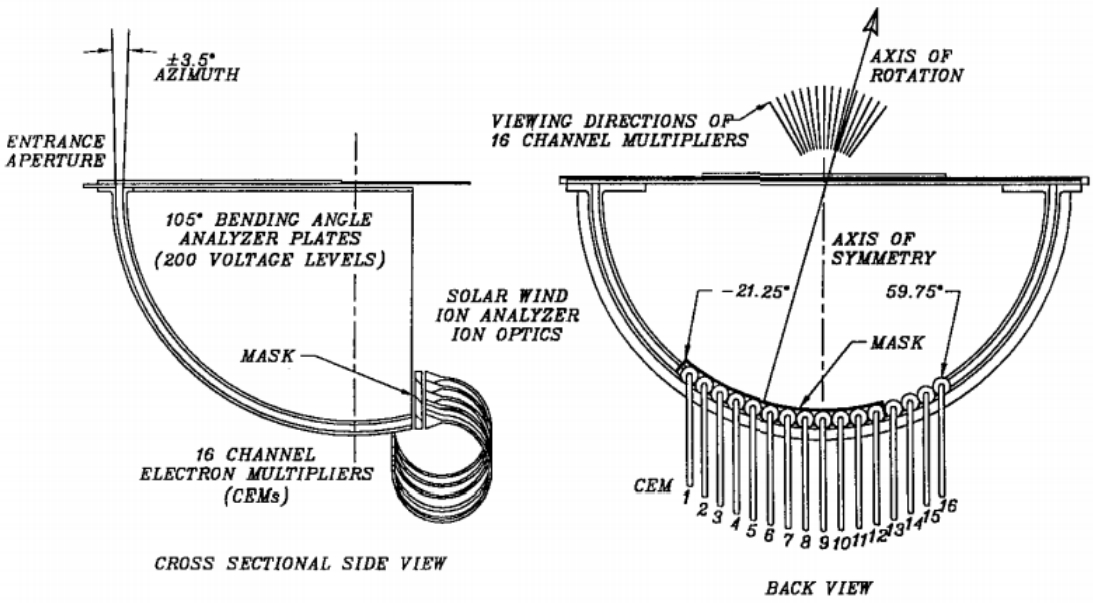

Fig. 2.9: A schematic showing the electro-optics of SWEPAM-I. The ion sensor is tilted with respect to the tilt axis so observations from CEMs 1 - 5 interleave with observations from CEMs 6 - 10 (McComas et al. 1998).

The electrons or ions enter the electrostatic analysers through the aperture and arrive at the gap between the electrostatic analyser plates. The bending angle of the analyser is 120° for SWEPAM-E and 105° for SWEPAM-I. The analysers are biased by a high voltage on the inner plate (positive for SWEPAM-E, negative for SWEPAM-I), such that only particles within the required energy range and azimuthal directions can pass through. The CEM sensors lie beyond the electrostatic analysers (seven channels for SWEPAM-E and 16 for SWEPAM-I) and detect the transmitted electrons or ions. Particles entering the instrument from different polar angles will be detected by different CEM sensors, and using this with knowledge of the spacecraft spin phase allows for the determination of their incident angle.

2.4.2 Magnetometer (MAG)

The magnetometer onboard ACE (Smith et al. 1998) is a twin triaxial flux-gate magnetometer, which was a flight spare from the magnetometer instrument flown on *Wind*. The only modifications made to it were to accommodate the ACE data bus and to change the sampling rate of the instrument. It is designed to measure the dynamic vector magnetic field, including measurements of interplanetary shocks, waves and other features that govern the acceleration and transport of energetic particles. The two sensors are located 4.19 m from the centre of the spacecraft, mounted on booms on opposing solar panels (see Figure 2.8) and share a data processing unit mounted on the top deck of the spacecraft. This dual configuration improves the instrument calibration by allowing accurate removal of the dipolar portion of the spacecraft magnetic field, and also provides redundancy in the event of a hardware failure.

Each sensor includes an orthogonal triaxial arrangement of ring-core flux-gate sensors, the basic principles of which have been described in section 2.2.2.4. MAG can provide measurements with a resolution of 3 and 6 vector s^{-1}. It also provides 1 second resolution data in real time for space weather forecasting. The measurements are accurate ($\pm$0.1 nT), precise (0.025%) and sensitive (0.0005 nT/Hz) with low noise of $<$0.006 nT RMS for 0 - 12 Hz. It can measure the magnetic field in eight dynamic ranges between $\pm$ 4 nT and $\pm$ 65536 nT.

2.5 *Wind*

Wind is part of NASA's Global Geospace Science mission, along with the *Polar* spacecraft (Harten and Clark 1995), launched on 1 November 1994. It carries a payload of eight instruments to measure waves, fields and particle distributions near the magnetopause and bow shock, as well as in the solar wind. The main science objectives of *Wind* include to provide complete plasma, energetic particle and magnetic field measurements for magnetospheric and ionospheric studies, to investigate basic plasma processes occurring in the near-Earth solar wind and to provide baseline ecliptic plane observations at 1 AU for inner and outer heliospheric missions. After a period of about 2 years *Wind* was placed

in a halo orbit about the L1 point for continuous observations of the solar wind, but has been moved to several different locations since then, including the second Lagrange point (L2). *Wind* is now permanently back at L1, currently in a more complex 'petal' orbit, which can take the spacecraft up to 60° out of the ecliptic plane and between 10 and 28 R_E from the Earth. *Wind* is a spinning spacecraft with its spin axis normal to the ecliptic plane, pointing towards the Sun, and a spin rate of 20 rpm. A diagram of the *Wind* spacecraft is shown in Figure 2.10. In this thesis, the 3-D Plasma (3DP) instrument and the Energetic Particles: Acceleration, Composition Transport (EPACT) instrument were used to obtain particle measurements and the WAVES instrument was used to obtain radio measurements, all in Chapter 3.

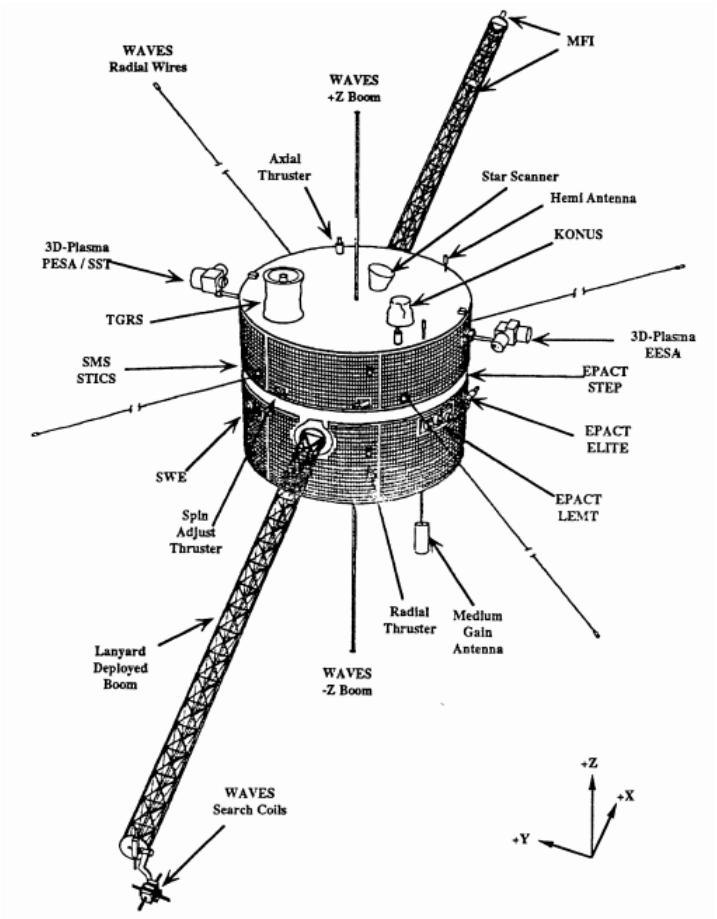

Fig. 2.10: A diagram of the *Wind* spacecraft (Harten and Clark 1995).

2.5.1 Energetic Particles: Acceleration, Composition and Transport (EPACT) investigation

The EPACT investigation (von Rosenvinge et al. 1995) consists of multiple telescopes, with the objective of studying the acceleration, composition and transport of energetic particle populations, including particles from solar flares, particles accelerated by interplanetary shocks and galactic cosmic rays. Its measurement objectives were to provide energy spectra of electrons and atomic nuclei of different charge and isotopic composition, over an energy range from 0.1 to 500 MeV/nucleon, to provide isotopic composition of medium energy particles (2 - 50 MeV/nucleon) extending up to Z=90, and to determine the angular distribution of these fluxes.

In order to achieve the measurement of such an extensive dynamic range of particles, the instrument contains three Low Energy Matrix Telescopes (LEMT), two Alpha-Proton-Electron Telescopes (APE), an Isotope Telescope (IT) and a Supra Thermal Energetic Particle Telescope (STEP). APE and IT are contained within the ELectron Isotope TElescope (ELITE) package. All of these solid state detector telescopes use the $\mathrm{d}E/\mathrm{d}x$ by E method of particle identification, apart from STEP, which measures the time-of-flight and energy. The STEP telescope measures the total energy by using start stop micro-channel plate (MCP) detectors in addition to a solid state detector. Between them, these telescopes cover electrons in the energy range 0.2 - 10 MeV, protons in the range 1.4 - 120 MeV, helium ions between 0.04 and 500 MeV/nucleon and iron ions in the range 0.02 - 300 MeV/nucleon.

The look directions of these telescopes, combined with the spin of the spacecraft allows for a wide field of view. The three LEMT telescopes are directed 25° above, 25° below, and in line with the ecliptic. The STEP telescopes are pointed 26° above and below the ecliptic, preventing direct solar UV from entering the fields of view. The APE and IT telescopes both look in the ecliptic plane, with the APE-B telescope mounted as far from the telescope as possible, in order to allow for an unobstructed forward field of view and an almost unobstructed backwards field of view.

2.5.2 Three-dimensional Plasma and Energetic Particle Analyser (3DP)

The 3-D Plasma Analyser (Lin et al. 1995) is designed to measure full 3D distributions of suprathermal electrons and ions from solar wind plasma down to low energy cosmic rays with high time resolution and sensitivity, a wide dynamic range, and good energy and angular resolution. The scientific goals of the instrument include to study particle acceleration and transport and wave-particle interactions, to monitor particle input to and output from the magnetosphere and to explore the suprathermal electron population from the solar wind to low energy cosmic rays.

The instrument consists of three detector systems: three arrays of semi-conductor detector telescopes that measure electrons and ions above ∼20 keV, and the electron electrostatic analysers (EESA) and ion electrostatic analysers (PESA) that measure ions and electrons from ∼3 eV to 30 keV. Wave-particle interactions on fast timescales can also be studied due to the addition of the Fast Particle Correlator, which combines electron data from EESA with plasma wave data from the WAVES instrument (Bougeret et al. 1995). The top-hat symmetrical spherical section electrostatic analysers have MCP detectors and either 180° or 360° fields of view. They provide an energy resolution of $\Delta E/E \approx 0.2$, an angular resolution between 5.6° and 22.5° and full 4π sr coverage in one-half or one spin of the spacecraft. The lower energy measurements taken by these electrostatic analysers are not used in this thesis.

The double-ended semi-conductor detector telescopes are arranged as three arrays, each with a pair of telescopes. Each telescope has two or three closely sandwiched passivated ion implanted silicon detectors. They provide an energy resolution of $\Delta E/E \approx 0.3$, an angular resolution of 22.5° x 36° and a full 4π sr coverage in one spin of the spacecraft. They are mounted at the end of a 0.5 m boomlet, in order to minimize the effects of the spacecraft potential and to provide unobscured fields of view. Ions and electrons are cleanly separated in a similar way to the STEREO/SEPT instrument. One end of the telescope is covered by a thin foil which leaves the electron spectrum unchanged, but absorbs ions below 400 keV, while the other end is surrounded by a magnet

which sweeps away electrons with energies <400 keV. This means that in the absence of any higher energy particles, the foil detectors only detect electrons and the magnet detectors only detect ions. Higher energy electrons (up to ∼1 MeV) and ions (up to 11 MeV) are identified by the two double-ended telescopes that have a third detector. Each double-ended telescope has a field of view of 36° x 20°, with telescope 6 viewing the same angle as telescope 2, resulting in a total field of view of 180° x 20° for magnet detectors and for foil detectors.

2.5.3 WAVES

The WAVES instrument onboard *Wind* (Bougeret et al. 1995) is designed to provide comprehensive measurements of the radio and plasma wave phenomena in geospace, in order to help study the kinetic processes that are important in the solar wind and in key boundary regions of the geospace. It is similar in design to S/WAVES, described in section 2.2.4.

The instrument contains two sensors (six antenna units consisting of three electric dipoles, and three orthogonally mounted magnetic search coils) with preamplifiers and two electronic stacks. The sensor outputs are first preamplified, then routed to the analysis electronics that consist of a low frequency (DC - 10 kHz) Fast Fourier Transform receiver, a broadband (4 - 256 kHz) multi-channel analyser designed to study electron thermal noise, a time domain waveform sampler, sampling to 120 000 s^{-1}, and two dual radio receivers that cover the band 20 kHz to 13.825 MHz (RAD1 and RAD2). In this thesis, only data from the RAD1 and RAD2 radio receiver were used, to identify radio bursts in Chapter 3.

Of the antennas, two are coplanar orthogonal wire dipoles of different lengths and were deployed after launch in the plane of spin of the spacecraft. The dipole lengths are limited by the observation frequencies of RAD1 and RAD2 respectively, with E_x reaching 100 m tip-to-tip, and E_y is 15 m long. The third, rigid, dipole (E_z) is 12 m long and is deployed along the spin-axis of the spacecraft and must be as stiff as possible due to stability considerations.

RAD1 consists of 2 super-heterodyne receivers and operates in the 20 - 1040 kHz range. One receiver is connected to the axial electric dipole antenna,

E_z, and the other with the sun of E_z and either spin plane antenna (E_x or E_y). This is called the SUM mode and synthesises an inclined dipole in order to determine the direction of arrival of received radiation. The receiving frequency is determined by a frequency synthesiser, driven by pre-determined observation programs. These programs reside in the DPU and make use of frequency tables and pointer lists. The frequency table consists of 16 observation frequencies of 4 kHz steps, selected among 256 possibilities, provided by the synthesiser. The pointer list describes how each of the frequencies are scanned during a cycle, which consists of 64 steps. RAD2 is very similar in design to RAD1, but covers a much higher frequency range (1.075 - 13.825 MHz). It only uses the shorter, E_y antenna system, because the longer antenna cannot be used above about 3.3 MHz (their full-wave resonance). As with RAD1, there are 256 frequencies available, but these are in steps of 50 kHz, and a standard cycle measures 48, rather than 64 steps.

2.6 Mars Express

Mars Express (Chicarro et al. 2004) was the first ESA planetary mission, and was launched on 2 June 2003 from the Baikonur Cosmodrome in Kazakhstan. The mission includes the Mars Express Orbiter, and the Beagle 2 lander. Beagle 2 was released on 19 December 2003, but contact was never established. It was declared lost on 6 February 2004, but has since been located intact on the surface, its solar panels having apparently failed to be deployed.

The Mars Express Orbiter is a 3-axis stabilised cube-shaped spacecraft with a high-gain antenna and body-mounted instruments. It has an elliptical orbit around Mars, with an apocentre of 11560 km and a pericentre of 260 km above the surface. The orbit has a quasi-polar inclination of 86.35° and a period of 6.75 hours.

The main scientific goals of the Mars Express Orbiter include: global colour and stereo high-resolution imaging, global infra-red mineralogical mapping of the surface, global atmospheric circulation and mapping of the atmospheric composition, study of the interaction of the atmosphere with the interplanetary medium and surface, radar sounding of the subsurface structure

and radio science to study the atmosphere, ionosphere, surface and interior. To achieve these goals, the orbiter carries seven instruments that can be split into two categories: those studying the solid planet through observations of the surface and subsurface, and those studying the atmosphere and environment of Mars. In this thesis, only data from the Analyser of Space Plasmas and Energetic Atoms, ASPERA is used, in Chapter 4.

2.6.1 Analyser of Space Plasma and Energetic Atoms (ASPERA-3)

ASPERA-3 (Barabash et al. 2006) is an energetic neutral atom analyser, with the main scientific objectives of determining the total ion escape for the major ion species, studying momentum, energy and mass deposition from the solar wind into the upper atmosphere/ionosphere, and investigating the morphological structure of the Mars interaction region, defining the local plasma characteristics.

The instrument consists of 4 sensors: an ion spectrometer, two energetic neutral atom (ENA) sensors and an electron spectrometer. The Ion Mass Analyser (IMA) is a separate unit to the ASPERA-3 main unit which contains the other sensors. It takes measurements of ions in the range 0.01 - 36 keV/charge, for ions H^+, He^+, H_2^+ and O^+, as well as for molecular ions in the range 20 - 80 amu/q. The two ENA sensors comprise a Neutral Particle Imager (NPI) and a Neutral Particle Detector (NPD). NPI measures the integral ENA flux from 0.1 - 60 keV with a high angular resolution, but no mass or energy resolution. NPD measures the ENA flux with a coarse angular resolution, but resolving velocity (0.1 - 10 keV) and mass (H and O). ELS, the electron spectrometer is a standard top-hat electrostatic analyser, covering the energy range 0.01 - 20 keV. A diagram of ELS is shown in Figure 2.11. Only data from ELS are used in this thesis.

ELS has an intrinsic full field of view of 4° x 360°, with the 360° aperture divided into 16 sectors. It is located on a scanning platform (along with NPI and NPD), which scans from 0 - 180°, providing the full 4π field of view, apart from the fraction blocked by the spacecraft body. It has an energy resolution of $\Delta E/E \approx 0.08$, a time resolution of 32 seconds and an angular resolution of 2° x 22.5°. ELS consists of a collimator system, followed by a spherical top-hat

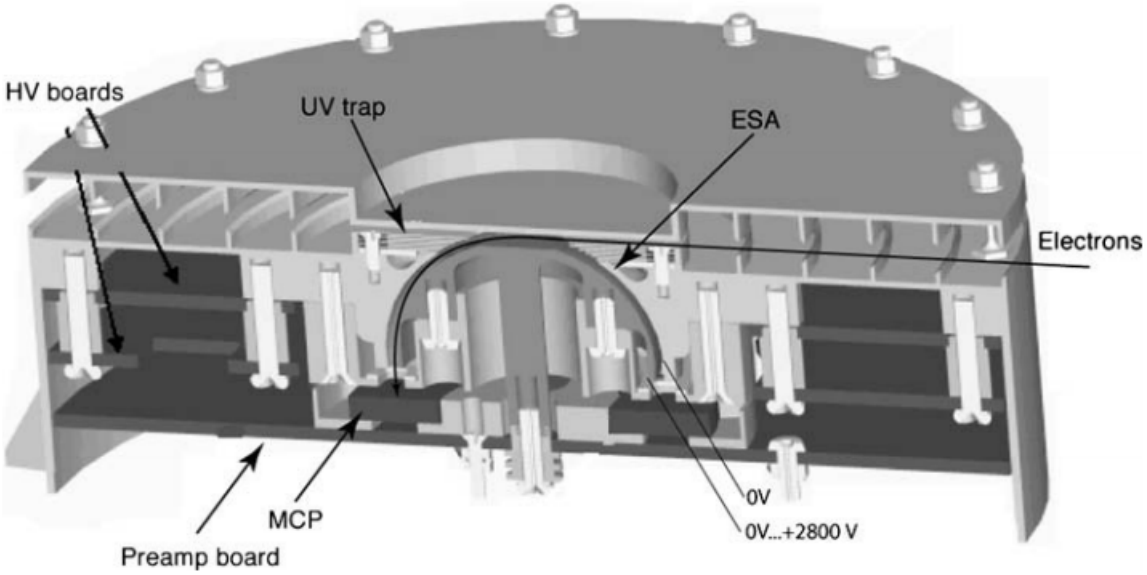

Fig. 2.11: A cut away view of the ELS sensor, including the electrostatic analyser voltages (Barabash et al. 2006).

electrostatic analyser that has a 17° opening angle and 90°. The collimator determines the plane of incidence for the particles entering the aperture (4° x 360°), where electrons are then deflected into the spectrometer by a positive voltage. They are filtered in energy by the the analyser plates and then hit a MCP stack. Differential spectral measurements are obtained by stepping the voltage of the ELS deflection plates in sequences. The 16 anodes behind the MCP define a 22.5° sector, and are each connected to a preamplifier. The signal generated by the preamplifier is then counted by the DPU.

2.7 Venus Express

Venus Express (Svedhem et al. 2007) is the first European mission to Venus, aiming to comprehensively investigate the Venusian atmosphere and plasma environment, as well as studying some of the surface physics. The key areas of scientific interest include: the atmospheric structure of Venus, its atmospheric dynamics, its atmospheric composition and chemistry, cloud layers and hazes, the energy balance and greenhouse effect, the plasma environment and escape processes, and the surface properties and geology.

The spacecraft was launched on 9 November 2005 from the Baikonur Cos-

modrone in Kazakhstan, arriving at Venus on 11 April 2006. Venus Express has a highly elliptical orbit with an apocentre of 66 000 km, a pericentre between 250 and 400 km, and a period of 24 hours. The spacecraft is based on the Mars Express design with minor modifications, mainly to allow it to cope with the thermal environment around Venus.

Venus Express has a payload of seven instruments, five of which were inherited from Mars Express or Rosetta, with the remaining two developed specifically for this mission.

2.7.1 Analyser of Space Plasma and Energetic Atoms (ASPERA-4)

ASPERA-4 (Barabash et al. 2007b) is a replica of ASPERA-3, carried on Mars Express, and described in section 2.6.1. Combining the measurements of these two identical instruments at both planets gives a useful tool for comparative magnetospheric studies. ASPERA-4 has the main objective of studying solar wind induced atmospheric escape. The specific questions it aims to address are: to determine how the Venus atmosphere is coupled with the solar wind and how this leads to mass added to, and removed from, the atmosphere, to determine the structure of the interaction region, how this interaction could contribute to water escape and if this process is the same as at Mars, to determine the mass composition of escaping plasma, to what degree this outflow is mass dependent and whether this can explain the loss of water, to understand the neutral-plasma interaction on Venus and how the presence of neutral gas can affect plasma dynamics, and finally to study the similarities and differences in the solar wind interaction with Earth and Mars.

2.7.2 MAG: the Magnetometer

The Venus Express Magnetometer (Zhang et al. 2006) is designed to measure the magnitude and direction of the magnetic field around Venus, which is essential to study the solar wind interaction with Venus, despite the planet's lack of an intrinsic magnetic field. The elliptical orbit of Venus Express allows it to sample the solar wind and ionosphere, as well as regions formed due to the interaction between them, such as the magnetosheath, magnetic barrier and magnetotail.

The instrument consists of two triaxial fluxgate sensors, an electronics box and a 1m long carbon fibre boom. The outboard sensor is mounted at the end of this boom, with the inboard sensor on the top floor of the spacecraft. As the Venus Express spacecraft was heavily based on Mars Express, which had no magnetometer, there was little effort to study the spacecraft's magnetic cleanliness. This dual magnetometer set-up is therefore critical to allow for the separation of the spacecraft disturbances from the ambient magnetic field. The magnetometer can operate over a wide dynamic range, between ± 32.8 and ± 8388.6 nT, with a digital resolution between 1 and 128 pT. While operating in the solar wind, it has a sampling rate of 1 Hz, increasing to 32 Hz within approximately 2 hours around pericentre and 128 Hz for 2 minutes around pericentre, in order to detect Venus lightning.

2.8 Cassini

The Cassini-Huygens mission is a collaboration between NASA and ESA, launched on 15 October 1997 from Cape Canaveral Air Force Station. It consists of the largely NASA-built orbiter Cassini, which includes a high-gain radio antenna contributed by the Italian Space Agency and an ESA-built Titan lander, Huygens. Cassini required four gravity-assists to reach Saturn, shown in Figure 2.12. First, it completed two fly-bys of Venus, followed by an Earth fly-by, then a final gravity assist manoeuvre, which took Cassini past Jupiter, allowing it to reach Saturn for orbit insertion on 1 July 2004, with a total transit time of seven years. The Huygens probe was released from Cassini on 25 December 2004 and successfully landed on Titan of 14 January 2005.

The Cassini-Huygens mission aimed to address several mysteries from previous Saturn observations. These included studying the internal heat source of Saturn, the origin of the rings, the origin of Enceladus' smooth surface, the nature of the dark material on Iapetus, the atmosphere of Titan and to characterize the surface of Titan.

Cassini-Huygens is one of the largest and most complex unmanned interplanetary spacecraft built. The orbiter carries 12 instruments, including four

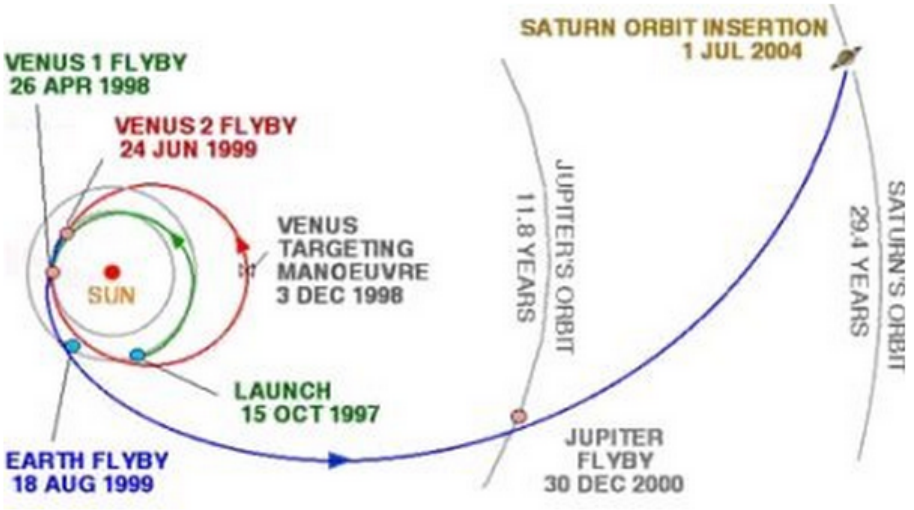

Fig. 2.12: The route taken by Cassini-Huygens to reach Saturn. The journey included two Venus fly-bys, one Earth fly-by and a Jupiter fly-by, taking seven years in total. `http://www.esa.int/Our_Activities/Space_Science/Cassini-Huygens/The_mission`

instruments to carry out remote optical sensing, two instruments to carry out microwave remote sensing, and six instruments to study fields, particles and waves. Of those six instruments, data from the Cassini Plasma Spectrometer (CAPS) and the Magnetometer (MAG) were used in this thesis.

2.8.1 CAssini Plasma Spectrometer (CAPS)

CAPS (Young et al. 2004) is designed to make 3D mass-resolved measurements of a variety of plasma phenomena found in Saturn's magnetosphere. It aims to understand the nature of saturnian plasmas, including their sources of ionisation and how they are accelerated, lost and transported. To achieve this, CAPS takes two types of complementary measurements: lower time resolution, high mass-resolution spectra of all ion species, and high time resolution velocity distributions of electrons and major ion species.

The CAPS instrument consists of three experiments: the Electron Spectrometer (ELS), the Ion Mass Spectrometer (IMS) and the Ion Beam Spectrometer (IBS). All three sensors are mounted on an actuator that rotates the entire instrument over roughly one-half of the sky every 3 minutes. IBS is designed to measure ion velocity distributions with high angular and energy resolution from 1 eV to 49.8 keV. The IMS is designed to measure the

composition of low concentration ion species and hot, diffuse magnetospheric plasmas from 1 eV to 50.28 keV, with an atomic resolution M/ΔM ∼70.

Only data from ELS is used in this thesis. This sensor is designed to take differential electron velocity distribution measurements from 0.6 eV to 28.25 keV, and take detailed studies of secondary electron fluxes that contribute to chemical and ionisation processes. This energy range covers thermal electrons at Titan and near the ring plane, as well as more energetic trapped electrons and auroral particles and will provide a global survey of plasma density, temperature and electron pitch distributions. ELS has a field of view of 5.2° x 160°, with an angular resolution of 5.2° x 20°. The sensor is a hemispherical top-hat electrostatic analyser, with electrons entering via a grounded baffle before passing between concentric electrostatic analyser plates and impacting on an annular MCP detector. The angular and energy resolution is dependent on the spacing between the two concentric hemispheres. Changing the voltage on the inner hemisphere in discrete steps allows the energy spectrum to be obtained, with the default mode consisting of 64 log-spaced energy steps scanning over the energy range in 2 seconds. The electron arrival direction in elevation is determined from the position it hits the detector and its direction in azimuth determined from position of the rotating actuator sweeping the sensor's field of view. The particle velocity distributions can then be deduced from knowledge of these two angles and the detector counting rates as a function of energy.

2.8.2 Cassini Magnetic Field Investigation

The magnetometer onboard Cassini (Dougherty et al. 2004) is a dual technique system, consisting of vector helium (VHM) and fluxgate magnetometers (FGM). There also exists the capability to operate the helium magnetometer in a scalar mode (SHM) to be used near the planet to determine the interior field with very high accuracy, which is the first time a scalar magnetometer has been used on a planetary mission.

The combination of the V/SHM and FGM allow for high sensitivity measurements over a wide dynamic range. The instrument can determine the absolute value of the field to an accuracy of 1nT and very sensitive measure-

ments of wave fields. The sensors are mounted on a 11 m boom with the V/SHM at the end and the FGM halfway along it, this spacing allowing for the spacecraft generated field variations to be better characterised.

In this thesis, the FGM is used for measurements of the Saturn magnetosphere in Chapter 4. The FGM is based on three single-axis ring core fluxgate sensors that are mounted orthogonally, the basic principles of which have been described previously (e.g. section 2.2.2.4). FGM covers a wide dynamic range, between ±40 and ±44 000 nT, resulting in dynamic resolutions in the range 4.9 pT - 5.4 nT. Switching between these ranges is automatic, with the DPU monitoring each FGM component field values.

2.9 Models

2.9.1 Enlil

Enlil is a 3D numerical time-dependent model of the heliosphere, available from the Community Coordinated Modeling Center (CCMC) at NASA (Odstrcil and Pizzo 1999a; Odstrcil et al. 2002, 2004). The model version used in this thesis is version 2.7. Enlil solves ideal fully ionized MHD equations for magnetic field, plasma mass, momentum and energy density. It can also solve two additional continuity equations, for the polarity of the radial component of the magnetic field and for the density of a transient, allowing it to be traced (Odstrcil and Pizzo 1999b). Enlil is designed to treat supersonic outflows in the limit where resistivity and viscosity are minimal and is based on the polytropic equation of state, $pV^n = C$, where p is the pressure, V is the specific volume, n is the polytropic index and C is a constant.

The model outputs the 3D distribution of the solar wind parameters and topology of the interplanetary magnetic field at any location within the computational domain. This extends from 0° to 360° in longitude and from the equator to ±60° in latitude, which is a sufficient range to minimise the impacts of neglecting high-latitude behaviour on the lower latitude solar wind. The outer boundary can be set to 2 AU, covering the inner solar system out to Mars, or to 10 AU, covering the solar system out to Saturn. The inner boundary of the Enlil model is set to lie in the super-critical flow region, where the

solar wind velocity exceeds the fast-mode MHD speed and is also supersonic, but the exact position of the boundary depends on the coronal model coupled to it. This can be from the Magnetohydrodynamic Algorithm outside a Sphere (MAS) coronal model, in which case the inner boundary of Enlil is 30 $R_\odot$, or the Wang-Sheeley-Arge (WSA) coronal model, in which case the inner boundary is 21.5 $R_\odot$. The default model resolution grid for the Enlil model is 256x30x90 (rxθxϕ), but higher resolutions are available with 512x60x180 and 1024x120x360.

MAS is a 3D MHD time-dependent finite-difference coronal model that extends from 1 to 30 $R_\odot$ (Riley et al. 2001). It takes an input at its inner boundary from synoptic magnetograms in order to determine the radial component of the magnetic field. A Parker solar wind solution is used to determine the plasma density and temperature at the base of the corona. The model solves equations for continuity, momentum, and energy as well as Maxwell's equations in spherical coordinates on a non-uniform grid. The grid sizes range from 81x81x64 to 121x121x128 (rxθxϕ). This initial coronal solution is advanced in time until it reaches a steady-state solution. MAS uses an ideal gas equation of state with a polytropic index of 1.05 to approximate heat conduction processes and thermal energy sources. As a result of using this simpler polytropic energy equation, the highest speeds achieved are too low (by about a factor of two), and the contrast between high and low speeds are too weak (Luhmann et al. 2004). To correct this, at the outer boundary of the model the speed is derived from an *ad hoc* description (Riley et al. 2001) which assumes that high-speed flows originate from coronal holes and low-speed flows from the boundaries of coronal holes. The plasma density and temperature are derived based on momentum flux conservation and the balance of thermal pressure. MAS can also be run as a heliospheric model, as part of the CORHEL software package.

The WSA coronal model (Arge and Pizzo 2000; Arge et al. 2004) is a semi-empirical model that simulates the solar magnetic field from the photosphere to 21.5 $R_\odot$. For the computation of the magnetic field up to 2.5 $R_\odot$, it uses the Potential-Field Source-Surface (PFSS) model (Levine et al. 1977) which

creates a source surface which is a hypothetical sphere centred on the Sun, using the PFSS approximation and constraining the magnetic field to be radial. It takes line-of sight magnetic field observations of the photosphere as the input at its inner boundary, obtained from the Kitt Peak observatory, Mount Wilson Observatory or the Global Oscillation Network Group (GONG). These observatories produce daily full-disk magnetograms which are assembled into synoptic maps for a whole Carrington rotation. The PFSS model computes a spherical harmonic solution for the potential magnetic field within 2.5 $R_\odot$, based on the map of radial fields at the inner boundary. From 2.5 $R_\odot$ out to 5 $R_\odot$, the Schatten Current Sheet model is used (Schatten et al. 1969; Schatten 1971). This model modifies the sign of the radial field to positive in order to prevent reconnection, creates a potential solution with the radial boundary conditions, and then restores the sign in the new solution at 5 $R_\odot$. By assuming a radial constant flow speed at this boundary, WSA uses an empirical relation to derive the solar wind speed based on the rate of divergence of the magnetic field at 5 $R_\odot$. At its outer boundary (21.5 $R_\odot$), which is the inner boundary for Enlil, WSA produces coronal maps of the radial components of magnetic field and solar wind velocity, with toroidal components generated by a Parker spiral solution.

A CME can be simulated by the Enlil model by using the 'cone model' addition to the ambient solar wind model. This is based on the observational evidence that a CME has more or less constant angular diameter in the corona as it is confined by the external magnetic field. The CME does not expand in latitude in the lower corona, but expands in interplanetary space due to the weaker external field. The method was initially suggested by Zhao et al. (2002) as a way to analyse halo CMEs observed in coronagraph images. The method considers a CME as a flat faced cone with a circular cross-section, which yields an expanding circular halo when aimed straight towards an observer, but in the more general case the direction of propagation is offset and the halo is seen as an ellipse with the direction of the minor axis passing through the origin (Sun centre). The cone model was developed analytically by Xie et al. (2004), using the major and minor axes of the ellipse, the distance from the origin and the

angle the minor axis makes with the horizontal to determine the CME propagation direction (heliospheric latitude and longitude) and angular width of the cone. With an image of a second self-similar ellipse earlier or later in time, the radial velocity of the CME can also be determined. With coronagraph images available from several viewpoints due to the STEREO spacecraft, kinematic properties of a CME can be obtained using a triangulation method (Pulkkinen et al. 2010) based on the projection matrix formulation. The CME parameters it returns include the latitude and longitude of the CME propagation direction, the CME speed, angular width and time of its arrival at 21.5 $R_\odot$ (the inner boundary of the Enlil model). Once these input parameters have been determined, the Enlil model can introduce an over-pressured plasma cloud into the simulated ambient solar wind, corresponding to this CME. This plasma cloud does not incorporate the internal magnetic signal of the CME however, which means that Enlil is unable to model the flux rope structure of an ICME.

2.9.2 Saturn Magnetopause Model

In Chapter 4 of this thesis, a model of Saturn's magnetopause is used to provide estimates of the solar wind dynamic pressure, D_p, and magnetopause stand-off distance, R_0. The model is developed by Arridge et al. (2006) and built on by Kanani et al. (2010). It is based on the understanding that the location and shape of a planetary magnetopause is determined by D_p, the orientation of the magnetic dipole with respect to the solar wind flow, and the distribution of stresses inside the magnetosphere. Estimating the solar wind dynamic pressure upstream of a spacecraft magnetopause crossing can be achieved by considering the pressure balance across the magnetopause, assumed to be holding the boundary in equilibrium.

The magnetopause can be considered as a surface where the total (particle and field) pressure within the magnetosphere balances the total pressure in the magnetosheath, although in truth these pressures will not perfectly balance and the boundary will be in motion. For example, increases in the solar wind dynamic pressure will cause the magnetosphere to compress, increasing the magnetic field strength, which exerts a greater pressure outwards, resulting in a new equilibrium location of the magnetopause.

In a simple approximation of the pressure balance, the dynamic pressure of the solar wind ($D_p = \rho u_{sw}^2$) and the thermal static pressure of the solar wind (P_0), balances the magnetic pressure of the magnetosphere ($B^2/2\mu_0$). However, the pressures external to the magnetosphere are actually the magnetosheath pressures rather than the solar wind pressures. These can be related via Bernoulli's equation and using the Rankine-Hugoniot jump conditions with the assumption that flow is adiabatic between the upstream bow shock and the magnetopause stagnation point. The dynamic pressure in the solar wind can then be related to that in the magnetosheath via the factor k, which indicates how much the pressure is diminished by the divergence of the flow and is dependent on the ratio of specific heats (γ) and the sonic Mach number in the solar wind.

The conditions away from the stagnation point depend on the flaring angle of the magnetopause, Ψ, which is the angle between the solar wind and the magnetopause normal. The improved pressure balance equation then becomes:

$$\frac{B^2}{2\mu_0} = kD_p cos^2\Psi + P_0 sin^2\Psi \tag{2.1}$$

To find estimates of the solar wind dynamic pressure, this method finds Ψ from a magnetopause model, using a functional form of the Earth's magnetopause (Shue et al. 1997), which is flexible enough to allow both the size and shape of the magnetopause to be pressure dependent. For a given magnetopause crossing, the model is scaled so it passes through the spacecraft position at that time. At the spacecraft position the normal vector to the model surface is calculated, and the scalar product of this model normal and the solar wind direction is used to calculate Ψ. The coefficient k is set to 0.881, which is valid in high Mach number regimes, as is the case at Saturn (Achilleos et al. 2006). In addition, Kanani et al. (2010) replace the constant static pressure P_0, with one dependent on the dynamic pressure. They also include internal plasma pressures in this pressure balance, based on measurements of ion pressures from the Cassini magnetospheric imaging instrument (MIMI) and electron pressures from CAPS/ELS.

The model magnetopause is rotationally symmetric about the x-axis. The

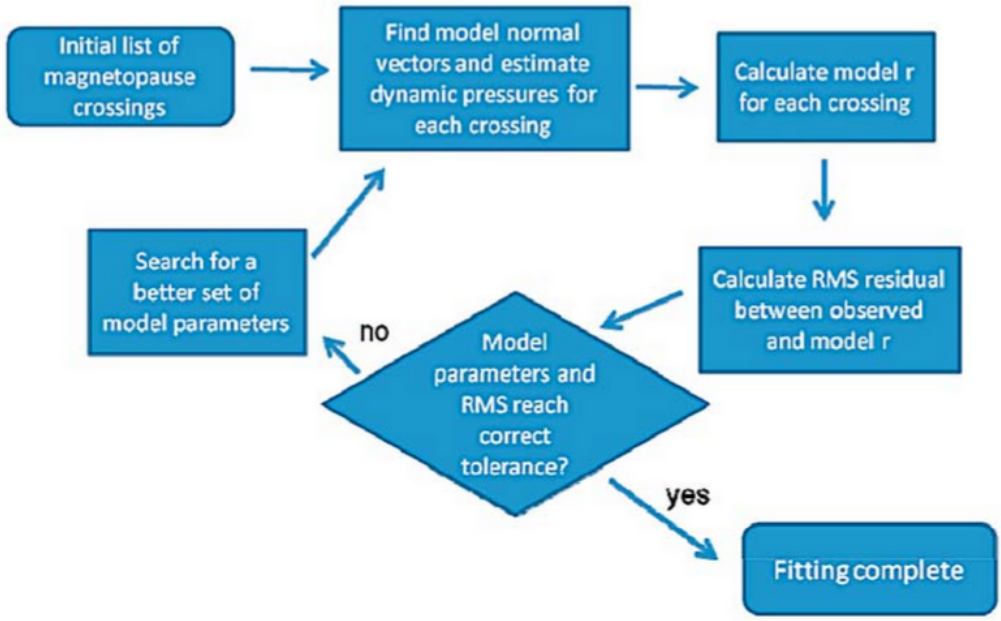

Fig. 2.13: A flow diagram showing the method for fitting the observed magnetopause crossings to the pressure-dependent functional form of the magnetopause (Kanani et al. 2010).

pressure dependent size and shape of the magnetopause is set through the equations: $R_0 = a_1 D_p^{-a_2}$ and $K = a_3 + a_4 D_p$, where R_0 is the magnetopause stand-off distance, affecting the size of the magnetopause, and K affects the shape of the magnetopause by changing how it flares. To fit the model magnetopause shape with pressure balance requires values for the dynamic pressure at each magnetopause crossing. These dynamic pressures are inferred by iteratively fitting the magnetopause shape for the coefficients a_i. At each iteration, the dynamic pressure is estimated via the method described above, using the currently fitted model to determine Ψ at each crossing. A non-linear fitting routine, based on an interior-reflective Newton method, then adjusts the parameters of the magnetopause shape model, which changes the dynamic pressure estimates. The iterations continue until the RMS residual and parameters of the model reach a tolerance of 10^{-6}. A flowchart describing this process is shown in Figure 2.13.

Chapter 3

An Investigation of the CME of 3 November 2011 and its Associated Widespread Solar Energetic Particle Event

In this chapter, the origins of a widespread SEP event, observed at the Earth and both STEREO spacecraft, are investigated. The SEP event is associated with a large CME which erupted from the farside of the Sun on 3 November 2011, at which time both STEREO spacecraft were located more than 90 degrees from Earth and could observe the CME eruption directly, with the CME visible on-disk from STEREO-B and off the limb from STEREO-A.

This work found that by studying the evolution and expansion of the associated CME, the timings of particles arriving at the STEREO spacecraft could be explained, but not those observed at the Earth. As the CME expands high in the corona, its edge reaches the footpoints of the magnetic field lines connecting each spacecraft to the Sun. When this occurs for the STEREO footpoints, the particles observed here are released.

The solar energetic particles were observed arriving first at STEREO-A, followed by electrons at the *Wind* spacecraft at L1, then STEREO-B, and finally protons arriving simultaneously at *Wind* and STEREO-B. By carrying out velocity-dispersion analysis on the particles arriving at each location, it was found that energetic particles arriving at STEREO-A were released first

and the release of particles arriving at STEREO-B was delayed by around 50 minutes.

The expansion of the CME and an associated EUV wave were studied using EUV and coronagraph images and were used to shed light on these particle release timings. It was found that the lateral expansion of the CME low in the corona ($\approx 1.1_{\odot}$) closely tracked the propagation of the EUV wave, with measured velocities of 240±19 $\mathrm{km\,s^{-1}}$ and 221±15 $\mathrm{km\,s^{-1}}$ for the CME and wave respectively. Higher up in the corona ($\approx 1.5_{\odot}$), the CME expansion is faster (674±38 $\mathrm{km\,s^{-1}}$), which allows the CME edge to reach the footpoints of the STEREO spacecraft at the time of their particle release.

This study builds on previous work by Rouillard et al. (2012), which studies a similar SEP event. While they show that the particle release time corresponds to the time that the edge of the CME reaches the magnetic footpoint of each spacecraft, this was only done considering the expansion of the CME low in the corona, as approximated by the evolution of the associated EUV wave. This work provides further evidence for this basic premise, while extending it by demonstrating that this method can also apply when considering how the CME expands at a greater height in the corona than the level of an EUV wave.

This chapter is based on work published in Prise et al. (2014).

3.1 Introduction

Solar energetic particle events tend to fall into two broad categories: impulsive events where particles are accelerated from a small region on the Sun such as a solar flare, and gradual events where particles are accelerated over a wider source such as a CME-driven coronal shock (Reames 1993).

As noted by Kahler (1994) and Tylka et al. (2003), gradual event SEPs are released initially close to the Sun ($\approx$3 – 10 $\mathrm{R_{\odot}}$) and then propagate out along the magnetic field lines. The longitudinal spread of the resulting SEP event can be at least 100 degrees (Cane and Erickson 2003; Kallenrode et al. 1993) and is dependent on how broad the shock is.

Observations of coronal and interplanetary shocks have improved our un-

derstanding of wide SEP events. Interplanetary shocks can be as wide as 180° in longitude (Cliver and Cane 1996; Torsti et al. 1999), which provides a very broad area for particle acceleration. Several signatures of shock formation in the corona have been identified, such as deflected streamers (Cliver et al. 1999; Sheeley et al. 2000) and the layer of electrons observed on the surface of the CME (Vourlidas et al. 2003). It has also been shown that these can be observed directly, along with pressure waves and shocks (Manchester et al. 2008).

The launch of STEREO (Kaiser et al. 2008) mission has provided a far better chance to study SEP events from multiple viewpoints. As the spacecraft separation increases, it has become evident that SEP events can be detected over a far wider range of longitudes than previously assumed, such as the event described by Dresing et al. (2012), where a source region on the back of the Sun produced an SEP event with a longitudinal spread of up to 300°. Rouillard et al. (2012) describe a wide SEP event detected at L1 and at STEREO-A (at this time separated by 88°), caused by a fast and wide CME. They observe a delay in the particle release time of particles arriving at L1, which they conclude is due to the time taken for the CME to expand to the longitude of the magnetic footpoint connected to L1.

Table 3.1: The detected onset times of various in-situ signatures studied, where they are detected, and where possible, the release time from the Sun.

Time (UT)	Event	Position	Release Time (UT)
22:10	CME and EUV wave	backsided, visible from ST-B	
22:20	Type III radio burst	ST-A, -B, & *Wind*	22:12
22:29	Electron onset	ST-A	
22:35	Type II radio burst	ST-B	22:27
22:59	Proton onset	ST-A	22:19±00:14
23:06	Electron onset	*Wind*	22:47±00:15
23:15	Electron onset	ST-B	
23:41	Proton onset	ST-B	23:00±00:08
23:41	Proton onset	*Wind*	

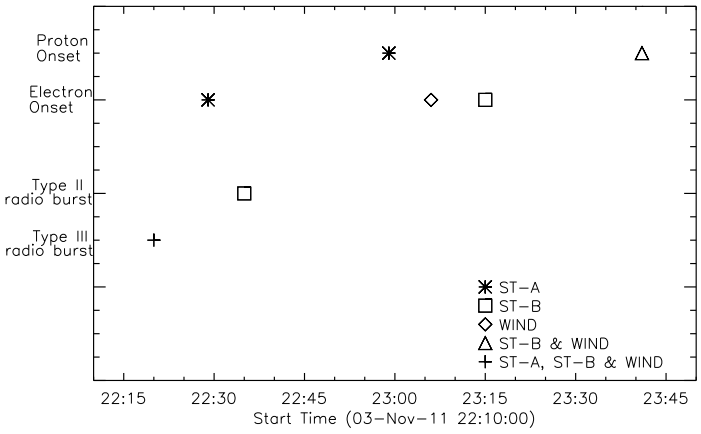

Fig. 3.1: When different in-situ signatures are detected at each spacecraft. The start time of the plot is 22:10 UT, the time of the CME eruption.

In the present study, the characteristics of a CME that erupted from the farside of the Sun on 3 November 2011 are analysed. This CME was accompanied by an EUV wave, and produced several in-situ signatures at 1 AU, including energetic particles and radio bursts. A summary of the timings of the CME and in-situ signatures is shown in Table 3.1 and Figure 3.1. At this time the STEREO spacecraft were past quadrature and were separated by 152°, 106° and 102° ahead and behind the Earth respectively. Figure 3.2 shows the positions of STEREO-A, STEREO-B, and the Earth, along with the direction of the erupting CME. The evolution of the CME and its associated EUV wave are analysed here, allowing the arrival times of the energetic particles at STEREO-A and STEREO-B to be explained.

3.2 Observations

The CME was directly observed by the STEREO/EUVI instrument, part of the SECCHI instrument suite. It was seen on the disk by STEREO-B and on the western limb of STEREO-A, with the eruption beginning at about 22:10 UT on 3 November 2011. In coronagraph images, provided by STEREO COR-1 and COR-2, it is seen erupting off the western limb of STEREO-A and off the eastern limb of STEREO-B, indicating that the CME originated at the farside of the Sun from the Earth. It is also observed from SOHO/LASCO, erupting off the eastern limb, consistent with observations of the erupting active region

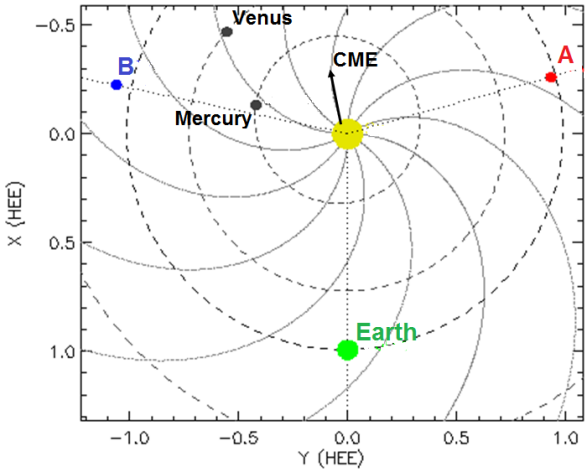

Fig. 3.2: Positions of STEREO-A, STEREO-B, and the Earth on 3 November 2011 22:00 UT. The direction of the erupting CME is indicated by the black arrow and the Parker spiral is also overlaid. This is a modified version of the plot found from stereo-ssc.nascom.nasa.gov/cgi-bin/make_where_gif.

on-disk in STEREO-B (see Figure 4.2). STEREO-A coronagraph observations show this CME has a plane-of-sky speed of 972 $\mathrm{km\,s^{-1}}$, which should suffer from very small projection effects as the CME erupts off the limb as viewed from STEREO-A.

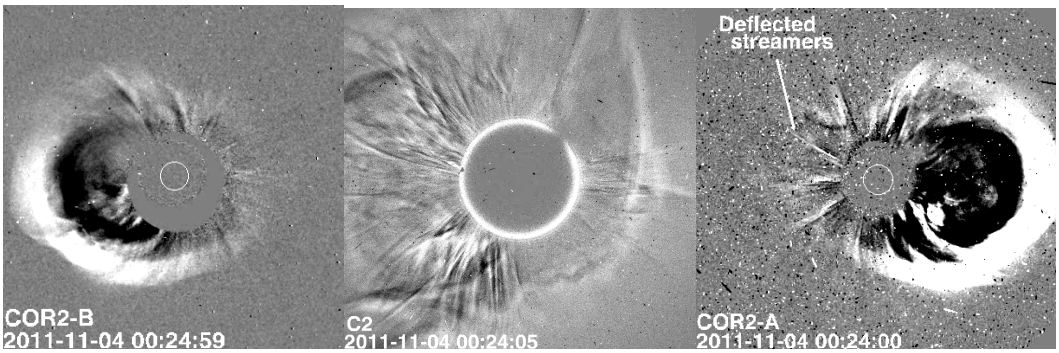

Fig. 3.3: Running-difference images from COR-2B, C2 (LASCO), and COR-2A showing the eruption of the CME as well as deflected streamers. The streamers appear in these running-difference images, indicating that they have moved from their previous position and have therefore been deflected.

Coronagraph observations of this CME show several signatures of pressure variations, including deflected streamers. The deflection of these streamers are observed as the streamers appearing in running-difference coronagraph images,

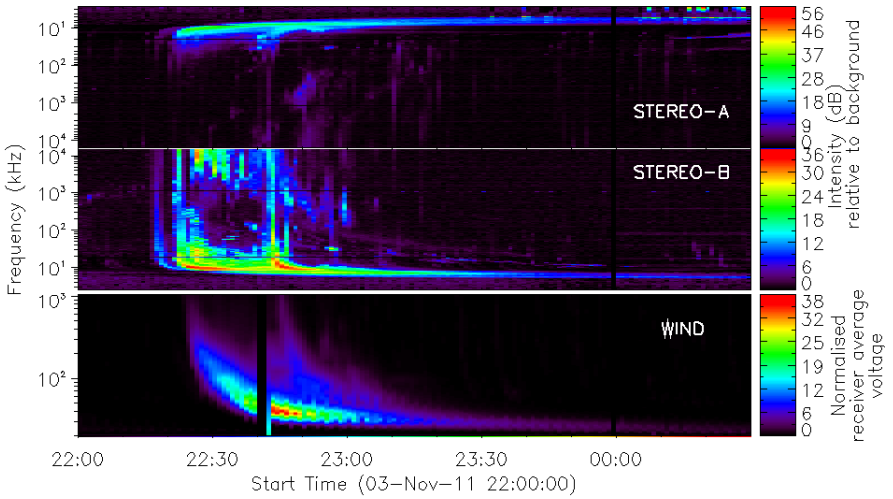

Fig. 3.4: Radio measurements made by S/WAVES at STEREO-A (top), STEREO-B (middle) and WAVES on *Wind* at L1 (bottom). The Type II radio burst is visible in the middle panel (STEREO-B) from approximately 22:35 – 00:10 UT. Type III radio bursts were also observed at all three locations at around 22:20 UT.

as this shows that the streamers have moved from their previous position. These deflected streamers appear in the coronagraph images at roughly 00:24 UT, on the opposite limb to the CME as seen in Figure 4.2. This suggests that the CME has an influence that extends to the other side of the Sun. Figure 3.4 shows the radio measurements around the time of this CME, taken from the S/WAVES instrument onboard the STEREO spacecraft, and WAVES onboard the *Wind* spacecraft, located at L1. A Type II radio burst, indicative of a CME–related shock, is detected by S/WAVES-B between 22:35 UT and around 00:00 UT. A Type III radio burst is also visible at all three locations, at around 22:20 UT.

3.2.1 Propagation of the EUV Wave and Lateral CME Expansion

The EUV wave associated with this eruption was observed from STEREO-B between 22:16 and ∼22:31 UT, travelling from the erupting active region near the eastern limb of STEREO-B, towards the middle of the disk. The direction of the propagation of the wave and position of the erupting active region (on the western limb of the disk as seen from STEREO-A), meant that it was not observed by STEREO-A.

The propagation of the wave was measured using an intensity-profile tech-

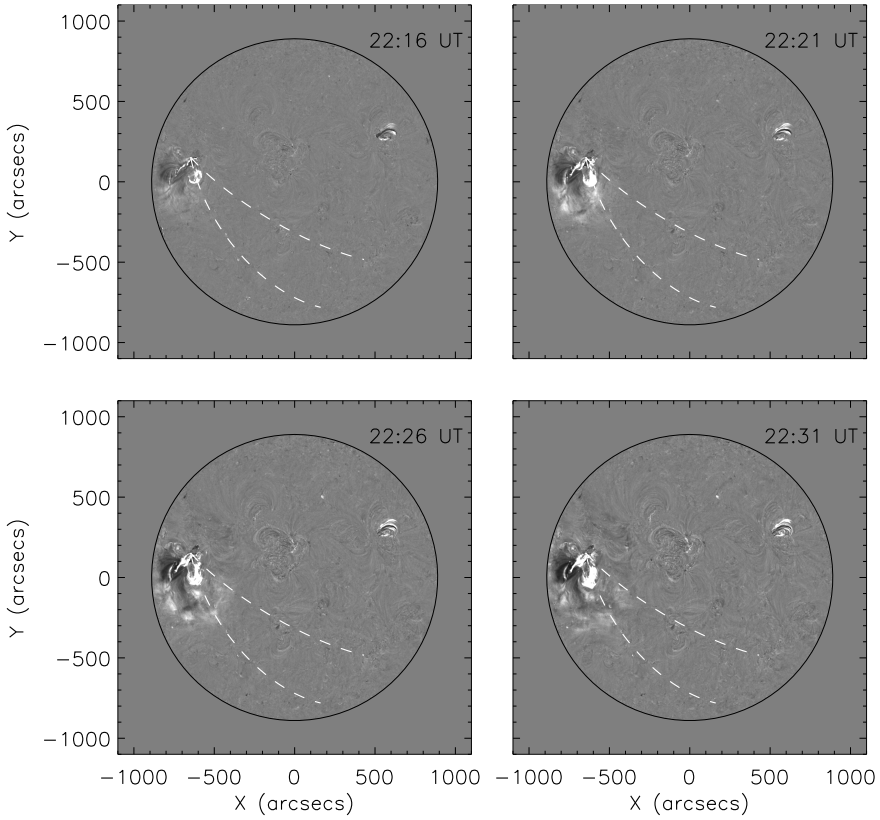

Fig. 3.5: Percentage base-difference images of the EUV wave in 195Å seen from 22:16 to 22:31 UT from STEREO-B. The white dashed lines indicate the region which was used to generate the intensity profiles.

nique (*cf.* Long et al. (2011a); Muhr et al. (2011); Long et al. (2011b)). This method calculates the intensity of percentage base-difference images (showing the percentage change in intensity with respect to a pre-event image) of the Sun in a defined arc sector from the source of the wave, as shown in Figure 3.5. The intensity is measured in several possible arc sectors and then the specific arc sector chosen that detects the maximum number of pulse identifications, in order to better track the propagation of the wave and ensure sufficient detections to allow determination of accurate kinematics. A Gaussian model is then fitted to the resulting intensity profile, allowing the determination of the position of the pulse with time (Figure 3.6). The error in these positions is the full width at half maximum (FWHM) of the Gaussian fitted to that pulse. The distance can then be plotted against the time to find the wave speed, as shown in Figure 3.7. This method only picked up the wave between 22:16 and 22:31

UT, propagating a distance of about 200 Mm in that time. The wave speed was found to be 221±15 $\mathrm{km\,s^{-1}}$, where the error is due to the uncertainty in the fit of the distance–time plot.

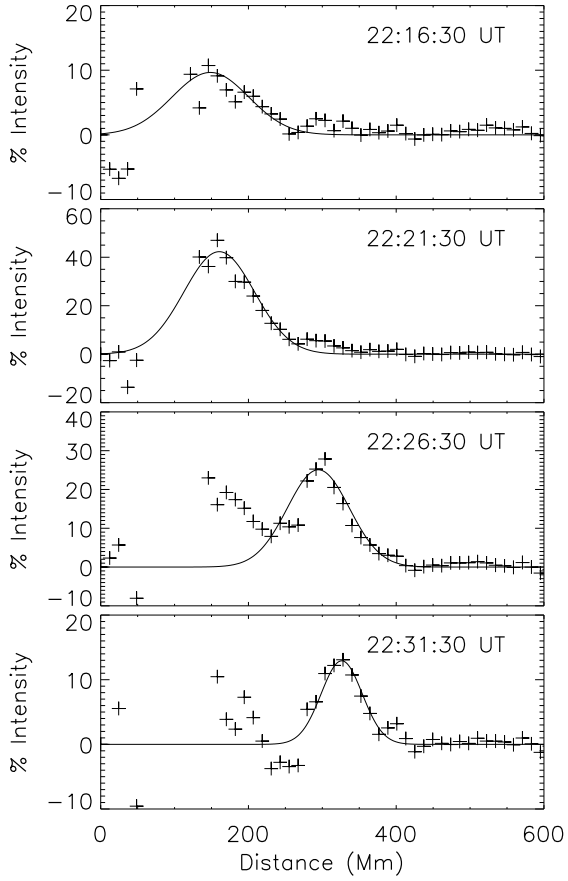

Fig. 3.6: Intensity profiles for the EUV wave (crosses) with the Gaussian fit of the wave over-plotted.

The lateral expansion of the CME was determined by tracking the CME edge using polar plots of EUVI and COR-1 images (see Figure 3.8). The expansion of the CME lower down in the corona was tracked between 22:10 and 22:50 UT by measuring the changing position angle of the edge of the CME over time, as seen in the polar plots. From this, the distance that the CME has expanded is calculated and the velocity found from a distance–time plot, shown in Figure 3.9. In this time the CME expanded by roughly 600 Mm. The position angle was measured three times and the standard error in these three independent measurements was used as to determine the uncertainty

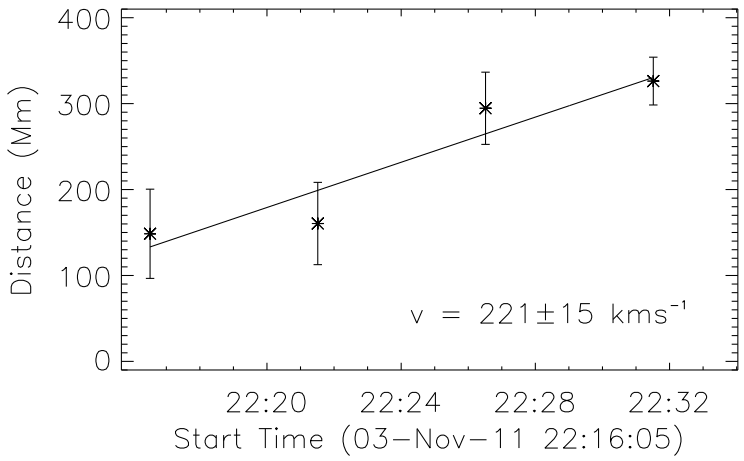

Fig. 3.7: Distance–time plot of the EUV wave. The distance is measured from the source point of the wave, defined as the flare position. v is the velocity of the wave found from this plot. The error bars are the FWHM of the Gaussian fit of the wave pulse from the intensity plots.

in the distance expanded by the CME. The velocity of this expansion at the level of EUVI was found to be 240±19 km s^{-1}, where the error comes from the uncertainty in the fit of the distance–time plot. This velocity suggests that the expansion of the CME (as defined by the moving edge of the CME seen in polar plots) initially roughly tracks the propagation of the EUV wave, as this speed is consistent with that of the wave within errors and the CME edge appears to track the EUV wave in images, as shown in Figure 3.10. The lateral expansion was also measured in COR-1 between 22:20 and 23:00 UT, using the same method with COR-1 polar plots. The CME was seen to expand by roughly 1200 Mm at this height and the velocity was found to be significantly higher than the expansion speed from EUVI polar plots, at 674±38 km s^{-1}.

3.2.2 Solar Energetic Particle Events

Energetic proton measurements (shown in Figure 3.11) were taken at the STEREO spacecraft using the HET and LET instruments in three energy bins each between 13 and 100 MeV for HET (13 – 21 MeV, 21 – 40 MeV, and 40 – 100 MeV), and 2.2 and 12 MeV for LET (2.2 – 4 MeV, 4 – 6 MeV, and 6 – 12 MeV). The proton measurements at L1 were taken with the EPACT in-

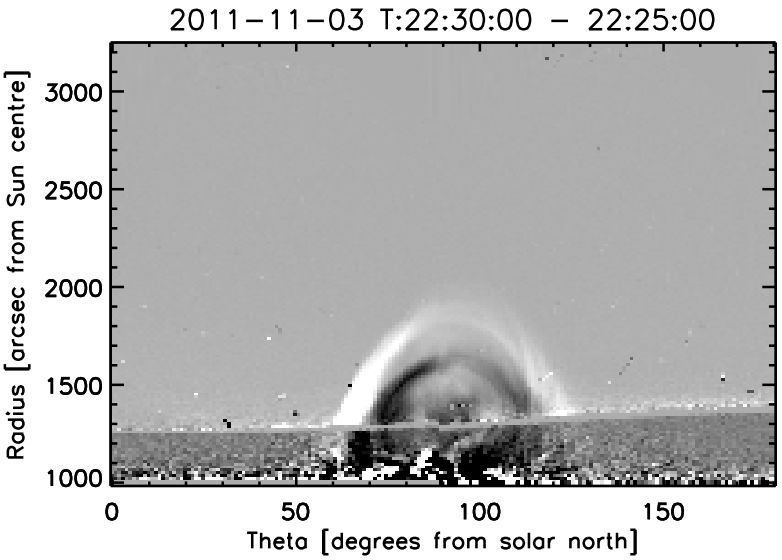

Fig. 3.8: A combined EUVI and COR-1 polar plot. The lateral expansion speed of the CME is calculated from the changing position angle of the edge of CME with time.

strument on the *Wind* spacecraft in two energy bins between 19 and 72 MeV (19 – 28 MeV and 28 – 72 MeV). Energetic electron measurements (shown in Figure 3.12) at the STEREO spacecraft use the SEPT instrument, measuring electrons in four energy bins between 0.03 and 0.47 MeV (0.03 – 0.06 MeV, 0.06 – 0.11 MeV, 0.11 – 0.24 MeV, and 0.24 – 0.47 MeV). The electron measurements at L1 use the 3DP instrument on the *Wind* spacecraft, which measures energetic electrons in three energy bins between 0.02 and 0.225 MeV (0.02 – 0.048 MeV, 0.043 – 0.138 MeV, and 0.127 – 0.225 MeV).

Solar energetic particles were detected at both STEREO spacecraft and at *Wind* after the eruption of this CME. Energetic electrons arrived first at STEREO-A at 22:29±00:09 UT followed by protons 30 minutes later. Accelerated electrons were detected at *Wind* at 23:06±00:09 UT and STEREO-B at 23:15±00:07 UT, and energetic protons then arrived at *Wind* and STEREO-B simultaneously at 23:41 UT.

The onset times were determined using the method described by Krucker et al. (1999), where the electron or ion background flux is subtracted and the curves normalised in units of standard deviation, σ. An upper limit for the

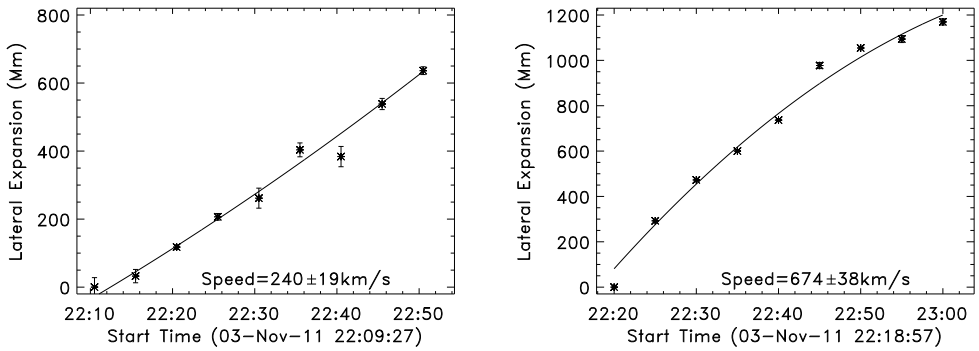

Fig. 3.9: Distance-time plot of the lateral expansion of the CME as measured from polar plots of EUVI (left) and COR-1 (right). The distance is determined using polar plots such as those in Figure 3.8 and the velocities found are 240±19 $\mathrm{km\,s^{-1}}$ for EUVI and 674±38 $\mathrm{km\,s^{-1}}$ for COR-1.

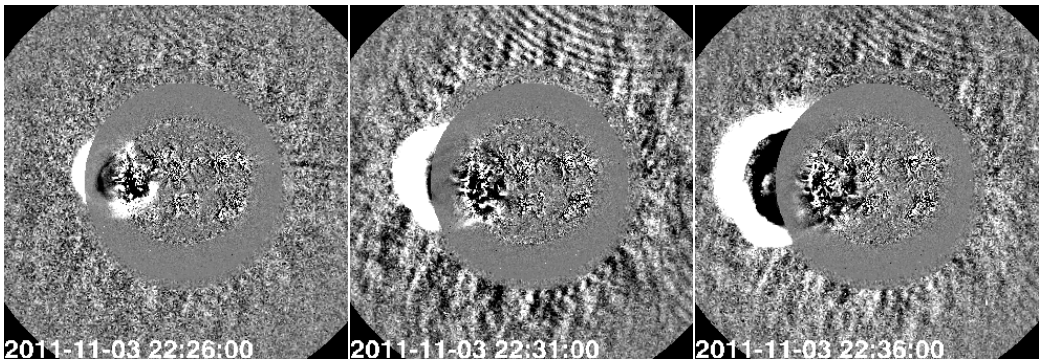

Fig. 3.10: Combined EUVI and COR-1 running-difference images showing that the EUV wave visible in EUVI seems to track the expansion of the CME

onset time is then defined as the time when this normalised flux first goes above 4σ. The actual onset time is then taken to be the time increment after the latest time that the normalised flux is negative prior to the upper limit. The difference between this onset time and the upper limit is then the uncertainty in the onset time.

Velocity-dispersion analysis was carried out on the accelerated protons detected at the STEREO spacecraft in order to determine the solar particle release (SPR) time and path length of the protons. This analysis involves plotting the onset times versus $\beta^{-1} = (v/c)^{-1}$ for particles from different energy intervals. The slope of the straight fit line multiplied by c gives the path length

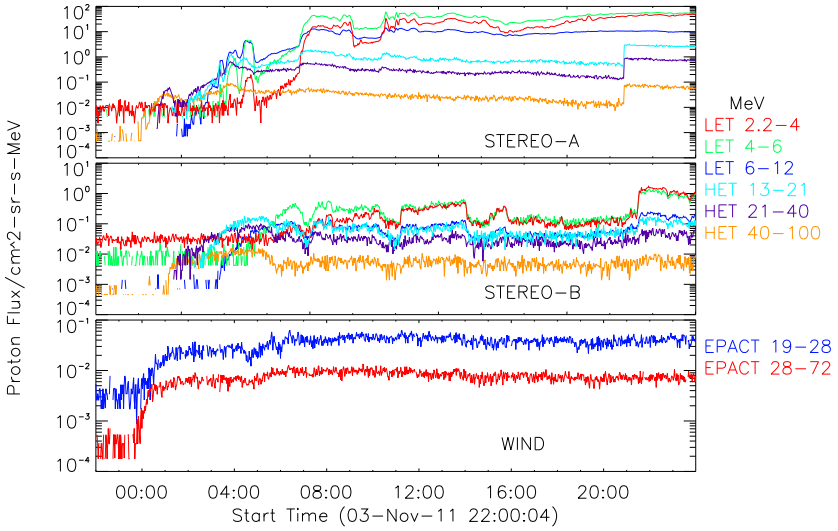

Fig. 3.11: Proton flux intensity measured at STEREO-A (top), STEREO-B (middle) and *Wind* (bottom). The flux at the STEREO spacecrafts were measured in six energy bands between 2.2 and 100 MeV from the HET and LET instruments. The flux at *Wind* was measured in two energy bands between 19 and 72 MeV from the EPACT instrument.

and the intercept gives the initial SPR time. Velocity dispersion of protons arriving at *Wind* was not carried out due to the fewer energy bins available; instead velocity dispersion was done on energetic electrons arriving at *Wind*. This is shown in Figure 3.13. The release time of protons at STEREO-A was found to be 22:19±00:14 UT, with a path length of 1.97±0.22 AU. By comparison the release time at STEREO-B is delayed by around 50 minutes from the CME eruption until 23:00±00:08 UT, which is during the Type II radio burst seen at STEREO-B, with a path length of 1.89±0.13 AU. Velocity dispersion of electrons arriving at *Wind* yielded an SPR time of 22:47±00:15 UT, with a path length of 1.86±1.44 AU.

3.3 Discussion

By considering the expansion of the CME and the positions of the footpoints of the magnetic field lines connecting each spacecraft to the Sun, conclusions can be drawn about the origin of the apparent delay in particle-release times and the order of the particle onsets. Consistent with the work done by Rouillard et al. (2012) it is found that the release time of particles arriving at each location is dependent on the time for the CME to expand to the magnetic

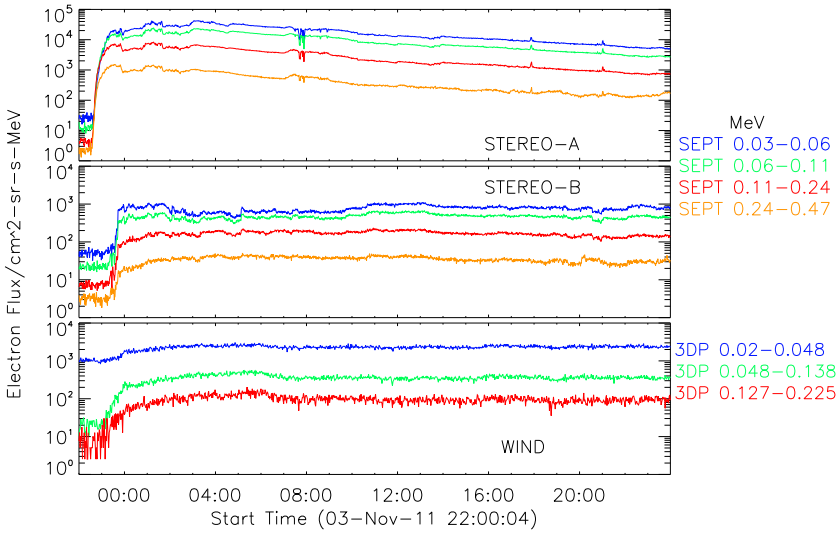

Fig. 3.12: Electron flux intensity measured at STEREO-A (top), STEREO-B (middle) and *Wind* (bottom). The flux at the STEREO spacecrafts were measured in four energy bins between 0.03 and 0.47 MeV from the SEPT instrument. The flux at *Wind* was measured in three energy bins between 0.02 and 0.225 MeV from the 3DP instrument.

footpoints of each spacecraft. The locations of these magnetic footpoints were calculated using Parker spiral theory with the average solar wind speed measured in-situ at each spacecraft during the onset of the SEP events. Those speeds were ≈315 $\mathrm{km\,s^{-1}}$ at STEREO-A, ≈330 $\mathrm{km\,s^{-1}}$ at STEREO-B, and ≈265 $\mathrm{km\,s^{-1}}$ at *Wind*. The footpoint of STEREO-A is the closest to the erupting active region, despite this active region only being visible from STEREO-B. This can be seen from Figures 3.14 and 3.15, which are reverse-intensity Carrington plots with the magnetic footpoints of STEREO-A, STEREO-B, and *Wind* indicated, as well as the source point of the CME (white circles as labelled). As the CME expands it will therefore reach the footpoint of STEREO-A first, so particles arriving at STEREO-A have the earliest SPR time, as is observed. The CME should reach the footpoint of STEREO-B next, as this is closer to the CME source region than the footpoint of *Wind*, but instead the SPR time for SEPs arriving at *Wind* is observed to be earlier than STEREO-B.

In the work done by Rouillard et al. (2012), the initial expansion of the CME is approximated by the propagation of the EUV wave across the solar

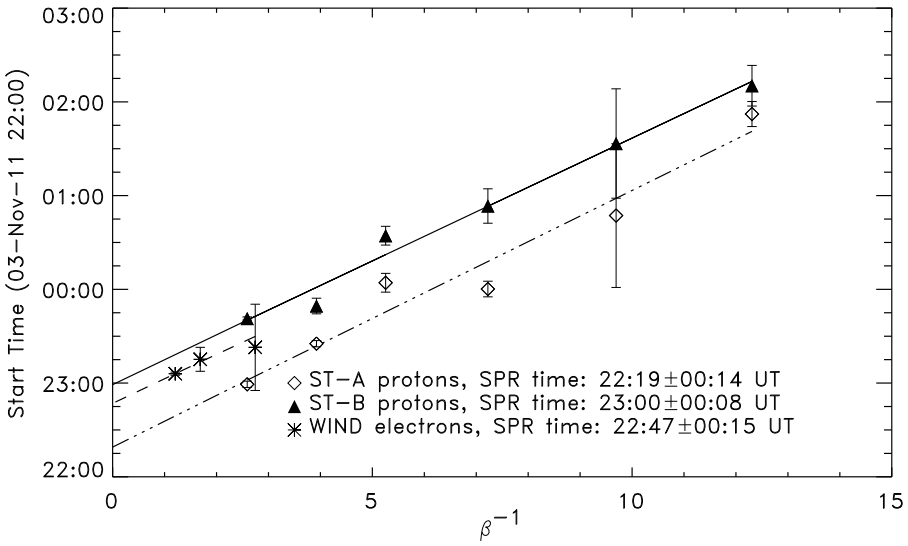

Fig. 3.13: Velocity dispersion of particle onset times *versus* the reciprocal of the relativistic β- function ($\beta^{-1} = (v/c)^{-1}$). This uses the onset of protons at STEREO-A (dot–dash line) and -B (solid line), and the onset of electrons at *Wind* (dashed line). The slopes of the fit lines multiplied by c give the path lengths and the intercepts give the solar particle release (SPR) times of the particles. The error in these fits yields the uncertainty in the derived SPR times and path lengths.

disk, as seen in EUV running difference images. In this study an intensity-profile method is employed, allowing for the wave to be tracked from 22:16 to 22:31 UT, which includes the particle release time of protons detected at STEREO-A. The polar plots at this height show that the CME was still expanding beyond this time however, from the initial eruption at 22:10 UT until 22:50 UT. The measured speed of the EUV wave was 221±15 $\mathrm{km\,s^{-1}}$. At this speed the wave, and therefore the edge of the CME at this height in the corona, would not reach the magnetic footpoints of any of the spacecraft by the respective SPR times, as is shown in Figure 3.14.

However, the CME did demonstrate a much faster expansion at the level of COR-1 (1.5 $\mathrm{R_\odot}$), with the lateral expansion speed measured to be 674±38 $\mathrm{km\,s^{-1}}$. The position of the edge of the CME at this height in the corona was estimated by determining the distance that the CME had expanded with this speed, in the time between the CME eruption time and the SPR time for each spacecraft (22:19, 23:00 and 22:47 UT for STEREO-A, STEREO-

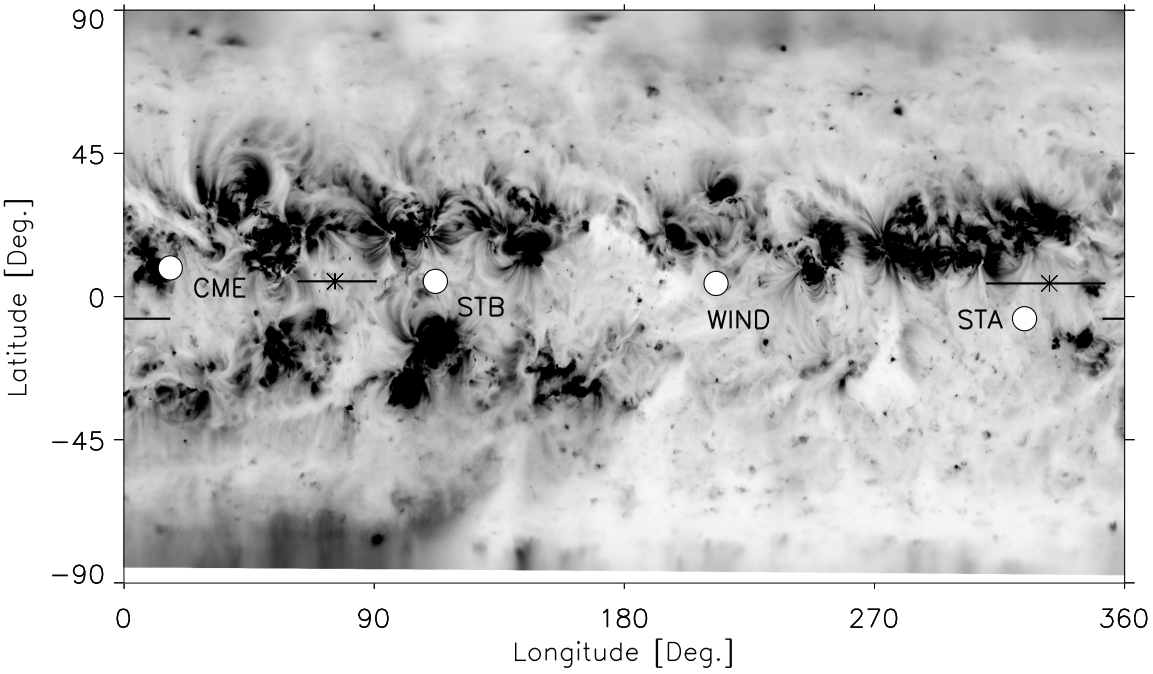

Fig. 3.14: A reverse-intensity Carrington map of EUV observations made in 195Å . The magnetic footpoints of STEREO-A, STEREO-B, and *Wind* are labelled, along with the source position of the CME (white circles). The black stars show the position of the edge of the CME, as calculated using the expansion speed from EUVI, at the SPR times of energetic particles in the three locations. The black lines show the uncertainty in this position, due to the uncertainty in SPR time and wave speed.

B, and *Wind* respectively). On Figure 3.15, the stars indicate the estimated position of the edge of the CME at each of these SPR times, using this higher expansion speed. The black lines indicate the uncertainty in this position using the uncertainty in the speed of the expansion and uncertainty in the SPR time. Figure 3.15 shows that the edge of the CME reaches the magnetic footpoints of both of the STEREO spacecrafts at the time of its particle release within errors. This indicates that the particles detected at STEREO-A and STEREO-B were released from the Sun at the time that the edge of the CME reached the magnetic footpoints of these spacecrafts, at the height of COR-1. The edge of the CME does not reach the footpoint connecting the *Wind* spacecraft to the Sun by the time of its SPR time, however.

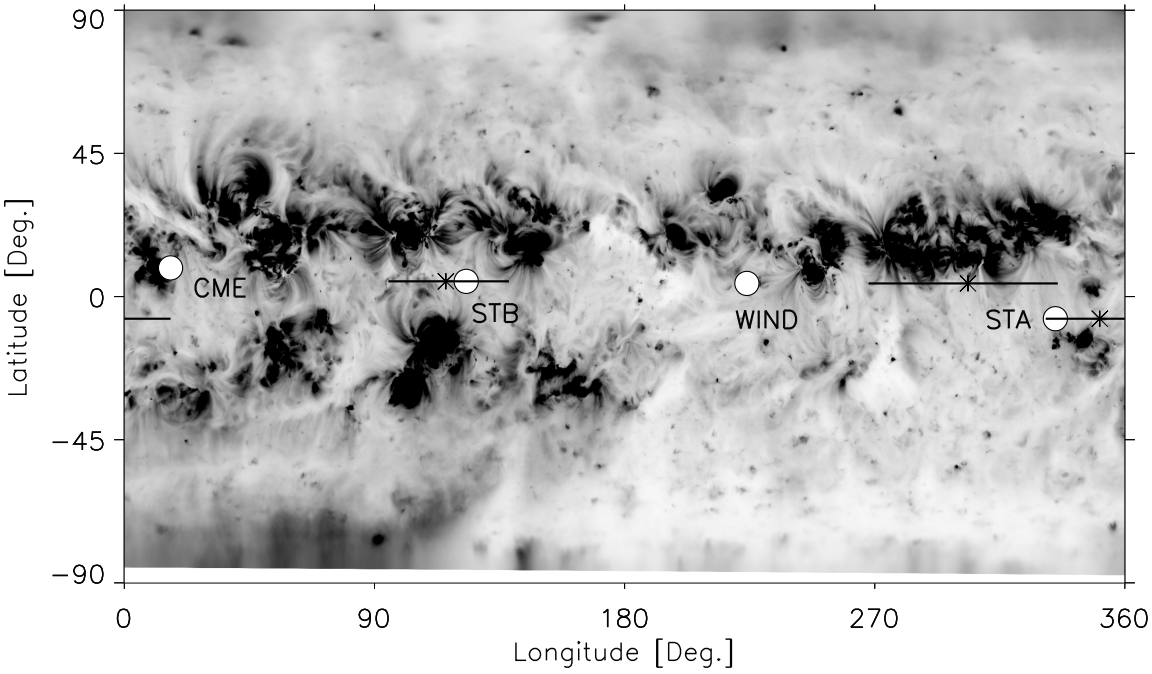

Fig. 3.15: The same figure as 3.14, but the black stars show the position of the edge of the CME, as calculated using the expansion speed from COR-1A, at the SPR times of energetic particles in the three locations.

3.4 Summary and Conclusion

This works aims to determine the causes of the widespread SEP event observed by multiple spacecraft, which were over 100° apart, on 3 November 2011. The event was associated with a large CME and an EUV wave. This section will briefly reiterate the work done and then summarise the main conclusions.

The evolution of this CME was studied from several viewpoints, both on the disk and with coronagraphs. The CME erupted from the farside of the Sun, but coronagraph images show deflected streamers appearing on the opposite side of the Sun to the eruption site, indicating that the CME's influence extends to the other side of the Sun. Radio measurements at this time detected a Type II radio burst at STEREO-B, which indicates the presence of a shock in this region.

The EUV wave associated with this CME was studied using an intensity-profile technique, which only detected it for 15 minutes and determined the wave speed to be 221±15 $\mathrm{km\,s^{-1}}$. The expansion of the CME across the Sun

is measured using polar plots of the Sun from EUVI and COR-1 images and demonstrates that the expansion of the CME lower down in the corona tracks the propagation of the associated EUV wave. The speed of the CME expansion is faster higher up in the corona at the height of the polar plots from COR-1: at 674±38 $\mathrm{km\,s^{-1}}$ compared to 240±19 $\mathrm{km\,s^{-1}}$ at the level of EUVI polar plots.

SEP events were detected at all three locations: STEREO-A, STEREO-B, and *Wind*, after the eruption of this CME, with protons and electrons arriving first at STEREO-A despite the CME being viewed on the disk from STEREO-B, but only off the limb from STEREO-A. Particle onset is then detected at *Wind*, followed by STEREO-B soon after. A velocity-dispersion analysis was carried out and showed that the SPR time is earliest for the particles arriving at STEREO-A (22:19±00:14 UT), then *Wind* (22:47±00:15 UT), and finally STEREO-B (23:00±00:08), 50 minutes after the eruption of the CME.

The expansion of the CME is used to estimate the position of the edge of the CME on the Sun at the solar-particle release times of each spacecraft. The footpoint of the magnetic field line connecting STEREO-A to the Sun is seen to be closer to the source location of the CME than the footpoint of STEREO-B. If the particles are released only when the CME reaches the footpoint of the spacecraft, this can explain why particles are observed at STEREO-A first.

By using the speed of the EUV wave to estimate the position of the CME, it is found that the edge of the CME does not reach the footpoints of any of the spacecraft at their respective SPR times. However, considering the faster expansion speed of the CME at the level of COR-1 polar plots, the edge of the CME was shown to reach the footpoints of both STEREO spacecrafts at their SPR times, but not the footpoint of the *Wind* spacecraft located at L1. This implies that for the particles arriving at the STEREO spacecrafts, the particles were released when the CME expanded higher up in the corona and reached the footpoints of these spacecrafts.

We therefore conclude that the delay in the release time of the energetic particles at STEREO-B in relation to STEREO-A can be attributed to the time for the CME to expand out to the magnetic footpoint of STEREO-B at

this higher altitude. The time for the CME edge to reach the footpoint of STEREO-A also corresponds to its particle release time, but this is not the case for the particles observed by *Wind*.

This work has attempted to explain the timing of energetic particles arriving at multiple spacecrafts in relation to a CME with an associated EUV wave. In doing so, it has built on previous work by Rouillard et al. (2012), who study a similar type of event. They demonstrate that the delay in particle release in the event can be explained by the time for the CME expansion (approximated as the propagation of the EUV wave) to reach the magnetic footpoints of the spacecrafts. However, while the CME lateral expansion speed as measured in COR-1 in this event is broadly consistent with the observed delay in particle release times, the speed of the EUV wave in the lower corona is not, and is not high enough to drive a shock in the lower corona. Also, the expansion of the CME does not reach the footpoint of *Wind* by 22:47 UT (the release time for particles arriving at *Wind*), even taking into account the uncertainty in this SPR time. This suggests that the particles observed at *Wind* are not associated with this CME, but originate from a different source.

Chapter 4

Analysis of a CME and CIR as they travel from the Sun passing Venus, Earth, Mars and Saturn

This chapter aims to study how different solar transients propagate and interact throughout the solar system, by studying an ICME and closely occurring CIR in June 2010. This work finds that the ICME (propagating behind the CIR) is accelerated by the high speed stream associated with this CIR. Solar wind modelling suggests that the ICME and CIR eventually merge and cause a compression of Saturn's magnetosphere, despite the initial ICME being fairly small, demonstrating that relatively weak solar transients can merge and cause large impacts further out in the solar system. The modelling also showed that in this case, the Enlil solar wind model predicted the timings of the ICME arrival at different locations better than the CIR, but did not simulate the observed acceleration of the ICME. This demonstrates the need for accurate modelling of the background solar wind in this instance, in order to improve the simulation of the ICME.

This work takes advantage of a good alignment in the solar system between Venus, STEREO-B, Mars and Saturn at this time, and makes use of data from planetary satellites and solar wind modelling in addition to solar telescopes. The CME erupted from the Sun at 01:30 UT on 20 June 2010, with v $\approx$ 600 km s^{-1}, as observed by STEREO-B, SDO and SOHO/LASCO. It arrived at Venus over 2 days later, some 3.5 days after a CIR is also detected

here. The CIR was also observed at STEREO-B and Mars, prior to the arrival of the CME. The CME is not directed Earthward, but the CIR is detected here less than 2 days after its arrival at Mars. Around a month later, a strong compression of the Saturn magnetosphere is observed by Cassini, consistent with the scenario that the CME and CIR have merged into a single solar transient. The arrival times of both the CME and the CIR at different locations were predicted using the Enlil with cone model. The arrival time of the CME at Venus, STEREO-B and Mars is predicted to within 20 hours of its actual detection, but the predictions for the CIR showed greater differences from observations, all over 1.5 days early. More accurate predictions for the CIR were found by extrapolating the travel time between different locations using the arrival times and speeds detected by STEREO-B and ACE. This chapter is based on work published in Prise et al. (2015).

4.1 Introduction

In recent years, spacecraft have been located at all planets in the inner solar system, at 3 different points at 1 AU, and at Saturn, allowing for the opportunity to study the impact of distinct solar transients on more than one location. Analysing a solar wind disturbance by observing it throughout the inner and outer solar system also provides the opportunity to study the characteristics of its propagation and learn more about its evolution as it travels through the solar system. Such solar wind transients can include ICMEs and CIRs.

CIRs are formed when a region of fast solar wind catches up with a region of slow solar wind creating a density enhancement at the interface between them, known as a Stream Interaction Region or SIR. The fast solar wind originates from coronal holes that become more frequent at lower solar latitudes during the declining phase of the solar cycle. These high speed streams of solar wind, and therefore the associated interaction region, rotate with the Sun, sweeping out large areas of longitude. If they persist for multiple solar rotations, they become known as CIRs (Gosling and Pizzo 1999). CIRs have been extensively modelled and compared with observations, for example using the Enlil solar wind model (e.g. Jian et al. (2011); Odstrcil and Pizzo (2009)).

Wood et al. (2010) constructed a 3D model of a CIR and generated synthetic white-light images that successfully reproduced its general appearance and evolution in the Heliospheric Imagers, HI-2, on the STEREO spacecraft. They note that the curvature of the CIR is compatible with the observed slow solar wind speed. As CIRs can be very long-lived structures in the heliosphere, and have the potential to influence vast areas of it, their propagation through the solar system is important to study.

ICMEs are the interplanetary counterparts of CMEs and occur more frequently during solar maximum. In comparison to CIRs they are short-lived solar transients, passing through the solar system with speeds of up to 2500 $\mathrm{km\,s^{-1}}$, but often cause stronger impacts on the Earth (e.g. Schwenn (2006)).

There have been several studies tracking solar transients through the inner solar system, using multipoint remote and in-situ observations to constrain the characteristics of the transients and learn more about their propagation. Rouillard et al. (2009) observe a complex solar storm consisting of multiple solar transients and track it from the Sun to Venus. The main ICME is observed as two parts, which they show could be caused by a single flux rope, demonstrating that this can be determined from white-light images. The presence of a flux rope is confirmed by in-situ measurements using Venus Express (VEx) and Messenger. Möstl et al. (2012) also make use of multipoint observations in the inner solar system to demonstrate that sympathetic solar eruptions can influence over a third of the heliosphere in the ecliptic, and that multiple viewpoints are sometimes the only way to gain a clear picture of a complex sequence of events. Nieves-Chinchilla et al. (2013) show that a specific stealth CME has been deflected by nearby coronal holes during its evolution, utilising remote observations from STEREO, SOHO and SDO, as well as in-situ measurements at Wind, ACE and Messenger.

Williams et al. (2011) track multiple CIRs through the inner solar system and assess methods to predict the arrival of CIRs at different locations. They find that their method, which extrapolates the CIR arrival at other locations using its speed and arrival at ACE, predicts arrival times better than an alternative method using STEREO/HI. Studies of propagation to the outer

heliosphere have been much less frequent. One such study, which tracks an ICME to the outer solar system, was carried out by Prangé et al. (2004). They successfully demonstrate that interplanetary shocks retain their ability to drive aurora throughout the solar system by tracking the propagation of an ICME from its eruption to the initiation of auroral storms on the outer planets. Hanlon et al. (2004) trace solar wind transients observed at Jupiter by Cassini back to 1 AU using ballistic projections. They find that this method provides good predictions of the conditions at 5 AU from measured parameters at the Earth when Cassini is within a few tens of degrees in longitude, and identify two transients at Jupiter as ICMEs and a third as an MIR.

Since then, several CIRs have been observed in the outer solar system, such as those detected by Cassini on its approach to Saturn in late 2003/2004 (Jackman et al. 2004, 2008). They also observe this highly structured solar wind being disrupted by ICMEs in November 2003 as a result of the Halloween storms, concluding that shocks can excite significant magnetospheric dynamics at Saturn. During the Cassini orbit insertion at Saturn, Jackman et al. (2005) and Achilleos et al. (2006) observe the arrival of a CIR at Saturn, and the resulting compression of the magnetosphere. Achilleos et al. (2006) conclude that Saturn's bow shock has velocities of up to 400 km s^{-1} and is governed by ion dynamics. Jackman et al. (2005) conclude that the compression leads to reconnection in the magnetotail, which injects hot plasma into the nightside magnetosphere and causes auroral signatures. Beyond Saturn, Liu et al. (2014) study a series of CMEs which are observed near the Earth and then modelled further out. These structures merge together and the model predicts their arrival at 120 AU, which is seen to correspond to a period of radio emissions and disturbance of galactic cosmic rays as observed by Voyager 1.

When CIRs and ICMEs interact they can form merged interaction regions (MIRs), regions where total solar wind pressure is enhanced, formed by multiple solar transients (Burlaga et al. 2003). Multiple ICMEs propagating at different speeds can catch up with one another as they travel and also merge to form MIRs. The resulting structure can strongly influence geomagnetic activity at the Earth (Rouillard et al. 2010), for example, if an ICME interacts with

a CIR or an earlier, slower ICME, this can cause a compression, resulting in an intensification of the magnetic field. This would be a particular issue if the constituent ICMEs contain magnetic clouds with a highly ordered magnetic field (Wang et al. 2003, 2005; Xiong et al. 2007). MIRs can be very complex and require multiple observations to verify how they have formed and what their structure is (Burlaga et al. 2003; Rouillard et al. 2010).

The interaction of multiple ICMEs with each other has attracted significant study. Wu et al. (2007, 2014) model the interactions of several ICMEs using the HAFv.2+3DMHD hybrid code, which combines the Hakamada-Akasofu-Fry code version 2 with a fully 3D time-dependent MHD code. They demonstrate that this model can help link ICMEs and shocks observed at 1 AU to their solar source, particularly in the case of complex or interacting ejecta. Wu et al. (2011); Wu et al. (2012) show that interactions with the background solar wind can cause the leading edges of ICMEs to become distorted or asymmetric, by simulating ICMEs with the same HAFv.2+3DMHD model. The interaction of two specific ICMEs were modelled by Lugaz et al. (2009) and Webb et al. (2009). Lugaz et al. (2009) conclude that the second, fast ICME catches up with the earlier, slower ICME and decelerates before merging with it, whereas Webb et al. (2009) suggest ICMEs may not have merged, but instead only partially interacted or the second ICME simply overtook the first. They also compare the results of four different models, including Enlil and HAFv.2 and find that they generally all agree on the events' appearance and kinematic evolution. It has also been observed that interacting ICMEs can lead to significant changes to the direction of propagation of the transients, sometimes resulting in strong deflections (Lugaz et al. 2012). Shen et al. (2012, 2013) find that the collision and deflection of ICMEs can be super-elastic, through both modelling and observations.

CME deflections are also observed as a result of interactions with the background solar wind and outer corona. Equatorward deflections of CMEs were first reported by MacQueen et al. (1986) near solar minimum, and further reported by e.g. Gopalswamy et al. (2003); Cremades and Bothmer (2004); Wang et al. (2011). This systematic deflection is due to the dominance of

large scale dipolar magnetic field and flow at solar minimum, in comparison to much less ordered conditions during solar maximum. Gui et al. (2011) verify that CME deflections in the inner corona are consistent in strength and direction with the gradient of magnetic energy density. However, as the density of magnetic field decreases with heliocentric distance, this effect should only be significant close to the Sun. Isavnin et al. (2014) find that 60% of the latitudinal deflection occurs below 30 $R_{\odot}$, suggesting that interactions with coronal holes may be the main cause of this deflection. Wang et al. (2004) characterise longitudinal deflections of ICMEs by their interaction with the Parker spiral, showing that faster ICMEs are blocked by the slow solar wind ahead and deflected eastwards, whereas slower ICMEs are accelerated by faster solar wind behind and deflected westwards. Wang et al. (2014) model a specific ICME and conclude that the deflection is due to the interaction of the ICME with the solar wind, rather than the gradient of the magnetic energy density which is the cause of deflection in the corona. Like Nieves-Chinchilla et al. (2013), Wood et al. (2012) observe a CME being deflected by nearby coronal holes. However, in this instance, only the ejecta is deflected, not the shock. Part of the shock expands more rapidly into the high speed wind stream from the coronal hole, and arrives at STEREO-A a day before the rest of the shock, travelling in normal solar wind, arrives at the Earth.

The Enlil solar wind model is used in this work to complement the observations and fill gaps (for example, as the transients propagate between Mars and Saturn). A detailed description of the model is given in Chapter 2. In this work, the cone model addition to Enlil is also used, which inserts a plasma cloud into the ambient solar wind to simulate a ICME. However, this plasma cloud doesn't incorporate the internal magnetic signal of the ICME, which is one of an ICMEs most significant parameters. This means that Enlil cannot model the flux rope structure of an ICME, so the simulated evolution of the ICME ejecta is not accurate. However, the propagation of any associated density enhancements, such as plasma sheath regions, shocks, solar wind pile-up or compression regions, is not affected by this. Although these regions cannot be specifically distinguished in the simulation, it can still provide a valid

estimate of the arrival of the associated solar wind disturbance at different locations in the solar system. In this study, we use the term 'ICME' to refer to the entire solar wind region altered by the CME transient, as defined by Rouillard et al. (2011) including any shock, sheath, solar wind pile-up and ejecta regions. We therefore refer to the solar wind disturbance as simulated by Enlil as an ICME, along with the structures identified in observations. The different regions of the ICME such as shock, solar wind pile-up and ejecta are explicitly stated when we are referring to them.

Multiple studies have been made of the performance of Enlil, comparing its predictions with in-situ observations and alternative CME propagation model results. Recent studies include those by Vršnak et al. (2014) which compares the Enlil+cone model with the analytical drag-based model, finding that the differences in the simulated and observed arrival times for ICMEs at L1 are similar for both models, at around 14 hours. Falkenberg et al. (2010) note that, despite Enlil being unable to simulate the internal magnetic structure of an ICME, the magnitude of the initial signal, arrival time and dynamic pressure of the event is still well reproduced at L1 when changing different Enlil input parameters from the default values. Taktakishvili et al. (2009) find an average error in ICME shock arrival times of six hours, with Enlil performing well when compared to a mean velocity and empirical shock arrival model. A number of studies make use of Enlil results at locations other than L1. In particular, Baker et al. (2009), Baker et al. (2011) and Baker et al. (2013) demonstrate that Enlil simulations can provide useful context for planetary exploration, specifically Messenger observations at Mercury, as the plasma instrument onboard cannot always adequately sample the solar wind distribution functions. Falkenberg et al. (2011b) compare ICME observations to Enlil simulations and find that the multipoint observations are crucial to validate the simulations, as two different ICMEs can seem very similar when observed at only one location. They also note that possible deflections of the ICME will increase uncertainty in the simulation, as this is less likely to be correctly modelled without the internal magnetic structure of the ICME. Falkenberg et al. (2011a) was a follow up to this study, which again uses in-situ

observations of ICMEs at Earth and Mars to evaluate Enlil predictions. They find that shocks can arrive almost simultaneously at Mars and Earth due to the presence of a high speed stream, allowing part of the CME shock front to travel faster than the rest. In addition to several studies that use Enlil+cone to predict the arrival of ICMEs at Earth, the ability of Enlil to reproduce the background solar wind has also been analysed. Lee et al. (2009), Jian et al. (2011) and Broiles et al. (2013) compare the performance of WSA/Enlil and MAS/Enlil to simulate the background solar wind and find that in general, both versions are capable of reproducing the large scale structure of the solar wind, but find that the timing can be off by 1 - 2 days. MacNeice et al. (2011) validates models and assesses the accuracy of WSA/Enlil in tracing field lines through the heliosphere. They find that the average error in the position of the footpoints of field lines is roughly 20°, which could correspond to timing errors of 1 - 2 days for structures in the ambient solar wind. The simulated values of solar wind parameters also show discrepancies with observations. For example, both Jian et al. (2011) and Broiles et al. (2013) find that Enlil significantly underestimates the magnetic field strength and total pressure. Jian et al. (2011) also find that the Enlil simulations underestimate the temperature, and that this is more extreme at 5.4 AU than 1 AU. However, the simulated density peaks were generally 2 - 4 times greater than observations for the SIRs studied by Jian et al. (2011), though Lee et al. (2009) find that in general WSA/Enlil yields densities similar to the observations at Enlil. Gressl et al. (2014) also compare the MAS/MAS model with these two versions of Enlil and find similar results, again with uncertainties in the time of arrival of a high speed stream of about 1 day.

In this study, we make use of multiple remote and in-situ observations sampling the inner and outer solar system to track two different solar transients. We observe a CME erupting from the Sun and track it through the inner solar system, where it is observed in-situ at Venus, STEREO-B and Mars. A CIR propagating ahead of the CME is observed in these three locations, as well as at Earth. We make use of the Enlil prediction model to estimate the time of arrival of both CIR and ICME and compare with the in-

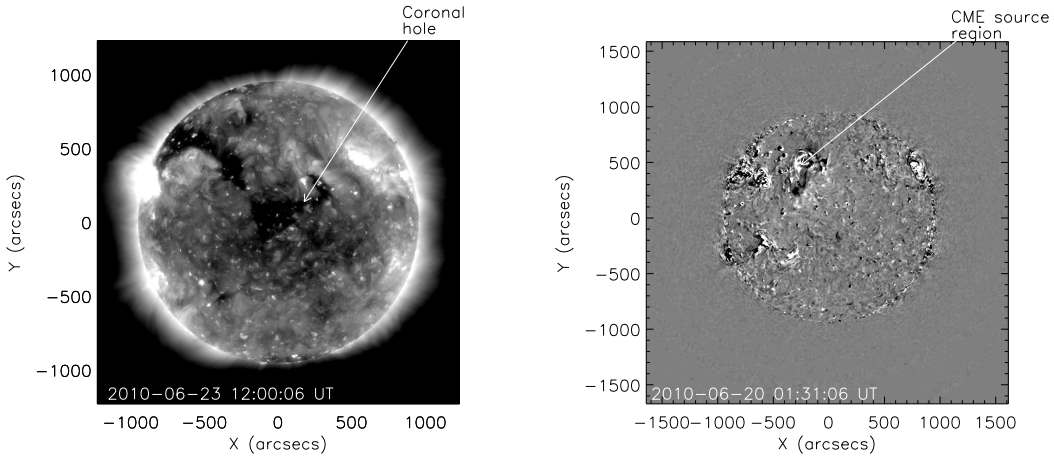

Fig. 4.1: Left panel: AIA/SDO image of the solar disk on 23 June 2010 in the 193 Å passband. The coronal hole labelled is the source of the high speed solar wind stream which causes the CIR. Right panel: Running-difference EUVI-B image at 01:30 UT showing the CME source location.

situ data to make an estimate of the accuracy through the solar system. Enlil results indicate that the ICME catches up with the CIR and merges with it. A strong magnetospheric compression that is consistent with this scenario is subsequently observed at Saturn.

4.2 Observations

4.2.1 Remote Observations

The CME was observed erupting at 01:30 UT on 20 June 2010, on the solar disk by STEREO-B/EUVI (at roughly N30E90), as seen in Figure 4.1, and also on the Eastern limb by SDO/AIA. The CME was seen clearly off the Eastern limb in the SOHO/LASCO-C3 and the STEREO-A/COR-2 coronagraphs, as shown in Figure 4.2. At this time, STEREO-B was 70° behind the Earth and STEREO-A was 74° ahead (see Figure 4.3). From this we can conclude that the CME was directed roughly towards STEREO-B, although it is not visible as a halo CME in STEREO-B coronagraphs. Height-time plots of SOHO/LASCO coronagraph observations give this CME a radial speed of 591 kms^{-1}.

As the ICME is directed towards STEREO-B, it is not observed by the Heliospheric Imagers here (HI-1B and HI-2B), however it is seen by HI-1A and

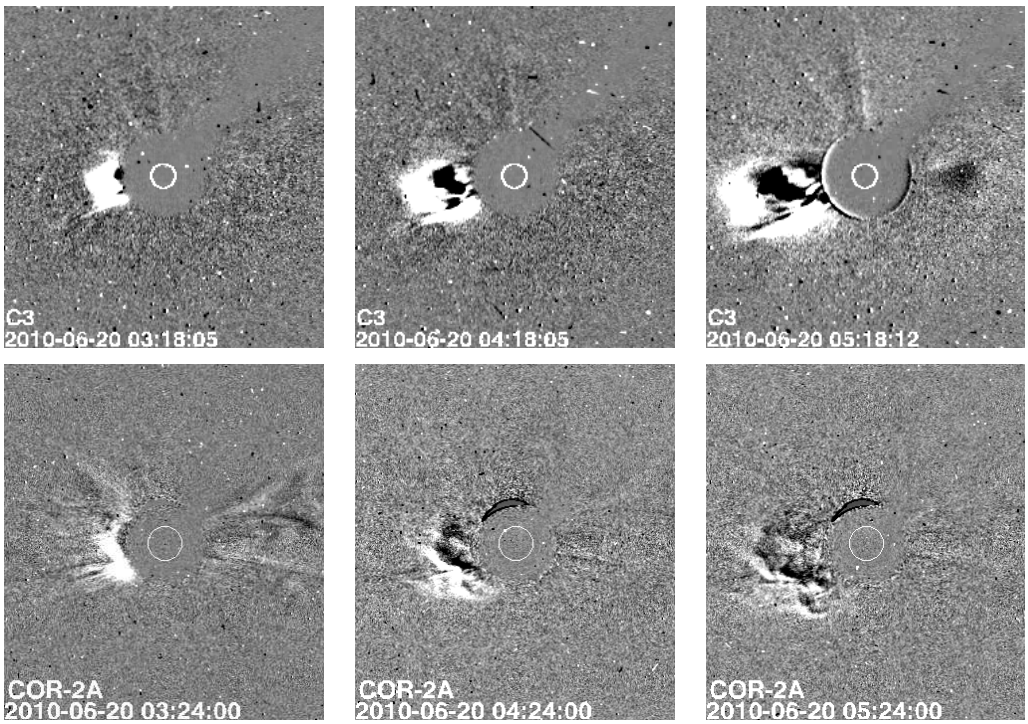

Fig. 4.2: Running difference images from LASCO C3 (top) and STEREO-A/COR-2 (bottom) coronagraphs, showing the eruption of the CME.

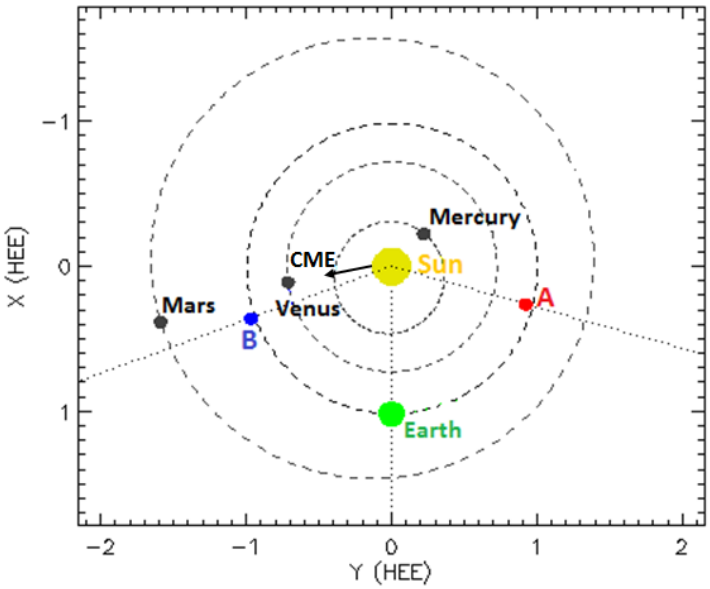

Fig. 4.3: Positions of the inner solar system planets and both STEREO spacecraft on 20 June 2010. The direction of the erupting CME is indicated by the black arrow.

HI-2A on board STEREO-A. The ICME enters the field of view of HI-1A at around 00:49 UT on 21 June and passes over Venus early on 22 June 2010, it then enters the field of view of HI-2A at around 08:09 UT 22 June. LASCO C2 observations showed this CME passing by an earlier, slower CME which is also directed roughly towards STEREO-B, but further southwards. In HI-1A observations it is clear that this ICME is directed far enough below the ecliptic plane that it will not hit any planets and therefore is unlikely to add further complexity to the scenario. It is observed entering the field of view of HI-1A at roughly 15:29 UT 22 June and passes below Venus at roughly 08:49 UT 23 June.

The source of the high speed stream associated with the CIR is a recurrent low latitude coronal hole, shown in Figure 4.1. It is visible on the solar disk as seen from AIA/SDO for several days and is roughly central on 23 June 2010.

4.2.2 Enlil Prediction Modelling

The arrival times of the ICME throughout the solar system were predicted using the Enlil+cone model. For the ambient solar wind, the Enlil model used the WSA coronal model and the input magnetogram from the Mount Wilson Observatory. The input parameters for the cone model of the CME were obtained from the CME Analysis Tool and included a longitude of E84°, a CME width of 27° and a velocity of 628 $\mathrm{km\,s^{-1}}$, which agrees fairly well with the direction and speed of the CME found above.

The Enlil run of the inner solar system (out to 2 AU) for this ICME shows it clearly impact Venus, STEREO-B and Mars, as shown in Figure 4.4. From this the CIR can also be seen passing through prior to the ICME.

An Enlil run of the same ICME in the outer solar system (out to 10 AU) does not show it impacting any of the outer planets. Instead it indicates that the ICME merges with the preceding CIR, beyond the orbit of Mars, and as such does not reach Saturn as an ICME, despite its favourable position (see Figure 4.5). The simulated CIR is predicted to impact Saturn roughly one month later.

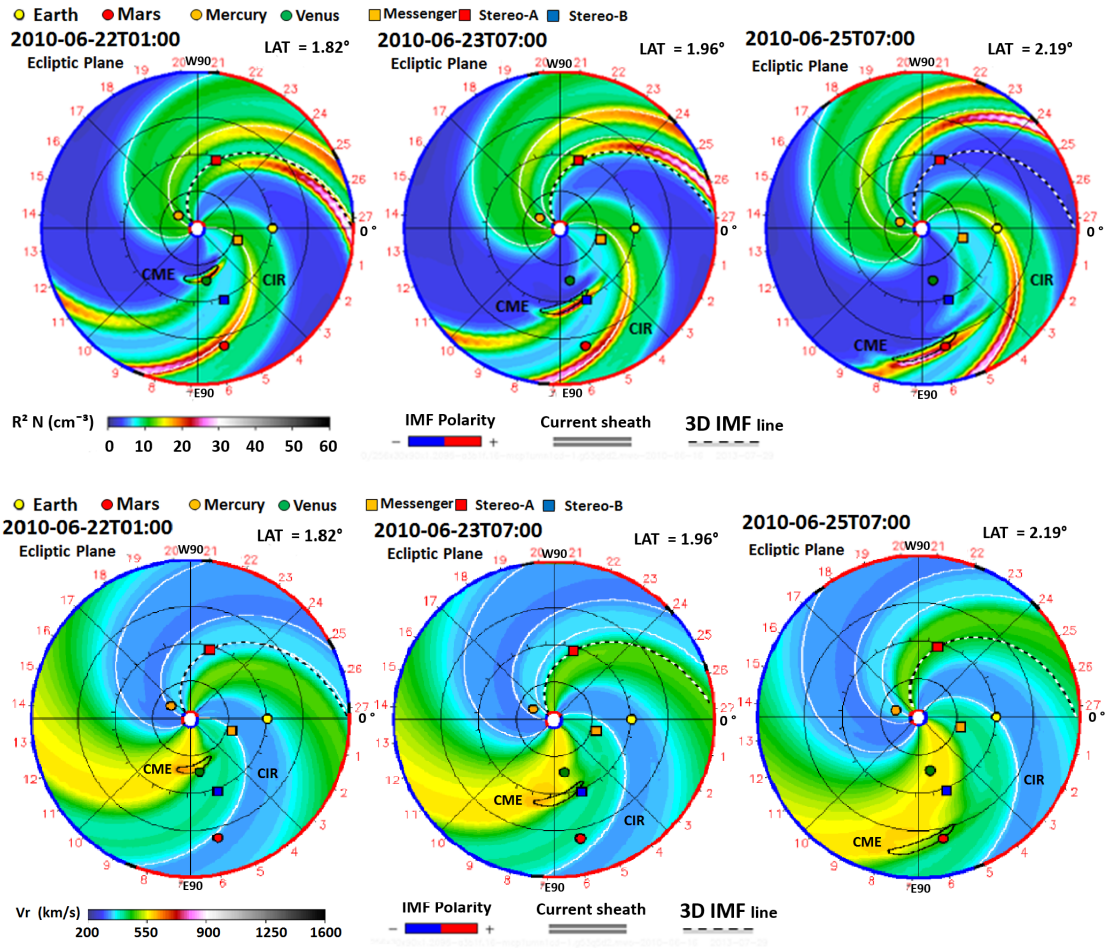

Fig. 4.4: Ecliptic view of the modelled solar wind density (top panel) and solar wind velocity (bottom panel) at three different time steps, indicating the CME arrival at Venus, STEREO-B and Mars. The scales for the density and velocity are given by the colour bars. The locations of Venus, STEREO-B, Mars, and other planets and spacecraft are indicated by the coloured symbols.

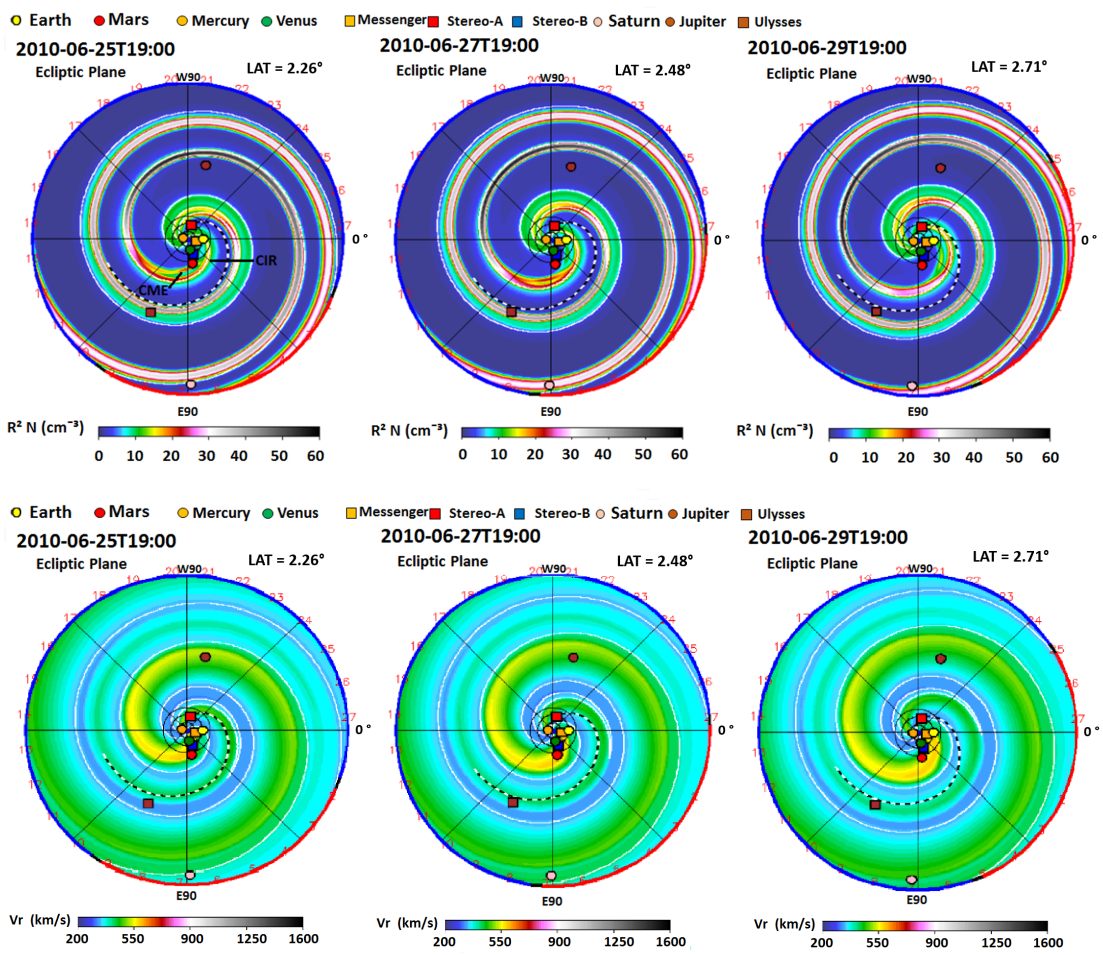

Fig. 4.5: Ecliptic view of the modelled solar wind density (top panel) and solar wind velocity (bottom panel) at three different time steps, showing the CME as it merges with the CIR beyond the orbit of Mars. The scale for the density and velocity are given by the colour bars. The locations of Venus, STEREO-B, Mars, and other planets and spacecraft are indicated by the coloured symbols.

4.2.3 The CIR and ICME at Venus

Both the CIR and the ICME are observed in-situ at Venus. Venus Express has a highly elliptical orbit, spending a short time within the exosphere of the planet. It completes roughly one orbit per day, and its plasma instrument ASPERA-4 is operational for several hours at apoasis and periapsis only. The Venus Express magnetometer is continuously operating, and therefore provides quite a clear indication of the arrival of both CIR and ICME, shown in Figure 4.6, although this identification would be strengthened by additional plasma measurements at Venus. The regular data gaps in the magnetic field data corresponds to when Venus Express is close to the planet, at the periapsis of its elliptical orbit. Venus has no intrinsic magnetic field, but the interaction of its ionosphere with the solar wind creates an 'induced magnetosphere', which has many similar features to a true magnetosphere, including bow shock followed by a magnetosheath region between the solar wind and the ionosphere (Bertucci et al. 2011). This results in sharp peaks in the magnetic field data that have been removed for clarity. The increase in magnetic field corresponding to the arrival of the CIR is slower than these regular spikes and is observed at 02:00 UT on 19 June 2010, with an associated increase in magnetic field variance in each component of the magnetic field. This indicates a compression of the magnetic field. However, this period of compressed magnetic field is very brief (lasting only 9.5 hours), which is much shorter than most CIRs. It is possible that this is due to the limited measurements here, as the CIR has only been identified by its magnetic field compression. If better plasma measurements were available at Venus, they may suggest a longer CIR duration. The Enlil-simulated total magnetic field strength is shown in the fifth panel of Figure 4.6 and shows an increase corresponding to the CIR, although it appears quite small in comparison to the much larger increase predicted for the ICME. This is the opposite of what is seen in the in-situ measurements, which shows the magnetic field magnitude of the CIR to be greater than that of the ICME. In addition, the duration of the ICME predicted by Enlil differs significantly from the in-situ observations, with the observed ICME lasting over three times longer than predicted by Enlil.

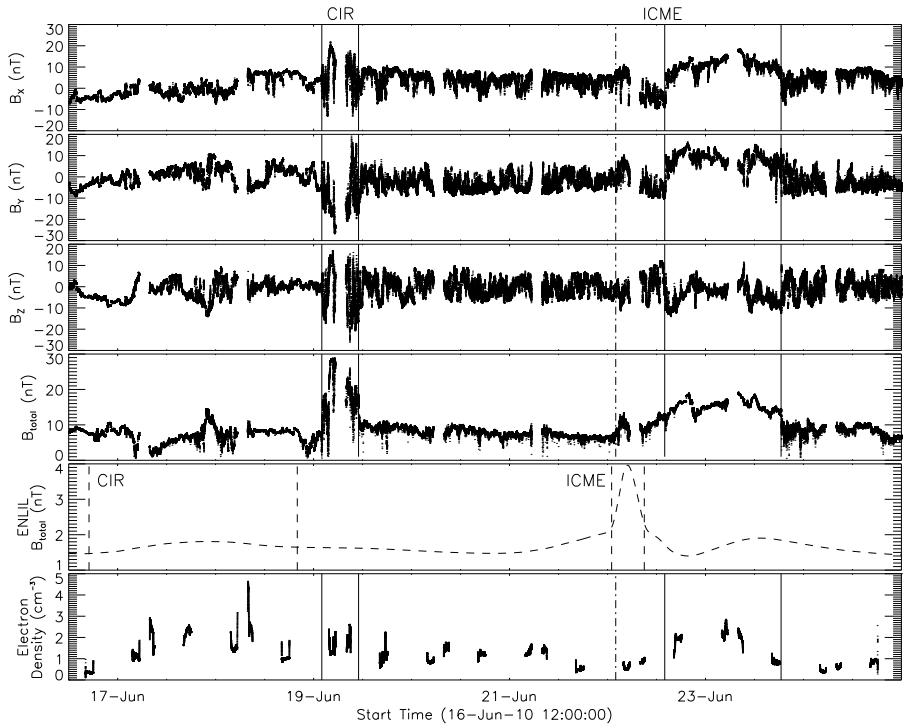

Fig. 4.6: The first four panels show the magnetic field measured by Venus Express in VSO coordinates, where x is positive in the direction of the Sun along the Venus-Sun line, y is in the orbital plane of Venus, positive in the direction opposing orbital motion and z is parallel to the pole of the orbital plane and is positive in the northward direction. The periodic data gaps correspond to when Venus Express is at periapsis, close to the planet, resulting in large spikes in magnetic field which have been removed for clarity. The actual CIR and ICME intervals (02:00 - 11:30 UT 19 June and 14:00 UT 22 June - 18:30 UT 23 June respectively) as suggested by the magnetic field data are indicated by the vertical lines. The fifth panel shows the total magnetic field at Venus as predicted by the Enlil model, with the dashed vertical lines indicating the predicted CIR and ICME intervals (17:00 UT 16 June - 20:00 UT 18 June and 14:00 UT 22 June - 18:80 UT 23 June respectively). The sixth panel shows the electron density as obtained from ASPERA-4 plasma moments.

Figure 4.6 also shows the electron density as calculated from the ELS ASPERA-4 plasma moments for the periods that it was sampling the solar wind. Plasma moments are calculated from the electron particle distribution function by integration and Gaussian fits. These are susceptible to noise, but are able to show large changes and reveal the boundaries between different plasma regions. Further details of their calculation can be found in Fränz et al. (2006). There are considerable data gaps, as the moments are only used when ASPERA-4 is operational in the solar wind (moments for the induced magnetosheath and ionosphere of Venus have been excluded). The first two vertical lines on the bottom panel of Figure 4.6 show the CIR interval suggested by the magnetic field data (when a magnetic field compression occurs), but there doesn't appear to be a significant increase in electron density associated with this period, though it is slightly higher than the period following it. There is some indication of an increase in the electron density prior to the magnetic field compression, which could agree with the suggestion that the CIR duration could be longer here with plasma measurements. However, there is no reason to expect a density increase to precede the magnetic field compression rather than coinciding with it as is usual with CIRs (Jian et al. 2006, 2008).

Figure 4.7 shows the ELS spectrogram for this period, with the CIR arrival marked by the first vertical line, as defined by the magnetic field compression. As stated above, ASPERA-4 collects data twice during an orbit, once high in its orbit (sampling the solar wind), for example from 16:03 to 17:57 UT 18 June, and once lower in the orbit, including the crossing into the induced magnetosheath and the ionosphere and back out again. This second period can be identified by the sudden increase of electron fluxes (e.g at around 05:40 UT 18 June), corresponding to the magnetosheath region of Venus on the inbound pass of Venus Express, followed by the ionosphere with lower electron fluxes and then a period of high electron fluxes again denoting the magnetosheath on the outbound pass of the Venus Express orbit. The figure shows that on the orbit directly following the arrival of the CIR, there is an increase in electron counts in both the solar wind and magnetosheath regions.

The ICME arrival is observed 3.5 days after the CIR (at 14:00 UT 22 June

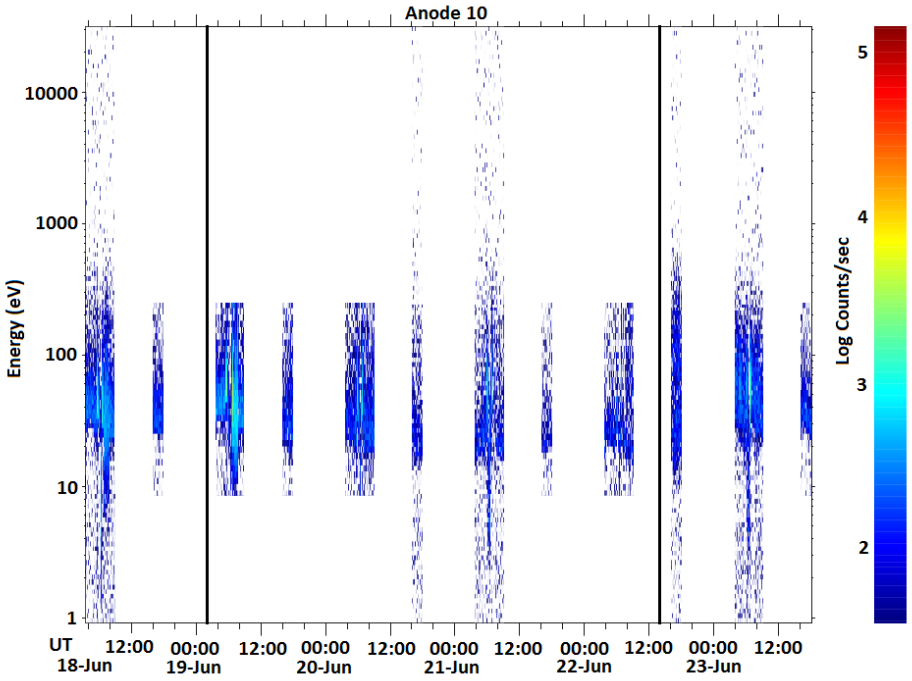

Fig. 4.7: The ELS spectrogram for Venus Express from 18 to 23 June, covering the period when the CIR arrived (first vertical line), and the ICME arrived (second vertical line). Once a day Venus Express reaches periapsis in its orbit, passing through the induced magnetosheath region, into the ionosphere and back out again. This is seen on the spectrogram as two regions of hot, dense electrons (the magnetosheath), bounding the cooler electrons of the ionosphere. There is an increase in the electron count rate in the solar wind and magnetosheath regions in the orbits following the arrival of the CIR and a noticeable increase in electron count rates and energy after the ICME arrival.

2010), as an increase in the total magnetic field and a period of less disturbed magnetic field, in contrast to the magnetic signature of the CIR, which was a compression of the magnetic field. This period of less disturbed magnetic field is defined as the ICME interval, shown by the solid lines. There is also an increase in electron density at this time (shown in the bottom panel of Figure 4.6), though it is possible that this electron density increase could start earlier, but it is difficult to determine with the data gaps. The increase in total magnetic field seems to begin around 12 hours earlier than the period of smoother magnetic field, at 02:00 UT on 22 June (indicated by the dot-dash vertical line), along with fluctuations in specific magnetic field directions. This is possibly a result of a solar wind pile-up region or similar travelling ahead of the ICME ejecta. These timings agree with data from HI-1A, which observed the ICME passing over Venus on 22 June.

ELS/ASPERA-4 spectrograms (see Figure 4.7) suggest an ICME arrival time consistent with the later time of 14:00 UT (second vertical line on Figure 4.7). ASPERA-4 is inactive from 18:01 UT 21 June - 03:49 UT 22 June and from 09:01 - 16:09 UT 22 June, over both 02:00 and 14:00 UT on 22 June. However, there is a noticeable increase in count rates of electrons at 16:09 UT, when the instrument is operating again after a break of 7 hours, but there is no clear difference between 18:01 UT on 21 June and 03:48 UT on 22 June, over the previous data gap, when the solar wind pile-up region possibly arrived.

4.2.4 The CIR and ICME at STEREO-B

At STEREO-B, both the ICME and CIR are observed, a few days after their arrival at Venus. The PLASTIC instrument allows the solar wind plasma to be sampled directly, and the magnetometer on board as part of the IMPACT instrument suite provides information on magnetic field variations, as shown in Figure 4.8. The CIR is observed to arrive at STEREO-B at 09:50 UT on 21 June 2010. As at Venus, the magnetometer observes a compression of the magnetic field, which lasts for around 20 hours at STEREO-B. The plasma properties of the solar wind at STEREO-B show an increase in proton temperature, an increase and then decrease in proton density and total pressure, and a slower increase in solar wind speed. At STEREO-B, there is a small increase

in density prior to the beginning of the CIR (starting early on 21 June), which may explain the possible density increase seen at Venus prior to the magnetic field compression. However, the time of this density increase is not used for the start of the CIR at STEREO-B, as the presence of several other necessary plasma characteristics seen at 09:50 UT gives a strong identification of the CIR at this later time. The Enlil-simulated parameters are also shown in Figure 4.8, but as with the simulated magnetic field strength at Venus, the changes corresponding to the CIR are much smaller in comparison to the ICME. As with the results at Venus, this is generally opposite to what is seen in the in-situ measurements, as the peaks of the ICME are not as high as the CIR in observations. The predicted durations of the ICME and CIR also differ from the observations, with the in-situ measurements showing a CIR duration of roughly 16 hours and an ICME duration of roughly 42 hours, compared with Enlil simulations predicting the opposite: a CIR duration of roughly 55 hours and an ICME duration of roughly 18 hours.

The increase in solar wind speed associated with the CIR continues for almost 2 days, until the arrival of the ICME ejecta at 08:00 UT 23 June. The signatures of this ICME are slightly unusual at STEREO-B. A region of smooth magnetic field is evident in all three components of the magnetic field at this time, but there is no overall increase in the total magnetic field. There is an increase in proton density, not as high as that of the CIR, but little indication of an enhancement of the total pressure. The velocity of the solar wind experiences another sharp increase slightly ahead of the arrival of the ICME, which then declines steadily during CME passage.

Neither the CIR nor the ICME have interplanetary shocks associated with them at STEREO-B. Therefore, any compression region travelling ahead of the ICME ejecta (as is suggested by Figures 4.6 and 4.7) cannot be a sheath region, but could be a pile-up of solar wind or compression region. Despite the evidence for a possible solar wind pile-up region at Venus, this region is not easy to identify in the plasma data at STEREO-B. A compression region or solar wind pile-up region travelling ahead of ICME ejecta would have an increase in density and potentially a compressed magnetic field and

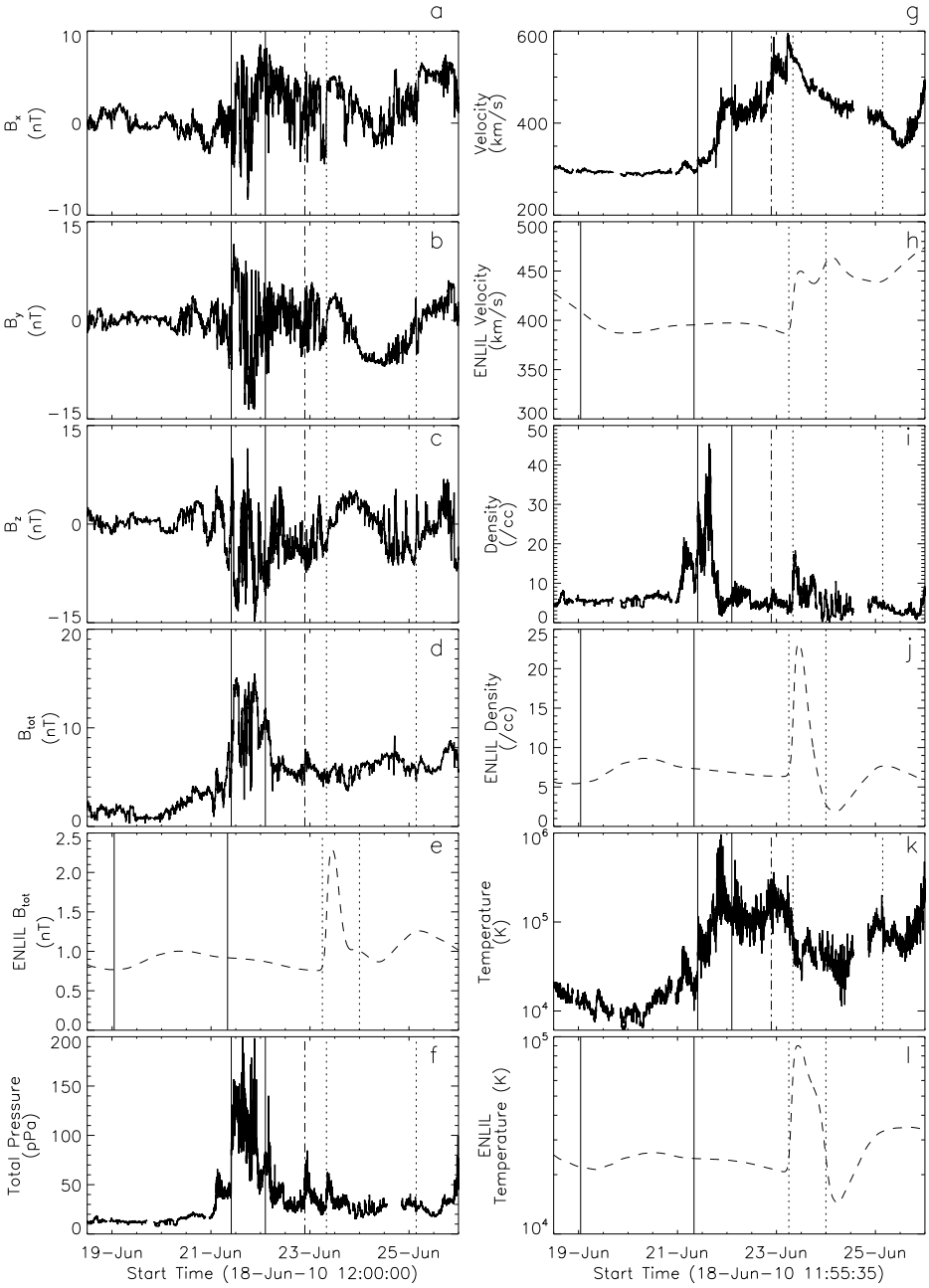

Fig. 4.8: PLASTIC and IMPACT data of the CIR and ICME arrival at STEREO-B and Enlil predictions. The observed and predicted CIR intervals (09:50 UT 21 June - 05:42 UT 22 June and 01:00 UT 19 June - 08:00 UT 21 June respectively) are indicated by the solid vertical lines and the observed and predicted ICME intervals (08:00 UT 23 June - 03:30 UT 25 June and 06:00 UT 23 June - 00:00 UT 24 June respectively) are indicated by the dotted vertical lines. The dot-dash line indicates the start of a possible sheath region ahead of the ICME ejecta.

raised temperature. The best possibility for the beginning of a compression region is marked on Figure 4.8 as the vertical dot-dash line, which lies at 21:30 UT 22 June. There is no significant increase in temperature, magnetic field magnitude or density observed, but there is a discontinuity and a small increase in these factors, and a more significant increase in solar wind velocity at this time. The magnetic field during this period remains disturbed since the earlier passage of the CIR.

4.2.5 The CIR and ICME at Mars

Similar to Venus Express, Mars Express also has an elliptical orbit, but completes 3-4 orbits per day. Its plasma instrument ASPERA-3 is only operational for several hours around periapsis. This fact, along with the lack of a magnetometer on Mars Express, has made detecting the CIR and ICME at Mars much harder than at previous locations. However, there is evidence of the arrival of two solar wind disturbances at Mars, although the timings are less reliable than those found at Venus, STEREO-B and Earth and the identification is much less certain. Plasma moments from ASPERA-3 ELS are shown in Figure 4.9 for the period 22 to 26 June, which encompasses the estimated arrival times of the ICME and CIR as given by Enlil predictions. As with Venus, Mars has no intrinsic magnetic field, but interacts with the solar wind to create an induced magnetosphere similar to that of Venus. As with Figure 4.6, only the moments for when ASPERA-3 is sampling the solar wind are displayed, resulting in large data gaps.

The electron density as found from plasma moments shows two peaks in density, about 1 day apart, which is less than the time between the arrival of the CIR and ICME at STEREO-B ($\sim$2 days). At STEREO-B there is a smaller density peak preceding the start of the CIR, beginning roughly 10 hours earlier. However, it is unlikely that the two peaks in density seen at Mars are associated with these two peaks at STEREO-B (the main CIR and the preceding density increase). The two peaks near the CIR at STEREO-B were closer together than peaks at Mars, and the earlier peak at STEREO-B is lower than the second, opposite to what is seen at Mars. As the calculated plasma moments are susceptible to noise, and only really show broad features,

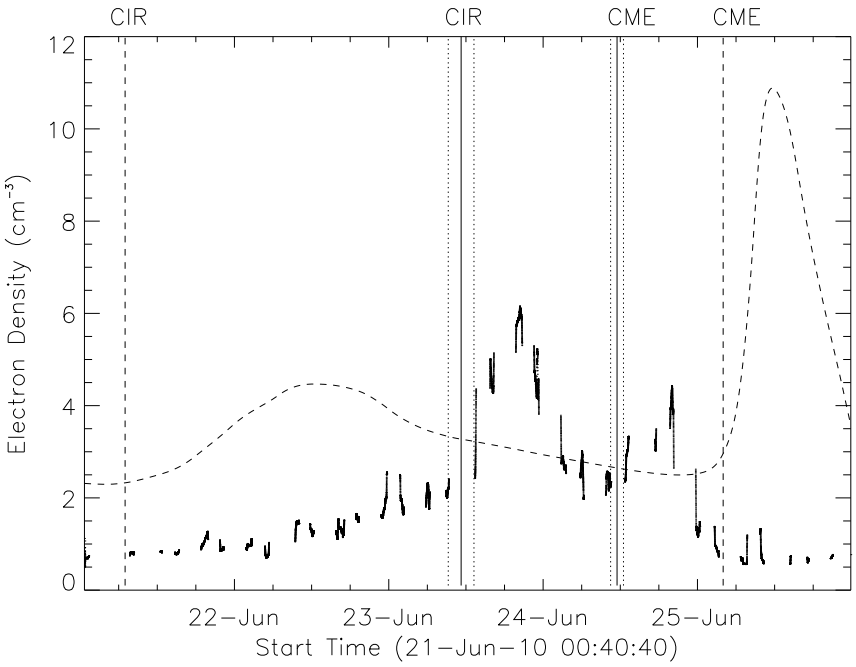

Fig. 4.9: Electron density measured at Mars while Mars Express was in the solar wind. The start time of the CIR and the ICME (11:15±02:00 UT 23 June and 11:30±01:00 UT 24 June respectively) are shown by the solid vertical lines, with the dotted lines indicating the uncertainty of these times. The overplotted dashed line shows the density as predicted by Enlil, with the vertical dashed lines indicating the start times of the CIR and ICME (07:00 UT 21 June ad 04:00 UT 24 June respectively).

it seems more likely that the two density peaks observed at Mars are two distinct structures. The first density peak begins between the second and third orbit of Mars Express on 23 June 2010, which is between 09:16 UT and 13:21 UT. The arrival time of this solar wind disturbance is therefore roughly 11:15±02:00 UT 23 June, with the uncertainty given as the time during which no measurements are taken in the solar wind. The peak in density occurs during the inbound pass of the fourth orbit of 23 June, which is between 19:41 and 20:40 UT (within the solar wind). The second peak begins during the second orbit of 24 June, between 10:30 and 12:40 UT. The arrival of this density peak is therefore given as 11:30±01:00 UT 24 June, around one day after the first. The peak of this density increase occurs during the outbound pass of orbit three of 24 June, corresponding to a time of roughly 20:00 UT 24 June.

The ELS spectrogram of this period is shown in Figure 4.10, with the start times of the two density peaks marked on as vertical lines. Similar to Venus Express spectrograms, each orbit of Mars Express includes a period close to the planet, where it crosses into the induced magnetosheath and ionosphere of the planet. This is visible in the spectrograms as two enhancements in electron count and energy (the magnetosheath), bounding a region of cooler electrons (the ionosphere). Mars Express is only in the solar wind outside of this period. After the arrival of the first density increase (first vertical line) there is a noticeable increase in count rate of the solar wind and magnetosheath region (particularly on the outbound pass), for two orbits, until June 24 (roughly when the first density peak ends), after which the count rate is low again. At around the time of arrival of the second density increase, there is an increase in energy of solar wind electrons and the count rate is also high. The count rate and energy of the magnetosheath region also begin to increase.

The plasma moments and spectrogram data at Mars show the arrival of two solar wind disturbances here, 24 hours apart. As the CIR was previously travelling ahead of the ICME, and the second density peak is lower than the first, as is the case for the CIR and ICME observed at STEREO-B, it is likely that the first density peak corresponds to the CIR and the second to the ICME.

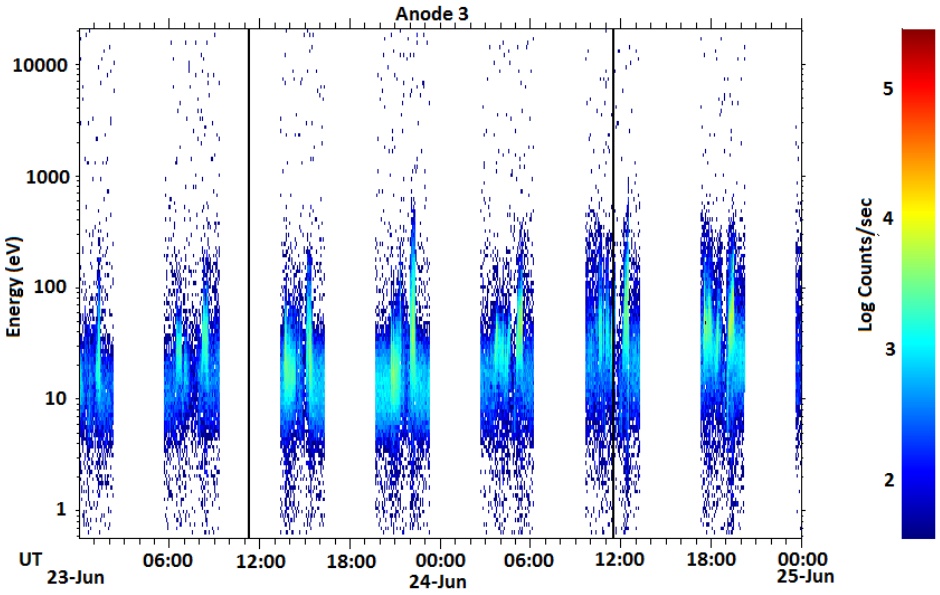

Fig. 4.10: The ELS spectrogram for Mars Express on 23 and 24 June, covering the period when the CIR and ICME are expected to arrive at Mars. The vertical lines indicate the start time of the CIR and ICME found from the start time of the density increases seen in the plasma moments data. Mars Express carries out ∼4 orbits per day, and during the periapsis of each one will pass through the induced magnetosheath of Mars, into the ionosphere and back out through the magnetosheath. This is seen in the spectrogram as two regions of hot dense electrons corresponding to the magnetosheath, and surrounding the cooler electrons of the ionosphere. There is a clear enhancement in the electron count rate after the arrival of the CIR, in both the solar wind and magnetosheath regions and electron energy also begins to increase at around the same time as the ICME arrival.

As there is only 24 hours separating these two peaks in density at Mars, it suggests that the ICME is closely approaching the CIR, as it has between Venus and STEREO-B. Therefore, if these structures merge it will occur not long after the ICME has passed Mars, fairly close to the planet.

4.2.6 The CIR at Earth

The source location of the CME is near the centre of the solar disc observed by STEREO-B (at roughly N30E90), as seen by Figure 4.1. Therefore, as can be seen from Figure 4.3, the CME is not directed towards the Earth and is not detected here. The CIR does impact the Earth almost 2.5 days after it arrives at Mars, and is detected by the ACE spacecraft at L1 as seen in Figure 4.11. The SWEPAM instrument measures the solar wind and observes a jump in plasma density at 21:30 UT 25 June, and an increase in solar wind velocity and temperature several hours later. This is accompanied by a period of compressed magnetic field, similar to what is observed at STEREO-B and Venus, as well as an enhancement of total pressure.

4.2.7 The CIR in the outer solar system

Unlike Venus and Mars, Saturn has a strong intrinsic magnetic field, generating a true magnetosphere, similar in structure to the terrestrial magnetosphere. It can be measured currently by the magnetometer onboard Cassini, which is currently orbiting Saturn. Cassini revolution 135 occurs around a month after the CME eruption on the Sun. The inbound part of the orbit indicates a quiet magnetosphere with regular oscillations (Espinosa and Dougherty 2000, 2001; Espinosa et al. 2003; Giampieri et al. 2006; Andrews et al. 2012), but the outbound pass is much more disturbed, as shown by the magnetometer data in Figure 4.12. On the outbound pass, Cassini first crosses the magnetopause and enters the magnetosheath of Saturn at 21:09 UT 26 July, as indicated by the decreased and disturbed region of magnetic field. For several days following this first magnetopause crossing, Cassini leaves and re-enters the Saturn magnetosheath on multiple occasions, as indicated by the shaded regions of Figure 4.12. The final magnetopause crossing occurs at 16:05 UT on 31 July. These transitions into the magnetosheath are also observed by the electron

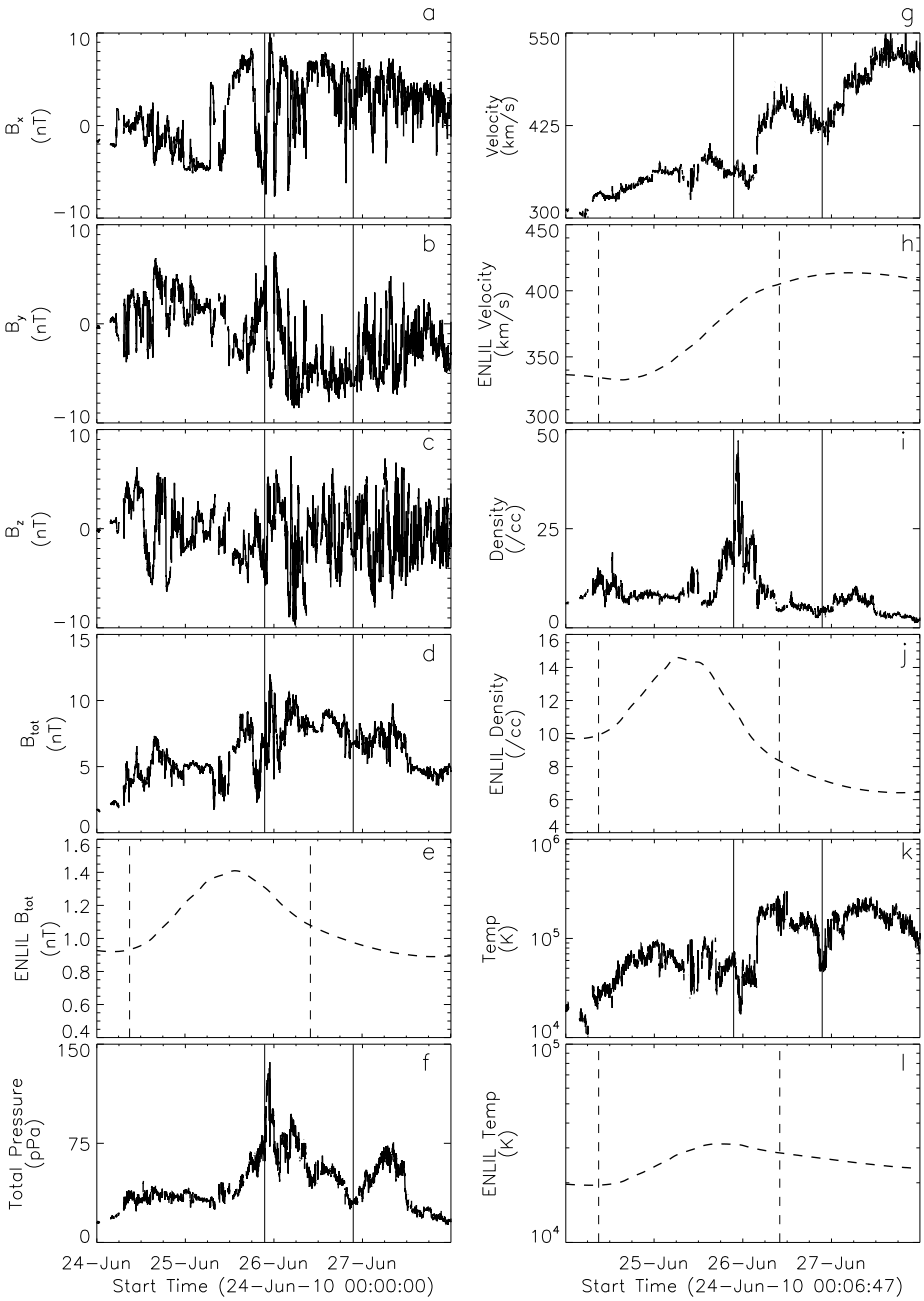

Fig. 4.11: ACE SWEPAM data of the CIR arrival at the Earth and Enlil predictions. The observed CIR interval (21:30 UT 25 June - 21:30 UT 26 June) is indicated by the solid vertical lines and the predicted CIR interval (09:00 UT 24 June - 10:00 UT 26 June) are indicated by the dashed vertical lines.

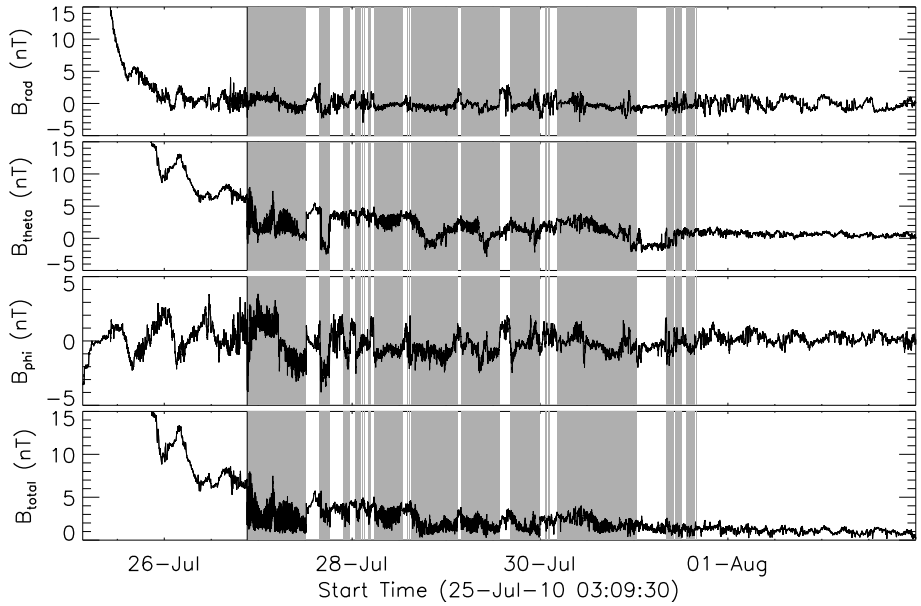

Fig. 4.12: The magnetic field as measured by Cassini in KRTP spherical coordinates, where r points from Saturn to the spacecraft, phi is parallel to Saturn's equator and theta completes the right handed set. The shaded regions indicate the times when Cassini is within the Saturn magnetosheath, with the black vertical line showing the time of the first magnetopause crossing.

spectrometer of the Cassini plasma instrument, CAPS ELS, which sees higher density and lower temperature electrons than in the magnetosphere. These magnetopause crossings are indicative of a compression of the magnetosphere of Saturn, as Cassini has encountered the magnetosheath much closer to the planet than usual. This compression could have begun at some point while Cassini was deep in Saturn's magnetosphere (from roughly 12:00 UT 24 July), and therefore did not detect a change until Cassini was further from the planet (during the outbound pass), or it could have occurred at any point up until the magnetopause crossing (≈21:00 UT 26 July). The Enlil prediction for the arrival of the CIR at Saturn is 02:00 UT 25 July, which falls within this period when a compression of the magnetosphere may have begun.

The location of the magnetopause crossings can be input to a model of the magnetopause in order to obtain an estimate of the solar wind pressure and the magnetopause stand-off distance (most commonly 22 or 27 R_s, where 1 R_s= Saturn radius = 60268 km, (Achilleos et al. 2008)) at this time. The

model described by Arridge et al. (2006) and built on by Kanani et al. (2010) is dependent on the pressure balance across the magnetopause boundary and uses a Newtonian form of the pressure balance equation to obtain estimates of the solar wind dynamic pressure and the stand-off distance of Saturn's magnetopause. Using the first magnetopause crossing on the outbound pass (at 21:09 UT 26 July), an estimate of solar wind dynamic pressure of 0.111 nPa and a stand-off distance of 16.0 R_s were found. The solar wind pressure found here is close to the pressure estimated for the CIR at Saturn as predicted by the Enlil model, 0.107 nPa, which is over six times the normal solar wind pressure at this distance from the Sun. For comparison, this magnetopause model was also run for the magnetopause crossing on the inbound pass of Cassini, which occurs at 07:15 UT on 15 July. This yielded an estimate of the solar wind pressure of 0.016 nPa and an estimate of magnetopause stand-off distances of 23.5 R_s. This confirms that a region of high pressure solar wind, almost seven times higher than the solar wind pressure during the inbound pass, has arrived at Saturn and compressed the magnetosphere significantly, by over 7 R_s . The solar wind pressure and stand-off distance estimated for the final magnetopause crossing on the outbound pass (16:04 UT 31 July) were 0.012 nPa and 25.0 R_s respectively, showing that by this time the region of high pressure solar wind has passed, and the Saturn magnetosphere has relaxed back to a less compressed state.

4.3 Comparison of CIR and CME arrival time predictions

4.3.1 Enlil predictions

The Enlil forecast model has provided predictions of the arrival times of both the CME and the CIR, which can be compared to the observed arrival times. These are shown in Figures 4.6, 4.8, 4.9 and 4.11, where Enlil results are overplotted with a dashed line or plotted on a separate panel, and the timings of the CME and CIR indicated with vertical lines. These timings are summarised in Table 4.1, with the difference between the predicted and detected arrival time given in brackets. Enlil predicts the arrival of the CME within 20 hours

Table 4.1: Summary of CIR and ICME arrival times and predicted arrival times, including Δt of the travelling time from Sun-Venus, Venus-STEREO-B, and STEREO-B-Mars. In brackets is given the difference between the predicted arrival time and the arrival time seen in the data.

Time of arrival	CIR observed	Enlil prediction	prediction from Earth	prediction from ST-B	CME observed	Enlil prediction
Δt (hrs)					60.5	48.5
at Venus (UT)	02:00 19/6	17:00 16/6 (-57h)	01:30 19/6 (-0.5h)	05:30 19/6 (+3.5h)	14:00 22/6	02:00 22/6 (-12h)
Δt (hrs)	56	56			18	28.5
at ST-B (UT)	09:50 21/6	01:00 19/6 (-57h)	02:30 21/6 (-7.5h)		08:00 23/6	06:30 23/6 (-1.5h)
Δt (hrs)	49.5	54			27.5	48.5
at Mars (UT)	11:15±02:00 23/6	07:00 21/6 (-52h)	02:00 23/6 (-9h)	14:30 23/6 (+3.5h)	11:30±01:00 24/6	07:00 25/6 (+19.5h)
Δt (hrs)	27.5	54				
at Earth (UT)	21:30 25/6	09:00 24/6 (-36.5h)		04:30 26/6 (+7h)		
at Saturn (UT)	12:00 24/7 - 21:00 26/7	05:00 25/7				

of the detected arrival. The prediction for the arrival at Mars is the furthest from the observed arrival: 19.5 hours after it is detected by Mars Express. The closest prediction is at STEREO-B, which is 1.5 hours early. The prediction for the CME arrival at Venus is 12 hours early.

The Enlil predictions of CIR arrival all show larger differences to the observed arrival times than the CME predictions, and all predict the arrival of the CIR earlier than it is detected in-situ. The greatest discrepancy is seen for Venus and STEREO-B, both 2 days and 9 hours too early, with the predictions then improving slightly as the CIR propagates. Repeating these predictions using alternative magnetograms or the MAS coronal model with Enlil did not improve the timings found for the CIR arrival.

4.3.2 Travel time predictions

Williams et al. (2011) describe a method to track CIRs through the inner solar system using the speed and arrival time of the CIR detected at one location and extrapolated elsewhere. The travel time between locations, Δt, can be deduced by the simple relation:

$$\Delta t = \frac{\delta r}{V_r} + \frac{\delta \beta}{\omega_{sun}}, \tag{4.1}$$

where δr is the radial distance between the two locations, $\delta\beta$ is the angle of solar longitude between the two locations and ω_{sun} is the equatorial rotation rate of the sun, 14.4° day^{-1}. V_r is the mean velocity of the CIR, calculated from the average of the minimum velocity of the low speed stream and the maximum velocity of the high speed stream. The method assumes that adjacent sources of fast and slow solar wind continue to emit coronal plasma at the same velocities, so that solar wind properties remain constant along a Parker field line. It also assumes that δr and $\delta\beta$ remain constant during the event, which is a reasonable approximation for the inner solar system.

This method to calculate the CIR arrivals was carried out twice; once extrapolating from the CIR detected at Earth, using V_r measured by ACE (411 km s^{-1}) and once extrapolating from STEREO-B, using V_r measured here (396 km s^{-1}). These speeds are comparable to the speed of the slow solar wind, in agreement with Wood et al. (2010). This provides two arrival time predictions for Venus and Mars and one each for STEREO-B and Earth, shown in Table 4.1. This method was not used to calculate the CIR's arrival at Saturn as the angle of solar longitude between each location will change significantly while the CIR propagates out to Saturn's orbit. The predictions of CIR arrival time found using this extrapolation method were all much closer to the observations than those found by the Enlil predictions. The closest prediction for this extrapolation method was found for the arrival of the CIR at Venus, as extrapolated from the Earth, and was only half an hour early. The predicted arrival time at Mars, extrapolated from the Earth, was the furthest from its detected arrival time at nine hours early. As the Earth and Mars are the furthest apart in both longitude and radial distance during this interval,

it is not surprising that this prediction is the least accurate.

4.4 Discussion

In this study, the passage of the CIR and ICME at each location (Venus, STEREO-B, Earth and Mars) is identified and the events are simulated using the Enlil prediction model. In this work, Enlil has not been used to carry out detailed modelling of the characteristics of the CIR and ICME, but its predictions of the arrival times of these events throughout the solar system are compared with observations, and also compaerd to an alternative timing prediction method for the CIR. In the case of the ICME, it is important to note that as Enlil doesn't simulate the internal magnetic field of the CME, what it really models is the solar wind disturbance that lies ahead of any magnetic cloud or ejecta material, which may include a shock, plasma sheath, compression region or solar wind pile-up region, although these cannot be distinguished in the model output. In this case, the ICME does not have an interplanetary shock associated with it (at least at STEREO-B, where the best plasma data are available), and so also cannot have a sheath region which lies behind an interplanetary shock. However, there was some indication of a solar wind pile-up region at Venus (Figure 4.6) and possibly at STEREO-B (Figure 4.8). At Mars, observations were very limited and it was impossible to draw any conclusions about the presence or timing of a solar wind pile-up region associated with the ICME here (4.9). This limitation in the Enlil model does not affect its ability to predict the arrival of a CIR at each location however. Table 4.1 summarises the arrival times of the ICME and CIR at each location and the predicted arrival times for comparison. The arrival times for the ICME at Venus and STEREO-B shown in this table correspond to the clear arrival of the ejecta, rather than any possible solar wind pile-up region, which was only tentatively identified.

Enlil predictions of the arrival times of the CIR show a significant difference to the observed arrival times at each location, with predicted times ranging from 36.5 hours too early (at Earth) to 57 hours too early (at Venus and STEREO-B). However, there is some sign in the electron density found

from plasma moments at Venus, that an increase may have begun some time earlier than the compression of the magnetic field, which would bring the arrival time of the CIR closer to that predicted by Enlil. This discrepancy in predicted arrival times on the order of 1 - 2 days agrees with previous results studying Enlil simulations of SIRs (Jian et al. 2011; Broiles et al. 2013) and large scale solar wind structures (Lee et al. 2009; MacNeice et al. 2011; Gressl et al. 2014). An alternative method to predict the CIR arrival, described by Williams et al. (2011) was also assessed, finding arrival times much closer to those predicted by Enlil. This method was a simple equation based on the co-rotation of the CIR, but relies on data obtained as the CIR reaches one location, to extrapolate the arrival time elsewhere.

In this study, at Venus, STEREO-B and Earth, Enlil significantly underestimates the magnetic field strength by roughly one order of magnitude for the solar wind, including the ICME and CIR. This agrees broadly with the findings of Jian et al. (2011) and Broiles et al. (2013), who also find Enlil substantially underestimates the solar wind magnetic field strength, although by not as much. The simulated temperature is also underestimated by around one order of magnitude, also in agreement with Jian et al. (2011), who find the temperature underestimated by about this much at 5.3 AU. The density simulated by Enlil for the solar wind agrees with the observations fairly well at the Earth and STEREO-B, although it overestimates the peak density for the ICME and underestimates it for the CIR, which disagrees with the findings of Jian et al. (2011), who found that Enlil overestimates the CIR density. At Mars the Enlil-simulated density is overestimated for the solar wind, CIR and ICME. The studies of Lee et al. (2009), Jian et al. (2011) and Broiles et al. (2013) all take place during the declining phase of solar cycle 23, whereas the events studied here occur at the beginning of cycle 24, which could have influenced the difference in the Enlil-simulated values. The duration of the CIR as simulated by Enlil was also overestimated, by roughly a factor of two at STEREO-B and Earth, which also agrees with the findings of Jian et al. (2011), who find CIR duration overestimated by an average factor of $\sim$2 at 1 AU, suggesting that the model cannot simulate enough compression within 1

AU.

The arrival times of the ICME at each location as predicted by Enlil were all closer to the detected arrival times than the CIR predictions, the largest discrepancy being for the arrival of the ICME at Mars. The ICME arrival prediction at Venus and STEREO-B were compared to the observed arrival times for the ICME ejecta given in Table 4.1. By comparing the Enlil predictions to the arrival times of a possible solar wind pile-up region (instead of the ejecta behind it), the prediction for the arrival of the ICME at Venus is much closer to observations, being only one hour earlier than the possible solar wind pile-up region at Venus (02:00 UT 22 June). At STEREO-B however, using the arrival time of the possible solar wind pile-up region for comparison worsens the Enlil prediction here, which is now 9.5 hours too early. The structure of the ICME cannot be identified at Mars, but if the timing used is only the arrival of the ICME ejecta, and a solar wind pile-up region lies ahead of this, then the Enlil prediction for Mars will show an even larger difference to the observations.

By considering the transit times of the ICME between each location in the Enlil model (as shown in Table 4.1), the ICME is seen to be decelerating overall from the initial input speed of 628 $\mathrm{km\,s^{-1}}$. This agrees with previous literature stating that an ICME with an initial speed higher than that of the ambient solar wind ($\sim$400 $\mathrm{km\,s^{-1}}$) will decelerate to roughly this speed (Gopalswamy et al. 2000; Yashiro et al. 2004). Similarly, an ICME travelling in faster ambient solar wind can accelerate nearly up to the speed of the ambient solar wind (Gosling and Riley 1996). Between STEREO-B and Mars the Enlil transit time of this ICME suggests that it has sped up again slightly. In the actual in-situ measurements, the transit times of the ICME between locations differ from Enlil predictions. It takes the ICME approximately 60 hours to reach Venus (a radial distance of $\approx$0.7 AU), 18 hours to travel between Venus and STEREO-B (a radial distance of $\approx$0.3 AU), and a further 28 hours to reach Mars (a radial distance of $\approx$0.6 AU). These locations in the inner solar system are not perfectly aligned, there being 10° in longitude between Venus and STEREO-B and 8° between STEREO-B and Mars. This means that each

location will encounter a different part of the curved ICME front, which will influence the observed arrival time of the ICME. As the ICME appears to be directed towards Venus (see Figure 4.3), STEREO-B will probably encounter the edge of the ICME, and therefore the arrival time of the ICME here will be later than the leading front of the ICME actually reaches 1 AU. This means the transit time of the ICME between Venus and STEREO-B is longer than it would be if these spacecraft were aligned, and similarly, the transit time between STEREO-B and Mars is shorter, as Mars is only 2° away from Venus. However, this cannot account for the overall transit time between Venus and Mars (only 2° apart in longitude), which is 45.5 hours. This gives an average speed of roughly 825 $\mathrm{km\,s^{-1}}$, suggesting that the ICME is accelerating overall. This increase in velocity of the ICME has occurred despite an initial speed which is higher than the ambient solar wind speed and is also true if the possible timings of a solar wind pile-up region at Venus and STEREO-B are used. This unexpected acceleration of the ICME could be due to the effect of the preceding CIR. At STEREO-B, where better plasma data are available, it can be seen that the ICME arrives during a period of high solar wind speed and lower proton density, indicating that the ICME is travelling within the high speed solar wind stream that follows the CIR. This high speed, low density region could be allowing the ICME to accelerate, as the ambient solar wind at this point is at a higher velocity than that of the ICME. The average speed of the ICME during its initial propagation from the Sun to Venus is $\sim$480 $\mathrm{km\,s^{-1}}$, which demonstrates the expected deceleration of an ICME, and at this point the CIR is over three days further ahead of the ICME. It is therefore possible that the ICME propagates normally initially, decelerating as it travels into the slower ambient solar wind, until it approaches the CIR and enters the associated high speed stream, at which point it begins to accelerate. The Enlil model predicts that the CIR would be further ahead of the ICME, so the ICME would decelerate for longer as it propagates through the inner solar system. The ICME simulated by Enlil only begins to show a slight acceleration while propagating between STEREO-B and Mars, when it gets closer to the CIR and its preceding high speed solar wind stream.

The transit times of the CIR between each location are also summarised in Table 4.1. These give a transit time of 56 hours for the CIR to travel from Venus to STEREO-B and 49.5 hours to travel from STEREO-B to Mars, which seems unreasonable for a stable structure such as the CIR. However, the CIR travels in longitude as well as radially, so the fact that these locations are not exactly aligned in the inner solar system contributes significantly to the distance travelled. At this time, STEREO-B lies $\sim$10° ahead of Venus in longitude and $\sim$8° ahead of Mars, meaning that the CIR takes longer to travel from Venus to STEREO-B and shorter to travel from STEREO-B to Mars, than it would do if they were all in line. The equation for the transit time of a CIR, given by Williams et al. (2011) can be used to estimate the effect of this. The time due to the longitudinal propagation of the CIR is equal to the difference in longitude divided by the equatorial rotation rate of the Sun (14.4° day^{-1}). For Venus to STEREO-B, this corresponds to roughly 20 hours and for STEREO-B to Mars, roughly 13 hours. Therefore, if Venus, STEREO-B and Mars were all exactly aligned in the inner solar system, the transit time for the CIR between them would be around 36 hours between Venus and STEREO-B and 63 hours between STEREO-B and Mars, which seems more reasonable.

Figure 4.13 gives a summary of the arrival times of these solar transients at each locations, showing the propagation of the ICME and the CIR throughout the solar system. It is clear from this that the ICME is catching up to the CIR in the inner solar system, as the overall structure of the CIR is slow in the radial direction and the ICME is travelling in the fast solar wind stream. The ICME should reach the CIR at some point beyond the orbit of Mars, before the CIR has reached the Earth (although it should be noted that it is a different part of the CIR which reaches the Earth). This is also evident from the Δt columns in Table 4.1, which show that the ICME is propagating faster than the CIR between each location. At Venus, the time difference between the arrival time of the CIR and CME is 84 hours, decreasing to 46 hours, then 24 hours at STEREO-B and Mars respectively, showing that the ICME is travelling faster than the CIR in the radial direction and will therefore eventually catch up with

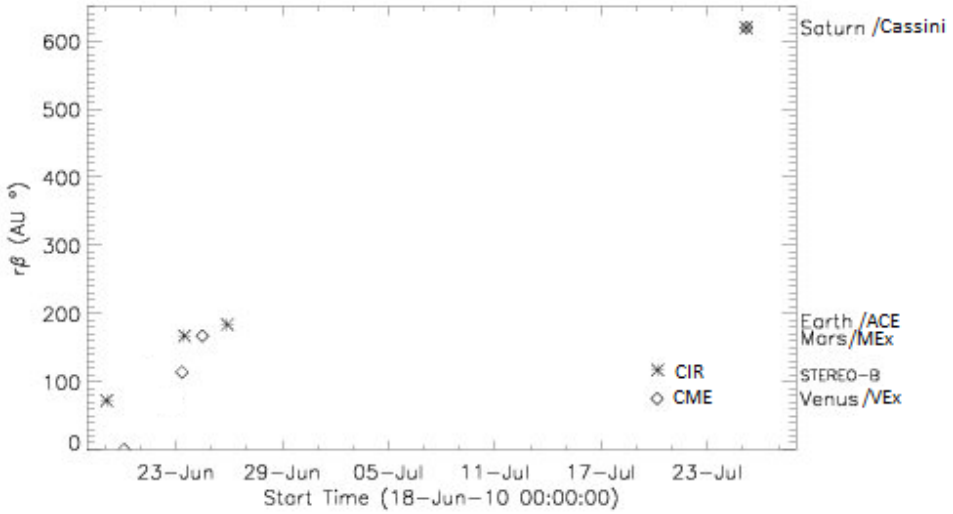

Fig. 4.13: A graphical representation of the timings of the CIR and ICME arrivals at different locations within the solar system, where rβ is the distance from the Sun in AU multiplied by the solar longitude in degrees. The CIR is denoted by the star symbols and the CME by the diamond symbols. The symbol at Saturn indicates that the two solar transients have merged by this point.

it. Enlil simulation of the event indicates that when the ICME encounters the CIR, it merges with it, as shown in Figure 4.5, though as the simulated CIR is further ahead of the ICME, they appear to merge later, after the CIR has passed Earth.

Within the inner solar system neither the CIR or the ICME are associated with shocks, but it is likely that the pressure waves bounding the CIR will have steepened to shocks by the orbit of Saturn, as most CIRs are bounded by shocks beyond 3 AU (Gosling and Pizzo 1999). However, as Cassini is not in the solar wind at this time, there are no plasma data available to identify a shock and this cannot be verified from observations. A pressure pulse could be capable of compressing Saturn's magnetosphere, providing it is strong enough and lasts an adequately long time. Although the CIR and ICME alone are relatively small, it appears that when they merge the resulting structure has either a strong enough pressure pulse, or shocks capable of strongly compressing the Saturn magnetosphere. Our observations also show that the ICME is likely to reach the CIR earlier than predicted by Enlil, as suggested by Figure 4.13, which will also influence the properties of any resulting merged region as

it propagates to Saturn.

While Enlil suggests that the ICME merges with the CIR and does not reach Saturn as a distinct structure, the interaction between these two structures is unlikely to occur exactly as predicted, as the internal magnetic field of the ICME is not simulated. If the ICME does continue to travel through the outer solar system as a separate solar transient, following the interaction with the CIR, it would be very difficult to draw conclusions about its propagation beyond this point. The average ICME speed required for this to arrive while Cassini is deep in the magnetosphere of Saturn (roughly 12:00 UT 24 July to 21:00 UT 26 July), when a magnetosphere compression may have begun, is 480 km s^{-1} or lower. This is somewhat higher than the speed of the slow solar wind, which would be expected as fast ICMEs will decelerate to roughly the speed of the ambient solar wind. However, it is worth noting that this ICME is observed to accelerate during its propagation through the inner solar system, so it is possible that it would have a higher average speed during its propagation out to the orbit of Saturn. This ICME is relatively weak, with a fairly low initial speed and no shock generated in the inner solar system. Despite this, the compression of the magnetosphere at Saturn is fairly strong, moving the magnetopause in by over 7 R_s, so it seems more likely that a stronger, merged structure caused the magnetosphere compression, rather than this ICME alone.

The values of solar wind dynamic pressure and magnetopause stand-off distance found from the magnetopause model of Arridge et al. (2006); Kanani et al. (2010) indicate a strong compression of the Saturn magnetosphere, as the stand-off distance has moved in by 7.5 R_s and the solar wind pressure is seven times higher. Achilleos et al. (2006) and Arridge et al. (2006) both look at several magnetopause crossings associated with a compression of Saturn's magnetosphere, and compare models of the magnetopause at this time. In general, magnetopause stand-off distance is between 15 - 30 R_s and solar wind dynamic pressure is between 0.008 - 0.1 nPa, which implies that the compression seen here is strong by comparison.

4.5 Summary and Conclusions

This study observes two different solar transients, a CIR, followed by a ICME, as they travel through the solar system, with the aim of gaining insight into how they propagate and interact. This section will briefly summarise the work done, before giving the main conclusions of the study.

The ICME erupted from the Sun early on 20 June 2010 and was directed roughly towards STEREO-B. The high speed stream associated with the CIR originates from a persistent coronal hole, visible in the centre of the solar disk as observed from SDO on 23 June. Signatures of these solar transients in plasma and/or magnetic data were observed at Venus, STEREO-B and Mars and the CIR was also observed at the Earth. The in-situ observations do not all yield the same parameters for easy comparison, but the timings of the transients arrivals at multiple locations have been successfully constrained, with some uncertainty (at Mars especially). The ICME does not have an interplanetary shock associated with it in the inner solar system, but a possible solar wind pile-up region was identified ahead of the ICME ejecta arrival at Venus and STEREO-B. The timings of a solar wind pile-up region are better compared to the Enlil predictions than the ejecta, as Enlil does not model the flux rope structure of an ICME. These arrival times in the inner solar system, along with Enlil simulation of the events, indicates that the ICME eventually reaches the preceding CIR and merges with it beyond the orbit of Mars.

As Enlil doesn't simulate the internal magnetic field of the ICME and with actual ambient solar wind conditions likely to be different to those simulated by Enlil, the properties of this merged interaction region cannot be determined. However, a compression of Saturn's magnetosphere is observed about a month later, consistent with when Enlil predicts the merged region would arrive. Modelling of the magnetopause of Saturn at this time suggests that this was a fairly strong compression, pushing the stand-off distance in to 16.0 R_s.

The Enlil simulation of these events was not used to carry out detailed modelling of these events, but to predict their arrival times at multiple locations for comparison with the observations. It was found that the predictions for the ICME were closer to the observed arrival times (all within 36 hours)

than those found for the CIR, which tended to be roughly 2 days early. The arrival of the CIR was better predicted using the method described by Williams et al. (2011), which extrapolates the arrival time between locations based on the average velocity measured. However, this method is limited by its need for velocity measurements of the CIR at one location before predicting the arrival at another. The Enlil predictions of the ICME arrival time show the ICME slowing down, as expected from a fast ICME propagating through slower ambient solar wind, whereas the observed arrival times indicate that the ICME is accelerating.

The main conclusions of this work included insights into the behaviour of the two solar transients studied, as well as some further understanding into the limitations and strengths of the Enlil prediction code, which is used extensively for space weather forecasting. This work demonstrates that the ICME observed here accelerates in the high speed stream of the CIR travelling ahead of it. Enlil simulations of this event predict the arrival of the ICME at different locations fairly well, but generally predicts the arrival of the CIR much earlier than it is observed. Therefore in the simulation, the CIR and associated HSS are further ahead of the ICME, so the model fails to simulate the observed acceleration. The Enlil simulation also suggested that the two transients observed in the inner solar system eventually merge and impact Saturn, causing the compression of the magnetosphere seen here. This demonstrates that relatively weak solar transients, like this fairly slow ICME, can merge and interact with other structures as it propagates, creating a resulting structure that can cause significant impacts further out in the solar system. These conclusions emphasise the need for accurate simulation of the background solar wind and other solar transients in order to correctly model propagating ICMEs and their possible consequences. The direction and speed of an ICME can change significantly due to interactions with other ICMEs and CIRs, and such interactions can lead to merged structures that could have greater impacts than the initial ICME.

Chapter 5

A Comparison of Solar Wind Observations at 1 AU with Simulation Results from ENLIL with Different Input Parameters

In this chapter, the Enlil solar wind model is assessed in more detail, by comparing the simulation results to in-situ observations at 1 AU from ACE and STEREO. The observations roughly cover two Carrington rotations, 2102 and 2103, running from 3 October 2010 to 2 December 2010. The performance of the model is also studied with various different input parameters, including changing the input magnetogram, the coronal model and the model resolution.

5.1 Introduction

While ICMEs tend to be the cause of some of the most significant space weather effects, the evolution of the ambient solar wind is still very important. Not only does this affect the propagation of an ICME, but large scale structures within the solar wind, such as SIRs or CIRs, can also impact and influence the Earth.

Stream interaction regions (SIRs) are associated with the high speed solar wind streams that originate from coronal holes and therefore rotate as the Sun does, sweeping out large areas of longitude. If this region persists for multiple solar rotations they become known as co-rotating interaction regions

(CIRs) (Gosling and Pizzo 1999). Coronal holes become more frequent at lower latitudes during the declining phase of the solar cycle, so during this time in particular CIRs can be very long-lived, stable structures in the solar system.

There have been many studies into the evolution of SIRs, making use of multi-spacecraft observations, at different heliocentric distances. This includes observations at Helios and Voyager (at this time located between 0.3 - 1.0 AU and 1.2 - 2.5 AU respectively (Gonzalez-Esparza et al. 2013)), Venus (Jian et al. 2008; Williams et al. 2011) and Earth, and Ulysses (Jian et al. 2011; Broiles et al. 2013). There have been fewer multi-spacecraft observations making use of the STEREO spacecraft, both lying at a heliocentric distance of $\sim$1 AU. However, Jian et al. (2013) have carried out a statistical survey of solar events detected at STEREO, including SIRs, and find that from a minimum longitude separation of 25°, SIRs can be absent from one spacecraft when observed at the other, indicating that solar sources of SIRs can change within one solar rotation.

Models that accurately simulate the background solar wind are important tools for space weather forecasting. The Enlil heliospheric model is one such predictive model, which is described extensively in Chapter 2. It is a 3D MHD model that can have multiple different input options. The stationary solar wind solution can take its input at the inner boundary from one of two coronal models: the Wang-Sheeley-Arge (WSA) (Arge and Pizzo 2000; Arge et al. 2003, 2004) or Magnetohydrodynamic Algorithm outside a Sphere (MAS) model (Riley et al. 2001; Riley et al. 2006). The inner boundary of this model makes use of synoptic maps derived from daily full-disk magnetograms from a number of possible sources. The magnetogram sources available on the CCMC runs-on-request service (http://ccmc.gsfc.nasa.gov/models/modelinfo.php?model=ENLIL) are the Kitt Peak Observatory, the Mount Wilson Observatory and the GONG observatory magnetogram source. Another Enlil run option provided by CCMC is to change the model resolution. The default setting of the simulation uses a spatial grid of 256x30x90, where 256 is the number of equally spread grid

points in the radial direction (from 0.1 - 2 AU), 30 is the number of equally spread grid points in latitude (perpendicular to the equatorial plane, in the range ±60°) and 90 is the number of equally spaced grid points in longitude (between 0° and 360°). Two higher resolution options are also available. In addition to simulating the background solar wind, Enlil can include the addition of the cone model, which inserts a density cloud into the ambient solar wind to simulate the propagation of an ICME.

The performance of Enlil in simulating the ambient solar wind has been extensively studied, including comparisons of different input magnetograms and coronal models. Several studies, e.g. Gressl et al. (2014) and Lee et al. (2009), report that the Enlil model performance can significantly vary between Carrington rotations, with the model able to simulate some Carrington rotations better than others. Both of these studies compare the performance of Enlil coupled with WSA and MAS coronal models to in-situ data observed at ACE. They find that in general, the overall structure of the solar wind is simulated by both models, although the arrival time uncertainty for large scale solar wind structures can be on the order of a day or two. Gressl et al. (2014) find the WSA/Enlil model gives slightly better arrival times (with typical uncertainties of up to 1 day) in comparison to the MAS/Enlil model (with typical arrival time uncertainties of 0.5 - 1.5 days). Jian et al. (2011) also study the behaviour of SIRs compared to Enlil simulations, at 1 AU and 5.3 AU and also find that timing predictions can be out by ∼1 day, although Enlil is generally able to simulate the occurrence and main features of SIRs and sector boundaries. While comparing MAS and WSA coronal models they find that MAS shows more pronounced differences between the fast and slow solar wind for velocity, temperature and magnetic field strength. MAS also predicts a shorter duration of the fast wind than WSA, leading to later predictions for SIR arrival time.

Jian et al. (2011) and Gressl et al. (2014) also study the impact of changing the magnetogram source used as an input to the Enlil results. They both find that changing the magnetogram source can significantly modify the simulation results produced by Enlil, for the arrival times of SIRs and magnitude

of the solar wind parameters, though it is not clear which magnetogram performs the best. There has been little work considering the impact of changing the resolution of the Enlil model, though Jian et al. (2011) speculate that improving the resolution of the Enlil model will reduce discrepancies between observations and simulation results. Taktakishvili et al. (2010) study the effect of the Enlil model resolution on the arrival time and resulting magnetopause stand-off distance from a CME when using the cone model addition to the Enlil code. They compare the default (lower) resolution option with two identical runs of higher resolution (in this earlier version of the model, 512x30x90 and 1024x30x90). In this instance, increasing the model resolution shifted the arrival time prediction earlier, increasing the error in arrival time, so if the initial prediction was late, the arrival time error would improve with increasing model resolution. Increasing the model resolution did not impact the magnetopause stand-off distance.

In this study, the ambient solar wind conditions at three locations at 1 AU are considered over two Carrington rotations in 2010. These in-situ measurements are compared with multiple Enlil simulations with different input conditions. This included varying the coronal model coupled to the Enlil heliospheric model (WSA and MAS), varying the input magnetogram sources (Kitt Peak, Mount Wilson and GONG), and varying the model resolution (256x30x90, 512x60x180 and 1024x120x360).

5.2 Observations and model runs

5.2.1 In-situ Observations

The ambient solar wind conditions were observed over Carrington rotations CR2102 (3 - 30 October 2010) and CR2103 (30 October - 26 November). In-situ measurements were taken at three different locations at 1 AU, using ACE and the STEREO spacecraft. At the beginning of this observing period, STEREO-A was 83° ahead of the Earth and STEREO-B was 78° behind the Earth, shown in Figure 5.1. By the end of this period they are close to quadrature, with STEREO-A 85° ahead of the Earth and STEREO-B 84° behind. The in-situ observations were taken using the identical IMPACT instruments

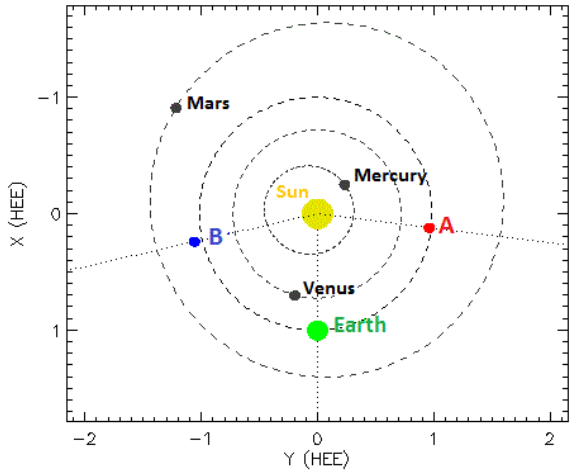

Fig. 5.1: The positions of the STEREO spacecraft and planets within the inner solar system on 3 October 2010.

onboard the STEREO spacecraft and the SWEPAM instrument and magnetometer onboard ACE.

A number of SIRs were identified at the three spacecraft during this period, as shown by Figures 5.2, 5.3 and 5.4. These figures show the observed solar wind conditions at each location during this period, using data from STEREO/IMPACT, ACE/MAG and ACE/SWEPAM. There were seven SIRs identified in the data at ACE, six at STEREO-B and five at STEREO-A. This implies that not all the SIRs were observed at all three locations, which is more likely while the STEREO spacecraft have a separation wider than $\sim 25^{\circ}$ (Jian et al. 2013). These SIRs are identified by a minimum of five of the following signatures: an increase and then decrease in density, velocity deflections, an increase in velocity, a pile-up of total pressure, an increase in entropy, an increase in proton temperature and a compression of the magnetic field. In Figures 5.2 - 5.4 these observed SIRs are shown bounded by solid vertical lines and numbered above the plots. On these Figures, the dashed line shows the Enlil-simulated solar wind conditions over the same period. This Enlil run uses the Kitt Peak magnetogram source, the WSA coronal model, and the default, lowest resolution option. For each SIR observed in the solar wind data, an attempt has been made to also identify them in the Enlil-simulated data. These are shown in the Figures as the shaded areas and also distinguished by

the numbering above the plots. Any additional SIRs in the simulated solar wind data, that do not correspond to observed SIRs, have not been labelled, or shaded out.

Identifying the same SIRs at multiple locations is not always obvious, but some have been distinguished. As these SIRs were all detected close to 1 AU, the propagation of the structure between each location was predominantly longitudinal. This means the speed is determined by the rotation of the Sun, namely $\approx 14.4^{\circ}$ day^{-1}. Using the known spacecraft separations during this period, it should take around 5 - 6 days for a SIR to propagate between STEREO-B and ACE and between ACE and STEREO-A, then a further 13 - 14 days to travel from STEREO-A to STEREO-B.

The first SIR observed at STEREO-B (labelled 1) corresponds to the first SIR observed at ACE, but this region does not persist to STEREO-A. It is seen in Figure 5.2, beginning at 08:00 UT 5 October with an increase in total magnetic field strength, density and total pressure and an enhancement of the proton temperature. The stream interface itself occurs at the peak in total pressure, also accompanied by the beginning of an increase in velocity. The end boundary of the SIR occurs at 16:00 UT 9 October, and is seen as the decrease in total pressure, density, temperature and magnetic field strength. SIR 1 is seen in Figure 5.3, beginning at 05:30 UT 10 October and ending at 16:00 12 October. The SIR begins with a clear increase in total pressure, magnetic field strength and density, reaching a maximum at the stream interface, at roughly the same time that the velocity begins to increase, the density begins to decrease and a stronger temperature enhancement occurs. The end of the SIR is accompanied by the decrease magnetic field strength and total pressure.

The first SIR at STEREO-A (labelled 2) appears to stand alone, with no corresponding SIRs at other locations. It begins at 22:00 UT 19 October with an increase in total pressure, density, magnetic field and velocity. The stream interface at the maximum if total pressure is accompanied by an enhancement in temperature and a sharp decrease in density. The SIR ends as the total pressure and magnetic field strength decrease, at 18:00 UT 21 October, as seen in Figure 5.4.

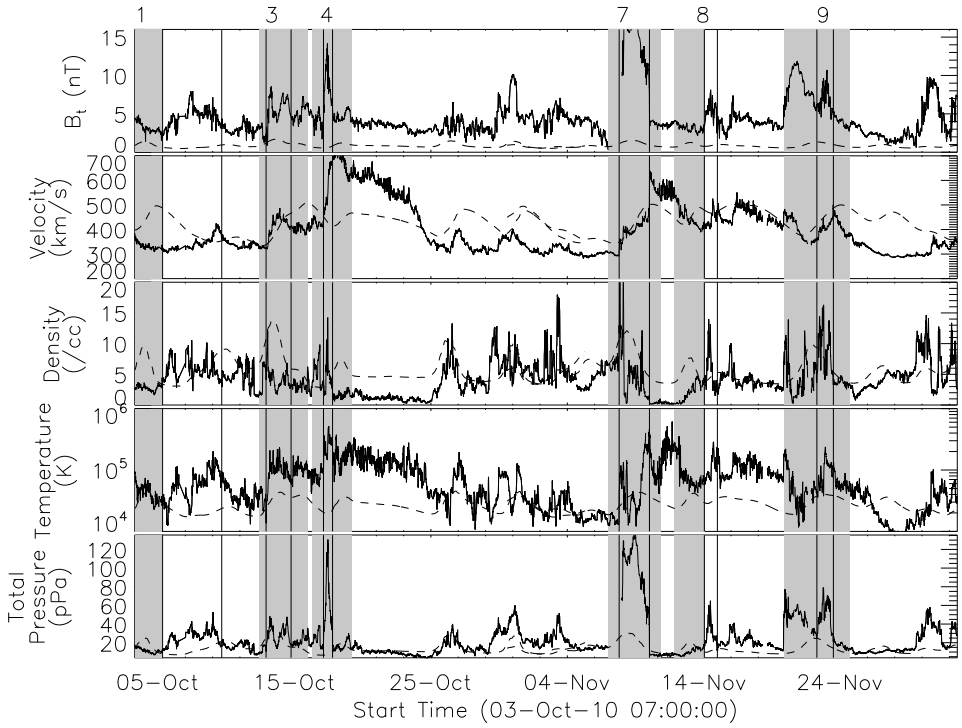

Fig. 5.2: In-situ measurements at STEREO-B for both Carrington rotations (CR2102 and CR2103) (solid line) compared with Enlil results for the same period (dashed line) using the Kitt Peak magnetogram source, WSA coronal model and lowest resolution option. From top to bottom the panels show total magnetic field strength, solar wind velocity, proton density, proton temperature and total pressure. The SIRs during this period are numbered, with observed SIRs bounded by solid lines and the equivalent simulated SIRs shaded in grey.

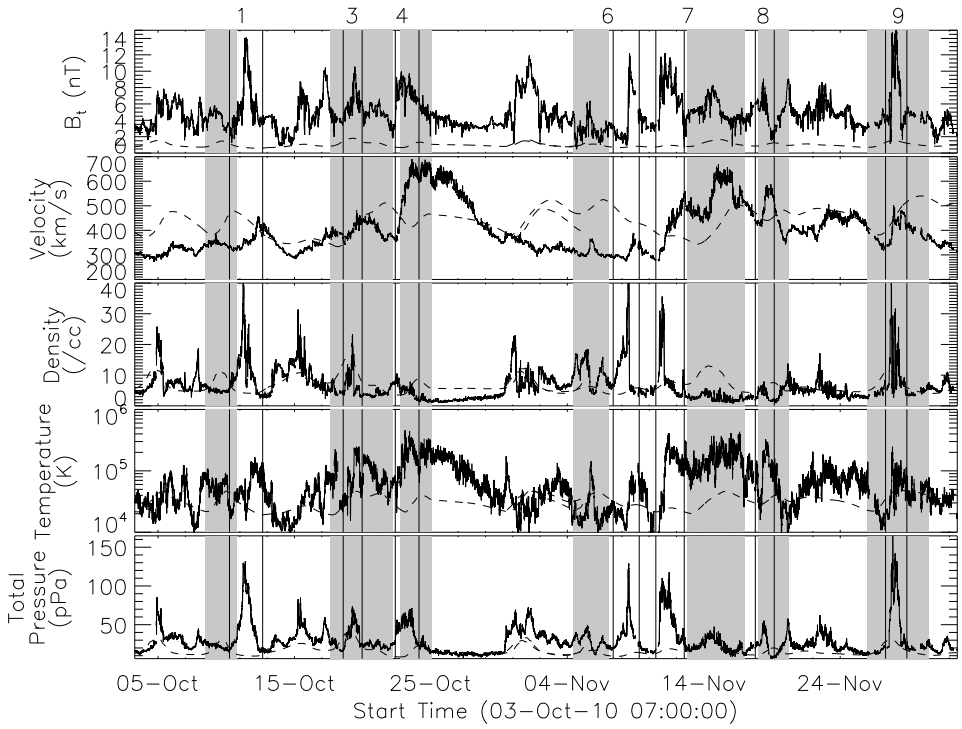

Fig. 5.3: In-situ measurements at ACE for both Carrington rotations (CR2102 and CR2103) (solid line) compared with Enlil results for the same period (dashed line) using the Kitt Peak magnetogram source, WSA coronal model and lowest resolution option. The panels are laid out as for Figure 5.2.

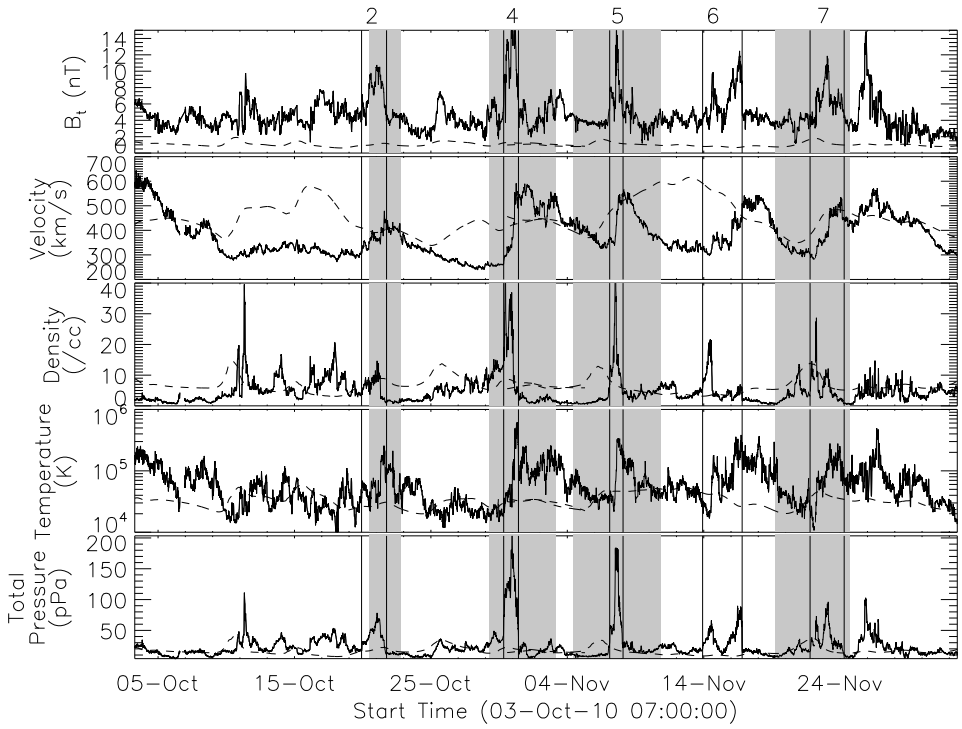

Fig. 5.4: In-situ measurements at STEREO-A for both Carrington rotations (CR2102 and CR2103) (solid line) compared with Enlil results for the same period (dashed line) using the Kitt Peak magnetogram source, WSA coronal model and lowest resolution option. The panels are laid out as for Figure 5.2.

The second SIR at STEREO-B (labelled SIR 3) is also seen at ACE, but not at STEREO-A, as with SIR 1. It starts at 22:00 UT 12 October, with an increase in total magnetic field strength, total pressure, velocity and temperature, as seen in Figure 5.2. The stream interface is not as clear in this SIR, as there is a dip in total pressure in the middle, but the end of the SIR occurs at 18:00 UT 14 October with a decrease in total pressure, total magnetic field strength, temperature and density. In Figure 5.3 at ACE, SIR 3 begins as an increase in all the parameters shown at 13:30 UT 18 October. The stream interface is clearer here, seen at the maximum of total pressure accompanied by a stronger enhancement in temperature and the beginning of the decrease in density. The end boundary of the SIR occurs at 23:00 UT 19 October, seen as a decrease in total magnetic field strength and total pressure.

SIR 4 is the third SIR observed at STEREO-B and ACE, and likely to be the second SIR observed at STEREO-A, although it arrives here slightly later than expected. At STEREO-B (Figure 5.2) it begins at 03:00 UT 17 October with an increase in all parameters shown in the figure. The stream interface occurs at the peak in total pressure, at which point there is also a stronger temperature enhancement and density begins to decrease, which continues to the end of the SIR at 19:00 UT 17 October. The end of the SIR is also defined by the decrease in total pressure and magnetic field. At ACE, SIR 4 begins at 09:30 UT 22 October with an increase in all parameters, seen in Figure 5.3. The stream interface is not as obvious here, as the peak in total pressure is not as sharp, but the end of the SIR is seen at 03:00 UT 24 October, as a decrease in the total pressure, density and magnetic field strength. At STEREO-A (shown in Figure 5.4) SIR 4 begins at 08:00 UT 30 October and ends at 10:00 UT 31 October, seen with similar properties as it was at STEREO-B.

The third SIR observed at STEREO-A is SIR 5, which is not observed prior to this point. It begins at 02:30 UT 7 November, with increases in total pressure, magnetic field and density, shown in Figure 5.4. The stream interface occurs at the peak in total pressure, accompanied by a decrease in density, a temperature enhancement and the beginning of the increase in velocity. SIR 5 ends at 07:00 UT 8 November, seen as a decrease in the total pressure, total

magnetic field strength and density.

SIR 6 is identified first at ACE, and subsequently at STEREO-A. In Figure 5.3, the SIR is seen to start at 08:30 UT 7 November with an increase in density and total pressure. The stream interface at the peak in total pressure is accompanied by an increase in total magnetic field strength and the beginning of a velocity increase, a temperature enhancement and the beginning of a density decrease. The end boundary of SIR 6 at ACE occurs at 06:30 UT 9 November, seen as a decrease in total pressure and magnetic field strength. At STEREO-A, SIR 6 arrives at 22:00 UT 13 November, seen as an increase in magnetic field strength, total pressure and density. The stream interface is less clear here, again because there is a dip in total pressure (as with SIR 3 at STEREO-B), but one of the peaks in total pressure does correspond to a temperature enhancement and the beginning of a density decrease and velocity increase. The end boundary of the SIR is seen as a decrease in total pressure and magnetic field, at 19:30 UT 16 November, as seen in Figure 5.4.

The fourth SIR seen at STEREO-B (SIR 7) is potentially identified at both other locations as well, as the fifth SIR at ACE and at STEREO-A. At STEREO-B it is seen in Figure 5.2 as an increase in all the parameters shown, starting at 19:00 UT 7 November. Again, there is a double peak in the total pressure, but the highest peak is likely to be the stream interface and is accompanied by a stronger temperature enhancement and the beginning of the density decrease. The end boundary of SIR 7 at STEREO-B is seen as a decrease in the density, total pressure and magnetic field, at 00:30 UT 10 November. This SIR at ACE arrives slightly earlier than expected, which could be due to the arrival of SIR 6 closely preceding it. It is observed beginning at 11:30 UT 10 November, with an increase in magnetic field, density and total pressure, as seen in Figure 5.3. At the stream interface, the total pressure reaches a maximum, the velocity begins to increase, there is a temperature enhancement and the density begins to decrease until the end of the SIR at 13:30 UT 12 November, where the total pressure and magnetic field also decrease. At STEREO-A SIR 7 begins at 19:00 UT 21 November and ends at 07:00 UT 24 November, seen in Figure 5.4, with properties similar to those

seen for SIR 7 at ACE.

SIR 8 is the fifth SIR identified at STEREO-B and the sixth at ACE. In Figure 5.2, the SIR is seen to begin at 01:00 UT 14 November, as an increase in density, total magnetic field and total pressure. The stream interface at the peak in total pressure also corresponds to a temperature enhancement, and the beginning of the density decrease and velocity increase. The SIR ends as the total pressure and magnetic field strength decrease, at 00:00 UT 15 November. At ACE, SIR 8 begins at 18:30 UT 17 November and ends at 04:00 UT 19 November, with the solar wind conditions showing similar trends to those seen for this SIR at STEREO-B (see Figure 5.3). It is not observed at STEREO-A, but it is likely that this is SIR 4, having persisted to the next solar rotation.

The final SIR seen at STEREO-B (SIR 9), is also identified at ACE, but not at STEREO-A (it would arrive here after this period of observations). This is believed to be SIR 5, having persisted to the next solar rotation. It begins at 07:00 UT 22 November at STEREO-B (see Figure 5.2), with an increase in total magnetic field strength, total pressure, density and velocity. The stream interface at the maximum of the total pressure is accompanied by a temperature enhancement and a density decrease until the end of the SIR, where the total pressure and magnetic field also decrease, at 12:00 UT 23 November. SIR 9 arrives at ACE at 08:00 UT 27 November as an increase in total magnetic field, density and total pressure, ending at 21:30 UT 28 November with a corresponding decrease in these parameters. The stream interface occurs at the peak in total pressure, along with the beginning of the velocity increase, a temperature enhancement and the beginning of the density decrease (see Figure 5.3).

A number of solar wind parameters were compared for the SIRs, summarised in Table 5.1. The table also gives the percentage errors between the observed values and Enlil-simulated values, for the reference Enlil run (described and discussed in section 5.2.2). The parameters compared were the SIR start time, SIR duration, peak value of total pressure, peak value of solar wind speed, peak value of total magnetic field strength, peak proton den-

sity and maximum temperature. The total pressure is equal to the magnetic pressure ($B^2/2\mu_0$), plus the thermal pressure (nk_BT) (Russell et al. 2005). The beginning and end of the SIRs are defined as explained above, but in general follow the duration of the pile-up of total pressure. The maximum values of total pressure, velocity, magnetic field strength, density and temperature within these periods are those defined in Table 5.1. For the seven SIRs that were observed at more than one location (all but SIR 2 and 5), the solar wind parameters were seen to vary quite substantially between different spacecraft. Most solar wind parameters demonstrated no consistent trend as the SIRs propagated between spacecraft, though the majority of SIRs show an increasing magnetic field and temperature as they propagate. The parameter showing the greatest difference overall between spacecraft observing the same SIR was the density, while the velocity shows the smallest variation between spacecraft.

5.2.2 Enlil runs

The Enlil model can be run for each Carrington rotation, with each run lasting slightly longer than the Carrington rotation. The runs for CR2102 last from 07:00 UT 3 October 2010 to 07:00 UT 5 November 2010 and the runs for CR2103 cover the period 14:00 UT 30 October 2010 to 14:00 UT 2 December 2010. The in-situ measurements have therefore been extended slightly beyond CR2102 and CR2103 to include the entire period simulated by Enlil.

In total, 11 different Enlil runs are considered in this study, with various different input parameters chosen for comparison. The basic model run, used as a reference to compare against, used the Kitt Peak observatory magnetogram source, with the WSA coronal model and the lowest resolution option (256x30x90). This was run for both Carrington rotations. To compare the two available coronal models, both Carrington rotations were run again with the Kitt Peak magnetogram source and lowest resolution option, but with the MAS coronal model. Both Carrington rotations were run twice more with the WSA coronal model and Kitt Peak magnetogram source, this time changing the resolution to 512x60x180 and 1024x120x360. To compare different magnetogram sources, further runs were requested for both Carrington rota-

Table 5.1: The in-situ parameters for all SIRs and the percentage errors between the observations and the Enlil model. Negative values mean the model has overestimated that parameter, a negative time difference means the simulated SIR arrives before the observations. The parameters given are maximum total pressure, P_t, maximum total magnetic field, B_t, maximum solar wind velocity, v_{max}, maximum solar wind density, n_{max}, maximum temperature, T_{max}, duration of SIR and start time of SIR.

	SIR 1		SIR 2	SIR 3		SIR 4		
	ST-B	ACE	ST-A	ST-B	ACE	ST-B	ACE	ST-A
P_t (pPa)	53.0	132	78.4	48.4	73.7	131	71.6	203
Enlil % error	52.9	76.9	71.7	26.1	44.1	85.7	68.7	89.1
B_t (nT)	7.93	14.1	10.8	8.58	10.6	14.2	10.0	18.5
Enlil % error	82.4	89.6	88.9	79.9	82.8	91.5	86.7	93.1
v_{max} (kms^{-1})	425	457	479	487	484	699	690	591
Enlil % error	-17.0	-4.61	15.0	-4.61	-5.89	33.2	32.4	26.0
n_{max} (cm^{-3})	10.6	45.8	14.6	12.1	23.3	14.2	10.5	46.5
Enlil % error	11.8	74.9	39.2	-13.8	32.8	48.5	17.7	81.1
T_{max} (MK)	0.201	0.166	0.257	0.235	0.248	0.520	0.458	0.624
Enlil % error	77.0	71.7	88.0	81.5	81.3	92.8	91.2	94.6
Duration (hrs)	104	58.5	44	44	33.5	16	33.5	26
Enlil % error	54.8	6.84	-25.0	-95.5	-184	-144	-64.2	-169
Start time	08:00	05:30	22:00	22:00	13:30	03:00	09:30	08:00
	5/10	10/10	19/10	12/10	18/10	17/10	22/10	30/10
Enlil difference (hrs)	-49	-41.5	14.5	-12.5	-23	11.5	9.5	-24.5

	SIR 5	SIR 6		SIR 7			SIR 8		SIR 9	
	ST-A	ACE	ST-A	ST-B	ACE	ST-A	ST-B	ACE	ST-B	ACE
P_t (pPa)	184	130	89.7	136	118	96.3	64.9	55.3	79.1	165
Enlil % error	81.5	87.1		77.0	71.9	61.8	68.4	63.8	68.2	81.3
B_t (nT)	15.7	12.2	12.5	17.6	12.2	11.9	8.12	9.08	10.7	15.6
Enlil % error	89.4	91.0		91.1	86.6	84.8	84.4	86.3	87.6	90.1
v_{max} (kms^{-1})	549	389	502	594	550	535	525	588	501	503
Enlil % error	-8.78	-34.9		15.4	8.45	9.49	6.77	17.8	0.136	-7.42
n_{max} (cm^{-3})	58.6	48.7	21.7	26.2	35.6	28.7	14.0	7.96	16.3	42.1
Enlil % error	78.0	87.2		53.8	63.5	51.6	44.9	4.79	39.9	72.7
T_{max} (MK)	0.337	0.135	0.384	0.777	0.411	0.279	0.287	0.327	0.238	0.247
Enlil % error	84.7	66.7		94.4	88.7	83.4	85.4	87.5	83.1	80.0
Duration (hrs)	23.5	46	69.5	53.5	50	60	23	33.5	29	37.5
Enlil % error	-560	-34.8		-73.8	-101	-118	-135	-61.2	-298	-189
Start time	02:30	08:30	22:00	19:00	11:30	19:00	01:00	18:30	07:00	08:00
	7/11	7/11	13/11	7/11	10/11	21/11	14/11	17/11	22/11	27/11
Enlil difference (hrs)	-64.5	-70.5		-19	55.5	-61	-53	9.5	-57.5	-27

tions using the WSA coronal model and the lowest resolution option, for the GONG observatory magnetogram source and the Mount Wilson observatory magnetogram source. However, the Mount Wilson observatory magnetogram for CR2102 was considered to have bad data according to the WSA model, so only returned the run for CR2103.

It was sometimes not easy to identify which simulated SIRs corresponded to each specific SIR observed in-situ. The SIRs were identified mainly by their timings (the closest appearing simulated SIR to a real SIR was taken to be its equivalent). Where possible, attempting to follow a simulated SIR to different spacecraft helped to decide upon which SIR it was. For example, if it was not clear which of two simulated SIRs corresponded to one observed SIR, following both to other spacecraft where it was clearer which SIR they simulated could be used to assume this same SIR is the one seen in the previous location.

In most instances, Enlil was able to simulate the SIRs, although none of the SIRs in CR2102 (1 - 4) were simulated using the Mount Wilson magnetogram source. In addition to this, SIR 2 was unable to be identified in the Enlil simulation using the GONG magnetogram source. There were also problems identifying SIR 6 at STEREO-A for a number of Enlil runs, including the basic model run used for comparison (using the Kitt Peak magnetogram source with the WSA coronal model and lowest resolution option). There was also no clear signal for this SIR at STEREO-A observed for the two higher resolution runs, or the GONG observatory magnetogram source. As well as these issues, the earliest instance of an SIR (SIR 1 at STEREO-B) appears to arrive even earlier for all Enlil runs, so the beginning of the SIR is not simulated for this SIR here in all the model runs, although the actual stream interface (peak of total pressure) is observed. In addition, many of the SIRs that were observed in-situ at only one or two locations, were modelled at more locations by Enlil. This was the case for SIRs 1 and 3, which were observed only at STEREO-B and ACE, but were simulated by Enlil at STEREO-A as well and SIRs 2 and 5, which were only observed in-situ at STEREO-A, but were seen in the model at STEREO-B and ACE prior to this.

The Enlil run that was used for reference and comparison (using the Kitt

Peak magnetogram, WSA coronal model and lowest resolution option) simulates a number of SIRs, not all of which correspond to the in-situ measurements. The results from this Enlil run are also shown on Figures 5.2, 5.3 and 5.4, where the shaded regions depict the simulated SIRs that correspond to the observed ones. At STEREO-B, this Enlil run simulated an additional four SIRs (two per Carrington rotation), in addition to the six observed here in-situ. The additional SIRs are seen in the simulations at around 25 October, 30 October, 15 November (although this was a small one) and 25 November. At Earth, an extra two SIRs were simulated in addition to the seven observed here, at roughly 4 October and 30 October. At STEREO-A this Enlil run also simulates an additional three SIRs, on ∼9 October, 14 October and 24 October. In particular the in-situ measurements show a period of around 20 days at STEREO-B and 15 days at ACE in the middle of these observations where no SIRs are observed, but this gap is not accurately simulated by this Enlil run, which shows one SIR here at ACE and two at STEREO-B.

Table 5.1 summarises the observed solar wind parameters for these SIRs and the percentage errors between these observations and the values simulated by this reference Enlil model run (apart from the start time, where the absolute difference in hours is given). For the percentage errors, if the value in the table is negative/positive, the simulation has overestimated/underestimated that parameter. When comparing the values of the SIRs simulated by this reference Enlil model run to the observations, for all SIRs Enlil underestimates the total magnetic field, temperature, and therefore also the total pressure. The percentage difference between the simulated and observed total pressure averaged over all SIRs at all locations was 69%. The simulated magnetic field strengths were underestimated by more than the total pressure, but the closest and furthest modelled value to the observations occurred for the same SIR and location as the total pressure. The difference between simulated and observed peak magnetic field strengths varied between 80% and 93% lower (see table 5.1). The underestimation of the peak temperature was of a similar order, with the percentage error averaged over all SIRs and locations being 84% lower. The density was also almost always underestimated by the Enlil

model, with quite a range of percentage errors (between 5% and 87%). The only exception was the simulated peak density for SIR 3 at STEREO-B, which overestimated the density by 14%.

In general, this Enlil run significantly overestimates the duration of every SIR. The exception to this is SIR 1, which is underestimated both at STEREO-B and ACE, as shown in table 5.1. At STEREO-B the simulation run does not catch the beginning of the SIR, so it is not surprising that the duration is underestimated here, but that doesn't explain the underestimation at ACE as well. The duration of all other SIRs were overestimated, usually more than double the observed duration. The simulated velocity was not consistently overestimated or underestimated across all SIRs and locations for this Enlil run. All the simulated peak velocities were closer to observations than most other parameters simulated by Enlil, which the percentage error between simulated and observed values ranging between 5% and 35%.

The simulated SIRs from this Enlil run arrived earlier than the observed SIRs more often than they arrived late, as seen in Table 5.1. SIR 1 is predicted to arrive ∼2 days earlier at both locations than it is observed (STEREO-B and ACE). SIR 3 also arrives early at both of these locations, but not by as much (12.5 and 23 hours at STEREO-B and ACE respectively). SIR 2 (observed at STEREO-A only) is one of the SIRs that is predicted to arrive late, by 14.5 hours. SIR 5 is observed at STEREO-A only and is predicted by Enlil to arrive over two days early. SIR 6 is observed in-situ at ACE and STEREO-A, but was difficult to identify in the Enlil simulation and could not be identified at all in the simulation at STEREO-A. At ACE this SIR is predicted to arrive early by almost three days. SIR 9 is predicted by Enlil to arrive early at both locations (by 57.5 and 27 hours at STEREO-B and ACE respectively). A number of the SIRs that are observed at more than one location do not show consistent behaviour across these locations. SIR 4 is predicted to arrive around 10 hours late at STEREO-B and ACE, but then about a day early at STEREO-A. As previously noted, SIR 4 does appear to arrive at STEREO-A slightly later than expected, which could contribute to this fact. SIR 7, which is also observed in-situ at all three locations, is predicted to arrive early at

STEREO-B (by 19 hours), late at ACE (by 55.5 hours) and early at STEREO-A (by 61 hours). Again, as noted above, SIR 7 is observed to arrive at ACE earlier than expected, which may explain the disparity with the simulation. SIR 8 is observed at two locations, but predicted to arrive over 2 days early at STEREO-B, and almost 10 hours late at ACE.

The in-situ measurements showed large differences in solar wind conditions for the same SIRs observed at different spacecraft, with no clear trend between them. The simulated parameters for this run show similar behaviour, although the differences between spacecraft are all smaller than those seen in-situ. As with the in-situ measurements, there does not appear to be much of a trend in how the simulated solar wind parameters vary as the SIRs propagate between different spacecraft, though all parameters were more likely to increase than decrease. In particular, the duration and peak density of the simulated SIRs increased as they propagated in all but one SIR (SIR 9 for duration and SIR 8 for density).

5.3 Comparison of Enlil Runs

As described above, several different Enlil runs were carried out, using different input parameters. This included three different magnetogram sources (Kitt Peak, GONG and Mount Wilson), two different coronal models (WSA and MAS) and three different resolution options (256x30x90, 512x60x180 and 1024x120x360). These runs were all compared against the reference Enlil run which used the Kitt Peak magnetogram source, the WSA coronal model and the lowest resolution option.

5.3.1 Comparison of Magnetogram Sources

There are three different options of magnetogram sources available for input into the Enlil simulation. For this observation period, the Mount Wilson magnetogram source was unable to be run with the WSA coronal model for CR2102, so only SIRs 5 - 9 were able to be simulated with this magnetogram source. The reference model, using the Kitt Peak magnetogram source, WSA coronal model and the lowest resolution option, was unable to simulate SIR 6 at STEREO-A and this was also the case for the Enlil run using the GONG

magnetogram source. However, the run using the Mount Wilson magnetogram source does see a SIR here at around this time, although it was small. In addition to this, the run using GONG was unable to simulate SIR 2 (observed in-situ at STEREO-A), which means that a comparison of the different magnetogram sources for this SIR was impossible.

The same seven parameters studied above are used to compare between these Enlil runs (the peak values of total pressure, total magnetic field, velocity, density, temperature, SIR duration and SIR start time). The differences between these simulated values and the observations are summarised by Figure 5.5. The dashed lines represent the case where the simulated values equal observations, the black points represent simulated values for the run using the Kitt Peak magnetogram source, the green points represent the GONG magnetogram source and the red points the Mount Wilson magnetogram source.

As with the reference model, both alternative magnetogram sources underestimated the total pressure peak of all SIRs at all locations, but there is no one magnetogram source that performs the best for all the SIRs. The difference between the observed and simulated values of total pressure was smallest for each SIR for different magnetograms, but each single SIR did have one magnetogram that gave the best estimate of total pressure at all locations it was observed (the best magnetogram source for each SIR did not vary across the spacecraft it was observed). The Kitt Peak magnetogram source performed best for SIRs 1 - 3, Mount Wilson for SIRs 5, 6, 8 and 9 and the GONG magnetogram source performed best for SIRs 4 and 7. The difference between observed values and those simulated using the Mount Wilson magnetogram source were always smaller than those simulated by Kitt Peak (the SIRs that Kitt Peak performs best for does not have a Mount Wilson simulation for comparison), but GONG simulated values could be better or worse than either of the other magnetogram sources. Averaged over all the SIRs and spacecraft, the percentage errors between observed and simulated values of the total pressure were similar for the three magnetogram sources. The GONG magnetogram source had the lowest average percentage error, with an average of 66%, followed by the Mount Wilson magnetogram source with an

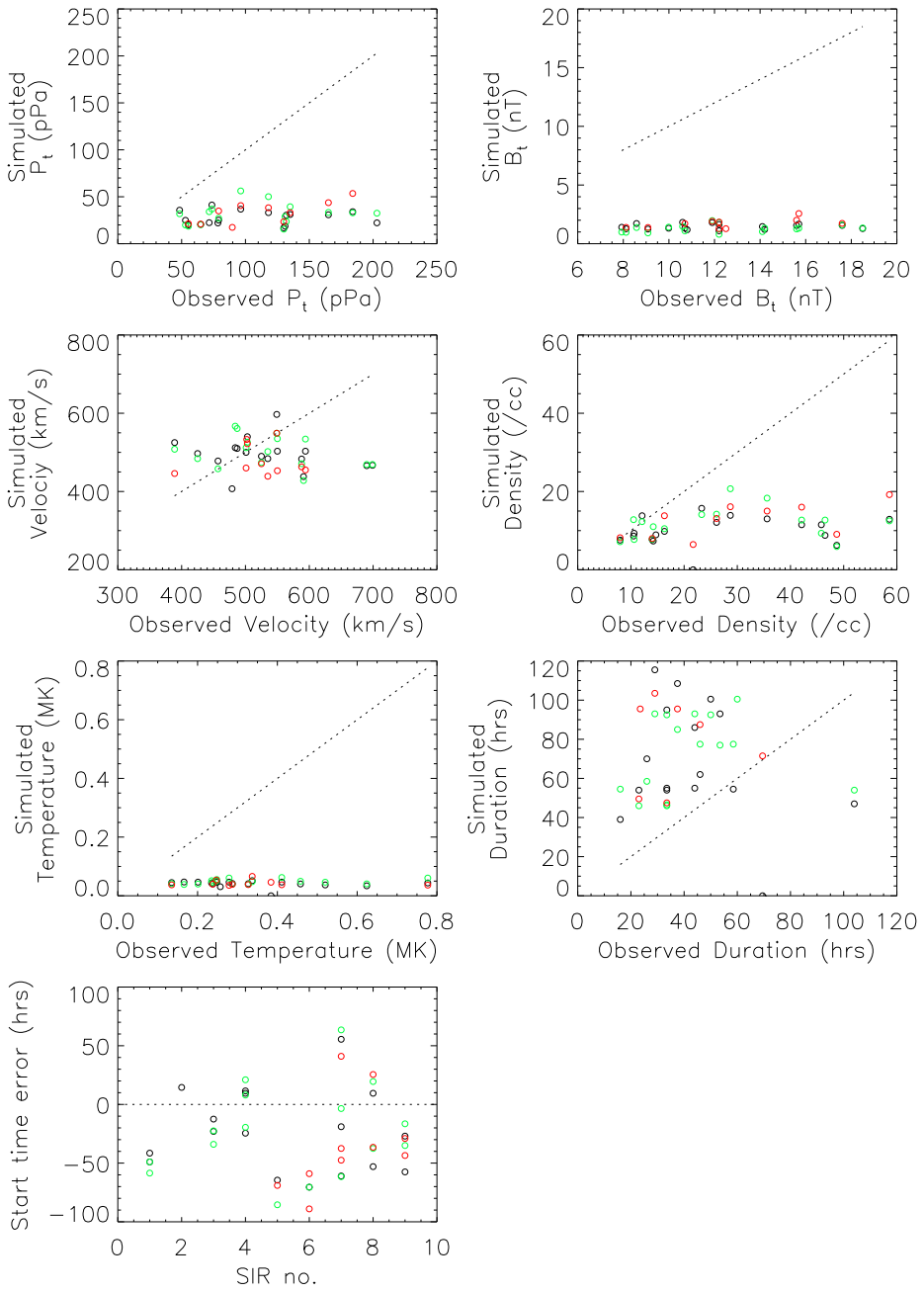

Fig. 5.5: Comparison of the solar wind parameters listed in Table 5.1 for Enlil runs using different magnetogram sources as an input. The dashed line corresponds to the case that the values simulated by the models are consistent with the observations. The black points are the values for the reference Enlil model (using the Kitt Peak magnetogram source), the green points are the values for the Enlil run using the GONG magnetogram source and the red points are the values for the Enlil run using the Mount Wilson magnetogram source.

average percentage error of 68%, then the reference model, using the Kitt Peak magnetogram source had the highest average error of 69%.

The total magnetic field is also consistently underestimated by all magnetogram sources, and shows the same trend as the total pressure. In almost all SIRs at all locations, the best performing SIR for the magnetic field strength was the same as for the total pressure. The percentage errors between simulated and observed values of total magnetic field strength were always higher than for the total pressure. Averaging over all SIRs and spacecraft, the Enlil run using the Mount Wilson magnetogram source had overall the lowest percentage errors between simulated and observed values of total magnetic field (86%), compared to 87% for the Kitt Peak magnetogram and 89% for the GONG magnetogram.

As with the reference model using the Kitt Peak magnetogram source, the Enlil runs for the other magnetogram sources also underestimate the peak temperature of every SIR at every location. For most SIRs, there was a single magnetogram source that gave the closest simulated value to the observed temperature, but this was only the same as the best magnetogram for total pressure and magnetic field for three of the SIRs. Overall, there was very little difference in the performance of the three magnetogram sources in estimating the temperature, as the percentage errors averaged over all spacecraft and SIRs were 83% for GONG, 84% for the reference model and 85% for Mount Wilson.

The peak density of the SIRs was also mainly underestimated for the Mount Wilson and GONG magnetogram sources, except for a few instances. This included the density simulated by the Enlil run with the GONG magnetogram source for SIR 3 at STEREO-B, which was also overestimated by the reference model. Most of the SIRs have a single magnetogram source that gives the best density estimate at all locations, and these were the same as the best magnetogram source for total pressure and magnetic field. In general, the percentage error between the simulated and observed peak density was lower than the error for the total pressure and magnetic field for all the magnetogram sources. As with the total pressure, for the peak density, the Mount Wilson

magnetogram source always performed better than the Kitt Peak source, but this only corresponded to a slight improvement in the averaged percentage errors (47% for Mount Wilson and 48% for Kitt Peak). The percentage error between observed and simulated values of the density averaged over all SIRs and spacecraft for the GONG magnetogram source was lower than both of these, at 45%.

The peak solar wind velocity was not consistently under- or over-estimated for all SIRs or spacecraft by the models, although in general, if the velocity was overestimated or underestimated by the reference model, it was also over or underestimated by the models with the other magnetogram sources. The percentage errors between simulated and observed velocities were the lowest overall, and this was true for all three magnetogram sources. The Enlil run using the Mount Wilson magnetogram source had the lowest average percentage error across all SIRs and spacecraft, at 9%. The Kitt Peak magnetogram source had the highest average percentage error for velocity (15%), closely followed by GONG magnetogram source (14%).

The duration of all simulated SIRs was overestimated for the other magnetogram sources as well, except SIR 1 at STEREO-B, where the beginning of the SIR is missed. For the SIRs in CR2103, as for previous solar wind parameters, there tended to be a single magnetogram that performed best for each SIR, however for the SIRs in CR2102 the best magnetogram source for the SIR varied between spacecraft. For example, for SIR4 at STEREO-B, the reference model using the Kitt Peak magnetogram source simulated the shortest duration (and therefore closest to the observations), but at ACE and STEREO-A, this was longer than the GONG magnetogram source. The percentage errors between the simulated and observed SIR durations were the highest of all the solar wind parameters considered. The errors averaged over all spacecraft and all SIRs ranged between 125% (for the GONG magnetogram source) and 157% (for the Mount Wilson magnetogram source).

The differences between the observed and simulated start times for all three Enlil runs varied between spacecraft and SIRs i.e. they were not consistently simulated arriving early or late. More of the SIRs were predicted to

arrive early than late, and if the reference model predicted an early or late arrival, the runs using the other magnetogram sources did the same. Out of the six SIRs that are observed at multiple locations, only 2 SIRs had one magnetogram source that best predicted the SIR arrival time at all locations (SIR 9 and 3), all other SIRs showed different magnetogram sources predicting the arrival time best at different spacecraft. For these different magnetogram sources, the prediction closest to the observed SIR arrival time was from the Enlil run with the GONG magnetogram source, for SIR 7 at STEREO-B, which is predicted to arrive only 3.5 hours earlier than observed. However, most predicted arrival times were a day or two from the observed SIR arrival times. Averaged over all the SIRs and spacecraft, the Mount Wilson magnetogram source predicted the SIR arrivals closest to the observed arrival, with an average difference of 28 hours. The reference Enlil run had an average difference between observed and predicted arrival times of 36 hours, and the GONG magnetogram source had the highest, at 38 hours.

5.3.2 Comparison of Coronal Models

There were two different coronal models available for input into Enlil, which are compared here. These were the Wang-Sheeley-Arge model (used in the reference model) and the Magnetohydrodynamics Algorithm outside a Sphere (MAS). The Enlil run using the MAS coronal model (with the Kitt Peak magnetogram source and lowest resolution option) was able to simulate all the SIRs observed in-situ, including SIR 6 at STEREO-A, which was not simulated by the reference model. The differences between the observed and simulated values for the parameters studied are summarised in Figure 5.6, which is set out in the same way as Figure 5.5, with the black circles representing the WSA coronal model and the orange circles representing the MAS coronal model.

The reference model, using the WSA coronal model, underestimated the total pressure for all SIRs at all locations. Although the Enlil run using the MAS coronal model mainly also underestimates the total pressure, it always predicted a higher value for the peak total pressure, so performed better than the WSA model for this solar wind parameter. The MAS model does in fact overestimate the total pressure in one instance (for SIR 8 at ACE). The

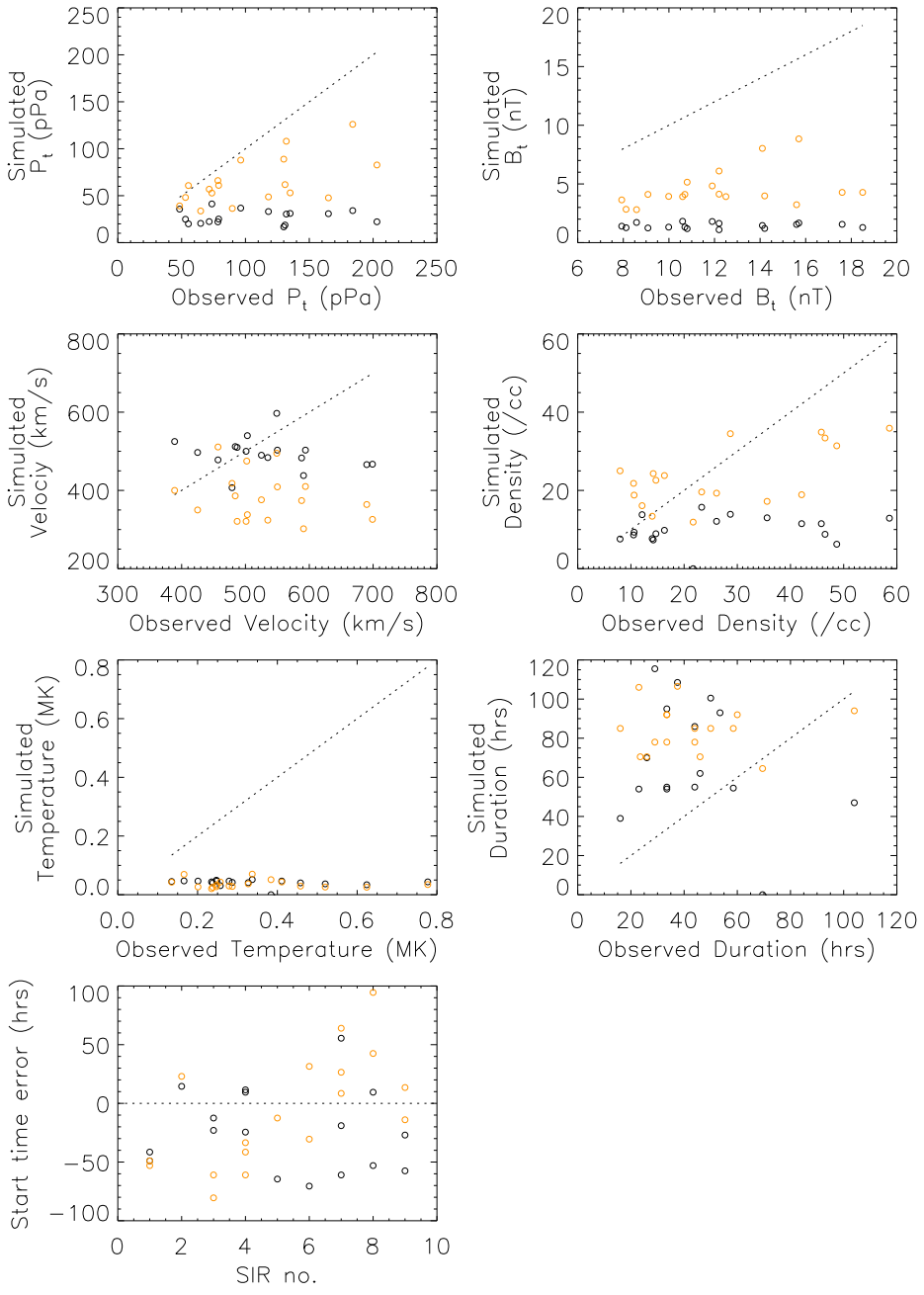

Fig. 5.6: Comparison of the solar wind parameters listed in Table 5.1 for Enlil runs using different coronal models as an input. The dashed line corresponds to the case that the values simulated by the models are consistent with the observations. The black points are the values for the reference Enlil model (using the WSA coronal model) and the orange points are the values for the Enlil run using the MAS coronal model.

percentage errors between the observed and simulated values reflect this, with the error for the MAS model averaged over all SIRs and locations being roughly half that of the WSA model.

The total magnetic field strength shows a very similar trend. Both coronal models underestimate the peak total magnetic field strength for all SIRs at all locations, but the MAS model provided a higher estimate in all instances. The total magnetic field strength was therefore always better predicted by the MAS coronal model. The averaged percentage errors between observations and simulations for this parameter were 87% for the Enlil run using the WSA coronal model and 62% for the run using MAS.

As with the reference model, the Enlil run using the MAS coronal model also underestimated the peak temperature of all SIRs at all locations. However, unlike the total pressure and magnetic field strength, in most cases the MAS model underestimated this parameter by more than the WSA model. This means that for the majority of SIRs, the WSA coronal model performed best for the estimate of the peak temperature. The MAS model provided the best estimate only for SIR 2, SIR 5, and SIR 1 at ACE. SIR 1 therefore does not have a single coronal model that best predicts its peak temperature at both locations. Despite this, the percentage errors between the observed and simulated temperature values averaged over all SIRs and all spacecraft were still the closest of all the parameters: 84% for the WSA coronal model and 86% for the MAS model.

For the WSA coronal model, the peak density of the SIR was almost always underestimated, and the MAS coronal model always predicted a higher value, as it did with the total pressure and magnetic field. However, in the case of the density, this often meant that the MAS coronal model had overestimated the peak value, which it did on almost half of all occasions. On these occasions, the MAS model prediction is only once closer to the observed value than the WSA model prediction (SIR 7 at STEREO-A). Overall, the Enlil run using the WSA model performed better than the MAS model, despite almost always underestimating the peak value. The percentage error between observations and simulations averaged over all SIRs and locations was 46% for the WSA

model, but 53% for MAS. As MAS varies between over- and under-estimating the peak density value, there are several SIRs for which no single coronal model performs the best (SIRs 1, 3, 4, 8 and 9). Of the remaining SIRs, the Enlil run with WSA is the best performing model for one (SIR 2), and MAS predicts the density closer to the observations for the others.

The velocity simulated by the Enlil model using the WSA coronal model was underestimated in around half of the SIRs and overestimated in the rest. The run using the MAS model usually predicted a peak velocity that was lower than the WSA estimate, so it underestimated the SIR peak velocity more frequently. The MAS model was also often overestimating the velocity of a SIR at one location and underestimating it at another location for the same SIR. Despite this, all SIRs had one model run which best predicted the SIR velocity at all locations where it was observed. This was the WSA coronal model for seven of the nine SIRs and the MAS coronal model for SIRs 2 and 6. This is reflected in the percentage errors between observed and simulated velocities, averaged over all SIRs at all locations, which are 15% for the run using the WSA coronal model and 27% for the run using the MAS coronal model.

As for the WSA coronal model, the Enlil run using the MAS coronal model also mainly overestimates the duration of the SIRs. The only exceptions to this were the duration of SIR 1 at STEREO-B (where it is unclear whether the beginning of the SIR is observed), and the duration of SIR 6 at STEREO-A. About half of the SIRs observed at multiple locations had a single run which performed the best (SIRs 3, 8 and 9), whereas the others had different coronal models performing better at different locations. The percentage differences between the observed and simulated SIR durations were larger than the percentage errors for all other SIR parameters. When averaged over all SIRs at all locations, the percentage errors were slightly higher for the WSA coronal model (147%) than the MAS coronal model (141%).

The arrival times of the SIRs are not consistently predicted to arrive either early or late for both coronal models and for several SIRs the arrival time is estimated early at one location and late at another (e.g. for the MAS coronal

model, SIR 9 is predicted to arrive 14 hours early at STEREO-B and 13.5 hours late at ACE). For most SIRs, there was a single coronal model run that predicted the closest arrival times to those observed. The only two exceptions were SIR 7, where the WSA coronal model predicted the arrival time at ACE closer than the MAS model, but at both STEREO spacecraft, the MAS model had the lower difference, and SIR 8, where the same was true for the SIR at ACE and STEREO-B. Over all SIRs observed at all locations, the Enlil run using the WSA coronal model preformed the best for the SIR arrival times. On average, the SIR arrival times predicted by the WSA model were 35.5 hours away from observations, whereas the average MAS model arrival times was over 41 hours away.

5.3.3 Comparison of Model Resolution

The default resolution of an Enlil run is 256x30x90, but two higher resolution options are also available: 512x60x180 and 1024x120x360. As with the reference model (using the default resolution), the Enlil runs using both higher resolution options were unable to simulate SIR 6 at STEREO-A. The mid resolution option was also unable to simulate this SIR at ACE. The differences between the observed and simulated values for the parameters studied are summarised in Figure 5.7.

The total pressure of the SIRs as simulated by the different Enlil runs was predominantly underestimated. For the reference model, the total pressure at all SIRs and all locations was underestimated and the peak total pressure increased as the resolution was increased. This meant that while the total pressure of almost all SIRs was underestimated by the mid and high resolution Enlil runs, on one occasion it was overestimated by both runs (SIR 3 at STEREO-B). This also means that in general, the higher the run resolution, the closer the estimate of total pressure was to the observed value. The only exception to this was SIR 3 at STEREO-B, where the mid resolution run provided the closest value to the observed total pressure. This trend is reflected by the percentage error between observations and simulations, averaged over all SIRs and locations. The lowest resolution run gave total pressures that were on average 69% too low, compared to 59% for the mid resolution run and

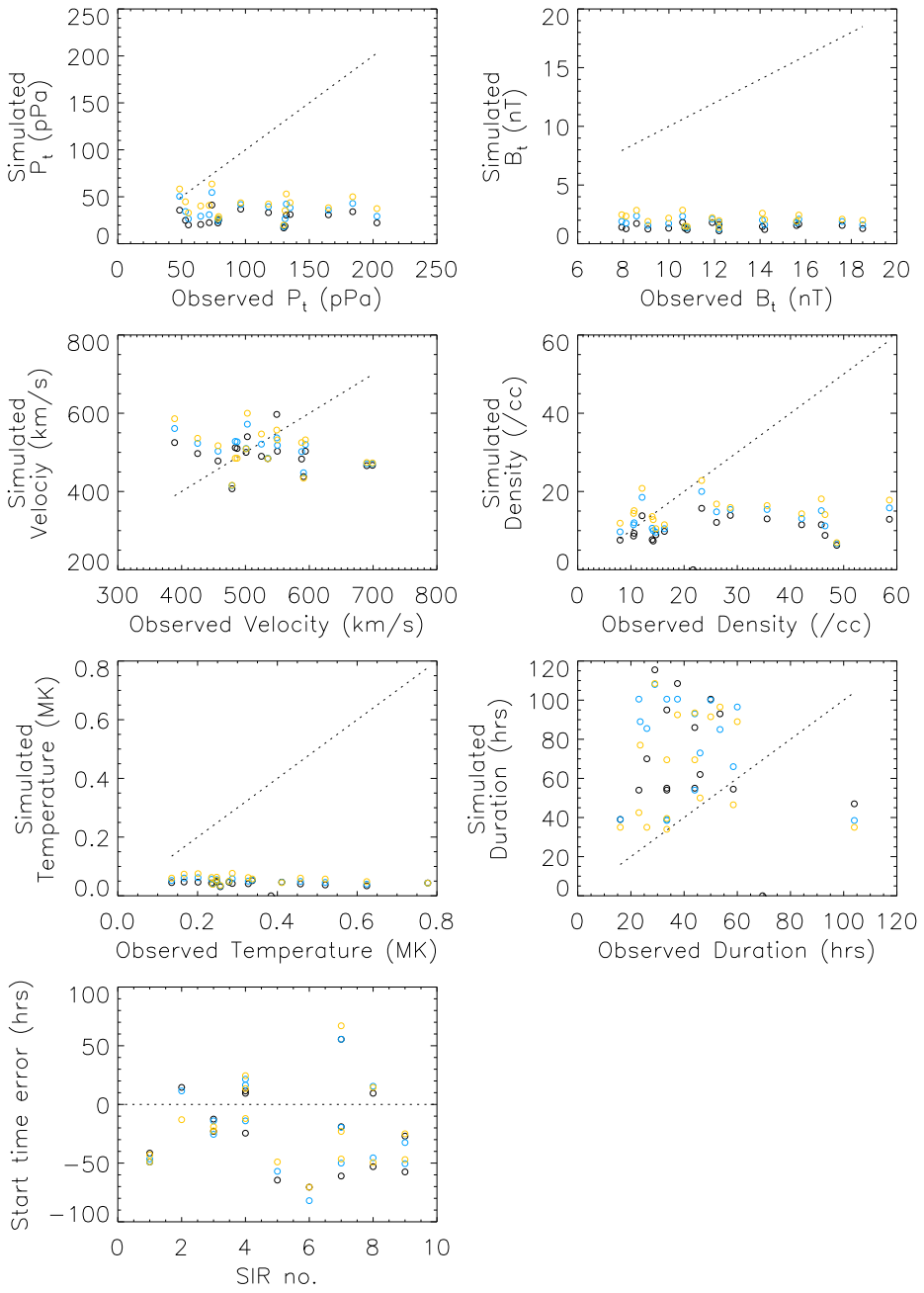

Fig. 5.7: Comparison of the solar wind parameters listed in Table 5.1 for Enlil runs using different resolution options as an input. The dashed line corresponds to the case that the values simulated by the models are consistent with the observations. The black points are the values for the reference Enlil model (using the lowest resolution choice), the blue points are the values for the Enlil run using the mid resolution option and the yellow points are the values for the Enlil run using the highest resolution choice.

55% for the high resolution run.

The total magnetic field simulated by these Enlil runs shows a very similar trend to the total pressure. The total magnetic field is also always underestimated by the lowest resolution run, and the peak magnetic field increases as the resolution is increased. The total magnetic field is also always underestimated by the two higher resolution runs, meaning that the highest resolution Enlil run provides a better estimate of the peak total magnetic field in every case. The average percentage errors between the observations and simulations were higher than for the total pressure, at 87% for the lowest resolution run, 84% for the mid resolution run and 81% for the highest resolution run.

The simulated temperature was also always underestimated by all three resolution runs, and in most instances the simulated value increased with resolution (as total pressure and temperature did), so for these cases the highest resolution run performed better. The only three occasions when the temperature peak did not increase with resolution was for SIR 7 at STEREO-B and ACE, and for SIR 9 at STEREO-B. For these cases, the simulated values for the three different resolution runs were all very close together. Overall though, the highest resolution run best produced the peak temperature of the SIRs, with an average percentage error between observations and simulations of 79%, compared to 83% for the mid resolution run and 84% for the lowest resolution run.

As the resolution of the Enlil runs are increased, the peak density for all SIRs increased. The density was generally underestimated, but there were several occasions where this was not the case, unlike for the total pressure, magnetic field and temperature, which were almost always underestimated. The density was overestimated by all three resolution models for SIR 3 at STEREO-B, and by just the highest two resolutions for SIR 1 at STEREO-B, SIR 4 at ACE and SIR 8 at ACE. As a result of this, the mid resolution run has the lowest percentage error between observations and simulations, averaged over all SIRs and all spacecraft (42%), compared to 45% for the highest resolution run (which was the run which returned the best peak density value most of the time) and 48% for the lowest resolution run.

The peak velocity simulated by the Enlil runs also often increased as the resolution increased, though not always. There was also a larger mix of under and over-estimation of the velocity (as shown by Figure 5.7). As was the case for the simulated density, the highest resolution run gave the peak velocity closest to the observed value on more occasions than the lower two resolution runs (about half the time), but the average percentage errors show that the differences overall were smaller for the mid resolution Enlil run (13%), compared to 15% for the lowest and highest resolution runs.

The duration of the SIRs were predominantly overestimated by these Enlil runs, as has been the case for the other model runs. The only SIR where this was not the case was again SIR 1, where the duration was underestimated by all three resolution runs at both STEREO-B and ACE, apart from the mid resolution run at ACE. Unlike the solar wind parameters discussed above, there is no clear trend in the duration as the model resolution is increased. Despite this, the highest resolution model still provides the best estimate of the duration on the majority of occasions. As with previous models, the percentage errors between the observed and simulated durations were the highest of all the parameters considered. In this case, the average percentage errors ranged between 147% for the lowest resolution model and 88% for the highest resolution model.

The start time of the SIRs were predicted to arrive early more often than late, but all three resolution runs predict a later arrival time for several SIRs. There were also three occasions where more than one model predicted the same arrival time of the SIR (e.g. the highest and lowest resolution models for SIR 6). This meant there was a mix of model resolutions that provided the best estimate of the arrival time, though the mid resolution run gave the best estimate on the fewest occasions. Averaging the time difference between observed and simulated arrival times over all SIRs at all locations for each model resolution shows that overall, the highest resolution model performs the best, with an average difference of 34.5 hours, compared to 35.5 for the mid and lowest resolution runs.

5.4 Discussion

This study has taken Enlil runs of the same two Carrington rotations, with changing magnetogram sources (Kitt Peak, Mount Wilson and GONG), coronal models (MAS and WSA), and resolution options (256x30x90, 512x60x80 and 1024x120x360) and compared the results to in-situ solar wind observations at ACE and both STEREO spacecraft. While these Enlil runs managed to successfully simulate most of the SIRs observed during this period, there were several SIRs that were not captured by several Enlil runs. These were usually small or transient SIRs, as was the case for the Enlil simulations run by Jian et al. (2011), where two SIRs were not simulated at 1 AU, despite clear signatures in observations. In this study, the transient SIR 2 was unable to be simulated by the GONG Enlil run, and SIR 6 was only simulated at STEREO-A by the run using the Mount Wilson magnetogram source and the run using the MAS coronal model.

Overall the performance of the Enlil runs with different magnetogram sources were very similar. The percentage errors between observed and simulated values of the solar parameters, when averaged over all SIRs and all spacecraft, were fairly close for each model run. Considering these averaged errors for the seven parameters studied (peak total pressure, total magnetic field, maximum velocity, maximum density, maximum temperature, SIR duration and SIR arrival time), the run using the GONG magnetogram source had the lowest average error for four parameters (total pressure, temperature, density and duration) and the Mount Wilson magnetogram source had the lowest average error for the other three parameters. Therefore there does not appear to be a single magnetogram source which performs the best across this period of observations, which agrees with previous work by Gressl et al. (2014). Jian et al. (2011) reported that the Kitt Peak magnetogram source (from the National Solar Observatory) produces hotter and faster fast solar wind than the Mount Wilson magnetogram source, along with earlier predictions of SIR arrival time. During CR2103 studied here, the velocity peak of the SIRs were all higher for Kitt Peak than Mount Wilson, and the temperature usually was too, although the SIR arrival time was only predicted earlier for the Kitt

Peak magnetogram source roughly half of the time. When considering each SIR during this period separately, none had one magnetogram that performed best for all the parameters. However, most had more than half of the parameters with the same magnetogram performing the best. This was the Kitt Peak magnetogram source for SIR 1 and 3, GONG for SIR 4 and 7 and Mount Wilson for SIRs 5, 6, 8 and 9. So, although no magnetogram performed the best overall, there was usually a single magnetogram that performed best for each SIR separately.

Overall, comparing the Enlil runs using these two different coronal models (WSA and MAS), there are several solar wind parameters for which one model clearly outperforms the other. Namely, the MAS coronal model always provided a better estimate of the total pressure and magnetic field, and WSA almost always provided a better estimate of the velocity and temperature (although both models underestimate the temperature by over 80%). For the other parameters considered here (density, duration and start time), the WSA model performs better overall for predicting the density and start times, and the MAS model better predicts the duration. Therefore, there is not one coronal model that performs the best for the majority of these parameters, however if an estimate of one parameter in particular was required, picking which coronal model to use may be more straightforward than choosing a magnetogram source. However, unlike for the comparison of magnetogram sources, each specific SIR did not have a single coronal model which performed the best for the majority of the properties considered. Both coronal models underestimate total magnetic field strength, total pressure and temperature, in agreement with previous work (Gressl et al. 2014; Lee et al. 2009; Jian et al. 2011), although the simulations here produce even lower estimates of the magnetic field strength, particularly for WSA.

Lee et al. (2009) and Jian et al. (2011) report that the fast solar wind simulated by MAS has higher velocities than WSA, but the maximum velocity of the SIRs here did not usually show that trend. Jian et al. (2011) further note that the MAS coronal model estimates a shorter duration for the fast wind, resulting in later predictions of the SIR. For the majority of the SIRs studied

here, the MAS model did predict a later SIR arrival than WSA, although there were still many instances when the MAS simulated SIR was earlier. Lee et al. (2009) and Gressl et al. (2014) find that in general, the MAS coronal model gives more instances of high density solar wind than the WSA model and tends to overestimate the density peaks, which agrees with what was found here, as the MAS simulated peak density was always higher than WSA.

For most of the parameters considered here, the Enlil-simulated estimate improved as the resolution increased. The exceptions to this were the density and velocity, where the mid resolution run was overall closest to the observed peak values, despite the highest resolution run providing estimates closer to the observations more often. Over all the SIRs, for all parameters, increasing the model resolution improved the results, with the highest or mid resolution runs having the lowest average percentage errors between simulated and observed values, and giving the estimate closest to observations for the majority of SIRs. There were several occasions when the lower resolution model did produce the estimate closest to the observed value. In particular, the start times of the SIRs showed no clear trend with model resolution, even though the highest resolution model does have the lowest averaged error in start time. Jian et al. (2011) speculate that discrepancies between observations and the Enlil simulations could be reduced by increasing the model resolution, which is found to mainly be the case here, although increasing the model resolution did not help the modelling of SIR 6 at STEREO-A, which was unable to be simulated by the reference model or the two higher resolution runs.

5.5 Summary and Conclusions

This work aimed to provide further insight into the Enlil model simulations of background solar wind structures such as SIRs. In particular, it aimed to identify how the simulation results change with different input parameters such as coronal model, input magnetogram, and model resolution, and which inputs would provide the best model results of the solar wind. To achieve this, simulation results of the ambient solar wind for two Carrington rotations (CR2102 and CR2103) were compared to in-situ solar wind observations at

three locations at 1 AU (ACE at L1 and the two STEREO spacecraft).

During the period studied, nine different SIRs were observed, two at one location only (STEREO-A), two at all three locations and five at two locations. The properties of these SIRs were studied by considering seven different parameters: SIR duration, SIR arrival time, peak total pressure, peak magnetic field strength, peak velocity, peak temperature and peak density. It was found that these parameters could vary substantially between spacecraft, although there was no clear trend for any parameter.

The in-situ observations at these three locations were compared against Enlil simulations for the same period. The basic Enlil run for comparison used the Kitt Peak magnetogram source, WSA coronal model and lowest resolution option available (256x30x90). It was found that for this run, the Enlil simulation always underestimated the total pressure, total magnetic field and temperature, as has been found in previous studies, but the underestimation of the magnetic field was larger than has been previously reported, sometimes as large as an order of magnitude. The density was almost always underestimated and the duration almost always overestimated. The simulated velocity was the parameter that came closest to observations, with the average percentage error being only 14%. The SIR arrival times were usually predicted to arrive early, sometimes by more than two days, though several were predicted also to arrive late.

The main conclusions of this work showed that changing the input parameters of the Enlil model modified the simulation results noticeably, but in the main, the temperature, total pressure and total magnetic field were still always underestimated, and the duration of all SIRs overestimated. When changing the magnetogram source from Kitt Peak to Mount Wilson or GONG observatories, it was found that there was no particular magnetogram source that performed the best over the entire period considered. However, usually a single magnetogram was found to best simulate each SIR, even if it did not perform best for other SIRs. This means that if simulating a single SIR, there may be one optimum magnetogram source to use, though it would not be clear what this was without comparisons between them. Changing the coronal

model that was input to Enlil from WSA to MAS was found to improve the simulation of several parameters, for example the magnetic field, which was still underestimated, but by less than the WSA model. However, using the MAS coronal model did not improve the simulation of all the parameters considered, and worsened it for some (e.g. velocity and temperature). Therefore, the choice of coronal model used would be dependent on which parameters were of most interest. The resolution of the Enlil model was also changed, leading to the conclusion that increasing the resolution tends to improve the estimates of the parameters considered here, across all the SIRs studied. The highest resolution Enlil runs can take up to a week complete, which would be unfeasible for use as a space weather forecasting tool. However, this work found that for almost all parameters studied, just increasing the resolution to the middle option still improved the model results.

Chapter 6

Conclusions and Future Work

This thesis has discussed work on the evolution and propagation of various solar transients throughout the solar system, including Solar Energetic Particle (SEP) events, Stream Interaction Regions (SIRs) and Interplanetary Coronal Mass Ejections (ICMEs). These solar transients can drive a wide variety of significant space weather effects, leading to large impacts at Earth. In order to mitigate these effects, accurate space weather forecasting tools and prediction models are required. Therefore increasing our understanding of how solar transients travel through the heliosphere, how they interact and how they influence each other is critical to be able to improve the accuracy of our models, as well as understanding the limitations of these simulations. In particular, this thesis makes use of a wide range of data sources and types, including remote sensing from solar telescopes, in-situ solar wind observations, planetary data and solar wind modelling, which has allowed for a more complete picture of the particular events studied and given a broader insight into these large-scale phenomena.

In Chapter 3 the evolution of a large CME on 3 November 2011 is studied, along with its associated EUV wave and the resulting widespread SEP event. The aim of the work was to investigate the origins of the widespread SEP event, which was observed at Earth and both STEREO spacecraft. This study verified previous work by Rouillard et al. (2012), showing that in large SEP events, with an associated CME, the release of particles from the Sun that are observed at a particular spacecraft can be delayed until the edge of the

expanding CME has reached the footpoint of the magnetic field line connecting that spacecraft to the Sun. This work is built upon in the case of the event studied here, and come to the conclusion that this delay in particle release can also be due to the expansion of the CME higher in the corona, rather than just down at the level of an EUV wave, as shown by Rouillard et al. (2012).

The CME associated with this event erupted from the back of the Sun, directed between the STEREO spacecraft, but slightly more towards STEREO-B. The expansion of the CME low down in the corona is seen to track the propagation of the EUV wave, while the expansion is much faster higher up in the corona. The particle event was observed at L1 and both STEREO spacecraft, with particles arriving at STEREO-A first, despite STEREO-B having a better view of the CME eruption. Velocity dispersion analysis shows that the solar particle release (SPR) time is also earliest for particles arriving at STEREO-A, followed by particles at L1, then STEREO-B. The CME source location is closest to the footpoint of the field line connecting STEREO-A to the Sun, which explains why the particles would be observed here first as the edge of the expanding CME would reach this footpoint first. The position of the edge of the CME at each of the SPR times is estimated from the expansion of the CME, and shows that it reaches the footpoints of both STEREO spacecraft at their respective SPR times, but only when considering the faster expansion of the CME, higher up in the corona. Overall, this work builds on previous studies demonstrating that SEP events can be incredibly widespread, and driven by events far from where they are observed. Their timings are not always simple to predict, and can be delayed depending on the expansion of the CME, not just low in the solar corona, but also higher up. This has significant implications for space weather, as it makes it much harder to forecast where and when energetic particles may be seen in association with a CME.

Further study of the longitudinal extent of gradual SEP events is needed to fully understand how the spread of such events is affected by the expansion of the CME that accelerates the particles. While this work showed that the timings of the energetic particles can be explained by the expansion of the CME higher up in the corona than previously established, it was still unable

to explain the presence of the particles observed at the Earth for this event. This demonstrates that work is still needed in this area in order to be able to predict when events are likely to occur at the Earth depending on their source location. SEPs are very difficult to forecast and different models take different approaches to the problem, but many rely on an understanding of the connectivity of the event to the Earth. This aspect of SEP forecasting models will need to be improved upon to take into account changing connectivity as a CME expands.

In Chapter 4 an ICME and CIR are studied as they travel out from the Sun, with the aim of understanding how they interact and propagate throughout the solar system. This work takes advantage of a favourable alignment of Venus, STEREO-B, Mars and Saturn in June 2010 to make use of planetary data as well as solar observatories, and is complemented by use of the Enlil solar wind model. The ICME is a relatively small one and is observed travelling ahead of the CIR at Venus, STEREO-B and Mars. The Enlil simulations of these structures suggest that they merge beyond the orbit of Mars and impact Saturn, leading to a significant compression of the magnetosphere. The ICME is observed to accelerate as it travels through the inner solar system, as a result of it catching up to the high speed stream associated with the preceding CIR. The Enlil predictions for the arrival of this ICME at each location were closer to the observations than the predictions for the CIR, but the simulation showed the ICME decelerating rather than accelerating. This discrepancy is due to the timing uncertainties of the CIR, which is predicted by Enlil to arrive at each location over 36 hours too early.

The main conclusions of this study found that the ICME could be accelerated as it travelled in the HSS, and that the poor simulation of the CIR timings prevented this from being accurately modelled by the Enlil prediction model. It also found that even a relatively weak ICME can merge with other solar wind structures and lead to significant solar wind impacts further out in the solar system, as this small ICME results in a large compression of Saturn's magnetosphere. This emphasises that the ambient solar wind conditions are important for the evolution of an ICME, as well as other transient structures

nearby that could merge and interact with it. This therefore needs to be accurately simulated for the propagation of an ICME to be correctly modelled and its timings and impacts predicted.

The evolution and propagation of ICMEs has been the topic of much previous study, including how they interact with the ambient solar wind, but there are still areas that need further research. In particular, more work is required to understand merged interaction regions, which can form as multiple ICMEs merge together, or with other solar wind structures such as SIRs and CIRs. These regions can cause greater geomagnetic effects than single events, and their impacts further out in the solar system can be more significant than expected from relatively weak constituents, which could be problematic for spacecraft in the outer solar system.

Chapter 5 studies the in-situ solar wind conditions over the course of two Carrington rotations and compares them to Enlil simulations, with the aim of investigating how changing the input parameters of the model impacts the simulation results. During this period, a number of SIRs were observed at 1 AU, using data from ACE and both STEREO spacecraft, and most were successfully simulated by Enlil. In general, it was found that the model underestimated most of the SIR parameters considered, in particular the total pressure, magnetic field strength and temperature. The duration of the SIRs were mainly overestimated and the parameter that was the closest to the observations was the peak SIR velocity. In this work, Enlil simulations using different input parameters were compared, by changing the input magnetogram source, the coronal model and the model resolution. It was found that changing these parameters significantly modified the simulation results, but it was not clear which combination of input parameters gave the best results for this period overall. The main conclusions of this comparison were that changing the magnetogram source can improve the simulation results for specific SIRs, but not consistently over the entire period considered, changing the coronal model can improve the simulation results for certain parameters, but not others and that increasing the model resolution generally improved the results overall.

As the Enlil model is currently used for space weather forecasting (for

example by the UK Met office and NOAA) it must be regularly improved and validated. Further work to build on the results shown in this thesis could study more combinations of Enlil's input parameters to see if these provide simulation results that are closer to observations, for example using the higher model resolutions with the MAS coronal model and the other magnetogram sources. Particular areas that would benefit from improvement include the simulation of ICMEs, which at the moment does not include the internal magnetic structure, and the timings of CIRs, which often show uncertainties of $\sim$ 1 - 2 days and can affect the propagation of ICMEs.

The launch of STEREO in 2006 has hugely enhanced the study of propagating solar transients, with the two spacecraft travelling at 1 AU ahead and behind the Earth providing much better data of the longitudinal extent and evolution of such structures. Unfortunately, contact has been lost with the STEREO-B spacecraft, so future measurements making use of the longitudinal separation of these spacecraft may be limited. Future study into this area must now work to interpret the many solar transients measured by the STEREO spacecraft and use this to improve modelling and forecasting of these events. As well as solar telescopes, there are now an unprecedented number of spacecraft throughout the solar system, many of which are capable of measuring the solar wind conditions. Taking advantage of these additional sources of data, complemented by models of the solar wind beyond the Earth can provide a unique insight into many solar transients throughout the heliosphere.

This thesis studies how different solar transients change and interact as they evolve, both in longitude and radially throughout the solar system. It finds that the behaviour of large transients can be heavily affected by other events associated with them, as well as nearby solar transients and the ambient solar wind that its propagating through. For example, in Chapter 3, the evolution of an ICME is shown to influence the timing and longitudinal spread of its associated SEP event and in Chapter 4, the propagation speed of an ICME is affected by a nearby CIR. Interactions between such transients can also change the strength of possible space weather impacts as they merge, as well as disturbing the direction and speed of propagation. The Enlil model

is used extensively for space weather forecasting, but still has issues that limit its ability to accurately model solar transients. Chapter 5 of this thesis shows that the simulation of the background solar wind by Enlil improves with increased model resolution, but this can take too long to run to be useful for space weather predictions and changing other input parameters did not consistently improve the performance of the model. These conclusions highlight the need for space weather prediction models such as Enlil to take into account a wider view of the heliosphere, incorporating accurate modelling of the ambient solar wind and multiple closely-occurring solar transients, rather than simulating single events in isolation. Improving the performance of such models is necessary to achieve this, as well as making use of multipoint widespread observations in order to enhance our knowledge of the interactions between transients and their environment as they propagate and evolve.

Bibliography

Achilleos, N., Arridge, C. S., Bertucci, C., Jackman, C. M., Dougherty, M. K., Khurana, K. K. and Russell, C. T. (2008), Large-scale dynamics of Saturn's magnetopause: Observations by Cassini, *Journal of Geophysical Research (Space Physics)* **113**, 11209.

Achilleos, N., Bertucci, C., Russell, C. T., Hospodarsky, G. B., Rymer, A. M., Arridge, C. S., Burton, M. E., Dougherty, M. K., Hendricks, S., Smith, E. J. and Tsurutani, B. T. (2006), Orientation, location, and velocity of Saturn's bow shock: Initial results from the Cassini spacecraft, *Journal of Geophysical Research (Space Physics)* **111**, 3201.

Acuña, M. H., Curtis, D., Scheifele, J. L., Russell, C. T., Schroeder, P., Szabo, A. and Luhmann, J. G. (2008), The STEREO/IMPACT Magnetic Field Experiment, *Space Sci. Rev.* **136**, 203–226.

Andrews, D. J., Cowley, S. W. H., Dougherty, M. K., Lamy, L., Provan, G. and Southwood, D. J. (2012), Planetary period oscillations in Saturn's magnetosphere: Evolution of magnetic oscillation properties from southern summer to post-equinox, *Journal of Geophysical Research (Space Physics)* **117**, 4224.

Arge, C. N. and Pizzo, V. J. (2000), Improvement in the prediction of solar wind conditions using near-real time solar magnetic field updates, *J. Geophys. Res.* **105**, 10465–10480.

Arge, C. N., Luhmann, J. G., Odstrcil, D., Schrijver, C. J. and Li, Y. (2004), Stream structure and coronal sources of the solar wind during the May 12th,

1997 CME, *Journal of Atmospheric and Solar-Terrestrial Physics* **66**, 1295–1309.

Arge, C. N., Odstrcil, D., Pizzo, V. J. and Mayer, L. R. (2003), Improved Method for Specifying Solar Wind Speed Near the Sun, *in* M. Velli, R. Bruno, F. Malara and B. Bucci (eds.), *Solar Wind Ten*, Vol. 679 of *American Institute of Physics Conference Series*, pp.190–193.

Arridge, C. S., Achilleos, N., Dougherty, M. K., Khurana, K. K. and Russell, C. T. (2006), Modeling the size and shape of Saturn's magnetopause with variable dynamic pressure, *Journal of Geophysical Research (Space Physics)* **111**, 11227.

Aschwanden, M. J. (2005), *Physics of the Solar Corona. An Introduction with Problems and Solutions (2nd edition)*.

Attrill, G. D. R., Harra, L. K., van Driel-Gesztelyi, L. and Démoulin, P. (2007), Coronal "Wave": Magnetic Footprint of a Coronal Mass Ejection?, *ApJ* **656**, L101–L104.

Badman, S. V. and Cowley, S. W. H. (2007), Significance of Dungey-cycle flows in Jupiter's and Saturn's magnetospheres, and their identification on closed equatorial field lines, *Annales Geophysicae* **25**, 941–951.

Baker, D. N., Odstrcil, D., Anderson, B. J., Arge, C. N., Benna, M., Gloeckler, G., Korth, H., Mayer, L. R., Raines, J. M., Schriver, D., Slavin, J. A., Solomon, S. C., Trávníček, P. M. and Zurbuchen, T. H. (2011), The space environment of Mercury at the times of the second and third MESSENGER flybys, *Planet. Space Sci.* **59**, 2066–2074.

Baker, D. N., Odstrcil, D., Anderson, B. J., Arge, C. N., Benna, M., Gloeckler, G., Raines, J. M., Schriver, D., Slavin, J. A., Solomon, S. C., Killen, R. M. and Zurbuchen, T. H. (2009), Space environment of Mercury at the time of the first MESSENGER flyby: Solar wind and interplanetary magnetic field modeling of upstream conditions, *Journal of Geophysical Research (Space Physics)* **114**, 10101.

Baker, D. N., Poh, G., Odstrcil, D., Arge, C. N., Benna, M., Johnson, C. L., Korth, H., Gershman, D. J., Ho, G. C., McClintock, W. E., Cassidy, T. A., Merkel, A., Raines, J. M., Schriver, D., Slavin, J. A., Solomon, S. C., Trvnek, P. M., Winslow, R. M. and Zurbuchen, T. H. (2013), Solar wind forcing at Mercury: WSA-ENLIL model results, *Journal of Geophysical Research: Space Physics* **118**(1), 45–57.

Barabash, S., Fedorov, A., Sauvaud, J. J., Lundin, R., Russell, C. T., Futaana, Y., Zhang, T. L., Andersson, H., Brinkfeldt, K., Grigoriev, A., Holmström, M., Yamauchi, M., Asamura, K., Baumjohann, W., Lammer, H., Coates, A. J., Kataria, D. O., Linder, D. R., Curtis, C. C., Hsieh, K. C., Sandel, B. R., Grande, M., Gunell, H., Koskinen, H. E. J., Kallio, E., Riihelä, P., Säles, T., Schmidt, W., Kozyra, J., Krupp, N., Fränz, M., Woch, J., Luhmann, J., McKenna-Lawlor, S., Mazelle, C., Thocaven, J.-J., Orsini, S., Cerulli-Irelli, R., Mura, M., Milillo, M., Maggi, M., Roelof, E., Brandt, P., Szego, K., Winningham, J. D., Frahm, R. A., Scherrer, J., Sharber, J. R., Wurz, P. and Bochsler, P. (2007a), The loss of ions from Venus through the plasma wake, *Nature* **450**, 650–653.

Barabash, S., Lundin, R., Andersson, H., Brinkfeldt, K., Grigoriev, A., Gunell, H., Holmström, M., Yamauchi, M., Asamura, K., Bochsler, P., Wurz, P., Cerulli-Irelli, R., Mura, A., Milillo, A., Maggi, M., Orsini, S., Coates, A. J., Linder, D. R., Kataria, D. O., Curtis, C. C., Hsieh, K. C., Sandel, B. R., Frahm, R. A., Sharber, J. R., Winningham, J. D., Grande, M., Kallio, E., Koskinen, H., Riihelä, P., Schmidt, W., Säles, T., Kozyra, J. U., Krupp, N., Woch, J., Livi, S., Luhmann, J. G., McKenna-Lawlor, S., Roelof, E. C., Williams, D. J., Sauvaud, J.-A., Fedorov, A. and Thocaven, J.-J. (2006), The Analyzer of Space Plasmas and Energetic Atoms (ASPERA-3) for the Mars Express Mission, *Space Sci. Rev.* **126**, 113–164.

Barabash, S., Sauvaud, J.-A., Gunell, H., Andersson, H., Grigoriev, A., Brinkfeldt, K., Holmström, M., Lundin, R., Yamauchi, M., Asamura, K., Baumjohann, W., Zhang, T. L., Coates, A. J., Linder, D. R., Kataria, D. O., Curtis, C. C., Hsieh, K. C., Sandel, B. R., Fedorov, A., Mazelle, C., Thocaven, J.-J.,

Grande, M., Koskinen, H. E. J., Kallio, E., Säles, T., Riihela, P., Kozyra, J., Krupp, N., Woch, J., Luhmann, J., McKenna-Lawlor, S., Orsini, S., Cerulli-Irelli, R., Mura, M., Milillo, M., Maggi, M., Roelof, E., Brandt, P., Russell, C. T., Szego, K., Winningham, J. D., Frahm, R. A., Scherrer, J., Sharber, J. R., Wurz, P. and Bochsler, P. (2007b), The Analyser of Space Plasmas and Energetic Atoms (ASPERA-4) for the Venus Express mission, *Planet. Space Sci.* **55**, 1772–1792.

Bertaux, J.-L., Leblanc, F., Witasse, O., Quemerais, E., Lilensten, J., Stern, S. A., Sandel, B. and Korablev, O. (2005), Discovery of an aurora on Mars, *Nature* **435**, 790–794.

Bertucci, C., Duru, F., Edberg, N., Fraenz, M., Martinecz, C., Szego, K. and Vaisberg, O. (2011), The Induced Magnetospheres of Mars, Venus, and Titan, *Space Sci. Rev.* **162**, 113–171.

Bieber, J. W., Clem, J., Evenson, P., Pyle, R., Ruffolo, D. and Sáiz, A. (2005), Relativistic solar neutrons and protons on 28 October 2003, *Geophys. Res. Lett.* **32**, 3.

Bougeret, J. L., Goetz, K., Kaiser, M. L., Bale, S. D., Kellogg, P. J., Maksimovic, M., Monge, N., Monson, S. J., Astier, P. L., Davy, S., Dekkali, M., Hinze, J. J., Manning, R. E., Aguilar-Rodriguez, E., Bonnin, X., Briand, C., Cairns, I. H., Cattell, C. A., Cecconi, B., Eastwood, J., Ergun, R. E., Fainberg, J., Hoang, S., Huttunen, K. E. J., Krucker, S., Lecacheux, A., MacDowall, R. J., Macher, W., Mangeney, A., Meetre, C. A., Moussas, X., Nguyen, Q. N., Oswald, T. H., Pulupa, M., Reiner, M. J., Robinson, P. A., Rucker, H., Salem, C., Santolik, O., Silvis, J. M., Ullrich, R., Zarka, P. and Zouganelis, I. (2008), S/WAVES: The Radio and Plasma Wave Investigation on the STEREO Mission, *Space Sci. Rev.* **136**, 487–528.

Bougeret, J.-L., Kaiser, M. L., Kellogg, P. J., Manning, R., Goetz, K., Monson, S. J., Monge, N., Friel, L., Meetre, C. A., Perche, C., Sitruk, L. and Hoang, S. (1995), Waves: The Radio and Plasma Wave Investigation on the Wind Spacecraft, *Space Sci. Rev.* **71**, 231–263.

Breus, T. K., Ness, N. F., Krymskii, A. M., Crider, D. H., Acuna, M. H., Connerney, J. E. P., Hinson, D. and Barashyan, K. K. (2005), The effects of crustal magnetic fields and the pressure balance in the high latitude ionosphere/atmosphere at Mars, *Advances in Space Research* **36**, 2043–2048.

Broiles, T. W., Desai, M. I., Lee, C. O. and MacNeice, P. J. (2013), Radial evolution of the three-dimensional structure in CIRs between Earth and Ulysses, *Journal of Geophysical Research (Space Physics)* **118**, 4776–4792.

Brueckner, G. E., Howard, R. A., Koomen, M. J., Korendyke, C. M., Michels, D. J., Moses, J. D., Socker, D. G., Dere, K. P., Lamy, P. L., Llebaria, A., Bout, M. V., Schwenn, R., Simnett, G. M., Bedford, D. K. and Eyles, C. J. (1995), The Large Angle Spectroscopic Coronagraph (LASCO), *Solar Phys.* **162**, 357–402.

Buffington, A., Jackson, B. V. and Korendyke, C. M. (1996), Wide-angle stray-light reduction for a spaceborne optical hemispherical imager, *Appl. Opt.* **35**, 6669–6673.

Bunce, E. J., Arridge, C. S., Clarke, J. T., Coates, A. J., Cowley, S. W. H., Dougherty, M. K., GéRard, J.-C., Grodent, D., Hansen, K. C., Nichols, J. D., Southwood, D. J. and Talboys, D. L. (2008), Origin of Saturn's aurora: Simultaneous observations by Cassini and the Hubble Space Telescope, *Journal of Geophysical Research (Space Physics)* **113**, 9209.

Burlaga, L., Berdichevsky, D., Gopalswamy, N., Lepping, R. and Zurbuchen, T. (2003), Merged interaction regions at 1 AU, *Journal of Geophysical Research (Space Physics)* **108**, 1425.

Byrne, J. P., Maloney, S. A., McAteer, R. T. J., Refojo, J. M. and Gallagher, P. T. (2010), Propagation of an Earth-directed coronal mass ejection in three dimensions, *Nature Communications* **1**.

Cane, H. V. and Erickson, W. C. (2003), Energetic particle propagation in the inner heliosphere as deduced from low-frequency (<100 kHz) observations of type III radio bursts, *J. Geophys. Res. (Space Phys.)* **108**, 1203.

Carmichael, H. (1964), A Process for Flares, *NASA Special Publication* **50**, 451.

Chen, P. F. (2011), Coronal Mass Ejections: Models and Their Observational Basis, *Living Reviews in Solar Physics* **8**, 1.

Chen, P. F., Wu, S. T., Shibata, K. and Fang, C. (2002), Evidence of EIT and Moreton Waves in Numerical Simulations, *ApJ* **572**, L99–L102.

Chicarro, A., Martin, P. and Trautner, R. (2004), The Mars Express mission: an overview, *in* A. Wilson and A. Chicarro (eds.), *Mars Express: the Scientific Payload*, Vol. 1240 of *ESA Special Publication*, pp.3–13.

Chollet, E. E., Mewaldt, R. A., Cummings, A. C., Gosling, J. T., Haggerty, D. K., Hu, Q., Larson, D., Lavraud, B., Leske, R. A., Opitz, A., Roelof, E. C., Russell, C. T. and Sauvaud, J.-A. (2010), Multipoint connectivity analysis of the May 2007 solar energetic particle events, *Journal of Geophysical Research (Space Physics)* **115**, 12106.

Cliver, E. W. (2009), History of research on solar energetic particle (SEP) events: the evolving paradigm, *in* N. Gopalswamy & D. F. Webb (ed.), *IAU Symposium*, Vol. 257 of *IAU Symposium*, pp.401–412.

Cliver, E. W. and Cane, H. V. (1996), The angular extents of solar/interplanetary disturbances and modulation of galactic cosmic rays, *J. Geophys. Res.* **101**, 15533–15546.

Cliver, E. W., Kahler, S. W., Neidig, D. F., Cane, H. V., Richardson, I. G., Kallenrode, M. B. and Wibberenz, G. (1995), Extreme "Propagation" of Solar Energetic Particles, *in* N. Iucci and E. Lamanna (eds.), *Internat. Cosmic Ray Conf.*, Vol. 4, p.257.

Cliver, E. W., Webb, D. F. and Howard, R. A. (1999), On the origin of solar metric type II bursts, *Solar Phys.* **187**, 89–114.

Crary, F. J., Clarke, J. T., Dougherty, M. K., Hanlon, P. G., Hansen, K. C., Steinberg, J. T., Barraclough, B. L., Coates, A. J., Gérard, J.-C., Grodent,

D., Kurth, W. S., Mitchell, D. G., Rymer, A. M. and Young, D. T. (2005), Solar wind dynamic pressure and electric field as the main factors controlling Saturn's aurorae, *Nature* **433**, 720–722.

Cremades, H. and Bothmer, V. (2004), On the three-dimensional configuration of coronal mass ejections, *A&A* **422**, 307–322.

Crider, D. H., Espley, J., Brain, D. A., Mitchell, D. L., Connerney, J. E. P. and Acuña, M. H. (2005), Mars Global Surveyor observations of the Halloween 2003 solar superstorm's encounter with Mars, *Journal of Geophysical Research (Space Physics)* **110**, 9.

Delaboudinière, J.-P., Artzner, G. E., Brunaud, J., Gabriel, A. H., Hochedez, J. F., Millier, F., Song, X. Y., Au, B., Dere, K. P., Howard, R. A., Kreplin, R., Michels, D. J., Moses, J. D., Defise, J. M., Jamar, C., Rochus, P., Chauvineau, J. P., Marioge, J. P., Catura, R. C., Lemen, J. R., Shing, L., Stern, R. A., Gurman, J. B., Neupert, W. M., Maucherat, A., Clette, F., Cugnon, P. and van Dessel, E. L. (1995), EIT: Extreme-Ultraviolet Imaging Telescope for the SOHO Mission, *Sol. Phys.* **162**, 291–312.

Domingo, V., Fleck, B. and Poland, A. I. (1995), The SOHO Mission: an Overview, *Solar Phys.* **162**, 1–37.

Dougherty, M. K., Kellock, S., Southwood, D. J., Balogh, A., Smith, E. J., Tsurutani, B. T., Gerlach, B., Glassmeier, K.-H., Gleim, F., Russell, C. T., Erdos, G., Neubauer, F. M. and Cowley, S. W. H. (2004), The Cassini Magnetic Field Investigation, *Space Sci. Rev.* **114**, 331–383.

Dresing, N., Gómez-Herrero, R., Klassen, A., Heber, B., Kartavykh, Y. and Dröge, W. (2012), The Large Longitudinal Spread of Solar Energetic Particles During the 17 January 2010 Solar Event, *Sol. Phys.* **281**, 281–300.

Dungey, J. W. (1961), Interplanetary Magnetic Field and the Auroral Zones, *Physical Review Letters* **6**, 47–48.

Edberg, N. J. T., Auster, U., Barabash, S., Bößwetter, A., Brain, D. A., Burch, J. L., Carr, C. M., Cowley, S. W. H., Cupido, E., Duru, F., Eriksson, A. I.,

Fränz, M., Glassmeier, K.-H., Goldstein, R., Lester, M., Lundin, R., Modolo, R., Nilsson, H., Richter, I., Samara, M. and Trotignon, J. G. (2009), Rosetta and Mars Express observations of the influence of high solar wind pressure on the Martian plasma environment, *Annales Geophysicae* **27**, 4533–4545.

Elphic, R. C., Russell, C. T., Slavin, J. A. and Brace, L. H. (1980), Observations of the dayside ionopause and ionosphere of Venus, *J. Geophys. Res.* **85**, 7679–7696.

Espinosa, S. A. and Dougherty, M. K. (2000), Periodic perturbations in Saturn's magnetic field, *Geophys. Res. Lett.* **27**, 2785–2788.

Espinosa, S. A. and Dougherty, M. K. (2001), Unexpected periodic perturbations in Saturn's magnetic field data from Pioneer 11 and Voyager 2, *Advances in Space Research* **28**, 919–924.

Espinosa, S. A., Southwood, D. J. and Dougherty, M. K. (2003), How can Saturn impose its rotation period in a noncorotating magnetosphere?, *Journal of Geophysical Research (Space Physics)* **108**, 1086.

Eyles, C. J., Harrison, R. A., Davis, C. J., Waltham, N. R., Shaughnessy, B. M., Mapson-Menard, H. C. A., Bewsher, D., Crothers, S. R., Davies, J. A., Simnett, G. M., Howard, R. A., Moses, J. D., Newmark, J. S., Socker, D. G., Halain, J.-P., Defise, J.-M., Mazy, E. and Rochus, P. (2009), The Heliospheric Imagers Onboard the STEREO Mission, *Sol. Phys.* **254**, 387–445.

Falkenberg, T. V., Taktakishvili, A., Pulkkinen, A., Vennerstrom, S., Odstrcil, D., Brain, D., Delory, G. and Mitchell, D. (2011a), Evaluating predictions of ICME arrival at Earth and Mars, *Space Weather* **9**, 0.

Falkenberg, T. V., Vennerstrom, S., Brain, D. A., Delory, G. and Taktakishvili, A. (2011b), Multipoint observations of coronal mass ejection and solar energetic particle events on Mars and Earth during November 2001, *Journal of Geophysical Research (Space Physics)* **116**, 6104.

Falkenberg, T. V., Vrnak, B., Taktakishvili, A., Odstrcil, D., MacNeice, P. and Hesse, M. (2010), Investigations of the sensitivity of a coronal mass ejection model (ENLIL) to solar input parameters, *Space Weather* **8**(6).

Feynman, J. and Hundhausen, A. J. (1994), Coronal mass ejections and major solar flares: The great active center of March 1989, *J. Geophys. Res.* **99**, 8451–8464.

Fränz, M., Dubinin, E., Roussos, E., Woch, J., Winningham, J. D., Frahm, R., Coates, A. J., Fedorov, A., Barabash, S. and Lundin, R. (2006), Plasma Moments in the Environment of Mars. Mars Express ASPERA-3 Observations, *Space Sci. Rev.* **126**, 165–207.

Galvin, A. B., Kistler, L. M., Popecki, M. A., Farrugia, C. J., Simunac, K. D. C., Ellis, L., Möbius, E., Lee, M. A., Boehm, M., Carroll, J., Crawshaw, A., Conti, M., Demaine, P., Ellis, S., Gaidos, J. A., Googins, J., Granoff, M., Gustafson, A., Heirtzler, D., King, B., Knauss, U., Levasseur, J., Longworth, S., Singer, K., Turco, S., Vachon, P., Vosbury, M., Widholm, M., Blush, L. M., Karrer, R., Bochsler, P., Daoudi, H., Etter, A., Fischer, J., Jost, J., Opitz, A., Sigrist, M., Wurz, P., Klecker, B., Ertl, M., Seidenschwang, E., Wimmer-Schweingruber, R. F., Koeten, M., Thompson, B. and Steinfeld, D. (2008), The Plasma and Suprathermal Ion Composition (PLASTIC) Investigation on the STEREO Observatories, *Space Sci. Rev.* **136**, 437–486.

GéRard, J.-C., Bunce, E. J., Grodent, D., Cowley, S. W. H., Clarke, J. T. and Badman, S. V. (2005), Signature of Saturn's auroral cusp: Simultaneous Hubble Space Telescope FUV observations and upstream solar wind monitoring, *Journal of Geophysical Research (Space Physics)* **110**, 11201.

Giampieri, G., Dougherty, M. K., Smith, E. J. and Russell, C. T. (2006), A regular period for Saturn's magnetic field that may track its internal rotation, *Nature* **441**, 62–64.

Golub, L. and Pasachoff, J. M. (1997), *The Solar Corona*.

Gonzalez-Esparza, J. A., Romero-Hernandez, E. and Riley, P. (2013), Study of Corotating Interaction Regions in the Ascending Phase of the Solar Cycle: Multi-spacecraft Observations, *Sol. Phys.* **285**, 201–216.

Gopalswamy, N. (2008), Type II Radio Emission and Solar Energetic Particle Events, *in* G. Li, Q. Hu, O. Verkhoglyadova, G. P. Zank, R. P. Lin, & J. Luhmann (ed.), *American Institute of Physics Conference Series*, Vol. 1039 of *American Institute of Physics Conference Series*, pp.196–202.

Gopalswamy, N., Lara, A., Lepping, R. P., Kaiser, M. L., Berdichevsky, D. and St. Cyr, O. C. (2000), Interplanetary acceleration of coronal mass ejections, *Geophys. Res. Lett.* **27**, 145–148.

Gopalswamy, N., Shimojo, M., Lu, W., Yashiro, S., Shibasaki, K. and Howard, R. A. (2003), Prominence Eruptions and Coronal Mass Ejection: A Statistical Study Using Microwave Observations, *ApJ* **586**, 562–578.

Gopalswamy, N., Yashiro, S., Akiyama, S., Mäkelä, P., Xie, H., Kaiser, M. L., Howard, R. A. and Bougeret, J. L. (2008), Coronal mass ejections, type II radio bursts, and solar energetic particle events in the SOHO era, *Annales Geophysicae* **26**, 3033–3047.

Gopalswamy, N., Yashiro, S., Temmer, M., Davila, J., Thompson, W. T., Jones, S., McAteer, R. T. J., Wuelser, J.-P., Freeland, S. and Howard, R. A. (2009), EUV Wave Reflection from a Coronal Hole, *ApJ* **691**, L123–L127.

Gosling, J. T. and Pizzo, V. J. (1999), Formation and Evolution of Corotating Interaction Regions and their Three Dimensional Structure, *Space Sci. Rev.* **89**, 21–52.

Gosling, J. T. and Riley, P. (1996), The acceleration of slow coronal mass ejections in the high-speed solar wind, *Geophys. Res. Lett.* **23**, 2867–2870.

Gosling, J. T., Hundhausen, A. J. and Bame, S. J. (1976), Solar wind stream evolution at large heliocentric distances - Experimental demonstration and the test of a model, *J. Geophys. Res.* **81**, 2111–2122.

Gosling, J. T., McComas, D. J., Phillips, J. L. and Bame, S. J. (1991), Geomagnetic activity associated with earth passage of interplanetary shock disturbances and coronal mass ejections, *J. Geophys. Res.* **96**, 7831–7839.

Gressl, C., Veronig, A. M., Temmer, M., Odstrčil, D., Linker, J. A., Mikić, Z. and Riley, P. (2014), Comparative Study of MHD Modeling of the Background Solar Wind, *Sol. Phys.* **289**, 1783–1801.

Grodent, D., Radioti, A., Bonfond, B. and Gérard, J.-C. (2010), On the origin of Saturn's outer auroral emission, *Journal of Geophysical Research (Space Physics)* **115**, 8219.

Gui, B., Shen, C., Wang, Y., Ye, P., Liu, J., Wang, S. and Zhao, X. (2011), Quantitative Analysis of CME Deflections in the Corona, *Sol. Phys.* **271**, 111–139.

Gurnett, D., Huff, R., Morgan, D., Persoon, A., Averkamp, T., Kirchner, D., Duru, F., Akalin, F., Kopf, A., Nielsen, E., Safaeinili, A., Plaut, J. and Picardi, G. (2008), An overview of radar soundings of the martian ionosphere from the Mars Express spacecraft, *Advances in Space Research* **41**(9), 1335 – 1346.

Haider, S. A. (2012), Role of solar X-ray flares and CME in the E region ionosphere of Mars: MGS observations, *Planet. Space Sci.* **63**, 56–61.

Haider, S. A., Abdu, M. A., Batista, I. S., Sobral, J. H., Kallio, E., Maguire, W. C. and Verigin, M. I. (2009), On the responses to solar X-ray flare and coronal mass ejection in the ionospheres of Mars and Earth, *Geophys. Res. Lett.* **36**, 13104.

Hanlon, P. G., Dougherty, M. K., Forsyth, R. J., Owens, M. J., Hansen, K. C., Tóth, G., Crary, F. J. and Young, D. T. (2004), On the evolution of the solar wind between 1 and 5 AU at the time of the Cassini Jupiter flyby: Multispacecraft observations of interplanetary coronal mass ejections including the formation of a merged interaction region, *Journal of Geophysical Research (Space Physics)* **109**, 9.

Harra, L. K. and Mason, K. O. (2004), *Space Science*, Imperial College Press.

Harten, R. and Clark, K. (1995), The Design Features of the GGS Wind and Polar Spacecraft, *Space Sci. Rev.* **71**, 23–40.

Hirayama, T. (1974), Theoretical Model of Flares and Prominences. I: Evaporating Flare Model, *Sol. Phys.* **34**, 323–338.

Howard, R. A., Moses, J. D., Vourlidas, A., Newmark, J. S., Socker, D. G., Plunkett, S. P., Korendyke, C. M., Cook, J. W., Hurley, A., Davila, J. M., Thompson, W. T., St Cyr, O. C., Mentzell, E., Mehalick, K., Lemen, J. R., Wuelser, J. P., Duncan, D. W., Tarbell, T. D., Wolfson, C. J., Moore, A., Harrison, R. A., Waltham, N. R., Lang, J., Davis, C. J., Eyles, C. J., Mapson-Menard, H., Simnett, G. M., Halain, J. P., Defise, J. M., Mazy, E., Rochus, P., Mercier, R., Ravet, M. F., Delmotte, F., Auchere, F., Delaboudiniere, J. P., Bothmer, V., Deutsch, W., Wang, D., Rich, N., Cooper, S., Stephens, V., Maahs, G., Baugh, R., McMullin, D. and Carter, T. (2008), Sun Earth Connection Coronal and Heliospheric Investigation (SECCHI), *Space Sci. Rev.* **136**, 67–115.

Hundhausen, A. J. and Gosling, J. T. (1976), Solar wind structure at large heliocentric distances - an interpretation of Pioneer 10 observations, *J. Geophys. Res.* **81**, 1436–1440.

Isavnin, A., Vourlidas, A. and Kilpua, E. K. J. (2014), Three-Dimensional Evolution of Flux-Rope CMEs and Its Relation to the Local Orientation of the Heliospheric Current Sheet, *Sol. Phys.* **289**, 2141–2156.

Jackman, C. M., Achilleos, N., Bunce, E. J., Cecconi, B., Clarke, J. T., Cowley, S. W. H., Kurth, W. S. and Zarka, P. (2005), Interplanetary conditions and magnetospheric dynamics during the Cassini orbit insertion fly-through of Saturn's magnetosphere, *Journal of Geophysical Research (Space Physics)* **110**, 10212.

Jackman, C. M., Achilleos, N., Bunce, E. J., Cowley, S. W. H., Dougherty, M. K., Jones, G. H., Milan, S. E. and Smith, E. J. (2004), Interplanetary

magnetic field at ˜9 AU during the declining phase of the solar cycle and its implications for Saturn's magnetospheric dynamics, *Journal of Geophysical Research (Space Physics)* **109**, 11203.

Jackman, C. M., Forsyth, R. J. and Dougherty, M. K. (2008), The overall configuration of the interplanetary magnetic field upstream of Saturn as revealed by Cassini observations, *Journal of Geophysical Research (Space Physics)* **113**, 8114.

Jian, L. K., Russell, C. T., Luhmann, J. G., Galvin, A. B. and Simunac, K. D. C. (2013), Solar wind observations at STEREO: 2007 - 2011, *in* G. P. Zank, J. Borovsky, R. Bruno, J. Cirtain, S. Cranmer, H. Elliott, J. Giacalone, W. Gonzalez, G. Li, E. Marsch, E. Moebius, N. Pogorelov, J. Spann and O. Verkhoglyadova (eds.), *American Institute of Physics Conference Series*, Vol. 1539 of *American Institute of Physics Conference Series*, pp.191–194.

Jian, L. K., Russell, C. T., Luhmann, J. G., MacNeice, P. J., Odstrcil, D., Riley, P., Linker, J. A., Skoug, R. M. and Steinberg, J. T. (2011), Comparison of Observations at ACE and Ulysses with Enlil Model Results: Stream Interaction Regions During Carrington Rotations 2016 - 2018, *Sol. Phys.* **273**, 179–203.

Jian, L. K., Russell, C. T., Luhmann, J. G., Skoug, R. M. and Steinberg, J. T. (2008), Stream Interactions and Interplanetary Coronal Mass Ejections at 5.3 AU near the Solar Ecliptic Plane, *Sol. Phys.* **250**, 375–402.

Jian, L., Russell, C. T., Luhmann, J. G. and Skoug, R. M. (2006), Properties of Stream Interactions at One AU During 1995 2004, *Sol. Phys.* **239**, 337–392.

Kahler, S. (1994), Injection profiles of solar energetic particles as functions of coronal mass ejection heights, *Astrophys. J.* **428**, 837–842.

Kahler, S. W., Sheeley, Jr., N. R. and Liggett, M. (1989), Coronal mass ejections and associated X-ray flare durations, *ApJ* **344**, 1026–1033.

Kaiser, M. L., Kucera, T. A., Davila, J. M., St. Cyr, O. C., Guhathakurta, M. and Christian, E. (2008), The STEREO Mission: An Introduction, *Space Sci. Rev.* **136**, 5–16.

Kallenrode, M.-B., Wibberenz, G., Kunow, H., Müller-Mellin, R., Stolpovskii, V. and Kontor, N. (1993), Multi-spacecraft observations of particle events and interplanetary shocks during November/December 1982, *Sol. Phys.* **147**, 377–410.

Kanani, S. J., Arridge, C. S., Jones, G. H., Fazakerley, A. N., McAndrews, H. J., Sergis, N., Krimigis, S. M., Dougherty, M. K., Coates, A. J., Young, D. T., Hansen, K. C. and Krupp, N. (2010), A new form of Saturn's magnetopause using a dynamic pressure balance model, based on in situ, multi-instrument Cassini measurements, *Journal of Geophysical Research (Space Physics)* **115**, 6207.

Kivelson, M. G. and Russell, C. T. (1995), *Introduction to Space Physics*.

Klein, L. W. and Burlaga, L. F. (1982), Interplanetary magnetic clouds at 1 AU, *J. Geophys. Res.* **87**, 613–624.

Kopp, R. A. and Pneuman, G. W. (1976), Magnetic reconnection in the corona and the loop prominence phenomenon, *Sol. Phys.* **50**, 85–98.

Krucker, S., Larson, D. E., Lin, R. P. and Thompson, B. J. (1999), On the Origin of Impulsive Electron Events Observed at 1 AU, *Astrophys. J.* **519**, 864–875.

Lee, C. O., Luhmann, J. G., Odstrcil, D., MacNeice, P. J., de Pater, I., Riley, P. and Arge, C. N. (2009), The Solar Wind at 1 AU During the Declining Phase of Solar Cycle 23: Comparison of 3D Numerical Model Results with Observations, *Sol. Phys.* **254**, 155–183.

Lemen, J. R., Title, A. M., Akin, D. J., Boerner, P. F., Chou, C., Drake, J. F., Duncan, D. W., Edwards, C. G., Friedlaender, F. M., Heyman, G. F., Hurlburt, N. E., Katz, N. L., Kushner, G. D., Levay, M., Lindgren, R. W., Mathur, D. P., McFeaters, E. L., Mitchell, S., Rehse, R. A., Schrijver, C. J.,

Springer, L. A., Stern, R. A., Tarbell, T. D., Wuelser, J.-P., Wolfson, C. J., Yanari, C., Bookbinder, J. A., Cheimets, P. N., Caldwell, D., Deluca, E. E., Gates, R., Golub, L., Park, S., Podgorski, W. A., Bush, R. I., Scherrer, P. H., Gummin, M. A., Smith, P., Auker, G., Jerram, P., Pool, P., Soufli, R., Windt, D. L., Beardsley, S., Clapp, M., Lang, J. and Waltham, N. (2012), The Atmospheric Imaging Assembly (AIA) on the Solar Dynamics Observatory (SDO), *Sol. Phys.* **275**, 17–40.

Lepping, R. P., Burlaga, L. F., Szabo, A., Ogilvie, K. W., Mish, W. H., Vassiliadis, D., Lazarus, A. J., Steinberg, J. T., Farrugia, C. J., Janoo, L. and Mariani, F. (1997), The Wind magnetic cloud and events of October 18-20, 1995: Interplanetary properties and as triggers for geomagnetic activity, *J. Geophys. Res.* **102**, 14049–14064.

Levine, R. H., Altschuler, M. D. and Harvey, J. W. (1977), Solar sources of the interplanetary magnetic field and solar wind, *J. Geophys. Res.* **82**, 1061–1065.

Liewer, P. C., Hall, J. R., Howard, R. A., de Jong, E. M., Thompson, W. T. and Thernisien, A. (2011), Stereoscopic analysis of STEREO/SECCHI data for CME trajectory determination, *Journal of Atmospheric and Solar-Terrestrial Physics* **73**, 1173–1186.

Lin, R. P., Anderson, K. A., Ashford, S., Carlson, C., Curtis, D., Ergun, R., Larson, D., McFadden, J., McCarthy, M., Parks, G. K., Rème, H., Bosqued, J. M., Coutelier, J., Cotin, F., D'Uston, C., Wenzel, K.-P., Sanderson, T. R., Henrion, J., Ronnet, J. C. and Paschmann, G. (1995), A Three-Dimensional Plasma and Energetic Particle Investigation for the Wind Spacecraft, *Space Sci. Rev.* **71**, 125–153.

Liu, Y. D., Richardson, J. D., Wang, C. and Luhmann, J. G. (2014), Propagation of the 2012 March Coronal Mass Ejections from the Sun to Heliopause, *ApJ* **788**, L28.

Liu, Y., Davies, J. A., Luhmann, J. G., Vourlidas, A., Bale, S. D. and Lin,

R. P. (2010a), Geometric Triangulation of Imaging Observations to Track Coronal Mass Ejections Continuously Out to 1 AU, *ApJ* **710**, L82–L87.

Liu, Y., Luhmann, J. G., Bale, S. D. and Lin, R. P. (2009), Relationship Between a Coronal Mass Ejection-Driven Shock and a Coronal Metric Type II Burst, *ApJ* **691**, L151–L155.

Liu, Y., Luhmann, J. G., Bale, S. D. and Lin, R. P. (2011), Solar Source and Heliospheric Consequences of the 2010 April 3 Coronal Mass Ejection: A Comprehensive View, *ApJ* **734**, 84.

Liu, Y., Thernisien, A., Luhmann, J. G., Vourlidas, A., Davies, J. A., Lin, R. P. and Bale, S. D. (2010b), Reconstructing Coronal Mass Ejections with Coordinated Imaging and in Situ Observations: Global Structure, Kinematics, and Implications for Space Weather Forecasting, *ApJ* **722**, 1762–1777.

Long, D. M., DeLuca, E. E. and Gallagher, P. T. (2011a), The Wave Properties of Coronal Bright Fronts Observed Using SDO/AIA, *ApJ* **741**, L21.

Long, D. M., Gallagher, P. T., McAteer, R. T. J. and Bloomfield, D. S. (2011b), Deceleration and dispersion of large-scale coronal bright fronts, *Astron. Astrophys.* **531**, A42.

Lugaz, N., Farrugia, C. J., Davies, J. A., Möstl, C., Davis, C. J., Roussev, I. I. and Temmer, M. (2012), The Deflection of the Two Interacting Coronal Mass Ejections of 2010 May 23-24 as Revealed by Combined in Situ Measurements and Heliospheric Imaging, *ApJ* **759**, 68.

Lugaz, N., Vourlidas, A., Roussev, I. I. and Morgan, H. (2009), Solar - Terrestrial Simulation in the STEREO Era: The 24 - 25 January 2007 Eruptions, *Sol. Phys.* **256**, 269–284.

Luhmann, J. G., Curtis, D. W., Schroeder, P., McCauley, J., Lin, R. P., Larson, D. E., Bale, S. D., Sauvaud, J.-A., Aoustin, C., Mewaldt, R. A., Cummings, A. C., Stone, E. C., Davis, A. J., Cook, W. R., Kecman, B., Wiedenbeck, M. E., von Rosenvinge, T., Acuna, M. H., Reichenthal, L. S., Shuman, S., Wortman, K. A., Reames, D. V., Mueller-Mellin, R., Kunow,

H., Mason, G. M., Walpole, P., Korth, A., Sanderson, T. R., Russell, C. T. and Gosling, J. T. (2008), STEREO IMPACT Investigation Goals, Measurements, and Data Products Overview, *Space Sci. Rev.* **136**, 117–184.

Luhmann, J. G., Solomon, S. C., Linker, J. A., Lyon, J. G., Mikic, Z., Odstrcil, D., Wang, W. and Wiltberger, M. (2004), Coupled model simulation of a Sun-to-Earth space weather event, *Journal of Atmospheric and Solar-Terrestrial Physics* **66**, 1243–1256.

MacNeice, P., Elliott, B. and Acebal, A. (2011), Validation of community models: 3. Tracing field lines in heliospheric models, *Space Weather* **9**(10), n/a–n/a.

MacQueen, R. M., Hundhausen, A. J. and Conover, C. W. (1986), The propagation of coronal mass ejection transients, *J. Geophys. Res.* **91**, 31–38.

Mahajan, K. K., Lodhi, N. K. and Singh, S. (2009), Ionospheric effects of solar flares at Mars, *Geophys. Res. Lett.* **36**, 15207.

Manchester, IV, W. B., Vourlidas, A., Tóth, G., Lugaz, N., Roussev, I. I., Sokolov, I. V., Gombosi, T. I., De Zeeuw, D. L. and Opher, M. (2008), Three-dimensional MHD Simulation of the 2003 October 28 Coronal Mass Ejection: Comparison with LASCO Coronagraph Observations, *Astrophys. J.* **684**, 1448–1460.

McComas, D. J., Bame, S. J., Barker, P., Feldman, W. C., Phillips, J. L., Riley, P. and Griffee, J. W. (1998), Solar Wind Electron Proton Alpha Monitor (SWEPAM) for the Advanced Composition Explorer, *Space Sci. Rev.* **86**, 563–612.

Mewaldt, R. A., Cohen, C. M. S., Cook, W. R., Cummings, A. C., Davis, A. J., Geier, S., Kecman, B., Klemic, J., Labrador, A. W., Leske, R. A., Miyasaka, H., Nguyen, V., Ogliore, R. C., Stone, E. C., Radocinski, R. G., Wiedenbeck, M. E., Hawk, J., Shuman, S., von Rosenvinge, T. T. and Wortman, K. (2008), The Low-Energy Telescope (LET) and SEP Central Electronics for the STEREO Mission, *Space Sci. Rev.* **136**, 285–362.

Moreton, G. E. and Ramsey, H. E. (1960), Recent Observations of Dynamical Phenomena Associated with Solar Flares, *PASP* **72**, 357.

Moses, D., Clette, F., Delaboudinière, J.-P., Artzner, G. E., Bougnet, M., Brunaud, J., Carabetian, C., Gabriel, A. H., Hochedez, J. F., Millier, F., Song, X. Y., Au, B., Dere, K. P., Howard, R. A., Kreplin, R., Michels, D. J., Defise, J. M., Jamar, C., Rochus, P., Chauvineau, J. P., Marioge, J. P., Catura, R. C., Lemen, J. R., Shing, L., Stern, R. A., Gurman, J. B., Neupert, W. M., Newmark, J., Thompson, B., Maucherat, A., Portier-Fozzani, F., Berghmans, D., Cugnon, P., van Dessel, E. L. and Gabryl, J. R. (1997), EIT Observations of the Extreme Ultraviolet Sun, *Sol. Phys.* **175**, 571–599.

Möstl, C., Farrugia, C. J., Kilpua, E. K. J., Jian, L. K., Liu, Y., Eastwood, J. P., Harrison, R. A., Webb, D. F., Temmer, M., Odstrcil, D., Davies, J. A., Rollett, T., Luhmann, J. G., Nitta, N., Mulligan, T., Jensen, E. A., Forsyth, R., Lavraud, B., de Koning, C. A., Veronig, A. M., Galvin, A. B., Zhang, T. L. and Anderson, B. J. (2012), Multi-point Shock and Flux Rope Analysis of Multiple Interplanetary Coronal Mass Ejections around 2010 August 1 in the Inner Heliosphere, *ApJ* **758**, 10.

Muhr, N., Veronig, A. M., Kienreich, I. W., Temmer, M. and Vršnak, B. (2011), Analysis of Characteristic Parameters of Large-scale Coronal Waves Observed by the Solar-Terrestrial Relations Observatory/Extreme Ultraviolet Imager, *Astrophys. J.* **739**, 89.

Müller-Mellin, R., Böttcher, S., Falenski, J., Rode, E., Duvet, L., Sanderson, T., Butler, B., Johlander, B. and Smit, H. (2008), The Solar Electron and Proton Telescope for the STEREO Mission, *Space Sci. Rev.* **136**, 363–389.

Munro, R. H., Gosling, J. T., Hildner, E., MacQueen, R. M., Poland, A. I. and Ross, C. L. (1979), The association of coronal mass ejection transients with other forms of solar activity, *Sol. Phys.* **61**, 201–215.

Nagy, A. F., Winterhalter, D., Sauer, K., Cravens, T. E., Brecht, S., Mazelle, C., Crider, D., Kallio, E., Zakharov, A., Dubinin, E., Verigin, M., Kotova,

G., Axford, W. I., Bertucci, C. and Trotignon, J. G. (2004), The plasma Environment of Mars, *Space Sci. Rev.* **111**, 33–114.

Ness, N. F. (1970), Magnetometers for Space Research, *Space Sci. Rev.* **11**, 459–554.

Nieves-Chinchilla, T., Vourlidas, A., Stenborg, G., Savani, N. P., Koval, A., Szabo, A. and Jian, L. K. (2013), Inner Heliospheric Evolution of a "Stealth" CME Derived from Multi-view Imaging and Multipoint in Situ observations. I. Propagation to 1 AU, *ApJ* **779**, 55.

Odstrcil, D. and Pizzo, V. J. (1999a), Distortion of the interplanetary magnetic field by three-dimensional propagation of coronal mass ejections in a structured solar wind, *J. Geophys. Res.* **104**, 28225–28240.

Odstrcil, D. and Pizzo, V. J. (1999b), Three-dimensional propagation of CMEs in a structured solar wind flow: 1. CME launched within the streamer belt, *J. Geophys. Res.* **104**, 483–492.

Odstrcil, D. and Pizzo, V. J. (2009), Numerical Heliospheric Simulations as Assisting Tool for Interpretation of Observations by STEREO Heliospheric Imagers, *Sol. Phys.* **259**, 297–309.

Odstrcil, D., Linker, J. A., Lionello, R., Mikic, Z., Riley, P., Pizzo, V. J. and Luhmann, J. G. (2002), Merging of coronal and heliospheric numerical two-dimensional MHD models, *Journal of Geophysical Research (Space Physics)* **107**, 1493.

Odstrcil, D., Pizzo, V. J., Linker, J. A., Riley, P., Lionello, R. and Mikic, Z. (2004), Initial coupling of coronal and heliospheric numerical magnetohydrodynamic codes, *Journal of Atmospheric and Solar-Terrestrial Physics* **66**, 1311–1320.

Parker, E. N. (1957), Sweet's Mechanism for Merging Magnetic Fields in Conducting Fluids, *J. Geophys. Res.* **62**, 509–520.

Parker, E. N. (1958), Dynamics of the Interplanetary Gas and Magnetic Fields., *ApJ* **128**, 664.

Pesnell, W. D., Thompson, B. J. and Chamberlin, P. C. (2012), The Solar Dynamics Observatory (SDO), *Sol. Phys.* **275**, 3–15.

Petschek, H. E. (1964), Magnetic Field Annihilation, *NASA Special Publication* **50**, 425.

Phillips, J. L., Luhmann, J. G. and Stewart, A. I. F. (1986), The Venus ultraviolet aurora - Observations at 130.4 NM, *Geophys. Res. Lett.* **13**, 1047–1050.

Phillips, K. J. H. (1992), *Guide to the sun*.

Pizzo, V. (1978), A three-dimensional model of corotating streams in the solar wind. I - Theoretical foundations, *J. Geophys. Res.* **83**, 5563–5572.

Prangé, R., Pallier, L., Hansen, K. C., Howard, R., Vourlidas, A., Courtin, R. and Parkinson, C. (2004), An interplanetary shock traced by planetary auroral storms from the Sun to Saturn, *Nature* **432**, 78–81.

Prise, A., Harra, L., Matthews, S., Long, D. and Aylward, A. (2014), An Investigation of the CME of 3 November 2011 and Its Associated Widespread Solar Energetic Particle Event, *Solar Physics* **289**(5), 1731–1744.

Prise, A. J., Harra, L. K., Matthews, S. A., Arridge, C. S. and Achilleos, N. (2015), Analysis of a coronal mass ejection and corotating interaction region as they travel from the Sun passing Venus, Earth, Mars, and Saturn, *Journal of Geophysical Research: Space Physics* **120**(3), 1566–1588. 2014JA020256.

Pulkkinen, A., Oates, T. and Taktakishvili, A. (2010), Automatic Determination of the Conic Coronal Mass Ejection Model Parameters, *Sol. Phys.* **261**, 115–126.

Pulkkinen, T. (2007), Space Weather: Terrestrial Perspective, *Living Reviews in Solar Physics* **4**(1).

Reames, D. V. (1993), Non-thermal particles in the interplanetary medium, *Adv. Space Res.* **13**, 331–339.

Reames, D. V., Barbier, L. M. and Ng, C. K. (1996), The Spatial Distribution of Particles Accelerated by Coronal Mass Ejection–driven Shocks, *ApJ* **466**, 473.

Richardson, I. G. and Cane, H. V. (1995), Regions of abnormally low proton temperature in the solar wind (1965-1991) and their association with ejecta, *J. Geophys. Res.* **100**, 23397–23412.

Riley, P., Linker, J. A. and Miki, Z. (2001), An empirically-driven global MHD model of the solar corona and inner heliosphere, *Journal of Geophysical Research: Space Physics* **106**(A8), 15889–15901.

Riley, P., Linker, J. A., Mikić, Z., Lionello, R., Ledvina, S. A. and Luhmann, J. G. (2006), A Comparison between Global Solar Magnetohydrodynamic and Potential Field Source Surface Model Results, *ApJ* **653**, 1510–1516.

Robbrecht, E., Patsourakos, S. and Vourlidas, A. (2009), No Trace Left Behind: STEREO Observation of a Coronal Mass Ejection Without Low Coronal Signatures, *ApJ* **701**, 283–291.

Rouillard, A. P. (2011), Relating white light and in situ observations of coronal mass ejections: A review, *Journal of Atmospheric and Solar-Terrestrial Physics* **73**, 1201–1213.

Rouillard, A. P., Davies, J. A., Forsyth, R. J., Savani, N. P., Sheeley, N. R., Thernisien, A., Zhang, T.-L., Howard, R. A., Anderson, B., Carr, C. M., Tsang, S., Lockwood, M., Davis, C. J., Harrison, R. A., Bewsher, D., Fränz, M., Crothers, S. R., Eyles, C. J., Brown, D. S., Whittaker, I., Hapgood, M., Coates, A. J., Jones, G. H., Grande, M., Frahm, R. A. and Winningham, J. D. (2009), A solar storm observed from the Sun to Venus using the STEREO, Venus Express, and MESSENGER spacecraft, *Journal of Geophysical Research (Space Physics)* **114**, 7106.

Rouillard, A. P., Lavraud, B., Sheeley, N. R., Davies, J. A., Burlaga, L. F., Savani, N. P., Jacquey, C. and Forsyth, R. J. (2010), White Light and In Situ Comparison of a Forming Merged Interaction Region, *ApJ* **719**, 1385–1392.

Rouillard, A. P., Odstřcil, D., Sheeley, N. R., Tylka, A., Vourlidas, A., Mason, G., Wu, C.-C., Savani, N. P., Wood, B. E., Ng, C. K., Stenborg, G., Szabo, A. and St. Cyr, O. C. (2011), Interpreting the Properties of Solar Energetic Particle Events by Using Combined Imaging and Modeling of Interplanetary Shocks, *ApJ* **735**, 7.

Rouillard, A. P., Sheeley, N. R., Tylka, A., Vourlidas, A., Ng, C. K., Rakowski, C., Cohen, C. M. S., Mewaldt, R. A., Mason, G. M., Reames, D., Savani, N. P., StCyr, O. C. and Szabo, A. (2012), The Longitudinal Properties of a Solar Energetic Particle Event Investigated Using Modern Solar Imaging, *Astrophys. J.* **752**, 44.

Russell, C. T., Luhmann, J. G., Cravens, T. E., Nagy, A. F. and Strangeway, R. J. (2007), Venus upper atmosphere and plasma environment: Critical issues for future exploration, *Washington DC American Geophysical Union Geophysical Monograph Series* **176**, 139–156.

Russell, C. T., Shinde, A. A. and Jian, L. (2005), A new parameter to define interplanetary coronal mass ejections, *Advances in Space Research* **35**, 2178–2184.

Safaeinili, A., Kofman, W., Mouginot, J., Gim, Y., Herique, A., Ivanov, A. B., Plaut, J. J. and Picardi, G. (2007), Estimation of the total electron content of the Martian ionosphere using radar sounder surface echoes, *Geophys. Res. Lett.* **34**, 23204.

Schatten, K. H. (1971), Current sheet magnetic model for the solar corona., *Cosmic Electrodynamics* **2**, 232–245.

Schatten, K. H., Wilcox, J. M. and Ness, N. F. (1969), A model of interplanetary and coronal magnetic fields, *Sol. Phys.* **6**, 442–455.

Schwartz, S. J., Henley, E., Mitchell, J. and Krasnoselskikh, V. (2011), Electron Temperature Gradient Scale at Collisionless Shocks, *Physical Review Letters* **107**(21), 215002.

Schwenn, R. (2006), Space Weather: The Solar Perspective, *Living Reviews in Solar Physics* **3**(2).

Sheeley, Jr., N. R., Howard, R. A., Koomen, M. J. and Michels, D. J. (1983), Associations between coronal mass ejections and soft X-ray events, *ApJ* **272**, 349–354.

Sheeley, N. R., Hakala, W. N. and Wang, Y.-M. (2000), Detection of coronal mass ejection associated shock waves in the outer corona, *J. Geophys. Res.* **105**, 5081–5092.

Shen, C., Wang, Y., Wang, S., Liu, Y., Liu, R., Vourlidas, A., Miao, B., Ye, P., Liu, J. and Zhou, Z. (2012), Super-elastic collision of large-scale magnetized plasmoids in the heliosphere, *Nature Physics* **8**, 923–928.

Shen, F., Shen, C., Wang, Y., Feng, X. and Xiang, C. (2013), Could the collision of CMEs in the heliosphere be super-elastic? Validation through three-dimensional simulations, *Geophys. Res. Lett.* **40**, 1457–1461.

Shibata, K., Masuda, S., Shimojo, M., Hara, H., Yokoyama, T., Tsuneta, S., Kosugi, T. and Ogawara, Y. (1995), Hot-Plasma Ejections Associated with Compact-Loop Solar Flares, *ApJ* **451**, L83.

Shue, J.-H., Chao, J. K., Fu, H. C., Russell, C. T., Song, P., Khurana, K. K. and Singer, H. J. (1997), A new functional form to study the solar wind control of the magnetopause size and shape, *J. Geophys. Res.* **102**, 9497–9512.

Siscoe, G. L. and Huang, T. S. (1985), Polar cap inflation and deflation, *Journal of Geophysical Research: Space Physics* **90**(A1), 543–547.

Smith, C. W., L'Heureux, J., Ness, N. F., Acuña, M. H., Burlaga, L. F. and Scheifele, J. (1998), The ACE Magnetic Fields Experiment, *Space Sci. Rev.* **86**, 613–632.

Smith, E. J. and Wolfe, J. H. (1976), Observations of interaction regions and corotating shocks between one and five AU - Pioneers 10 and 11, *Geophys. Res. Lett.* **3**, 137–140.

Stallard, T., Miller, S., Melin, H., Lystrup, M., Cowley, S. W. H., Bunce, E. J., Achilleos, N. and Dougherty, M. (2008), Jovian-like aurorae on Saturn, *Nature* **453**, 1083–1085.

Stone, E. C., Frandsen, A. M., Mewaldt, R. A., Christian, E. R., Margolies, D., Ormes, J. F. and Snow, F. (1998), The Advanced Composition Explorer, *Space Sci. Rev.* **86**, 1–22.

Sturrock, P. A. (1966), Model of the High-Energy Phase of Solar Flares, *Nature* **211**, 695–697.

Svedhem, H., Titov, D. V., McCoy, D., Lebreton, J.-P., Barabash, S., Bertaux, J.-L., Drossart, P., Formisano, V., Häusler, B., Korablev, O., Markiewicz, W. J., Nevejans, D., Pätzold, M., Piccioni, G., Zhang, T. L., Taylor, F. W., Lellouch, E., Koschny, D., Witasse, O., Eggel, H., Warhaut, M., Accomazzo, A., Rodriguez-Canabal, J., Fabrega, J., Schirmann, T., Clochet, A. and Coradini, M. (2007), Venus Express: The first European mission to Venus, *Planet. Space Sci.* **55**, 1636–1652.

Sweet, P. A. (1958), The Neutral Point Theory of Solar Flares, *in* B. Lehnert (ed.), *Electromagnetic Phenomena in Cosmical Physics*, Vol. 6 of *IAU Symposium*, p.123.

Taktakishvili, A., Kuznetsova, M., MacNeice, P., Hesse, M., Rastätter, L., Pulkkinen, A., Chulaki, A. and Odstrcil, D. (2009), Validation of the coronal mass ejection predictions at the Earth orbit estimated by ENLIL heliosphere cone model, *Space Weather* **7**, 3004.

Taktakishvili, A., MacNeice, P. and Odstrcil, D. (2010), Model uncertainties in predictions of arrival of coronal mass ejections at Earth orbit, *Space Weather* **8**, 6007.

Thompson, B. J., Plunkett, S. P., Gurman, J. B., Newmark, J. S., St. Cyr, O. C. and Michels, D. J. (1998), SOHO/EIT observations of an Earth-directed coronal mass ejection on May 12, 1997, *Geophys. Res. Lett.* **25**, 2465–2468.

Thompson, W. T., Davila, J. M., Fisher, R. R., Orwig, L. E., Mentzell, J. E., Hetherington, S. E., Derro, R. J., Federline, R. E., Clark, D. C., Chen, P. T. C., Tveekrem, J. L., Martino, A. J., Novello, J., Wesenberg, R. P., StCyr, O. C., Reginald, N. L., Howard, R. A., Mehalick, K. I., Hersh, M. J., Newman, M. D., Thomas, D. L., Card, G. L. and Elmore, D. F. (2003), COR1 inner coronagraph for STEREO-SECCHI, *in* S. L. Keil and S. V. Avakyan (eds.), *Soc. Photo-Optical Instrument. Eng. (SPIE) CS*, Vol. 4853, pp.1–11.

Torsti, J., Kocharov, L., Teittinen, M., Anttila, A., Laitinen, T., Mäkelä, P., Riihonen, E., Vainio, R. and Valtonen, E. (1999), Energetic (˜10-65 MeV) protons observed by ERNE on August 13-14, 1996: Eruption on the solar back side as a possible source of the event, *J. Geophys. Res.* **104**, 9903–9910.

Torsti, J., Riihonen, E. and Kocharov, L. (2004), The 1998 May 2-3 Magnetic Cloud: An Interplanetary "Highway" for Solar Energetic Particles Observed with SOHO/ERNE, *ApJ* **600**, L83–L86.

Tylka, A. J., Cohen, C. M. S., Dietrich, W. F., Krucker, S., McGuire, R. E., Mewaldt, R. A., Ng, C. K., Reames, D. V. and Share, G. H. (2003), Onsets and Release Times in Solar Particle Events, *in* T. Kajita, Y. Asaoka, A. Kawachi, Y. Matsubara and M. Sasaki (eds.), *Internat. Cosmic Ray Conf.*, Vol. 6, IUPAP, p.3305.

von Rosenvinge, T. T., Barbier, L. M., Karsch, J., Liberman, R., Madden, M. P., Nolan, T., Reames, D. V., Ryan, L., Singh, S., Trexel, H., Winkert, G., Mason, G. M., Hamilton, D. C. and Walpole, P. (1995), The Energetic Particles: Acceleration, Composition, and Transport (EPACT) investigation on the WIND spacecraft, *Space Sci. Rev.* **71**, 155–206.

von Rosenvinge, T. T., Reames, D. V., Baker, R., Hawk, J., Nolan, J. T., Ryan, L., Shuman, S., Wortman, K. A., Mewaldt, R. A., Cummings, A. C., Cook, W. R., Labrador, A. W., Leske, R. A. and Wiedenbeck, M. E. (2008), The High Energy Telescope for STEREO, *Space Sci. Rev.* **136**, 391–435.

Vourlidas, A. and Howard, R. A. (2006), The Proper Treatment of Coronal

Mass Ejection Brightness: A New Methodology and Implications for Observations, *ApJ* **642**, 1216–1221.

Vourlidas, A., Wu, S. T., Wang, A. H., Subramanian, P. and Howard, R. A. (2003), Direct Detection of a Coronal Mass Ejection-Associated Shock in Large Angle and Spectrometric Coronagraph Experiment White-Light Images, *ApJ* **598**, 1392–1402.

Vršnak, B., Temmer, M., Žic, T., Taktakishvili, A., Dumbović, M., Möstl, C., Veronig, A. M., Mays, M. L. and Odstrčil, D. (2014), Heliospheric Propagation of Coronal Mass Ejections: Comparison of Numerical WSA-ENLIL+Cone Model and Analytical Drag-based Model, *ApJS* **213**, 21.

Wang, Y., Chen, C., Gui, B., Shen, C., Ye, P. and Wang, S. (2011), Statistical study of coronal mass ejection source locations: Understanding CMEs viewed in coronagraphs, *Journal of Geophysical Research (Space Physics)* **116**, 4104.

Wang, Y.-M. (2000), EIT Waves and Fast-Mode Propagation in the Solar Corona, *ApJ* **543**, L89–L93.

Wang, Y. M., Ye, P. Z. and Wang, S. (2003), Multiple magnetic clouds: Several examples during March-April 2001, *Journal of Geophysical Research (Space Physics)* **108**, 1370.

Wang, Y., Shen, C., Wang, S. and Ye, P. (2004), Deflection of coronal mass ejection in the interplanetary medium, *Sol. Phys.* **222**, 329–343.

Wang, Y., Wang, B., Shen, C., Shen, F. and Lugaz, N. (2014), Deflected propagation of a coronal mass ejection from the corona to interplanetary space, *Journal of Geophysical Research (Space Physics)* **119**, 5117–5132.

Wang, Y., Zheng, H., Wang, S. and Ye, P. (2005), MHD simulation of the formation and propagation of multiple magnetic clouds in the heliosphere, *A&A* **434**, 309–316.

Warmuth, A., Vršnak, B., Aurass, H. and Hanslmeier, A. (2001), Evolution of Two EIT/Hα Moreton Waves, *ApJ* **560**, L105–L109.

Webb, D. F., Howard, T. A., Fry, C. D., Kuchar, T. A., Mizuno, D. R., Johnston, J. C. and Jackson, B. V. (2009), Studying geoeffective interplanetary coronal mass ejections between the Sun and Earth: Space weather implications of Solar Mass Ejection Imager observations, *Space Weather* **7**, 5002.

Williams, A. O., Edberg, N. J. T., Milan, S. E., Lester, M., Fränz, M. and Davies, J. A. (2011), Tracking corotating interaction regions from the Sun through to the orbit of Mars using ACE, MEX, VEX, and STEREO, *Journal of Geophysical Research (Space Physics)* **116**, 8103.

Wills-Davey, M. J., DeForest, C. E. and Stenflo, J. O. (2007), Are "EIT Waves" Fast-Mode MHD Waves?, *ApJ* **664**, 556–562.

Wood, B. E., Howard, R. A., Thernisien, A. and Socker, D. G. (2010), The Three-Dimensional Morphology of a Corotating Interaction Region in the Inner Heliosphere, *ApJ* **708**, L89–L94.

Wood, B. E., Wu, C.-C., Rouillard, A. P., Howard, R. A. and Socker, D. G. (2012), A Coronal Hole's Effects on Coronal Mass Ejection Shock Morphology in the Inner Heliosphere, *ApJ* **755**, 43.

Wu, C.-C., Dryer, M., Wu, S. T., Wood, B. E., Fry, C. D., Liou, K. and Plunkett, S. (2011), Global three-dimensional simulation of the interplanetary evolution of the observed geoeffective coronal mass ejection during the epoch 1-4 August 2010, *Journal of Geophysical Research (Space Physics)* **116**, 12103.

Wu, C.-C., Fry, C. D., Dryer, M., Wu, S. T., Thompson, B., Liou, K. and Feng, X. S. (2007), Three-dimensional global simulation of multiple ICMEs' interaction and propagation from the Sun to the heliosphere following the 25 28 October 2003 solar events, *Advances in Space Research* **40**, 1827–1834.

Wu, C. C., Liou, K., Wu, S. T., Dryer, M., Fry, C. D. and Plunkett, S. (2012), Heliospheric three-dimensional global simulation of multiple interacting coronal mass ejections during the Halloween 2003 epoch, *AIP Conference Proceedings* **1436**(1), 285–291.

Wu, S. T., Wu, C., Liou, K., Plunkett, S., Dryer, M. and Fry, C. D. (2014), Analyses of the Evolution and Interaction of Multiple Coronal Mass Ejections and Their Shocks in July 2012, *in* Q. Hu and G. P. Zank (eds.), *Astronomical Society of the Pacific Conference Series*, Vol. 484 of *Astronomical Society of the Pacific Conference Series*, Astronomical Society of the Pacific, San Fransisco, California, p.241.

Wuelser, J.-P., Lemen, J. R., Tarbell, T. D., Wolfson, C. J., Cannon, J. C., Carpenter, B. A., Duncan, D. W., Gradwohl, G. S., Meyer, S. B., Moore, A. S., Navarro, R. L., Pearson, J. D., Rossi, G. R., Springer, L. A., Howard, R. A., Moses, J. D., Newmark, J. S., Delaboudiniere, J.-P., Artzner, G. E., Auchere, F., Bougnet, M., Bouyries, P., Bridou, F., Clotaire, J.-Y., Colas, G., Delmotte, F., Jerome, A., Lamare, M., Mercier, R., Mullot, M., Ravet, M.-F., Song, X., Bothmer, V. and Deutsch, W. (2004), EUVI: the STEREO-SECCHI extreme ultraviolet imager, *Proc. SPIE* **5171**, 111–122.

Xie, H., Ofman, L. and Lawrence, G. (2004), Cone model for halo CMEs: Application to space weather forecasting, *Journal of Geophysical Research (Space Physics)* **109**, 3109.

Xiong, M., Zheng, H., Wu, S. T., Wang, Y. and Wang, S. (2007), Magnetohydrodynamic simulation of the interaction between two interplanetary magnetic clouds and its consequent geoeffectiveness, *Journal of Geophysical Research (Space Physics)* **112**, 11103.

Yashiro, S., Gopalswamy, N., Akiyama, S., Michalek, G. and Howard, R. A. (2005), Visibility of coronal mass ejections as a function of flare location and intensity, *Journal of Geophysical Research (Space Physics)* **110**, 12.

Yashiro, S., Gopalswamy, N., Michalek, G., St. Cyr, O. C., Plunkett, S. P., Rich, N. B. and Howard, R. A. (2004), A catalog of white light coronal mass ejections observed by the SOHO spacecraft, *Journal of Geophysical Research (Space Physics)* **109**, 7105.

Young, D. T., Berthelier, J. J., Blanc, M., Burch, J. L., Coates, A. J., Goldstein, R., Grande, M., Hill, T. W., Johnson, R. E., Kelha, V., McComas,

D. J., Sittler, E. C., Svenes, K. R., Szegö, K., Tanskanen, P., Ahola, K., Anderson, D., Bakshi, S., Baragiola, R. A., Barraclough, B. L., Black, R. K., Bolton, S., Booker, T., Bowman, R., Casey, P., Crary, F. J., Delapp, D., Dirks, G., Eaker, N., Funsten, H., Furman, J. D., Gosling, J. T., Hannula, H., Holmlund, C., Huomo, H., Illiano, J. M., Jensen, P., Johnson, M. A., Linder, D. R., Luntama, T., Maurice, S., McCabe, K. P., Mursula, K., Narheim, B. T., Nordholt, J. E., Preece, A., Rudzki, J., Ruitberg, A., Smith, K., Szalai, S., Thomsen, M. F., Viherkanto, K., Vilppola, J., Vollmer, T., Wahl, T. E., Wüest, M., Ylikorpi, T. and Zinsmeyer, C. (2004), Cassini Plasma Spectrometer Investigation, *Space Sci. Rev.* **114**, 1–112.

Zhang, T. L., Baumjohann, W., Delva, M., Auster, H.-U., Balogh, A., Russell, C. T., Barabash, S., Balikhin, M., Berghofer, G., Biernat, H. K., Lammer, H., Lichtenegger, H., Magnes, W., Nakamura, R., Penz, T., Schwingenschuh, K., Vörös, Z., Zambelli, W., Fornacon, K.-H., Glassmeier, K.-H., Richter, I., Carr, C., Kudela, K., Shi, J. K., Zhao, H., Motschmann, U. and Lebreton, J.-P. (2006), Magnetic field investigation of the Venus plasma environment: Expected new results from Venus Express, *Planet. Space Sci.* **54**, 1336–1343.

Zhao, X. P., Plunkett, S. P. and Liu, W. (2002), Determination of geometrical and kinematical properties of halo coronal mass ejections using the cone model, *Journal of Geophysical Research (Space Physics)* **107**, 1223.

Zurbuchen, T. H. and Richardson, I. G. (2006), In-Situ Solar Wind and Magnetic Field Signatures of Interplanetary Coronal Mass Ejections, *Space Sci. Rev.* **123**, 31–43.